Investigation of Partial Discharge and Electromagnetic Wave Signal Propagation Characteristics as a Fundamental Study of Diagnosis Technique Improvement on Three-phase Gas Insulated System

Umar Khayam

December, 2007

Doctoral Dissertation

Investigation of Partial Discharge and Electromagnetic Wave Signal Propagation Characteristics as a Fundamental Study of Diagnosis Technique Improvement on Three-phase Gas Insulated System

Umar Khayam
(Student Number: 05586402)

Supervisor: Prof. Masayuki Hikita

Department of Electrical and Electronic Engineering
Graduate School of Engineering
Kyushu Institute of Technology

December, 2007

TABLE OF CONTENTS

Chapter 1

Introduction

1.1 Trends in Energy and Future Electric Power System

The world population is predicted to increase rapidly. According to the United Nation in the world population prospect, it is expected to reach 9.1 billion and grows 34 millions people annually by 2050 [1]. Therefore, energy consumption is also predicted to strongly increase accompanying the population growth. The ratio of the electric power consumption to total energy consumption will extremely increase due to its easy transmit, convenience at the time of using and its cleanliness from the environmental aspect. The world net electricity consumption will nearly double over the next two decades. World energy demand is projected to growth at an average rate of 2.6% per year, from 14.3 thousands GWh in 2002 to 26 thousands GWh in 2025 [2].

Natural energy resources on the other side, such as coal and natural gas, etc., will be exhausted within next few centuries. From the environmental view of point, the problem of acid rain, global warming, and destruction of ozon layer, etc also becomes a huge concern in the recent year. More over, recent trends of deregulation in the global electric energy market also become one factor for change in the electric power system.

Considering above conditions, the future electric power system should satisfy the following properties: capable to carrying of mass power transmission and high reliability; compact and offers significant saving in land use; esthetically acceptable; environmental friendly and enable to be installed in cities very close to the load. Especially in highly populated urban areas, space is so scarce in comparison to population that it would be difficult to provide land for substation facilities as well as for power transmission.

Dealing with the above objectives and technical requirements in the electric power system, three-phase gas insulated system (GIS) is one of the suitable alternatives.

1.2 Three-phase Electric Power

Three-phase electric power is a common method of electric power transmission. It is a type of polyphase system mainly used to power motors and many other devices. A three-phase system uses less conductor material to transmit electric power than equivalent single-phase, two-phase, or direct-current systems at the same voltage.

In a three-phase system, three circuit conductors carry three alternating currents (of the same frequency) which reach their instantaneous peak values at different times. Taking one conductor as a reference, the other two currents are delayed in time by one-third and two-thirds of one cycle of the electrical current. This delay between "phases" has the effect of giving constant power transfer over each cycle of the current, and also makes it possible to produce a rotating magnetic field in an electric motor.

Three-phase systems may or may not have a neutral wire. A neutral wire allows the three-phase system to use a higher voltage while still supporting lower voltage single-phase appliances. In high voltage distribution situations, it is common not to have a neutral wire as the loads can simply be connected between phases (phase-phase connection).

Three-phase has properties that make it very desirable in electric power systems. Firstly, the phase currents tend to cancel one another (summing to zero in the case of a linear balanced load). This makes it possible to eliminate the neutral conductor on some lines; all the phase conductors carry the same current and so can be the same size, for a balanced load. Secondly, power transfer into a linear balanced load is constant, which helps to reduce generator and motor vibrations. Finally, three-phase systems can produce a magnetic field that rotates in a specified direction, which simplifies the design of electric motors. Three is the lowest phase order to exhibit all of these properties.

1.3 Gas insulated switchgear (GIS)

GIS was first developed in various countries between 1968 and 1972 [3]. After about 5 years of experience, the use rate increased to about 20% of new substations in countries where space is limited. Nowadays, gas insulated equipment is a major component of power transmission and distribution system all over the world, especially in densely populated area.

Generally, there are four major type of electrical equipment using gas-insulated technology with SF_6 as insulation and or interruption purposes, those are: gas-insulated switchgear (GIS), gas-insulated transformer (GITr), gas insulated circuit breaker (GCB), and gas insulated transmission line (GITL). Sometimes substation utilizing gas-insulated equipment is also named GIS (gas-insulated substation). In this study, unless and otherwise stated, in general the system with gas as insulation medium will be noted as gas-insulated system (GIS).

International experience with GIS is described in a series of CIGRE papers (CIGRE, 1982; 1992; 1994). The IEEE (IEEE Std. C37. 122-1993; IEEE Std. C37. 122,1-1993) and the IEC (IEC, 1990) have standards covering all aspects of the design, testing, and use of GIS. IEEE also has a guide for specifications for GIS (IEEE Std. C37. 123-1996) [3].

Gas insulated substation are modular systems consisting of a gas tight (for example coaxial) enclosure in which an insulating gas is confined. The high voltage conductor is centered by spacers. Instead of pure SF_6, gas mixtures of SF_6 and N_2 can be used to reduce costs of the equipment and SF_6 leakages. A GIS has, besides the straight parts, more complex parts such as circuit breakers, disconnecting and earthing switches, T-junctions and bends. GIS offers the following advantages [4]:

1. The space occupied by the switchgear is greatly reduces. Compared to conventional open air substation, GIS needs only about 10-15% floor area.
2. It is totally unaffected by atmospheric conditions such as polluted or saline air in industrial and coastal areas, or desert climates.
3. It possesses a high degree of operational reliability and safety to personnel.
4. It is easier to install in difficult site conditions (e.g., on unstable ground or in seismically active areas).
5. In addition to having a dielectric strength much greater than that of air, SF_6 gas has the advantages of being nontoxic and nonflammable.
6. It is safe, noise free, reliable and require minimum maintenance.
7. It is prefabricated and is of modular construction, thereby allowing easier installation and flexible design even under adverse site conditions.

However, GIS requires continuous gas monitoring, gas tight construction and pressure relief devices. More ever, due to sensitivity of the dielectric strength of SF_6 gas to several factors, extreme care is required in manufacture, installation,

and maintenance. GIS can be located indoors or outdoors. Even though basic design of both types is the same, the equipment for outdoor GIS requires additional weatherproofing to suit the climatic conditions.

There are two basic types of designs of GIS. At low-rated voltage of <200kV, all three-phases have usually a common enclosure, i.e., 3-in-1 construction; whereas at higher-rates voltages, each phase uses its own separate enclosure, i.e, single-phase construction. Recently, the application of three-phase GIS has been increasing. Three-phase in one tank type GIS 550 kV has been applied [5-6]. If single-phase auto/reclose is a requirement, then for the circuit breaker at least, single-phase construction is preferable even at lower voltages. In a 3-in-1 construction, a single-phase fault within the GIS usually transforms into a phase-to-phase fault and consequently an enclosure burn-through is avoided. Sometimes a single-phase arrangement is adopted for the circuit breaker while a 3-in-1 arrangement is used for the “back parts”, i.e, bus bar, connectors, etc.

The GIS designs are in modular form and various components can be assembled as desired. SF_6 gas pressure between 0.2 and 0.5 MPa is used and is determined based on voltage rating, cost, and equipment size and reliability considerations. Systems operating at low pressures will have relatively larger size, but will more defect tolerant and comparatively more reliable than the high pressure systems. Typical service stress levels used for GIS are about 7 to 8 kVrms per mm per MPa of gas pressure [3]. However, the barrier insulators are restricted to stress levels of less than 4kVrms per mm [3]. Thus, the working stress of GIS is significantly lower than the breakdown strength of SF_6. By this approach, the manufacturers hope to ensure the long-term dielectric integrity of SF_6 gas equipment, provided normal quality and service procedures have been maintained.

Provision is generally made for a solid grounding of the entire GIS enclosure. In addition, automatic grounding switches are provided for grounding of the cables whenever the isolators are opened.

1.4 Three-phase GIS Common Enclosure Configuration

The GIS enclosure forms an electrically integrated, grounded casing for the entire switchgear. The GIS enclosure can be either of three-phase type or of the single-phase type. Figure 1.1 – 1.3 show one-line diagram, gas sectional and sectional view of a typical three-phase common enclosure GIS, respectively. Fig. 1.4 shows photograph of three-phase gas-insulated switchgear.

Developing three-phase common-enclosure switchgear involves three major considerations:

1. inter phase insulation coordination,
2. minimized inter phase electric field stress, and
3. maximized current capacity.

Insulation coordination between phases requires thorough EMTP surge analysis for a wide variety of fault scenarios. The insulation strength ratio of 1.5 phase-to-phase to phase-to ground will provide enough protection.

Minimizing electromagnetic stress between phases involves spacing conductor supports so as to suppress harmonics, then evaluating the optimal conductor layout in both computer-based simulations and real-time experiments.

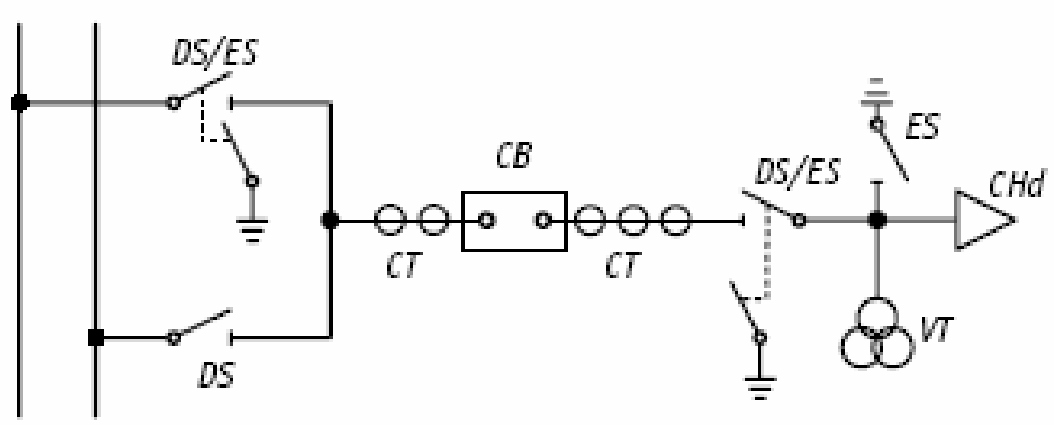

Fig. 1.1 One-line diagram of a typical of three-phase enclosure GIS [7]

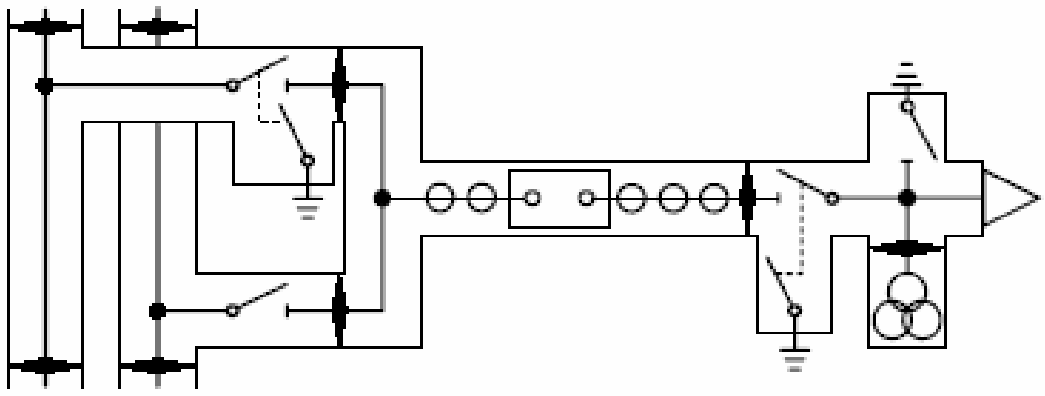

Fig. 1.2 Gas section of a typical of three-phase enclosure GIS [7]

Maximizing current capacity entails analyzing eddy current losses due to leakage flux. High current capacity GIS reduce such losses through the use of internal magnetic shields.

Computer-based analysis plays an indispensable role in resolving these and other design issues. Three dimensional analyses and a variety of simulation devices help boost reliability from the design stage on.

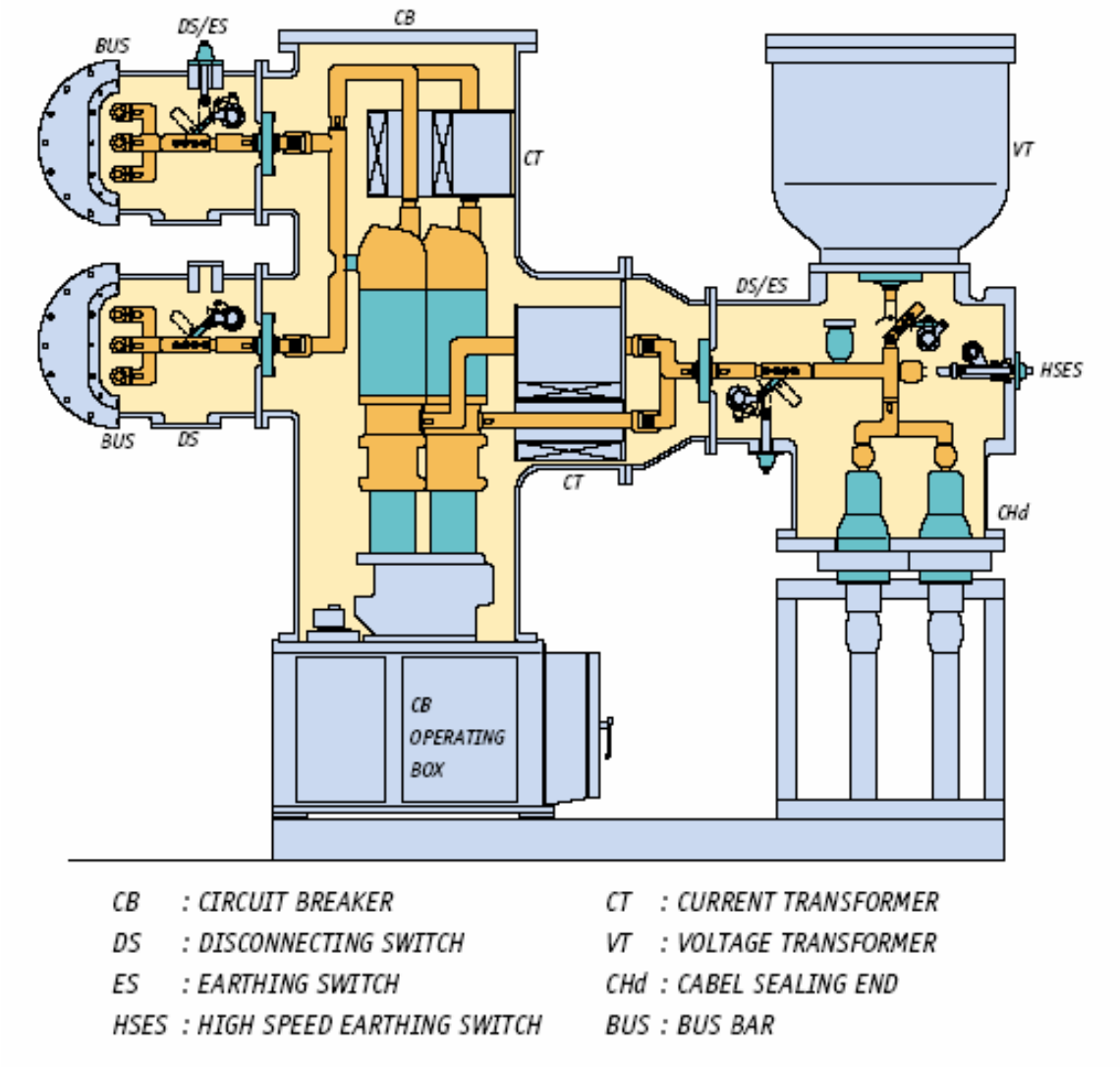

Fig. 1.3 Sectional view of a typical of three-phase enclosure GIS [7]

Fig. 1.4 Photograph of three-phase gas-insulated switchgear

The advantages of the three-phase common enclosure design are:

1. Three-phase common-enclosure designs offer less space and smaller parts count. This of course means fewer parts to fail and thus greater reliability.
2. A smaller number of enclosure is required per feeder (one-third).
3. In the case of a three-phase common enclosure, an arc between phase and ground will, within a few milliseconds, evolve into a phase to phase fault between conductors, owing to ionization of the gap, and at the same time the phase-ground arc will extinguish. Consequently, an enclosure burn-through is not possible.
4. For the same parameters (voltage level, conductor size, clearances between phases and phase-to-ground) the resultant field stress in a common three-phase enclosure is approximately 30% less that in a single phase enclosure and hence less likely to cause failure.
5. The absence of complicated tie rods and linkages between poles for the circuit breaker, isolator, and grounding switch drives simplifies the drive system.

1.5 PD Diagnosis on GIS

In order to keep GIS in a state in which it can perform a required function, maintenance is essential in its whole lifetime. Maintenance of power system equipment can be classified as:

1. Corrective maintenance (CM): actions carried out after functional failure, i.e. repair, and overhaul, partial or total replacement of equipment.
2. Time based maintenance (TBM): preventive actions carried out at predetermined intervals given by time or number of operations independent of the equipment.
3. Condition based maintenance (CBM): preventive actions carried out dependent on the condition of the equipment. The condition is inspection on-line or at intervals that are fixed or dependent on the former inspection results.

In practice, the TBM and CBM may include a certain degree of corrective maintenance. In the past, TBM is the main maintenance strategy. Recently there has been an indication of a change from TBM procedures – characterized by fixed maintenance intervals – to CBM, which is scheduled in accordance with the deterioration. The change is due to the intention of improving the reliability and reducing the operation cost of power system.

The recent trend of deregulation of electricity industry stimulates intensive competition among power corporations. They have to reduce their maintenance and updating costs to survive in the competition. CBM can help power corporations to control their maintenance and updating costs to survive in the competitions. CBM can help power corporations to control their maintenance and updating costs by three ways. CBM can improve the reliability of power system by avoiding a major failure and the consequent unplanned outage. Then the repair and outage costs can be reduced. Secondly, the maintenance cost can be reduced by delimiting the unnecessary maintenance work. Finally, decommission might be postponed while the condition of GIS is above a certain standard. CBM can offer important savings by extending the lifetime of GIS.

The key factor of CBM is the knowledge of the condition of GIS. It allows money to be saved and the electric network to be operated in a way that considers reliability as well as economy. Therefore, it is important to develop suitable diagnosis methods to determine this condition.

1.6 PD Detection on GIS

Partial discharge (PD) detection is an effective method to diagnosis the insulation condition of GIS. PD is electrical discharge that does not completely bridge the electrodes. Many defects in GIS might cause PD, such as protrusions on electrode and enclosure surface, free conducting particles, floating components, etc. Although PD magnitudes are usually small, they cause progressive deterioration and may lead to ultimate failure. Hence, it is essential to detect their presence before major insulation failure occurs.

PD in SF_6 generates extremely short electrical pulse accompanied with electromagnetic wave, mechanic vibration, chemical reaction, and optical emission. PD detection methods have been developed based on these physical and chemical phenomena. These methods can be divided into four classes:

1. Electrical method: to detect PD in the terms of current pulses, voltage fluctuation on conductor and electromagnetic wave (EMW), for example: IEC 60270 method and UHF sensor.
2. Mechanical method: to detect PD in the terms of mechanical vibration or sonic wave, for example: acoustic emission sensor.
3. Chemical decomposition analysis: to detect PD-induced decomposition gases, for example: gas detection tube, gas chromatography, CNT gas sensor.
4. Optical detection: to detect optical emission accompanied with PD, for example PMT.

In these methods, optical detection methods seem to be hopeless due to the difficulty of sensor installation and low sensitivity. The other three classes of methods have been extensively studied in the past decades, especially ultra high frequency (UHF) method, IEC 60270, and acoustic emission method.

IEC 60270 is a direct PD detection method to measure voltage fluctuation on conductor due to PD. The apparent charge can be calibrated by using a pulse signal generator. Now it is a standard detection method. A coupling capacitor is essential for IEC 60270 method and the sensitivity is dependent on the capacitances of object sample and coupling capacitor. Usually it is difficult to find a coupling capacitor in the field.

UHF method has a high sensitivity of 0.3 pC and is insensitive to noise such as TV and broadcasting, because the sensor is installed inside GIS. Now UHF method is still an active research subject in the world.

AE method is based on detection of acoustic signals arising both from pressure wave caused by PD and free particles bouncing on the chamber floor. Usually AE sensor can be easily attached to the outside of GIS chamber so it is suitable for PD detection in the field. It can be used for PD location by finding the place where the intensity is the largest. It is insensitive to electromagnetic interface but sensitive to sonic interface.

Chemical analysis method has been continuously studied in the past decades. PD in SF6 gas causes decomposition of the gas, mainly SF4. However, SF4 is a highly reactive gas and it reacts further, typically with traces of water vapor, to form the more stable compound SOF_2 and SO_2F_2. These are the two most common diagnostics gases by using a gas chromatograph and mass spectrometer. Recently, carbon nano tube (CNT) has been recognized as an effective PD detection method [8].

1.7 Research Trend of PD Diagnosis on Three-phase Equipment

Discharge investigations on single-phase power equipment have been well-established for many years. However, there are only a few reports on discharges in three-phase equipment. The investigation of partial discharge in three-phase equipment conducted so far can be classified in some groups:

1. Three-phase electric field characteristics
2. Particle movement in three-phase GIS
3. Three-phase PD detection and measurement

1.7.1 Three-phase Electric Field Characteristics

There is a distinct difference between electrical field configurations of single-phase and three-phase configurations. In a single-phase construction there is a well defined field between two electrodes and the field strength at an arbitrary spot has one unambiguous value. Zero electric field always occurs periodically in the single-phase construction. When the voltage equals to zero volt, the electric field is also zero. In three-phase construction the electrical field rotates and the field changes continuously. Also, there is no zero electric field in three-phase construction. When the voltage of one of phases equals to zero, the voltage in the other phases is not zero. The differences on electric field characteristics result in different electric field stress between single-phase and three-phase.

Electric field characteristics under three-phase voltage have been studied by many researchers [9-15]. In the first step of three-phase equipment design, electric field is calculated. The calculation method has been developed since more than thirty years ago. The newest simulation method and the result in three-phase electric field calculation are described in [14].

S. Yanabu, et al (1989) discussed periodic changes of the electric field at a certain point in the three-phase construction. While the voltage phase varies from 0 to 2π, the locus of the field vector forms an ellipse, as shown in Figure 1.5. They also showed the periodic change of field vector at different point as shown in Figure 1.6.

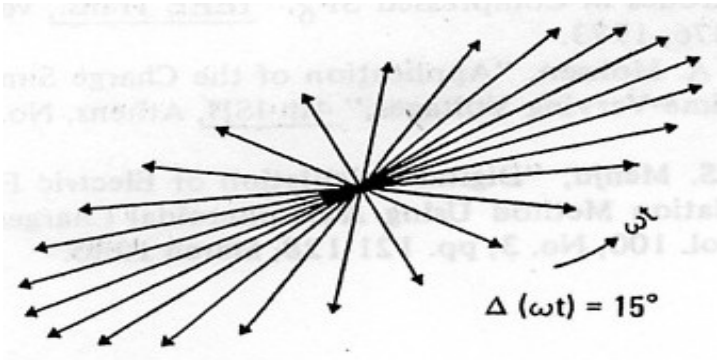

Fig. 1.5 Periodic changes of field vector in 3 phase GIB [6]

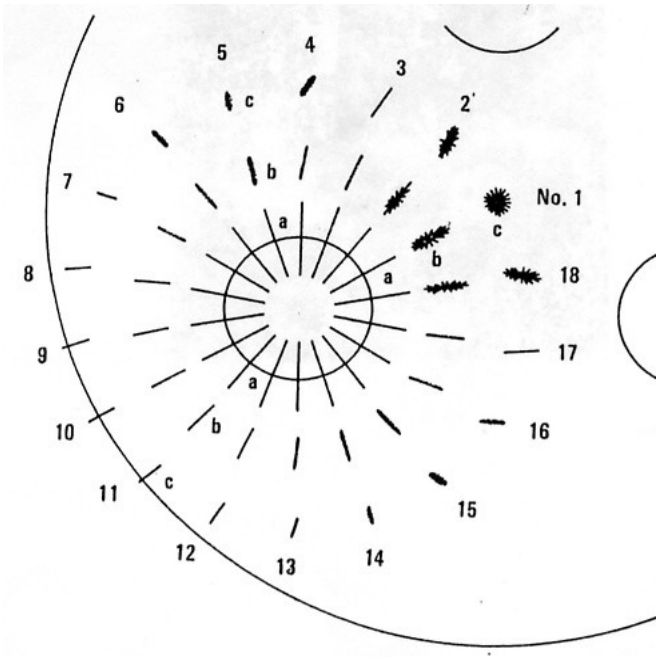

Figure 1.6 Periodic changes of field vector at different points in three-phase GIB [6]

The vector locus is elliptic. On the electrode surface (a in number 1 through 18 in the figure), for example, the locus is linear because electric lines of force are vertical to the conductor surface. In the center of the GIB, the locus is truly circular. While at a given point (e.g. number 3 b in the GIB), the locus is nearly linear, and at number 1b, it is elliptic, as shown in Fig. 1.6 [6,15].

Such complicated behaviors are very different with behavior of single-phase field. The distinct differences between electrical field configurations of single-phase and three-phase configurations lead us to think that discharge characteristic under three-phase voltage is different from single-phase. Discharge characteristic under three-phase electric field need to be investigated for development of diagnosis technique in three-phase equipment.

1.7.2 Particle Movement in Three-phase GIS

Yanabu et al (1989) investigated the behavior of metallic particles motion in three-phase SF_6 gas insulated bus. The test results revealed that in a three-phase electric field, unlike in a single-phase field, metallic particles were trapped on and around the high voltage conductors and revolved circumferentially as shown in Fig. 1.7.

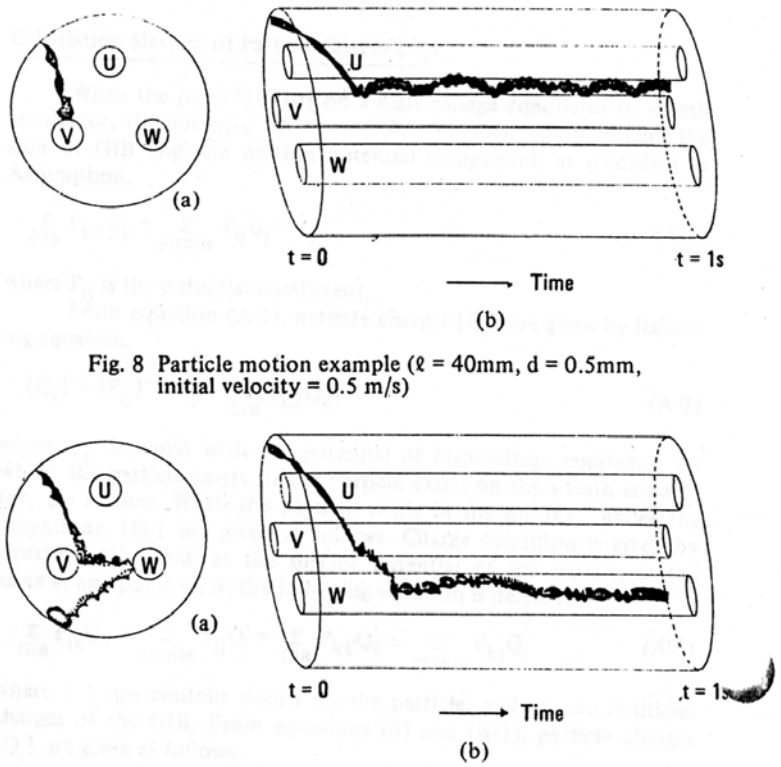

Fig. 8 Particle motion example (ℓ = 40mm, d = 0.5mm, initial velocity = 0.5 m/s)

Fig. 1.7 Simulation results of particle motion in three-phase GIB [6]

The simulation showed that it was closely related to location and periodic changes in the electric field provided by the three-phase gas insulated bus (GIB) [6].

Kumar et al (2003) made comparison of the free metallic particles movement in single-phase and three-phase GIB by charge simulation method. The particle movement in three-phase GIB under three-phase voltage was observed to be less in magnitude as compared to the particle movement inside three-phase GIB with voltage applied only to a single-phase, as shown in Fig. 1.8 and 1.9 [16].

Amarnath et al (2003) made simulation of coating effect on particle movement in three-phase GIB. The particle movement on coated electrodes was found to be very less compared to uncoated electrode system [17].

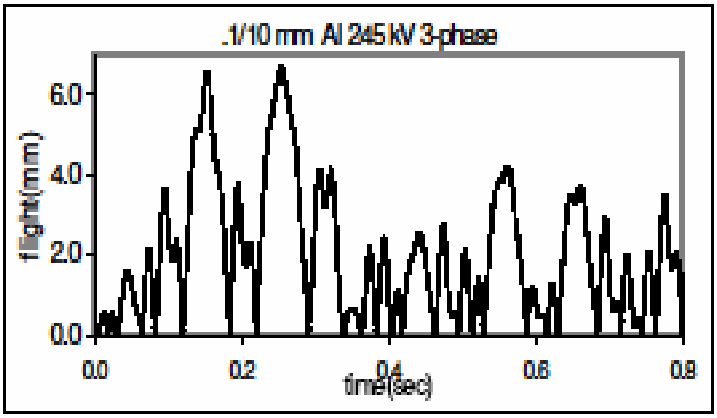

Fig. 1.8 Simulation results of movement of aluminum particle with voltage applied on all three-phase bus [16]

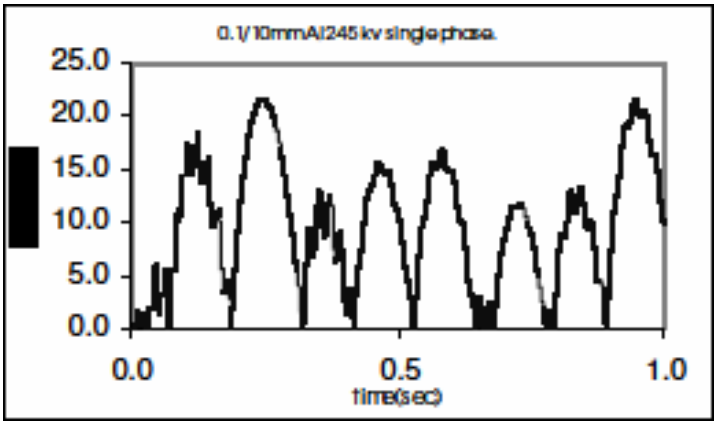

Fig. 1.9 Simulation results of movement of aluminum particle with voltage applied on one bus only [16]

Kumar et al (2005) made simulation two dimensional movement of free metallic particle in a three-phase 245 kV common enclosure GIS. The movement of an aluminum particle for a given voltage is higher than that of cooper for the identical conditions [18].

1.7.3 Three-phase PD Detection and Measurement

The first investigation on partial discharge detection in three-phase construction has been done by Kreuger et al (1987). They developed three circuits that could be chosen for discharge detection in three-phase construction. These circuits were analyzed and their characteristics were given. They concluded that discharges in three-phase constructions can be detected well in the presence of a three-phase electric field. This way of detecting has advantage as compared with the usual single-phase test which the electric field between electrodes is equal to the field in practice and differs considerably from that in a single-phase test circuit. They also have made test on three-phase belted-type cable using single-phase voltage and three-phase voltage. They observed that there are considerable differences between results with the conventional single test and those with the three-phase circuit as shown in Fig. 1.10 [19].

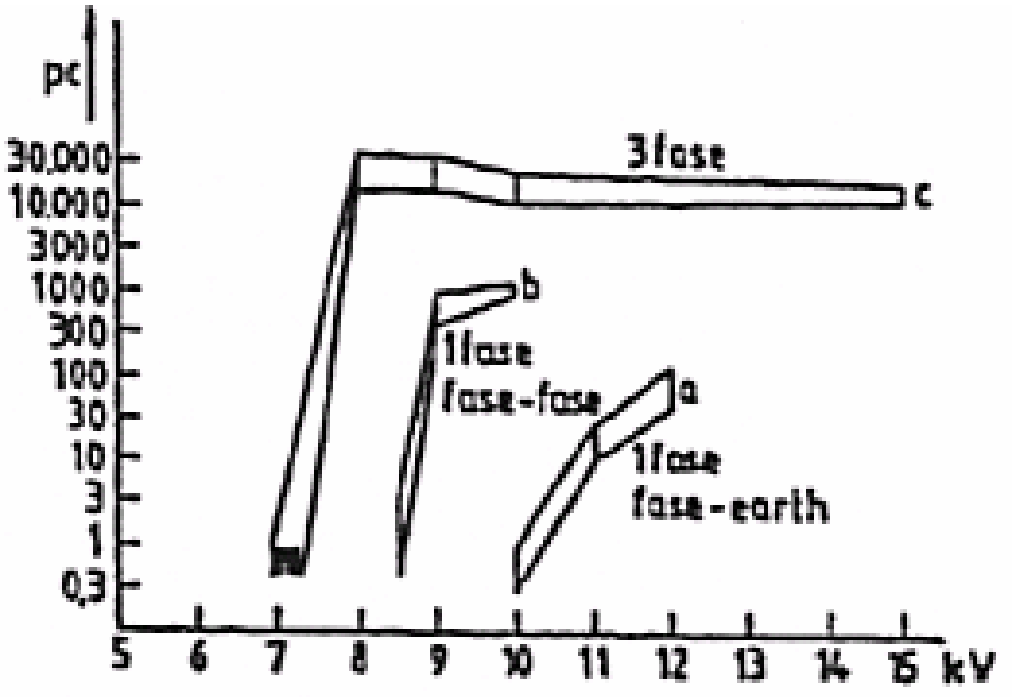

Fig. 1.10 Comparison of three-phase vs single-phase test [19]

Shihab et al (1989) developed single-phase testing techniques which yield PD results similar to those obtained when using three-phase detection. They constructed four types of PD measurement circuits. They found that single-phase test voltage, floating sheath, and straight PD detection has sensitivity similar to three-phase detection. They concluded that PD characteristics of three-cores belted-type cables determined using single-phase testing technique may differ greatly from the actual discharge performance of the cable when subjected to three-phase voltage condition in service. In order to achieve meaningful results concerning the voltage rating and the life expectancy of the cable, careful consideration must be given as to the way of energizing the cable and the PD response characteristics of single-phase test configurations [20].

Knapp et al (1999) reports results with the new sensitivity verification for ultra high frequency (UHF) partial discharge (PD) detection applied to three-phase SF6 gas-insulated substations (GIS) for rated voltages up to 170 kV. The procedure was developed by CIGRE WG 15/33.03.05. The aim is to examine the practical use of the proposed procedure and to investigate its extension to an unconventional sensor type. UHF PD measurements were carried out on a typical GIS section via potential grading electrodes. The results demonstrate the ability of these already built-in devices to serve as UHF sensors, to replace additional sensors sufficiently, and to make further design efforts unnecessary, if UHF diagnostics are required. Measurements, the experimental setup and the adequate test-vessel are described. The sensitivity of the new sensor is compared to the sensitivity of the IEC 60270 method and to other UHF sensors. Results concerning the detection of characteristic defects demonstrate the sensitivity of the new sensor arrangement [21].

Idea on development of multi terminal measurement system to measure partial discharge in three-phase equipment started from 1997, since Lortie et al published their paper about multi-terminal measurement method in ISH 1997 [22, 23].

Heinrich et al (2003) developed new method for multi-channel time-synchronous PD measurements and a special evaluation procedure to distinguish PD signals from common mode noise. The synchronous PD measurement technique is based on a new developed digital PD measurement device, which allows a high precision synchronous PD measurement on multiple locations. Fig. 1.11 shows the schematic of digital synchronous PD measurement system [24].

They also developed three-phase amplitude relation diagram (3PARD) to

evaluate measurement results. The first application of this method was recognition of different PD sources at a stator of a high voltage machine and the investigation of PD signal coupling between windings [24]. The construction of 3PARD setup is showed in Fig. 1.12. First step of the construction of the 3PARD is to determine the PD pulse with the highest apparent charge, which is normally the original PD impulse caused by the high voltage stress in the winding insulation system, whereas two other impulses measured on other two phases are usually product of cross talk between the phases.

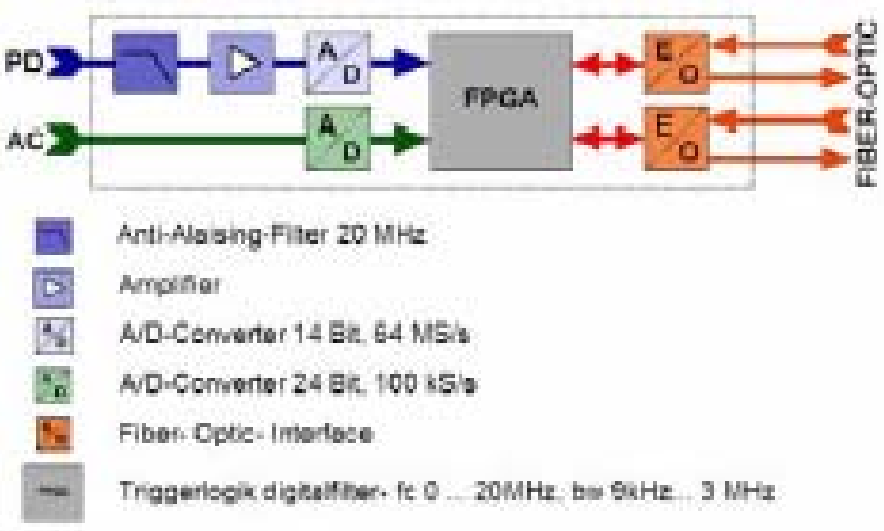

Fig. 1.11 Digital synchronous PD measurement system [24]

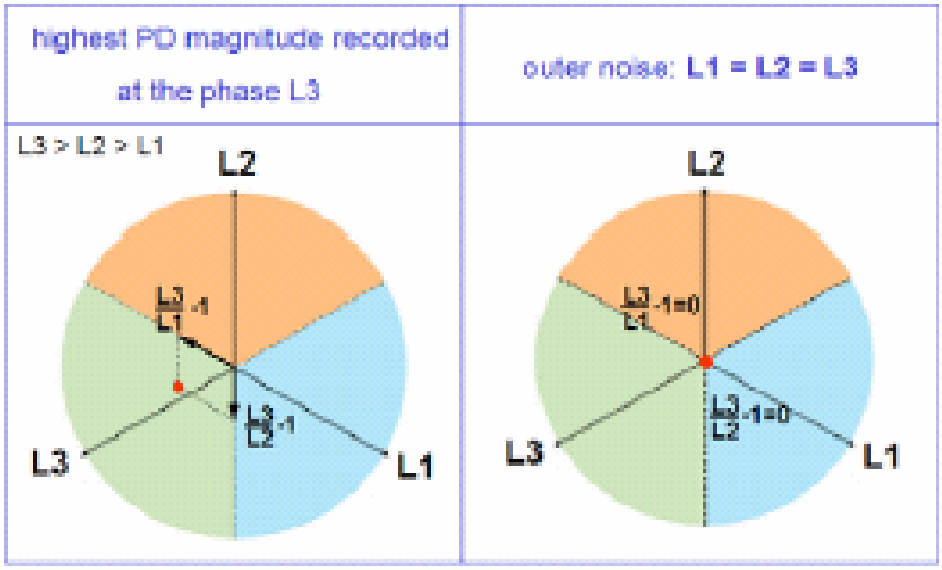

Fig. 1.12 Construction of 3PARD [24]

In Fig.1.12 (left), the highest magnitude is recorded at the phase L_3. Subsequently the highest charge will be divided with the charge of other two impulses and subtract with 1. The subtraction of 1 is needed to distinguish the electrical interferences, which usually have the pulse-like nature of PD but occur with almost same amplitude on all three-phases of the machine, $L_3/L_1-1=L_3/L_2-1=0$ if $L_1=L_2=L_3$. Finally, the results of the subtractions will be vectorial added as shown in Figure 1.12. Through the repetition of this procedure for great number of recorded PD impulses and due to the unique PD pulse to coupling magnitude ratio, every PD source within the machine as well as outer noise appears as clear distinguishable concentration of vector sum points (cluster) in a 3PARD. Subsequently each cluster can be separated for further investigation.

The transformation is done for a large number of pulses, e.g. 1,000 to 100,000. The frequency of occurrence is displayed in different colors from blue (=rare) to red (=very often). This allows a statistical differentiation of random coupling and very strong coupling. Thus PD signals and noise from all three-phases can clearly be separated in the 3PARD, as shown in Fig. 1.13.

Schaper et al (2003) developed new synchronous digital multi terminal PD measurement technique to detect partial discharge in three-phase transformer. This technique is based on the determination of cross-talk PD signals between three-phases of the power windings. The result from this PD measurement is an amplitude relation between adjacent phases that can be displayed in a three-phase amplitude relation diagram (3PARD) [25].

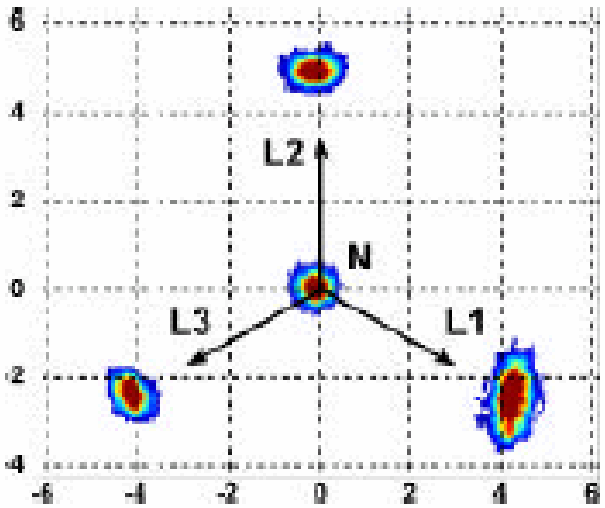

Fig. 1.13 Example of the 3PARD separation of PD calibration on three-phases (L1, L2, L3) and star point (N) [24]

Kalkner et al (2005) used the measurement system in [36] to detect three-phase PD on rotating machines simultaneously. Synchronous multi-terminal PD measurement technique in combination with the new 3PARD evaluation method enables distinction and separation of several parallel active PD sources within stator winding of rotating machine and external interference [26].

Kalkner et al (2005) also reports about the investigation of PD signal propagation and coupling between windings in rotating machine and about the correlation between results of the evaluation achieved with 3PARD and the location of the test pulse injection point. Fig. 1.14 shows the example of PD online data and Fig. 1.15 shows the related 3PARD diagram. Discharge signals contain two frequency components; first one “fast” mode is present for higher frequency while the second is the “slow” mode for lower frequency. “Slow” component travels through entire winding conductor and can be measured after transient time that depends on the origin of the discharge. “Fast” mode propagates due to capacitive and inductive coupling [27].

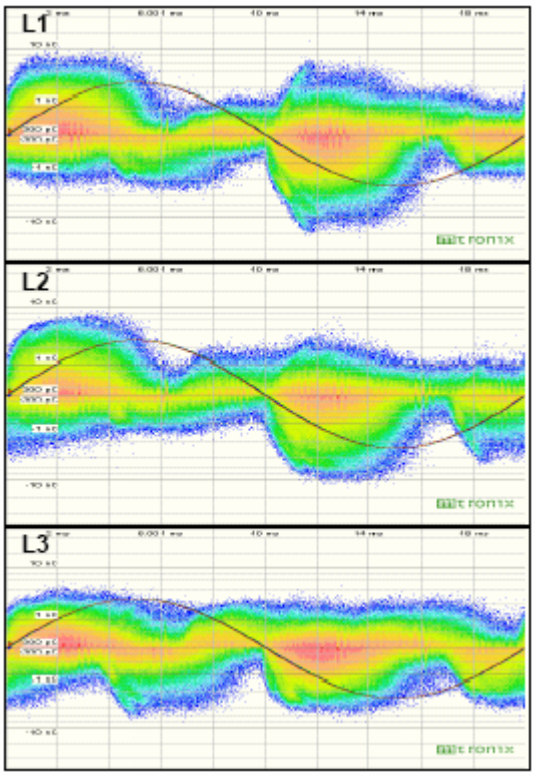

Figure 1.14 On-line PD pattern [27]

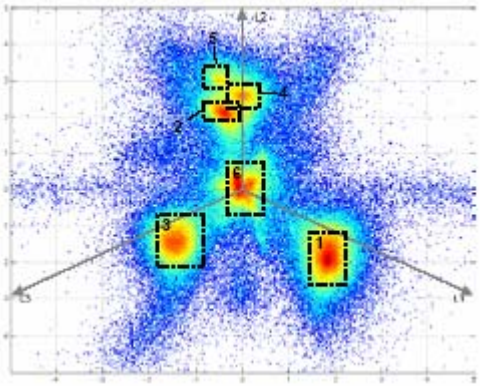

Fig. 1.15 3PARD analysis [27]

Jafari et al (2005) found diagnosis problem in three-phase transformer whether the discharge came from one source or multiple source. They investigated multi-source PD in three-phase transformer. They concluded that when three distinct PD sources exists on three-phases, the generated PD pulse sets are not synchronous and if PD source are completely similar, there is 120^0 phase difference between PD sets [28].

Akbari et al (2005) developed new multi channel PD detection system to measure PD in three-phase transformer. They developed methods to localize PD in three-phase transformer based on pilot signal and based on amplitude the detected pulses [29].

Reid et al (2005) introduced an integrated measurement strategy for simultaneous fault identification by combining the UHF and IEC 60270 techniques. Using a combined measurement system, PD activity has been recorded simultaneously in terms of radiated UHF pulse energy and the apparent charge measured according to IEC 60270. When the energy of UHF pulses is plotted against the corresponding apparent charge for a variety of PD test cells, characteristic patterns appear. Various elements within these patterns will depend on different aspects of the PD mechanism, which will in turn be governed by the type and number of defects in the insulation sample. In addition, investigation of UHF frequency band energies may also help identify specific mechanisms associated with PD. This simultaneous measurement strategy may allow us to classify PD activity with a greater degree of confidence than conventional phase-resolved measurements when several sources are active or if interference is present [30].

From some reviews above, it is found that the number of reports on three-phase PD detection increases recently. Although research on this field increased recently, it is mostly related to development of three-phase PD measurement technique. There are still many unclear and unsettle problem. PD characteristics and PD mechanisms under three-phase voltage have not been clear yet. Localization of PD, assessment of insulation condition, and electromagnetic wave propagation characteristic under three-phase voltage has also not been clear yet. Further, PD signal processing and development of diagnosis on three-phase equipment have not been developed yet. Therefore, there are still wide opportunities for research development in this field. Because of the difference in characteristic between three-phase and single-phase equipment and increase of application of three-phase equipment, research on three-phase PD characteristic and diagnosis will increase

in the future.

1.8 Research Objective

In summary of the above review of research trend of PD diagnosis on three-phase equipment, the investigation of partial discharge (PD) characteristics under three-phase electric field on three-phase equipment is needed because of the following. Firstly, there is a distinct difference in electric field characteristics between single-phase and three-phase construction. The electric field in single-phase equipment is linear, while one in three-phase equipment rotates and changes continuously [6,15]. It can be expected that the PD characteristics in three-phase equipment are different from ones in single-phase equipment. Further, the particle movement inside the three-phase gas insulated system is influenced strongly by three-phase electric field [6]. Secondly, for the reason of its compactness and low cost, the application of three-phase equipment (three-phase in one tank), such as three-phase GIS and three-phase gas insulated bus (GIB), has been increasing [5,6]. Thirdly, application of single-phase testing technique to three-phase equipment may give some erroneous results [19, 20]. Fourthly, three-phase equipment is energized by three-phase voltage on on-line PD monitoring of medium and high voltage equipment [15]. It differs from common practice for off-line test which is to energize only one phase. Therefore, investigation on PD characteristics in three-phase equipment is very important.

As stated in the preceding sections, PD investigations on three-phase equipment have been reported. The topics included rotating electric field in three-phase equipment [6,15] and its effects on PD characteristics [32-39] and particle movement on three-phase equipment [6,16-18], development of three-phase PD detection method using single-phase test voltage [19-20], and development of PD measurement technique on three-phase equipment [21-31]. Although fundamentals aspects of excitation and propagation of PD signal in three-phase power cable have been reported, PD excitation was only explained with simulation [15]. PD characteristics, mainly explained from measurement on three-phase construction, more specific on three-phase GIS, have not been reported.

From these viewpoints, the author has studied characteristics of PD and its electromagnetic wave signal propagation from a particle in a three-phase construction of GIS model under three-phase voltage as a fundamental study on

development of diagnosis technique in three-phase GIS [32-39].

Three-phase equipment differs from single-phase equipment in two aspects: configuration (three conductors in a duct) and applied voltage (three-phase voltage). Effect of these differences on the electric field, electrical discharge, and electromagnetic wave propagation in three-phase gas insulated system is studied in this dissertation.

The objectives of the present study are to clarify partial discharge phenomena and electromagnetic wave propagation emitted by partial discharge in three-phase gas insulated system, as a fundamental study of diagnostic technique improvement on three-phase equipment. The following research steps are conducted to achieve the objectives:

1. Clarification of electric field characteristics in three-phase construction under three-phase voltage.
2. Clarification of effect of three-phase configuration and three-phase voltage on PD characteristics in three-phase GIS.
3. Clarification of effect of three-phase electric field on PD characteristics in three-phase GIS.
4. Clarification of PD induced electromagnetic wave propagation characteristics in three-phase GIS.

1.9 Dissertation Outline

This dissertation presents the results of an investigation of PD and its electromagnetic wave propagation in three-phase gas insulated system. The obtained results are expected to be useful for development of an advanced insulation diagnostic technique on three-phase GIS. This dissertation consists of six chapters including this chapter.

Chapter 1 consists of introduction..

Chapter 2 consists of experimental setup and measurement system. Two different types of three-phase GIS model used in the experiment are explained. Experimental setup, experiment apparatus, and partial discharge measurement system, are explained.

In Chapter 3 PD characteristics of a particle adhered at different positions in

three-phase construction are reported. The position dependent sensitivity, PDIV characteristics, phase dependence of PD on applied voltage, and cross interference phenomena are discussed.

Chapter 4 deals with the effect of elliptical nature of rotating electric field on PD distribution pattern in three-phase equipment. This chapter explains the characteristics of electric field in three-phase electric equipment. The rotating electric field phenomena and its parameters are discussed. The difference in the electric field between single-phase and three-phase equipments is explained. The effect of elliptical nature of rotating electric field on PD distribution pattern in three-phase equipment is explained.

Chapter 5 reported the propagation properties of EMW emitted by PD in three-phase GIS.

Chapter 6 presents the conclusions, the practical significance of the present investigation and future development.

References

1. United Nation,"World Population Prospects", 2004, http://www.un.org/esa/population/publications/WPP2004/wpp2004.htm, (download on Dec 13, 2007)
2. Energy Information Administration,"International Energy Outlook 2005", http://www.iea.doe.gov/oiaf/ieo/download.html, (download on Dec 13, 2007)
3. L.L Grigsby,"The Electric Power Engineering Handbook: Sub Chapter 5.1 Gas Insulated Substations", Boca Raton: CRC Press LLC, 2001.
4. M.A Salam, H. Anis, El-Morshedy, R. Radwan,"High Voltage Engineering", Marcel Dekker, Inc, New York, 2000。
5. S. Yanabu, Y Murayama, and S. Matsumoto,"SF_6 Insulation and its Application to HV Equipment", IEEE Transactions on Electrical Insulation, Vol. 26, No.3, pp 358-366, 1991.
6. S. Yanabu, H. Okubo, S. Matsumoto,"Metallic Particle Motion in three-phase SF_6 Gas Insulated Bus", IEEE Transactions on Power Delivery Vol. PWRD-2, No. 1, January 1987.
7. Hitachi,"123-145 kV Three-phase Common-Enclosure Gas Insulated Switchgear".
8. Weidong Ding,"Partial Discharge Detection in Gas Insulation System using a Carbon Nanotube Gas Sensor", Dissertation, Kyushu University, 2006.
9. Takayoshi Misaki, Hideki Yamamoto, Koshi Itaka,"An Analysis of Three Dimensional Asymmetric Field Distribution in SF_6 Gas Insulated Cable", IEEE Transaction on Power Apparatus and Systems, Vol. PAS-92, pp. 2024-2031, 1973.
10. M.M.A. Salama, R. Hackam, A. Nosseir, A. Soliman, T. El-Shiekh,"Methods of Calculations of Field Stresses in a Three-core Power Cable", IEEE Transaction on Power Apparatus and Systems, Vol. PAS-103, No. 12, pp. 3434-3441, 1984.
11. M.M.A. Salama, R. Hackam, A. Nosseir,"Voltage Rating of a Three-core Power Cable from Consideration of Discharges in Voids", IEEE Transaction on Power Apparatus and Systems, Vol. PAS-103, No. 12, pp. 3442-3447, 1984.
12. N.H. Malik, A.A. al-Arainy, "Electrical Stress Distribution in Three-core Belted Power Cables", IEEE Transactions on Power Delivery, Vol. PWRD-2, No. 3, pp. 589-595, July 1987.

13. H. Okubo, S. Yanabu,"Development of Three Dimensional Electric Field Analysis by Segment Arrangement Based on Charge Simulation Method", Journal IEEJ Vol. 110, pp. 699-706, No. 10, 1990.
14. Jesus A. Gomollon, Roberto Palau," Steady State 3-D-Field Calculations in Three-phase Systems With Surface Charge Method," IEEE Transactions on Power Delivery, Vol. PWRD-20, No. 2, pp. 919-924, April 2005.
15. P.C.J.M. van der Wielen: "On-line Detection and Location of Partial Discharges in Medium-Voltage Power Cables", Doctoral Dissertation, T.U. Eindhoven, (2005).
16. Ratonesh Kumar et al, "Vertical Movement of Free Metallic Particles in a three-phase Common Enclosure Gas", XIIIth International Symposium on High Voltage Engineering, Netherlands 2003.
17. J. Amarnath et al, "Particle Trajectories in a three-phase Common Enclosure GIB on Coated Electrodes", XIIIth International Symposium on High Voltage Engineering, Netherlands 2003.
18. Ratnesh Kumar, K.D. Srivastava, B.P. Singh, "Two Dimensional Movement of Free Metallic Particle in a three-phase 245 kV Common Enclosure Gas Insulated Substation (GIS)", XIVth International Symposium on High Voltage Engineering, Paper F-26, China, 2005.
19. Kreuger, F.H, Sonneveld, W.A, Van Aalst, R.J. "Three-phase Detection", Report 700-05, CIGRE Symphosium 05-87, Vienna, 1987.
20. Kreuger, F.H, Samir Shihab, "Partial Discharge Measurement on Three-core Belted Power Cables", IEEE Transactions on Power Delivery, Vol. 4, No. 2, April 1989
21. M. Knapp, R.Feger, K. Feser,"Application of The CIGRE Sensitivity Verification for UHF PD Detection in Three-phase GIS", XIth International Symposium on High Voltage Engineering, London, 1999.
22. Lortie, R. Aubin, J. Vaillancourt, G.H. , Su,Q,"Partial discharge detection on power transformers using a multi-terminal measurement method", ISH 19997, Montreal, Quebec, Canada, 1997.
23. Ronald Plath,"Multi-channel PD Measurement", XIVth International Symposium on High Voltage Engineering, Paper J-04, China, 2005.
24. R. Heinrich, S. Schaper, W. Kalkner, R. Plath, A. Bethge,"Synchronous Three-phase PD Detection on Rotating Machones", XIIIth International Symposium on High Voltage Engineering, Netherlands 2003.
25. S.Schaper, W. Kalkner, R.Plath, H. Emanuel,"Synchronous Multi Terminal

PD Detection on Power Transformer", XIIIth International Symposium on High Voltage Engineering, Netherlands 2003.

26. W. Kalkner, A. Obralic, M. Kaufhold, R. Plath,"Investigation of PD-Pulse Propagation and Coupling between Three-phases of a Stator of a Rotating Machine", XIVth International Symposium on High Voltage Engineering, Paper B-44, China, 2005.
27. W. Kalkner, A. Obralic, A. Bethge, R. Plath,"Synchronous Three-phase Partial Discharge Detection on Rotating Machines", XIVth International Symposium on High Voltage Engineering, Paper G-042, China, 2005.
28. A.M. Jafari, A. Akbari,"Multi-Source Partial Discharge Diagnosis in Three-phase High Voltage Devices", XIVth International Symposium on High Voltage Engineering, Paper G-051, China, 2005.
29. Akbari, A.M. Jafari, M. Kharezi, "Partial Discharge Localisation in Power Transformers with Delta Connected Windings", XIVth International Symposium on High Voltage Engineering, Paper G-052, China, 2005.
30. A.J. Reid, L. Yang, M.D. Judd, B.G. Steward, and R.A. Fouracre,"An Integrated Measurement Strategy for Simultaneous Fault Identification: Combining the UHF and IEC60270 Techniques", XIVth International Symposium on High Voltage Engineering, Paper G-058, China, 2005.
31. Stefan Schaper, Wilfried Kalkner, Ronald Plath,"Synchronous Multi-terminal On-Site PD Measurements on Power Transformer", XIVth International Symposium on High Voltage Engineering, Paper G-121, China, 2005.
32. Umar Khayam, Toshio Ishitobi, Shinya Ohtsuka, Satoshi Matsumoto, Masayuki Hikita," Effect of Elliptical Nature of Rotating Electric Field on Partial Discharge Pattern in a Three-phase Construction", IEEJ Transactions on Fundamentals and Material A Vol. 127 No. 9, 2007.
33. Umar Khayam, Shinya Ohtsuka, Satoshi Matsumoto, Masayuki Hikita,"Investigation of Partial Discharge Characteristics in Air from Artificial Defect under Three-phase Voltage", Proceeding of 2005 Korea-Japan Symposium on Electrical Discharge and High Voltage Engineering, Paper PA-2, pp. 100-103, Ansan, Korea, Nov 3-4, 2005.
34. Umar Khayam, Shinya Ohtsuka, Satoshi Matsumoto, Masayuki Hikita,"Partial Discharge Measurement on Three-phase Construction", Proceeding of The 8th IEEE International Conference on Properties and Applications of Dielectric Materials (ICPADM), Vol.1, Paper K-4, pp.301-304, Bali, INDONESIA, June 26-30, 2006.

35. Umar Khayam, Toshio Ishitobi, Shinya Ohtsuka, Satoshi Matsumoto, Masayuki Hikita,"Partial Discharge Distribution Pattern in Three-phase Electric Field", Proceeding of Japan Korea Joint Session on Annual Conference of Fundamental and Material Society, Paper JK2-8, pp. 34, Kumamoto, JAPAN, Aug. 21-22, 2006.
36. Umar Khayam, Toshio Ishitobi, Shinya Ohtsuka, Satoshi Matsumoto, "Effect of Eccentricity of Rotating Electric Field on Partial Discharge Pattern in Three-phase Construction", Proceeding of Asian Conference on Electrical Discharge (ACED), Paper P1-15, pp. 466-469, Sapporo, JAPAN, October 16-19, 2006.
37. Umar Khayam, Toshio Ishitobi, Shinya Ohtsuka, Satoshi Matsumoto, Masayuki Hikita,"Effect of Foreign Particle on Rotating Electric Field and Partial Discharge Characteristics in Three-phase Construction", Proceeding of The 14th International Symposium on High Voltage Engineering (ISH), T7-502, Ljubljuna, SLOVENIA, August 27-31, 2007.
38. Umar Khayam, Yuu Nishiuchi, Shinya Ohtsuka, Masayuki Hikita, N. Otaka, Y. Takehara, Y. Kobayashi,"Measurement and Analysis of Frequency Spectrum of Electromagnetic Wave Signal Emitted by Partial Discharge in Three-phase Gas Insulated Switchgear using UHF Method", Proceeding of 2007 Korea-Japan Symposium on Electrical Discharge and High Voltage Engineering, Paper 16A-a3, pp. 7-11, Tokyo, JAPAN, Nov. 15-17, 2007.
39. Umar Khayam, Yuu Nishiuchi, Shinya Ohtsuka, Masayuki Hikita, N. Otaka, Y. Takehara, Y. Kobayashi,"Application of Single-phase PD Monitoring Device in Three-phase GIS", Proceeding of The 2008 Annual Meeting of IEEJ, Paper 6-187, Japan, March 2008.

Chapter 2

Experimental Setup and Measurement System

2.1 Introduction

This chapter contains experimental setup and partial discharge (PD) measurement system used in this research. The measurement system was developed to investigate discharge and its electromagnetic wave (EMW) signal propagation characteristics in three-phase gas insulated system (GIS). The model of three-phase GIS, experimental setup, and PD measurement device are described.

Measurement systems developed in this study are as follows:

1. Measurement of PD current signal using IEC 60270
2. Measurement of PD current signal flowing on three-phase conductor and the tank simultaneously using wide band current transformer.
3. Measurement of EMW emitted by PD using UHF method.

The apparatus used for investigating the PD and EMW emitted by PD consists of two systems:

1. Simplified model of three-phase GIS in air at atmospheric pressure (Model I).
   The IEC 60270 method and CT are used simultaneously in this model. The measurement system is called measurement system I. This system is to investigate PD phenomena in three-phase GIS.
2. Model of three-phase GIS filled with SF_6 gas at atmospheric and higher pressure (Model II).
   The UHF method is used in this model. The measurement system is called measurement system II. This system is to investigate EMW emitted by PD in three-phase GIS.

2.2 Three-phase GIS Model

There are two types of three-phase GIS model used in the experiment. The first model is a trial model (Model I). It was used to observe basic phenomena in three-phase GIS. The second model is close to the actual three-phase GIS. It was

used to observe PD and EMW propagation characteristics in three-phase GIS. The electrode system was arranged to simulate three-phase electric field in three-phase equipment. The conductors were arranged in an isosceles triangle construction. The maximum voltage of three-phase transformer used for the experiment was 52 kV. The dimensions of the tank and the conductors were about one fifth of an actual 275 kV three-phase GIS. The measurement system attached on two types of three-phase GIS model was different. The first model used CT, detecting impedance, and coupling capacitance in PD measurement. The second model used UHF sensors. The specifications of each GIS model and their measurement system are shown in Table 2.1 and Table 2.2, respectively. The measurement system I is attached to model I while the measurement system II is attached to model II.

Table 2.1 GIS Model Specification

	Model I	**Model II**
GIS Model	open tank	close tank
Length (mm)	300	1506
Tank diameter (mm)	150	155 / 490
Tank thickness (mm)	2	5
Conductor diameter (mm)	25	20 / 40
Tank material	Aluminum	Aluminum
Conductor material	Steel	Aluminum
Insulation	Air	SF_6
Pressure (Mpa)	constant (0.1)	variable (0.1 - 1)

Table 2.2 Measurement System

	Measurement System I	**Measurement System I**
PD Sensor	PD current sensor	PD induced EMW sensor
	1 k ohm Detecting Impedance	UHF (0-1.5MHz)
	CT (10kHz-250MHz)	
	Coupling capacitor	
Measurement device	Oscilloscope (Tektronix TDS3034, 300MHz, 2.5GSa/s)	Oscilloscope (Infinium 1.5 GHz, 8GSa/s)
	Spectrum Analyzer (Anritsu 9kHz-3GHz)	PD Monitoring (PDM) Device (Hitachi 9kHz - 1.5 GHz)
	PD measurement device (paradise)	

2.2.1 Model I

Three-phase GIS model I was composed of a tank model 150 mm in diameter, 300 mm in length, 2 mm in thickness, and three-phase conductors 25 mm in diameter. The shape of the tank is designed in the form of corona cage [1]. The tank is designed by considering the capacitances between high voltage conductors and the tank and the electric field caused by high voltage conductors. Both edge parts of the tank are bent to reduce the electric field on the edge of the tank. The capacitance between high voltage conductors and the tank is designed very small to get higher voltage on the capacitance and to increase the measurement sensitivity. The small capacitance is reached by shortening the length of the tank. The layout and photograph of the model are shown in Fig. 2.1 until Fig 2.3.

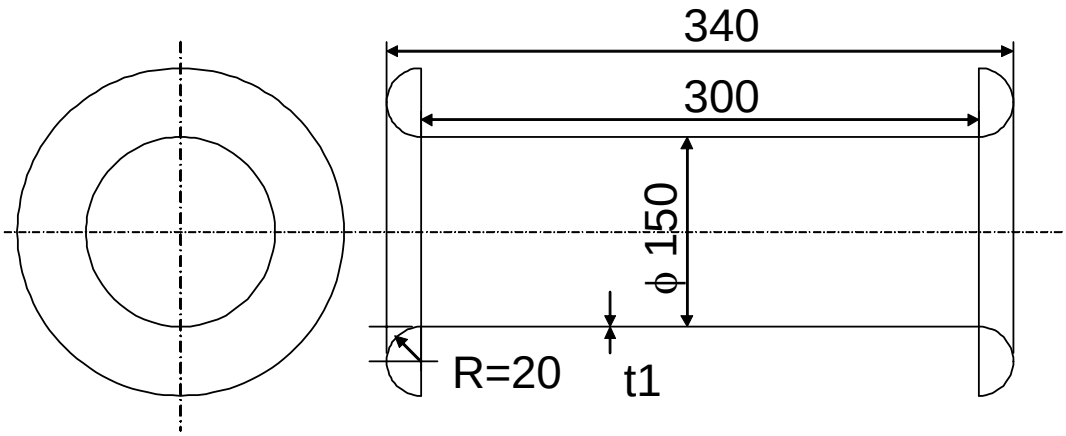

Figure 2.1 Layout of the tank model I

Figure 2.2 Photograph of the tank model I

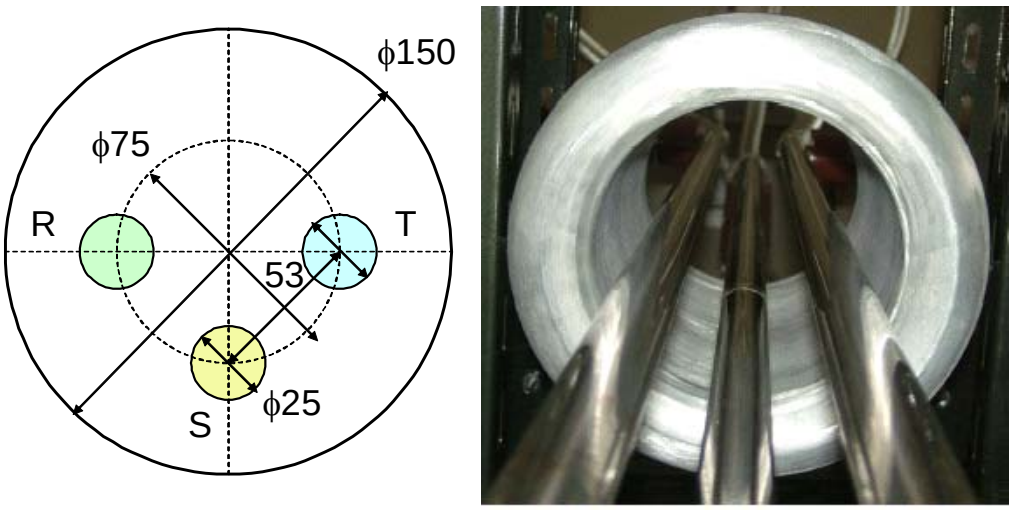

Figure 2.3 Layout (left side) and photograph (right side) of three-phase conductor of three-phase GIS model I

2.2.2 Model II

Fig. 2.4 – 2.7 shows the layout and photograph of three-phase SF_6 GIS model used in the experiment. It was composed of two different size tanks, separated by a spacer. The smaller tank (TANK I) 155 mm in diameter, 800 mm in length, 5 mm in thickness, is observation tank in which the particle was put. The dimensions of the tank and the conductors were about one-fifth of an actual 275 kV three-phase GIS.

The bigger tank (TANK II) 490 mm in diameter, 450 mm in length, and 5 mm in thickness was connected to the three-phase voltage supply. The conductors inside tank A and tank B are 20 mm and 40 mm in diameter, respectively. The three-phase conductors were composed in isosceles triangle arrangement. The tank contains SF_6 gas. The gas pressure inside the GIS can be changed for experiment purposes. .

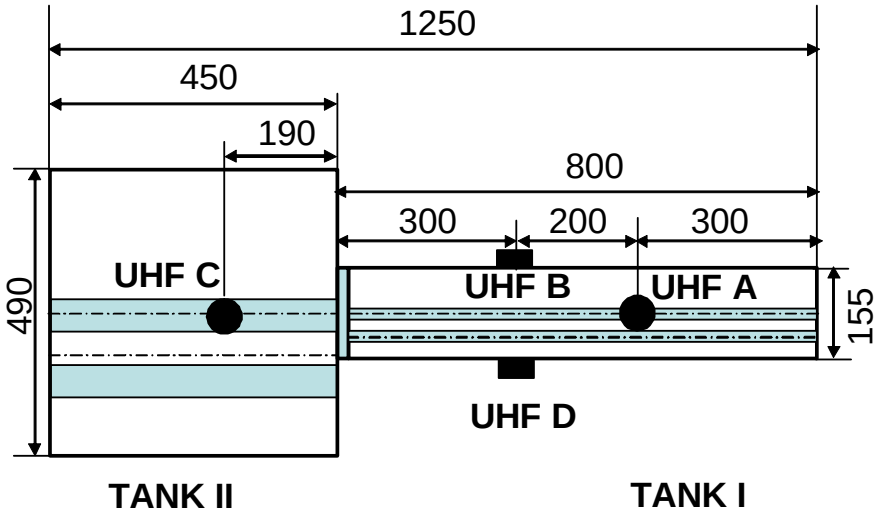

Fig. 2.4 Layout of three-phase GIS model II

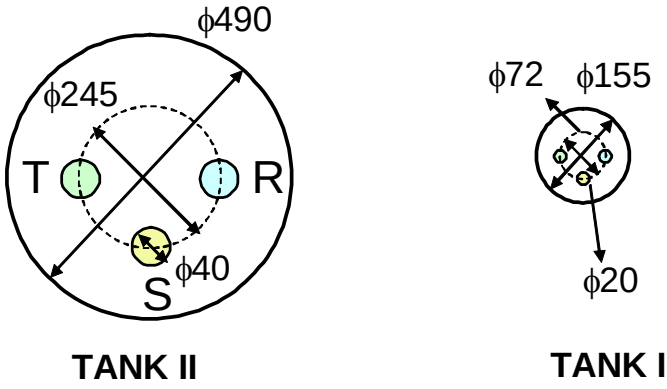

Fig. 2.5 Layout of three-phase conductor inside three-phase GIS model II

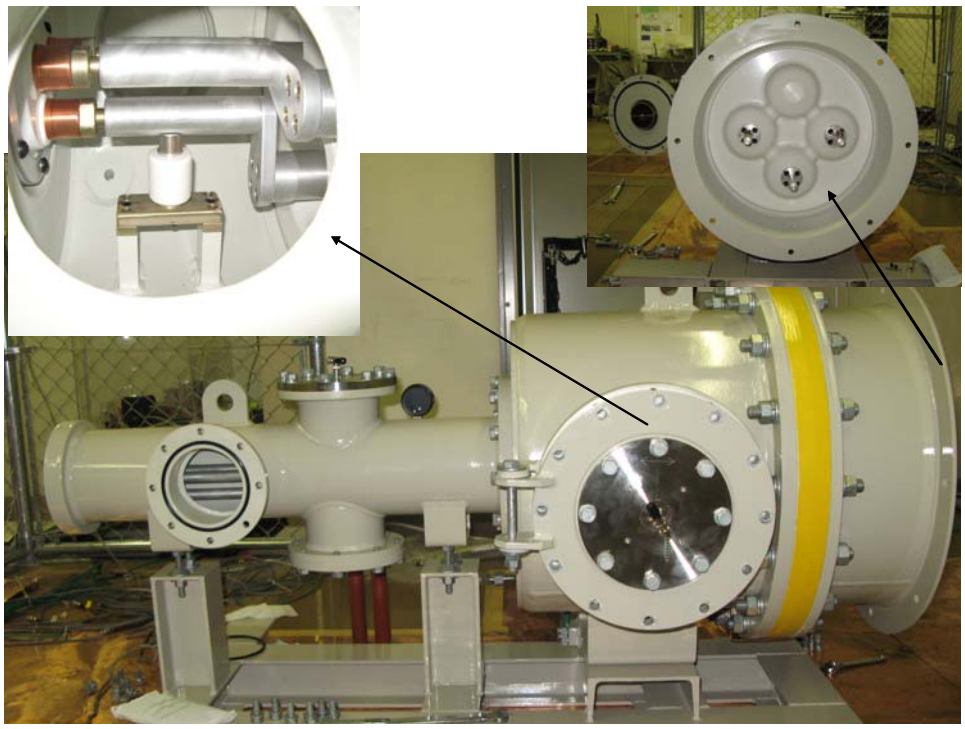

Fig. 2.6 Photograph of three-phase GIS model II

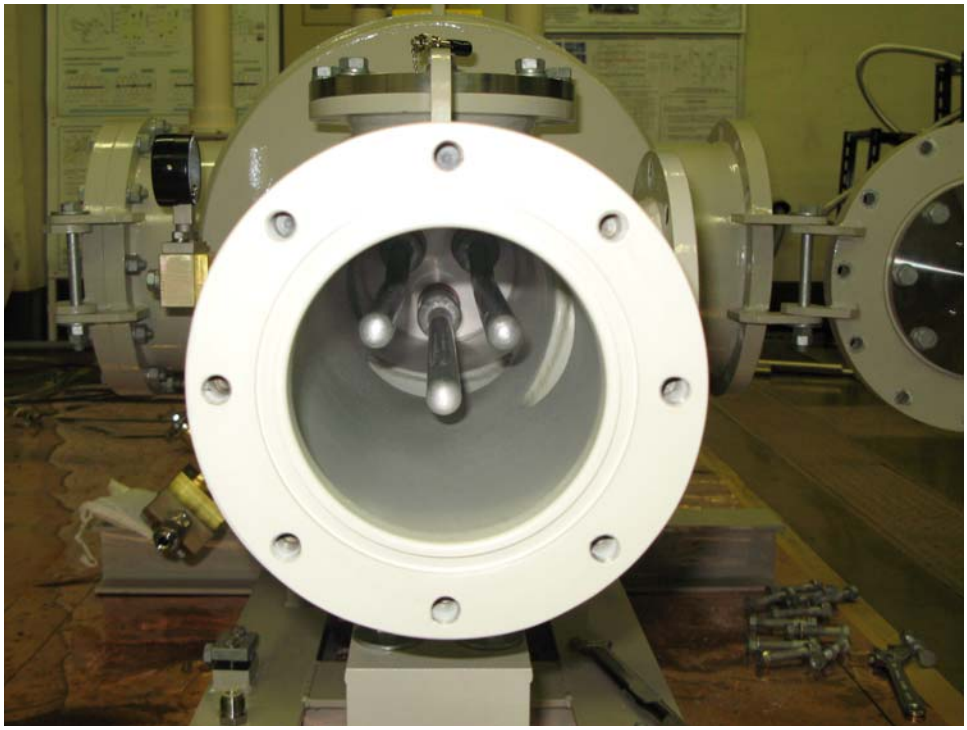

Fig. 2.7 Photograph of three-phase conductors inside GIS model II

2.3 Experimental Setup of Model I

The experimental circuit is shown in Figure 2.8. The experiments were conducted in laboratory air. Three-phase AC voltage was supplied from a three-phase 200 V/52 kV, 5 kVA corona free transformer through 20 kΩ limited resistor. PD signal flowing on each phase was measured with three current transformers, namely CT_R, CT_S, and CT_T. They were clamped on the line connecting the coupling capacitors and the capacitive dividers on R, S, and T phases, respectively. PD signal flowing from the tank to ground was detected by CT, namely CT_{TANK}, and 1 kΩ detecting impedance (DI). The frequency response of the CT (ETS Lindgren 94430-1) covers from 10 kHz to 250 MHz. Applied voltage was measured with capacitive dividers consisting of 500 pF and 450 nF capacitances. PD signals and applied voltage were observed simultaneously with a four-channel oscilloscope (Textronix 3034, 300 MHz, 2GS/sec). Photograph of experimental equipments is shown in Figure 2.9.

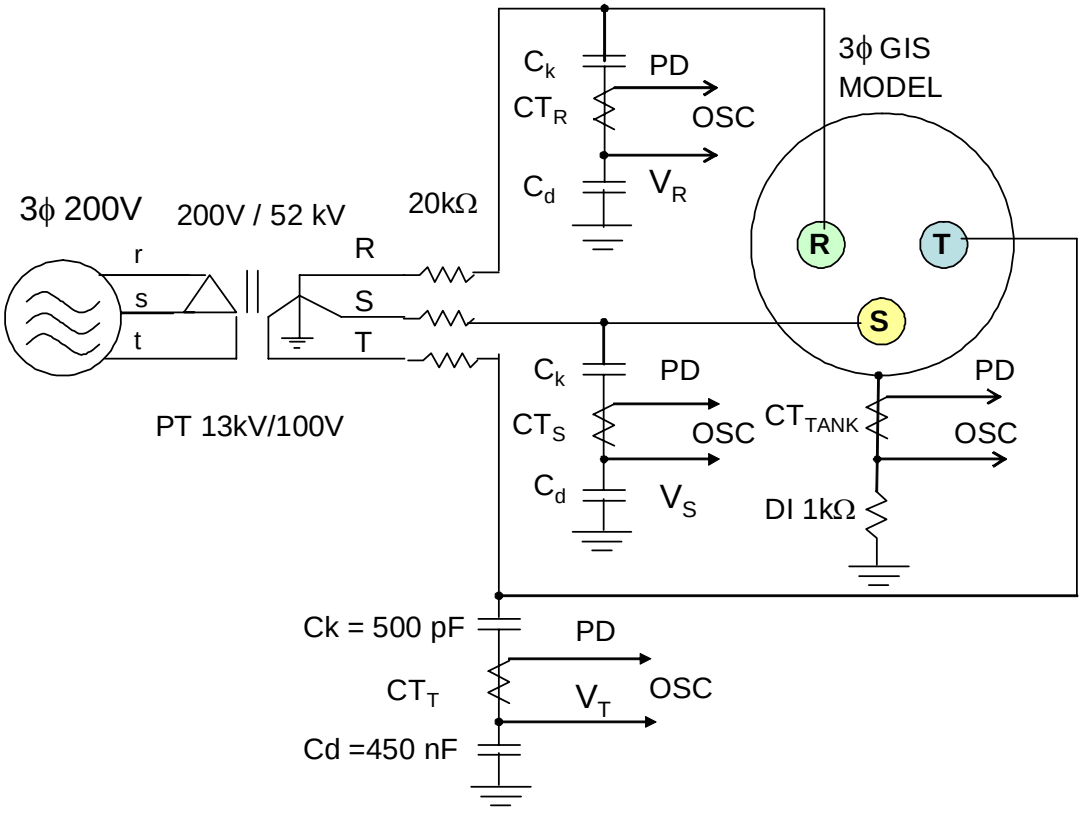

Fig. 2.8 Equivalent circuit of experimental setup I

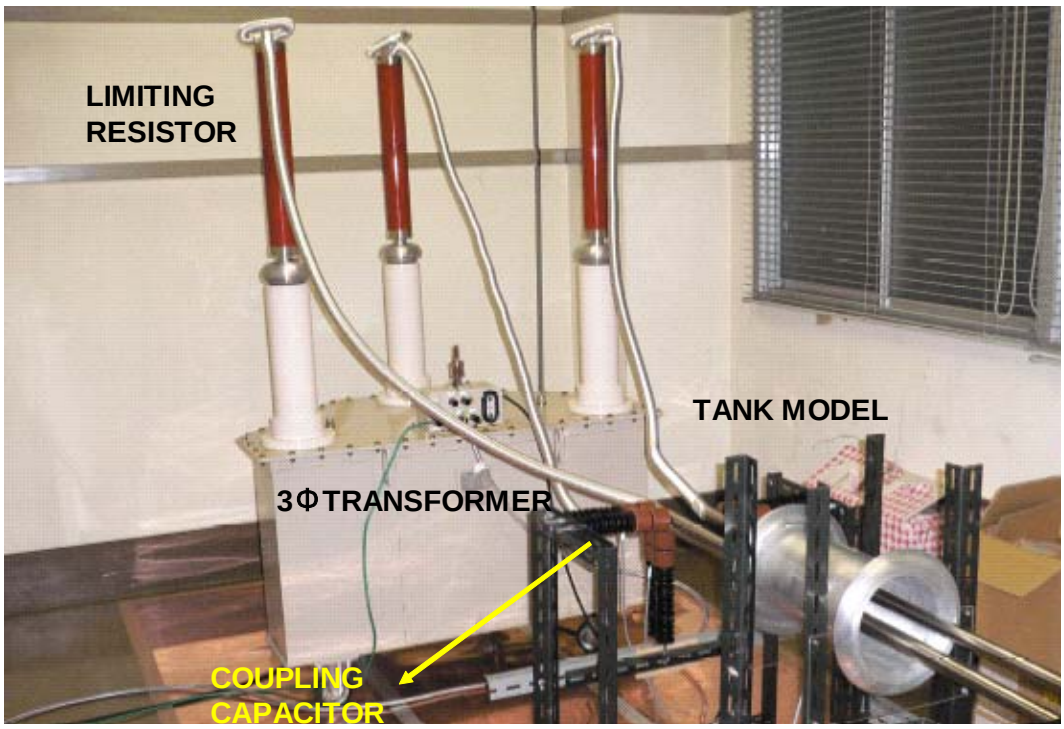

Figure 2.9 Photograph of experiment equipment I

2.4 Experimental Setup of Model II

The experimental setup is shown in Fig. 2.10. The three-phase GIS model was energized by the same transformer previously described. The maximum voltage of three-phase transformer used for the experiment was 52 kV. The experiment was conducted until 70% of the maximum voltage, 36 kV, due to the safety reason.

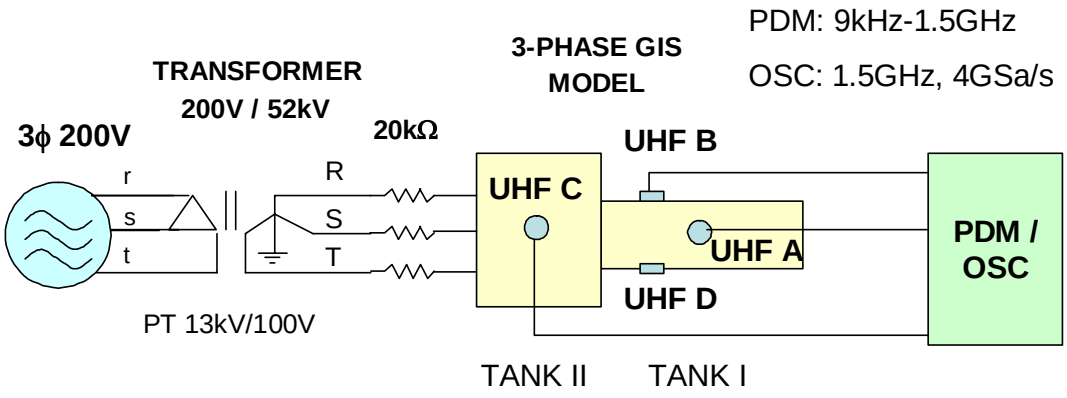

Fig. 2.10 Equivalent circuit of experimental setup II

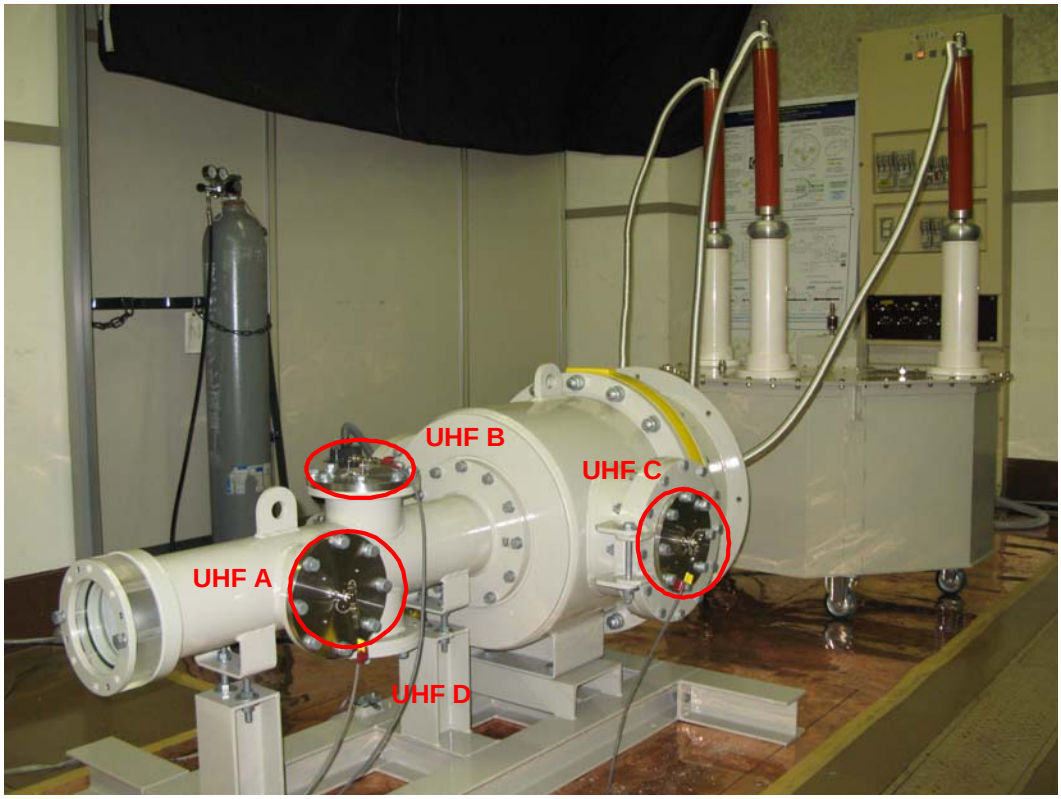

Figure 2.11 Photograph of experiment equipment II

The internal UHF sensors, UHF A, B, and C, are installed inside the three-phase GIS for measurement of EMW signals excited by PD. The position of sensors was shown in Fig. 2.4, 2.10, and 2.11. The UHF sensors have frequency band 500-1500 MHz with the sensitivity below 0.3 pC [2]. The principle of UHF technique is that the current pulse which forms PD has very short rise time less than 50 ps [3]. These pulses excite the EMW in the GIS tank into multiple resonances at frequencies up to 20 GHz. Although the duration of the current pulse is only a few nanoseconds, these microwave resonances persist for several microseconds. They may readily be picked up by UHF couplers fitted either inside the GIS chambers, or over dielectric apertures in the chamber wall. The PD signals can then be amplified and displayed. Unless otherwise mentioned, the measurement was carried out using UHF A sensor

A digital four channels oscilloscope (1.5 GHz, 8 GSa/s) and the portable type PD monitoring device (PDM) with three channels were utilized to carry out various measurements. The oscilloscope was used to measure EMW signal waveform in time domain. The PDM contains spectrum analyzer with frequency band 9 kHz-1.5 GHz. The PDM detects UHF EMW emitted by PD and display

two kind of waveform: frequency and phase spectrum. It automatically identifies its cause by expert diagnostics software. It contains data base of PD pattern in single-phase GIS. It needs to be examined whether it can be used properly for PD diagnosis on three-phase GIS.

2.5 Partial Discharge Source

A needle electrode made from cooper was adhered on the conductor or on the tank to produce PD. The diameter of a particle was 0.1 mm. The radius of particle tip was 0.05 mm. The particle length was 5mm and 27 mm for model I and model II, respectively. It was fixed to the tank or to the surface of the conductor using copper tape. The particle position is normal to the surface of the conductor or the tank. For model I, the particle was put inside the tank at the middle of the tank. For model II, the particle was put in the observation tank (small tank / tank I), at the position 500 mm from the spacer, or 300 mm from the end side of the tank. The particle position can be changed in the experiment. The particle positions and their notations in the cross section of the tank are shown in Fig. 2.12. Particle position is notated with a big character and an index in front of the character, P_{α}.

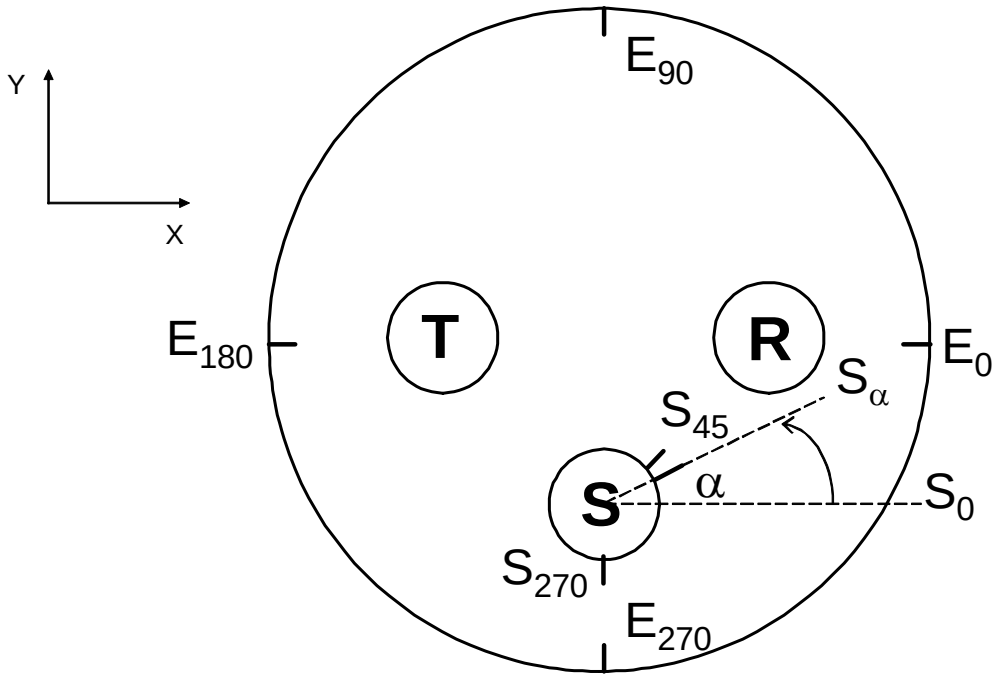

Fig. 2.12 Particle position and notation

The character is used to explain the particle position at R, S, T conductors or on the tank. Particle on R, S, T conductor, and particle on the tank or on the enclosure (E) is notated as R, S, T, and E, respectively. The index α is used to explain the particle position (in degree) relative to the positive x axis in the counter clock wise direction. For example, S270 means the particle at S conductor, 270^0 or -90^0 from positive x axis. The example of photograph of the particles is shown in Fig. 2.13.

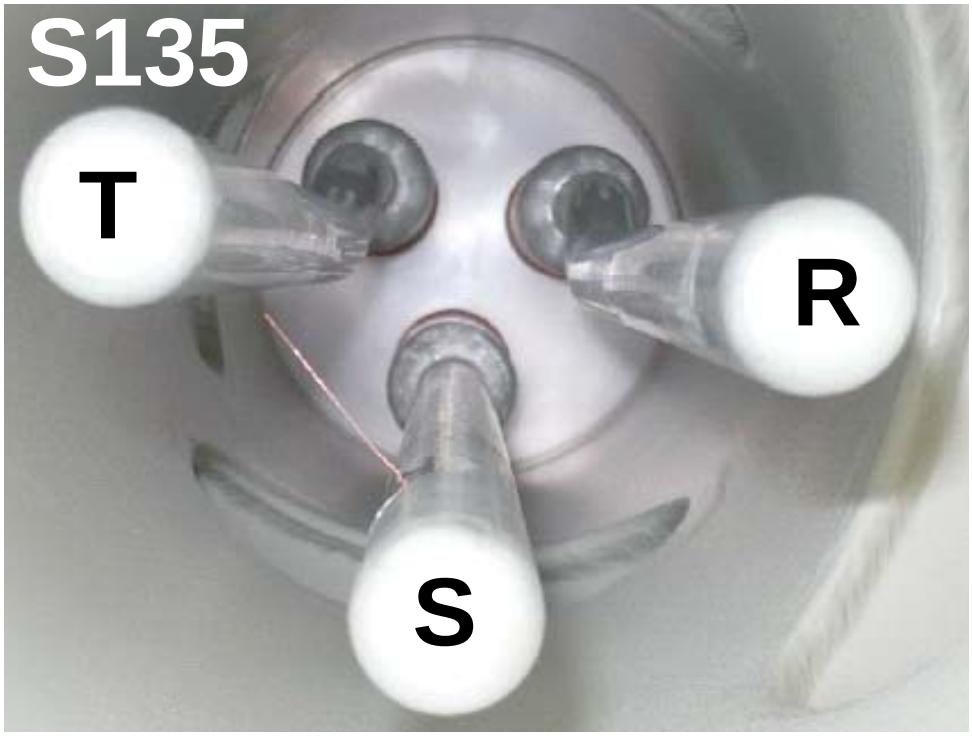

Fig. 2.13 Photograph of S135 particle inside three-phase GIS Model II

2.6 PD Measurement System and Devices

2.6.1 PD Measurement System According to IEC 60270

Figure 2.14 shows a standard partial discharge measurement method system based on the IEC 60270 recommendations. This standard PD detection circuit is composed of a coupling capacitor, a coupling device and a partial discharge detector. The coupling capacitor provides the closed circuit required for the discharge displacement. The coupling device converts the input current (discharge

displacement in the leads) into voltage pulses. These voltage pulses are registered by an oscilloscope and recorded by computer for further analyze.

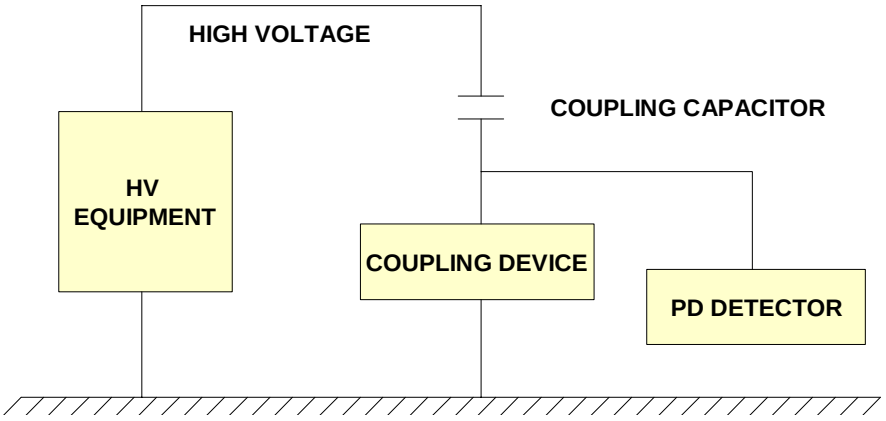

Fig. 2.14 PD measurement system according to IEC 60270

2.6.2 Detecting Impedance

Detecting impedance (DI) is a self developed PD measurement device. The impedance is chosen as 1 kΩ rather than 50 Ω to enhance the measurement sensitivity. The DI enable to measure PD current signal which has frequency range up to 300 MHz. The equivalent circuit of DI is shown in Fig. 2.15. The main component of DI is 1 kΩ resistor. The other components are capacitance, inductance, diode, and arrester. Arresters and diode were placed in the circuit in order to have an extra protection from the surge pulses generated when the breakdown occurs.

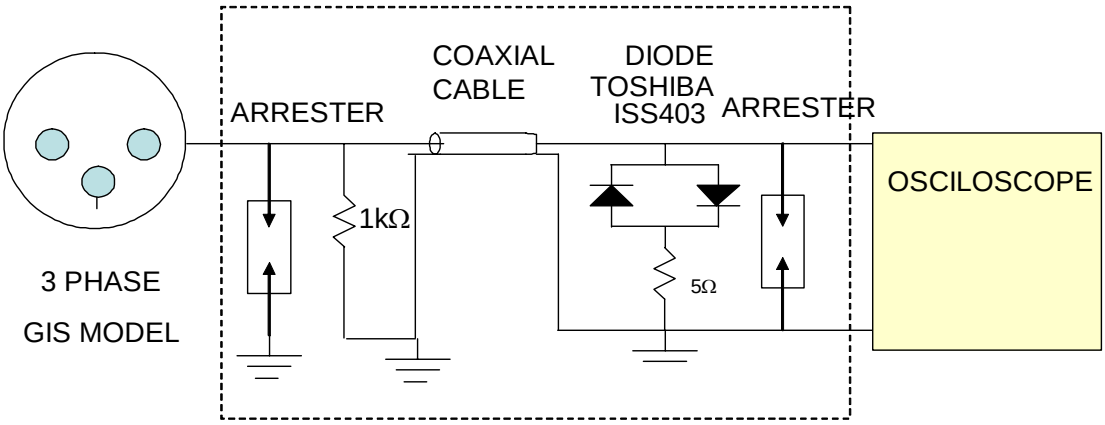

Figure 2.15 Detecting Impedance Circuit (in the dashed line box)

2.6.3 Current transformer (CT)

The ETS-Lindgren CT model 94430-1 was used in the measurement of PD current. It is a clamp-on CT designed for use with electromagnetic interference (EMI) test receiver or spectrum analyzer or with any similar instrument having 50 ohm input impedance to determine the intensity of current present in an electrical conductor. The CT has a frequency range from 10 kHz to 250 MHz with 50 ohm output impedance. It can simply clamped around the test conductor, consisting of one turn primary winding with the current probe forming the core and secondary winding of an radio frequency (RF) transformer [4] . The equivalent circuit of the CT is illustrated in Fig. 2.16. The sensitivity of the CT in microamperes is dependent upon the sensitivity in microvolt of the receiving equipment which is used. Table 2.3 shows the relationship of the receiver sensitivity in microvolt to that of CT in microampere based on 8 ohm of transfer impedance of this model [4]. The discharge current (I_d) in microamperes in the conductor under test is determined from reading of CT output in microvolts (E_s) divided by CT transfer impedance (Z_T) [4].

Table 2.3 Typical sensitivity of 94430-1 series CT [4]

Test Equipment Sensitivity in Microvolts	**94430-1 $Z_T = 6\ \Omega$**
5	0.625
2	0.25
1	0.125
0.1	1.0125

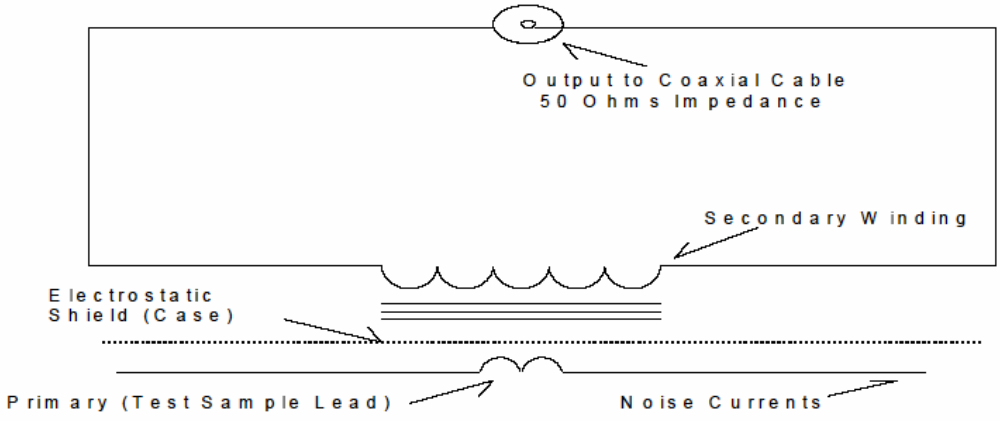

Fig. 2.16 Equivalent circuit of CT [4]

Table 2.4 Electrical specification of CT [4]

Electrical Specifications	94430-1 94430-1L
Frequency Range (L Models 20 Hz)	10 kHz to 250 MHz
Transfer Impedance	6 Ohms 10 to 250 MHz, 3 Ohms @ 1 MHz, 0.6 Ohms @ 100 kHz, 0.1 Ohms @ 10 kHz
RF Current Range (RF CW)	16.0 Amps
RF Current Range (Pulse)	70 Amps See Table 3
Maximum Power Current	200 Amps (DC to 400 Hz)
Maximum Power Voltage	No limitation, subject to adequate conductor insulation
Sensitivity Under Rated Load	0.125 microamperes with one microvolt sensitivity receiver and 8 Ohms transfer impedance

The equation is as follow,

$$I_d = E_s / Z_T \quad (2.1)$$

or, in dB

$$I_d\ (\mathrm{dB\mu A}) = E_s\ (\mathrm{dB\mu V}) - Z_T\ (\mathrm{dB}) \quad (2.2)$$

The transfer impedance (Z_T) of CT is determined throughout the frequency range as shown in the electrical specification in table 2.4 and Fig. 2.17 [4].

2.6.4 PD Monitoring Device (PDM)

In the second experiment, PDs are measured with UHF sensor and the portable PD monitoring device (PDM). The PDM detects UHF electromagnetic waves emitted by a PD, and automatically identifies its cause. Fig. 2.18 shows the photograph of PDM.

Measurement Principle

The PD generated in SF6 gas serves as a steep pulse waveform, and emits electromagnetic waves, with broad band frequencies, especially UHF band (300MHz – 3 GHz). EMW spreads insides the GIS with little attenuation, because

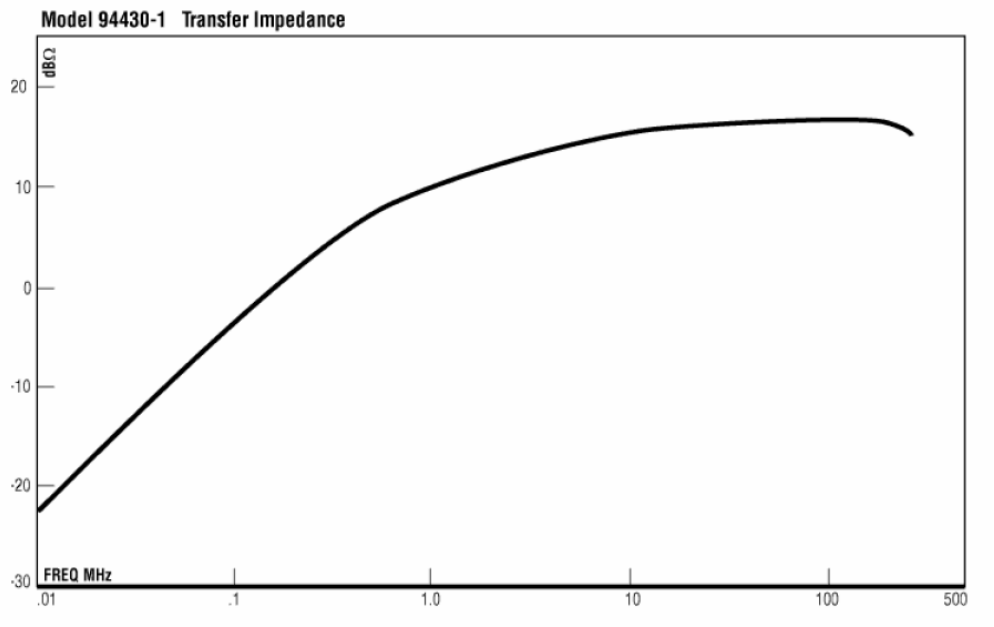

Fig. 2.17 Transfer impedance as a function of frequency response [4]

GIS plays a role of a waveguide. UHF sensors may be built in the GIS or mounted on the GIS spacers or inspection windows. The portable type PDM device measures UHF electromagnetic waves and diagnoses the insulation status inside the GIS by expert diagnostic software.

The system detects these electromagnetic waves as a partial discharge signal by PD sensor mounted on spacer and output two kind of waveform (frequency spectrum and phase spectrum) analyzed by spectrum analyzer as result of the measurement. The existence and cause of PD can be presumed by these waveforms. Frequency spectrums are acquired by sweeping central frequency of band-path filter from 9 kHz to 1.5 GHz at high speed repeatedly. Phase spectrums are acquired by fixing the central frequency of band-path filter at frequency at where maximum value is detected in frequency spectrum. A measured signal is compared with the reference waveforms stored in a PC. At the first stage, actual PD and external noise signals are classified by means of phase patterns. Then, through the Neural Network one reference waveform is selected to identify the PD cause. Fig. 2.19 shows phase pattern characterized by each defect. Fig. 2.20 shows procedure of diagnosis by neural network having special branch structures.

Fig. 2.18 PD Monitoring Device

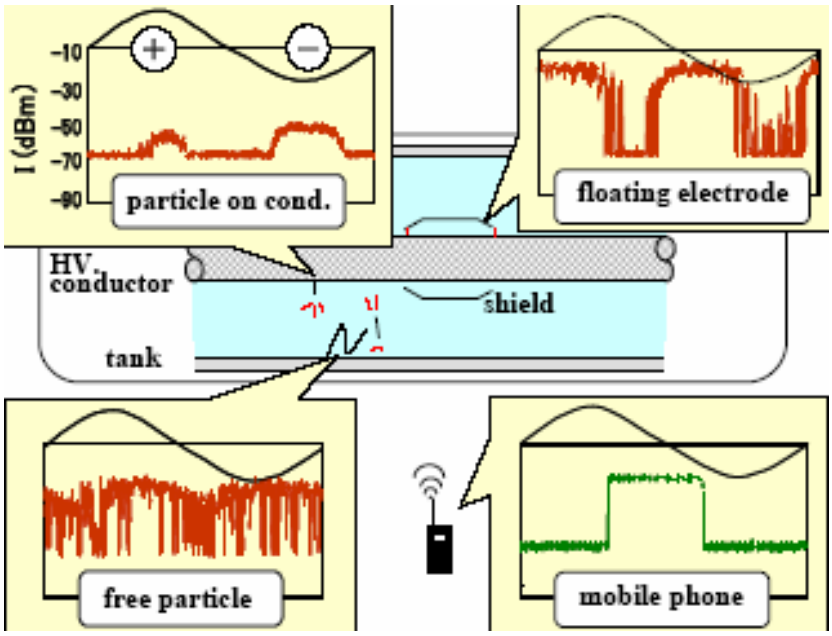

Fig. 2.19 Phase pattern characterized by each defect [2]

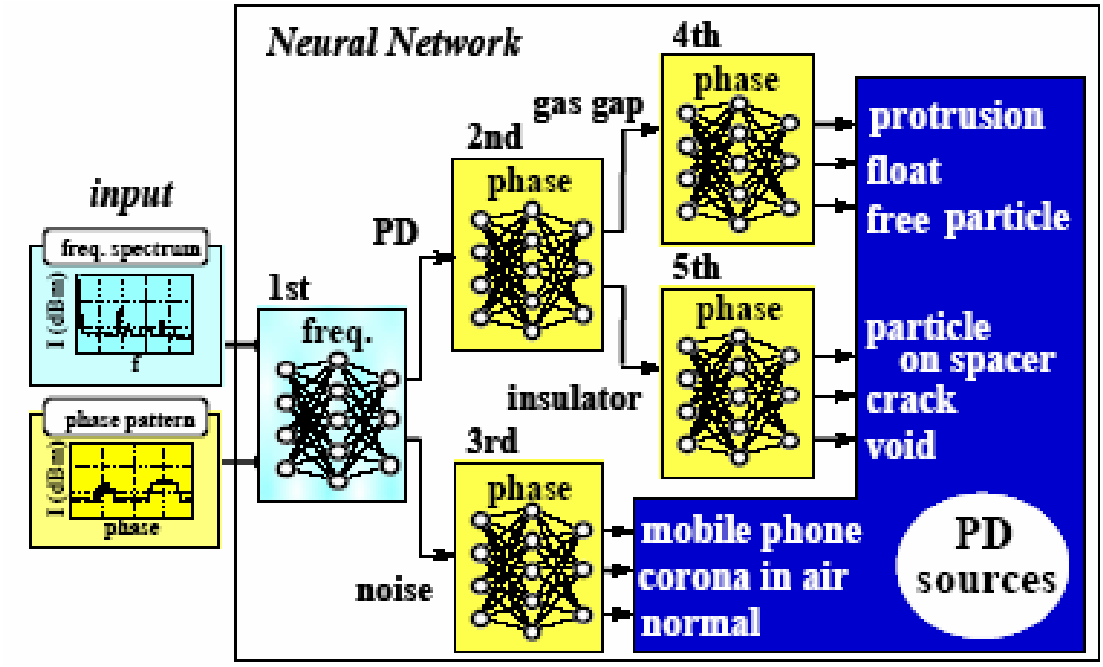

Fig. 2.20 Procedure of diagnosis by neural network having special branch structures [2]

References

1. Dieter Kind," Introduction on High Voltage Experimental Technique: Chapter 3.6 Partial Discharge Experiment", 1993
2. Hitachi Engineering and Services Co. Ltd: "Portable Type of PDM Device", 2006.
3. M.D. Judd, O. Farish: "High Bandwidth Measurement of Partial Discharge Current Pulses", ISEI Paper of IEEE Vol. 2, June 1998, pp 436-439.
4. ETS-Lindgren L. P, "Equipment manual EMCO model 94430 series current probe", Rev. E, February 2005.

Chapter 3
Partial Discharge Characteristics under Three-phase Electric Field In a Three-phase Construction

3.1 Introduction

This chapter deals with PD characteristics from a particle in a three-phase construction under three-phase voltage. Analysis of three-phase PD measurement system, PD occurrences and cross-interference phenomena in three phase construction are reported.

3.2 Experimental Setup

The measurement system was developed to investigate discharge characteristics under three-phase voltage. The model, the experiment setup, and PD sources have been explained in Chapter 2. GIS Model I and the measurement system I were used in the experiment. The experiments were conducted in laboratory air.

3.3 Analysis of Three-phase PD Measurement System

The measurement system was calibrated to verify the relation between the reading of the PD measurement system (mV) and injected charge (pC) and to verify sensitivity of the measurement system. The calibration of PD measurement system was done by injecting positive and negative known charges from a pulse calibrator to some injecting points as follows: phase to phase (R-S, R-T, S-T) and phase to tank (R-Tank, S-Tank, T-Tank) respectively. The high frequency current was measured with the PD measurement system and observed with the oscilloscope. The schematic of calibration circuit is shown in Figure 3.1. The examples of calibration results are shown in Figures 3.2 and 3.3.

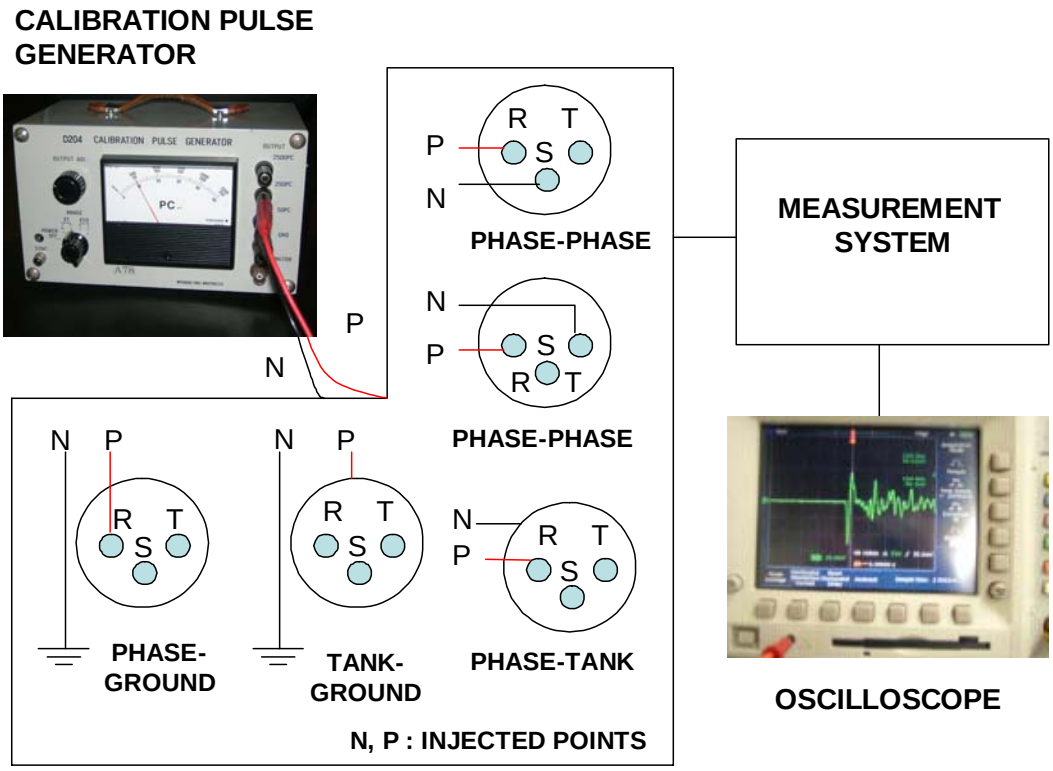

Figure 3.1 Calibration circuit of PD measurement system

Figure 3.2 shows the response of CT clamped on S phase (CT_S) when charges are injected to some different points. It appears that CT_S detected charges injected to S phase. In addition, it also detected charges injected to another points, such as R-T, R-tank, and T-tank. It means that charges injected to one phase were also induced to the other phases and to the enclosure. It appears that the response of charges injected to S phase is higher than that injected to the other points. It means that CT_S has high sensitivity for discharge occurring around S phase.

Figure 3.3 shows the response of CT clamped on the line connecting the tank and ground (CT_{TANK}) when charges are injected to some different points. It appears that the response of charges injected to the tank (phase-tank or tank-phase) is higher than those injected to the other points (phase-phase). It means that CT_{TANK} has high sensitivity for discharge occurring between the conductor and the tank.

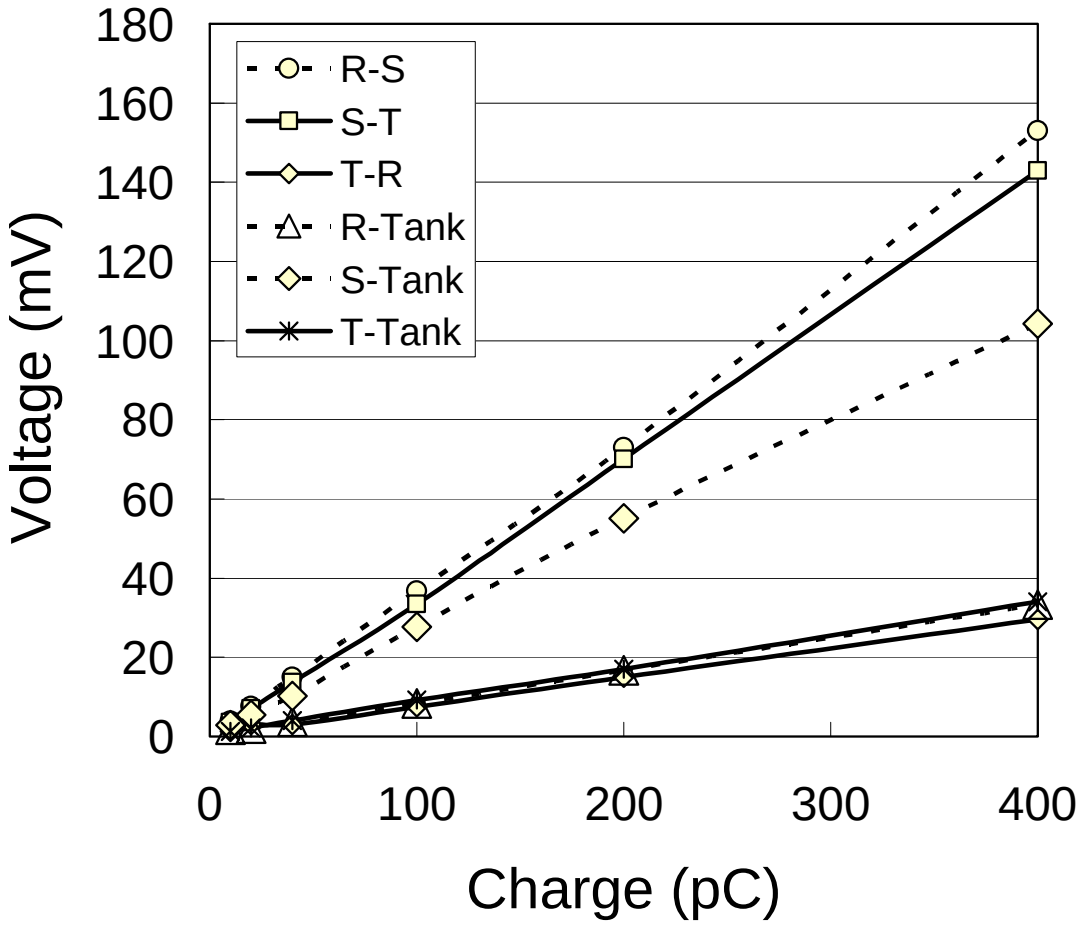

Figure 3.2 Calibration results of CTS

The results indicate some guidance for PD measurement on three-phase construction as follows.

1. PD occurring on one of three phase conductor induces charges to the other phases and the enclosure.
2. Measuring PD current flowing in one of three-phase conductors is sensitive for discharges which occur around the conductor (between the conductor and the tank, and between the conductor and the other conductors), but less sensitive for discharges which occur between the other two conductors and between the other conductors and the tank (Figure 3.2).

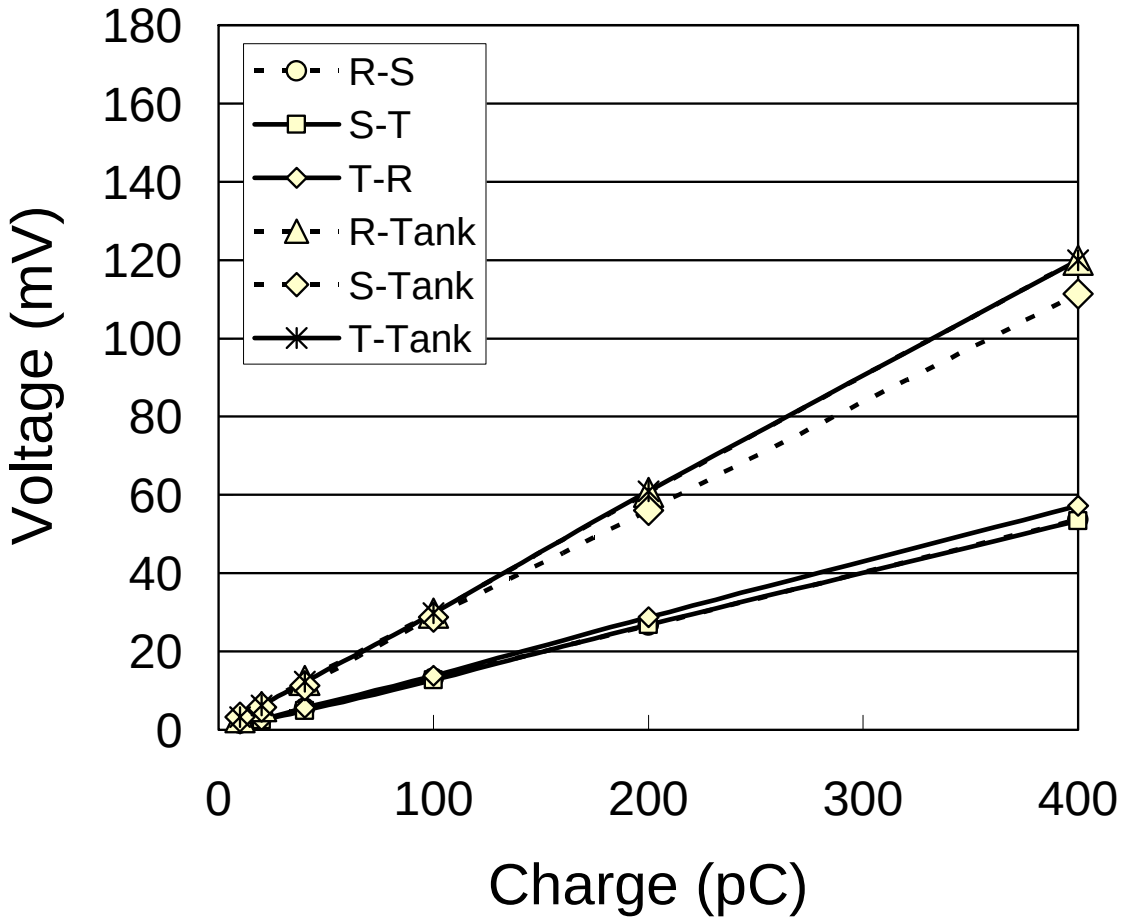

Figure 3.3 Calibration results of CTTANK

3. Measuring PD current flowing from the enclosure (tank) to ground is sensitive for discharges which occur between each conductor and the tank, but less sensitive for discharges which occur between the conductors (Figure 3.3).
4. Measuring PD current only at the enclosure of three phase construction or only at one of the phases will result in position dependent sensitivity for PDs.

The calibration results indicate that PD measurement must be conducted on three phases simultaneously to obtain measurement results of PD occurring in entire region of three-phase construction with high sensitivity.

3.4 Experimental Results

3.4.1 The Dependence of PDIV on Particle Position

Partial discharge from a particle placed at different positions on high voltage (HV) conductor and the tank was measured. The particle positions and their notations have been explained in 2.5. The diameter of a particle was 0.1 mm. The particle length is 5 mm.

PD inception voltage (PDIV) of these particles is shown in Figure 3.4. The results show that negative PDIV (PDIV N) is lower than positive PDIV (PDIV P) for the particles on HV conductor. On the contrary, PDIV N is higher than PDIV P for the particles on the tank. PDIVs of a particle adhered on different positions differed, depending on the particle position. PDIVs vary between 4 kV and 6 kV for a particle adhered on the different positions on the conductor and between 8 kV and 11 kV for a particle on the different positions on the tank. Namely, PDIV of a particle on the tank is higher than PDIV of a particle on the conductor. PDIV of a particle on the region between phases (R315, S90, and S135) is around 4 kV, lower than PDIV of a particle on the other places. The interpretation on these results will be discussed further in sub chapters 3.5.1 and 3.5.2.

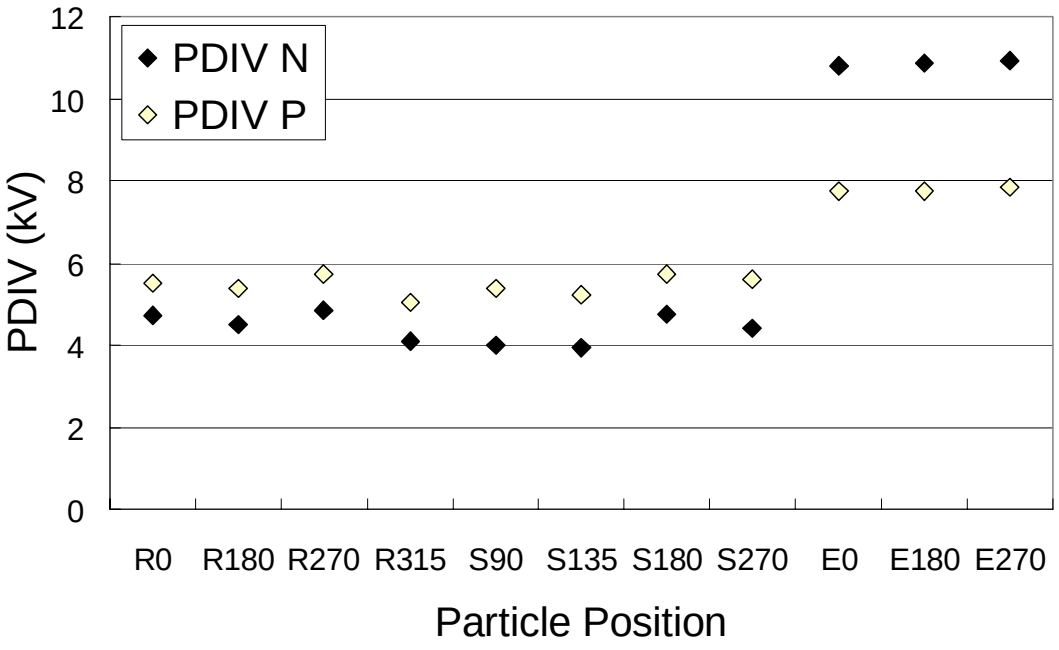

Figure 3.4 PDIV of particles on the conductor and on the tank

3.4.2 The Phase Dependence of PD Occurrence on Particle Position

Figures 3.5 to 3.7 show experimental results of PD occurrence at PD inception voltage (PDIV) from a particle on some different positions. Figure 3.8 and 3.9 show the examples of PD occurrences during two cycles of applied voltage at PDIV for a particle adhered on the conductor and a particle adhered on the tank respectively. It appears in Figure 3.8 that PD pulse of S45 particle occurs when the phase θ_S of S voltage is around 247^0. On the other hand, PD pulse of S270 particle occurs when $\theta_S = 270^0$. Then, it appears on Figure 3.9 that PD pulses of particle on the tank E180 and E270 occur at $\theta_S = 330^0$ and $\theta_S = 90^0$, respectively. The other experimental results are summarized on Figure 3.7. It is found from the Figure 3.7 that phases where PD appears at PDIV depended on the particle position. The interpretation on these results will be discussed further in 3.5.2.

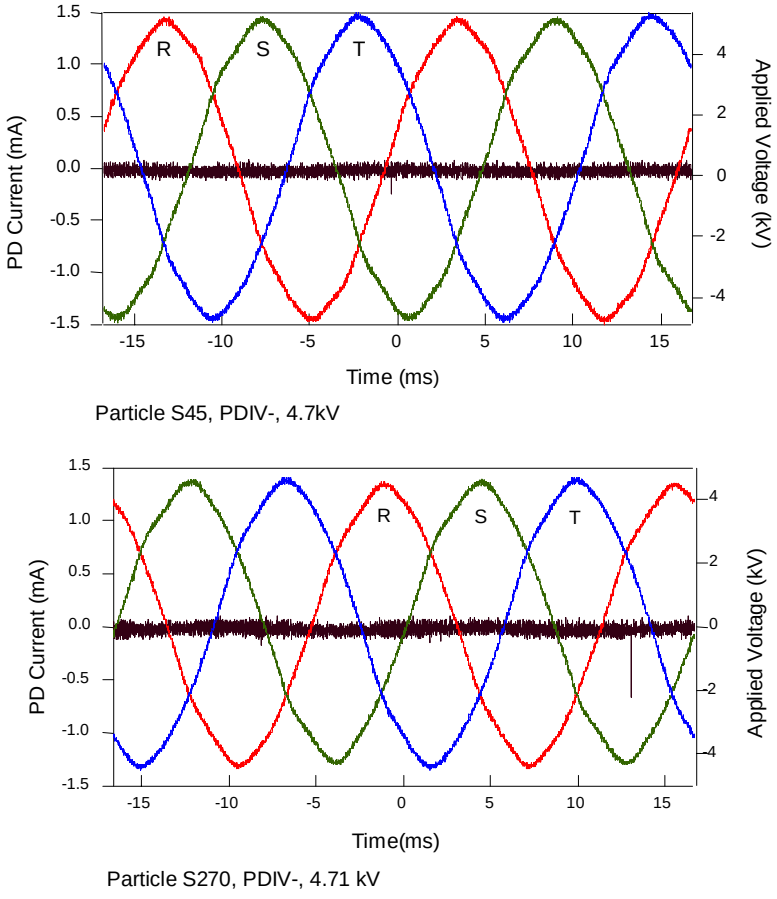

Figure 3.5 PD occurrences on 2 cycles of applied voltage at PDIV
(Particle on the conductor)

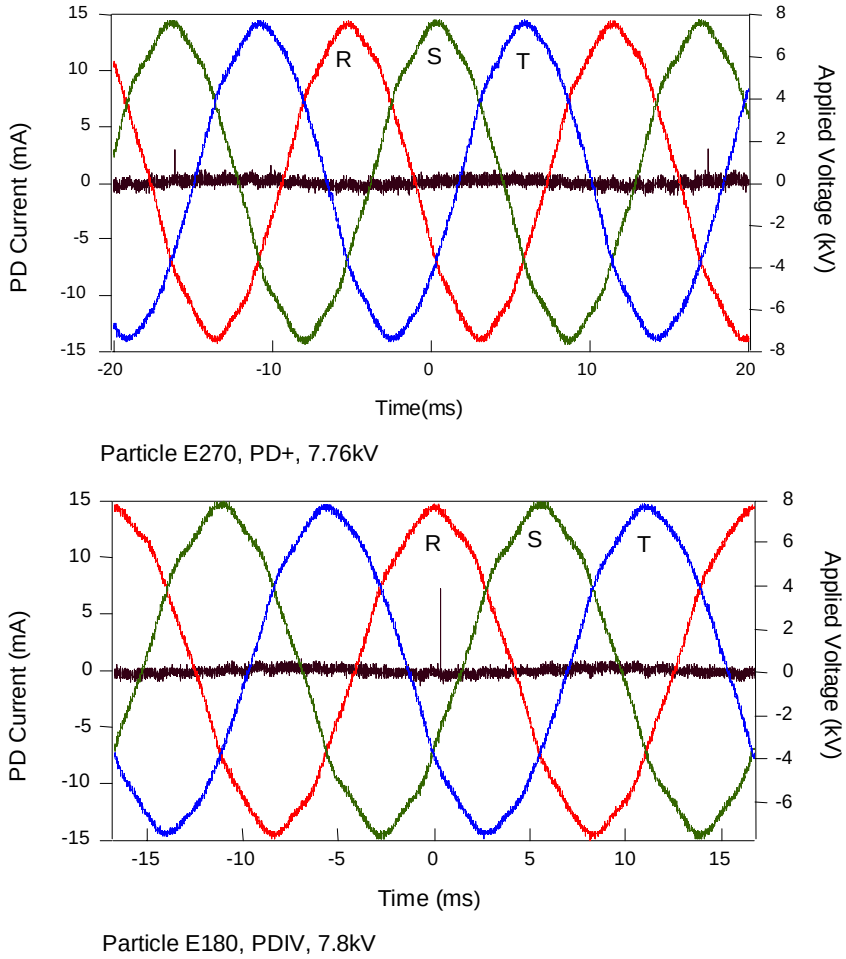

Figure 3.6 PD occurrences on 2 cycles of applied voltage at PDIV (Particle on the tank)

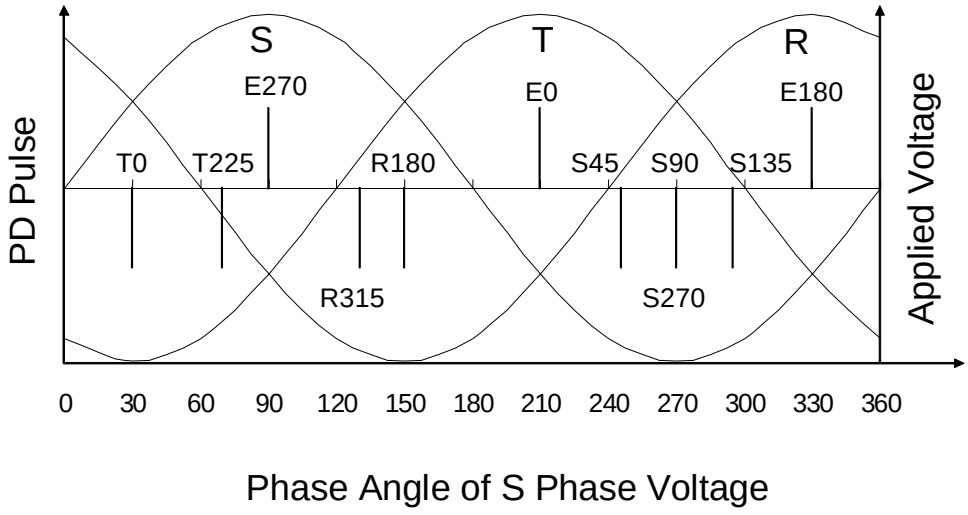

Figure 3.7 Experimental result resume of phase of applied voltage at PDIV for a particle on some different positions

3.4.3 Cross Interference Phenomena

Figure 3.8 shows waveform of discharge current flowing on each phase for S90 particle. PD currents measured by CT_R, CT_S, CT_T, and CT_{TANK} were 0.40mA, 0,88mA, 0.48mA, and 0.25mA, respectively. It appears that discharge caused by particle on S phase caused currents to flow on R, S, and T phases and to the enclosure. It means that the discharge occurring on one phase was induced and detected on the other phases. The charge was also induced to the tank.

For further analysis the magnitude of PD currents flowing on each phase measured by CT is classified. The magnitude of PD current flowing on each phase and the enclosure are normalized. Then, the maximum of normalized currents flowing on each phase, that is further called as magnitude ratio (A), were determined. The magnitude ratio is classified as follows: low (L) for A <0.4; medium (M) for 0.4≤A<0.7; and high (H) for A≥0.7.

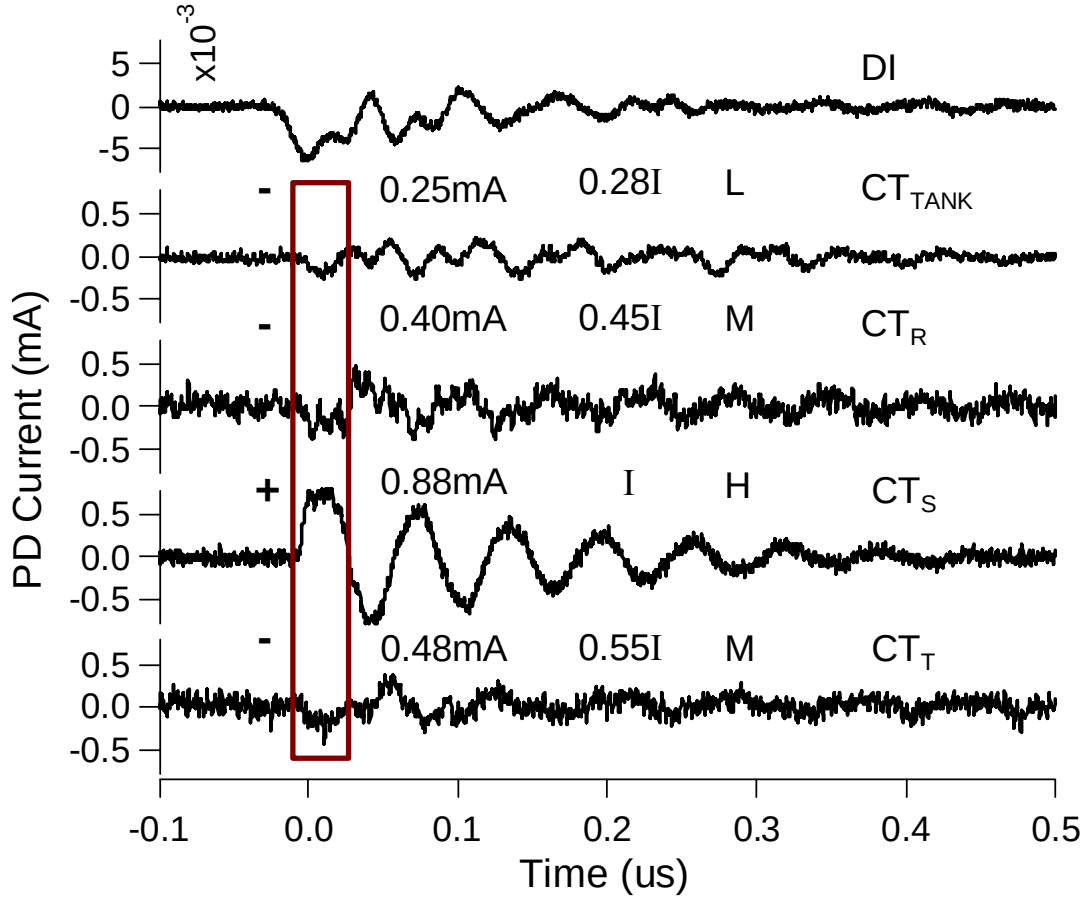

Figure 3.8 PD current waveform measured for S90 particle

Based on the classification, PD pulses from S90 particle as shown in Figure 3.8 result in low and negative current detected by CT_{TANK}, medium and negative current detected by CT_R and CT_T, high and positive current measured by CT_S. Example of the other results is summarized in Table 3.1. Even though it is not shown here, the repetition of the experiment on the same condition showed that the magnitude ratio is constant and independent of magnitude of PD current pulse. These results indicate that the ratio of magnitude of PD current flowing on each phase provides information of the particle position on the cross section of three phase construction. The interpretation of these results will be discussed further in sub chapter 3.5.3 in terms of cross-interference phenomena.

Table 3.1 Polarity and magnitude level of discharge currents measured for particles on S conductor

Particle Position	PD Polarity	Discharge Current			
		CT_{TANK}	CT_R	CT_S	CT_T
S90	PD-	L-	M-	H+	M-
S90	PD+	L+	M+	H-	M+
S45	PD-	L-	L-	H+	H-
S45	PD+	L+	L+	H-	H+
S270	PD-	H-	L-	H+	L-
S270	PD+	H+	L+	H-	L+
S135	PD-	L-	H-	H+	L-
S135	PD+	L+	H+	H-	L+

3.5 Discussion

3.5.1 PDIV Occurrence

The PDIV characteristics are discussed first. The results show that PDIV- is lower than PDIV+ for the particles on HV conductor, while PDIV- is higher than PDIV+ for the particles on the tank. Let us discuss these results. Positive PD is generated by an electron initiated by collision detachment of negative ions in high electric field region [14]. Thus, positive PD generation depends on whether or not negative ions exist around the particle tip. The negative ions at positive PD inception phase can be derived from PD in the previous cycle and or cosmic rays.

The high field region initiating PD is so restricted that, even under continuous three-phase AC voltage application, the generation of an initial electron would be necessary condition for PD initiation. On the other hand, negative PD is generated by an initial electron derived from the field emission from the electrode surface [14]. Thus, the generation of an initial electron for negative PD depends only on the electric field strength on the electrode surface. Therefore, an initial electron can be generated more easily for negative PD than for positive PD.

In the case of the particle on S conductor and faced to the bottom of the tank, the polarity of particle tip is negative when applied voltage S phase is in negative half cycle. Therefore, the first PD occurs in the negative half cycle of S voltage. In the case of the particle is attached on the bottom of the tank and faced to S conductor, the polarity of the particle tip is negative when the polarity of S voltage is positive. Therefore, the first PD occurs in the positive half cycle of S voltage.

3.5.2 Relation between Electric Field inside the Three-phase Construction and PD Occurrences

PDIV is determined by PDIV criterion which depends on effective ionization coefficient, $\overline{\alpha}$ [14-15]. PDIV criterion is given by Schumann equation as follows.

$$\int_0^{X_C} \overline{\alpha}(x)\, dx = K$$

where $\overline{\alpha} = \alpha - \eta$. α is Townsend's first ionization coefficient and η is the attachment coefficient, and both are functions of the electric field, atmospheric pressure, and temperature. X_C is the distance from the highly electrode surface and the point near electrode surface where $\alpha=\eta$. It is sometimes called the critical avalanche length or the boundary of the corona layer. K = 20 for air at 1 atm [15].

PDIV therefore depends on the electric field on the tip and the field distribution along the axis of the particle since $\overline{\alpha}$ is a function of the electric field intensity. For air [15]:

$$\alpha / p = 22\,(E/p - 0.244)^2 \qquad \text{for } 0.244 < E/p < 0.5$$

where E is electric field intensity in kV/cm, while p is air pressure in kPa. Because the electric field on the particle tip is much higher than on the other part, PDIV is influenced mainly by the electric field on the particle tip.

Let's observe the electric field characteristics inside the three-phase

construction. The electric field on each particle tip was calculated at 1 kV applied voltage for the comparison convenience. Figure 3.9 shows periodic change of absolute electric field on the particle tips during one cycle of S applied voltage at different positions (R315, S45, E270, and T0). The electric field calculation point is determined so that the electric field at the point at PDIV is equal to critical electric field E_{cr} in air at atmospheric pressure (E_{cr} = 3 kV/mm). The critical electric field is the field at which the ionization begin to take place if $\alpha = \eta$. The electric field calculation point is X_C = 0.02 mm from the particle tip surface.

Let's observe Figure 3.9. At certain position (x,y) inside the three phase construction the electric field is rotating with varying magnitude, i.e sinusoidal in two perpendicular directions without necessarily coinciding zero crossings. The electric field stress on each point inside the construction varies with the phase of the applied voltage. Every half cycle the field achieves the minimum and the maximum values. Every a half cycle the pattern of the electric field stress is repetitive.

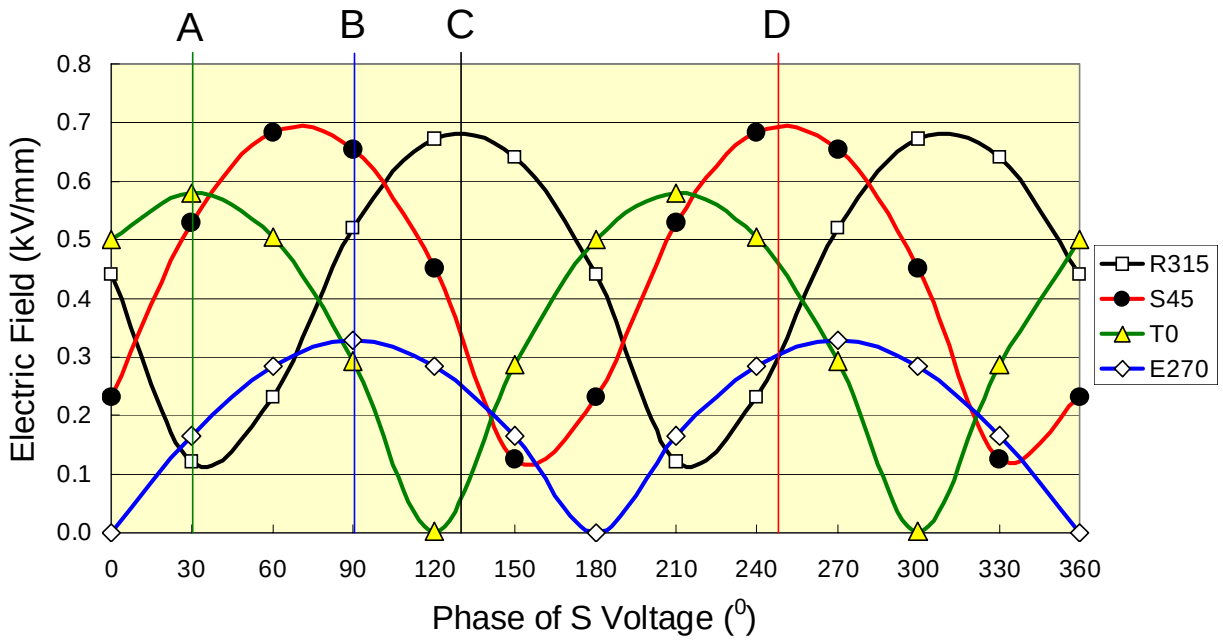

Figure 3.9 Periodic change of absolute electric field on the particle tips

It is found in Fig. 3.9 that the phase and value of the maximum electric field depends on the particle position. For example, the maximum electric fields occur at $\theta_S = 30^0$, $\theta_S = 90^0$, $\theta_S = 127^0$, $\theta_S = 247^0$ for T0, E270, S45, and R315 particles, respectively (see lines A, B, C and D). These electric field characteristics result in the phase dependence of PD occurrence at PDIV on the particle position. The maximum electric fields are 0.58 kV / mm, 0.33 kV / mm, 0.67 kV / mm, and 0.69 kV / mm for T0, E270, S45, and R315 particles, respectively. It is reasonable because the gap distance and the electrode configuration of the three-phase construction depend on the particle position.

Figure 3.10 shows the maximum electric field on the particle tip of a particle at various positions at 1 kV of applied voltage. It is found that the electric field on the particle tip depends on particle position. More ever, the electric field of the particle on the conductor faced to the other conductor (phase-phase region), for example R315 and S135, is higher than that on the other place. These electric field calculations explain reasonably the experimental results: PDIV of particles with the same size depend on the particle position; and PDIV of the particles on the conductor facing to the other conductor (phase-phase region) is lower than that on the conductor facing to the tank.

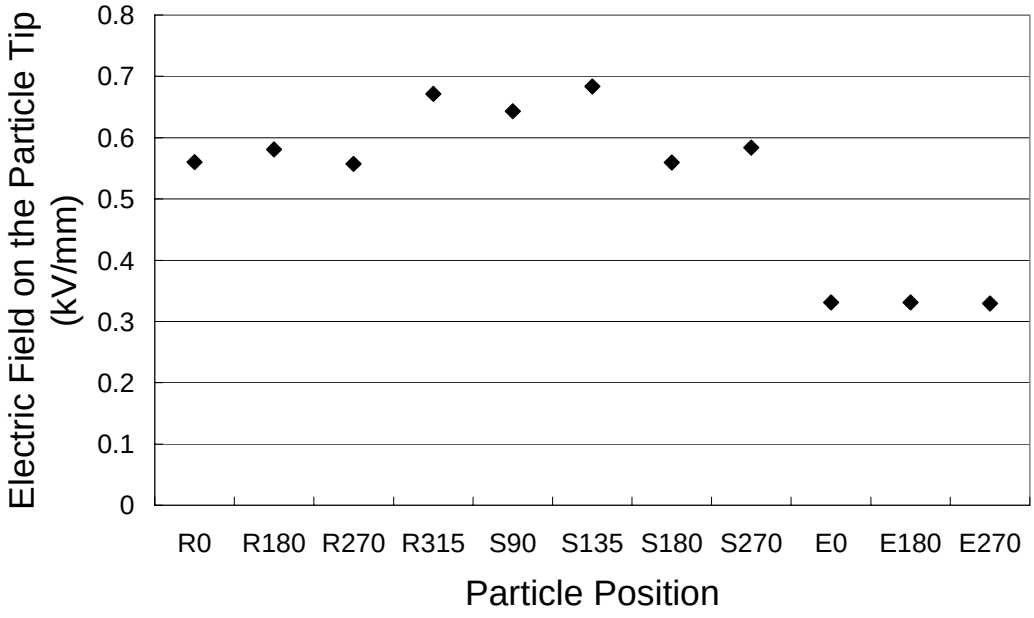

Figure 3.10 Electric field on the particle tip at 1 kV applied voltage

Figure 3.11 summarizes phase angle of S applied voltage at maximum electric field for a particle attached on the different position on R, S, and T conductors and on the tank. In general, PD of a particle set on one phase conductor occurs on the peak of applied voltage at the related phase. The effects of the other phases take place when the particle faces to another conductor, resulting in the shifting of the phase of maximum electric field and PDIV from the peak of applied voltage. These calculation results explain the experimental results summarized on Figure 3.10. For example, both calculation and experimental results indicate that negative PDIV of S45 particle occurred at $\theta_S = 247^0$, while negative PDIV of E270 particle occurred at $\theta_S = 90^0$. Note that negative PDIV is easier to occur than positive PDIV for a particle adhered on the conductor and on the contrary for a particle adhered on the tank.

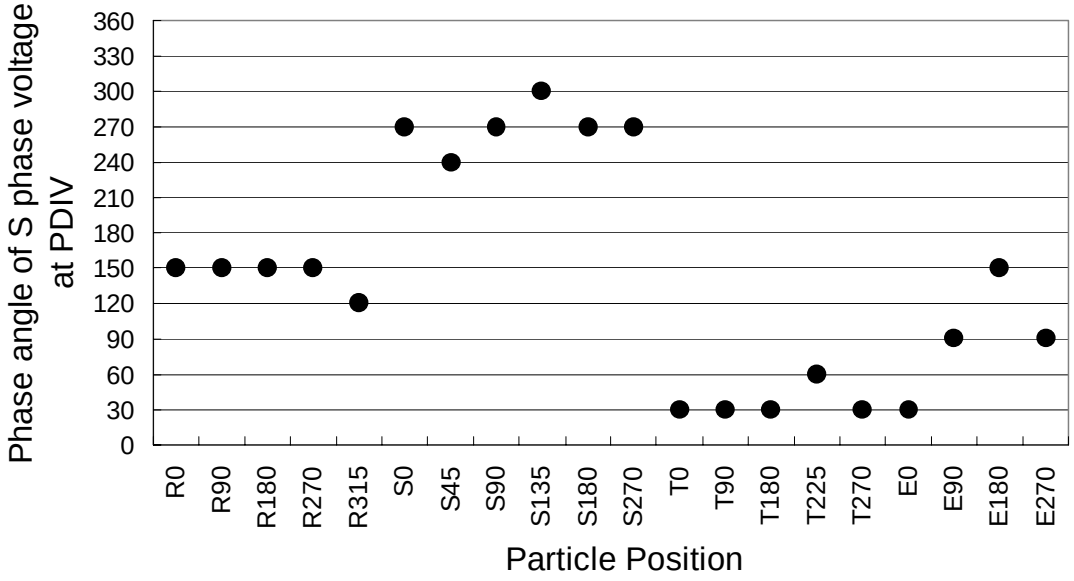

Figure 3.11 Phase where the maximum electric field appears for a particle on the different position

3.5.3 Cross Interference Phenomena

The experimental results revealed that discharge from a particle on one phase conductor caused currents to flow on the other phases, not only on the phase where the particle exists. The equivalent circuit of three-phase configuration with S90 particle and the measurement system are shown in Figure 3.12 to explain the

phenomena. PD resulting from S90 particle is described as a pulse source. Insulation regions between the tank and each conductor and between conductors are described as their equivalent coupling capacitors; those are C_R, C_S, C_T and C_{RS} C_{ST} and C_{RT}. By LCR meter, the capacitances are estimated to be C_R=9.5 pF, C_S=7.9 pF, C_T=9.6pF, C_{RS}=5.3 pF, C_{RT}=3.7 pF, C_{ST}=6.1 pF.

Let us analyze the circuit. If negative discharge occurs in S90 particle, a small amount of charge is induced to R and T phase. A large amount of charge flow in S phase conductor to ground (path S). Since the current flows toward positive sign of CTS, it is measured as positive current by CT_S. Then the current is divided into three directions: R conductor (path R), T conductor (path T), and the tank (path TANK). Since they flow toward negative sign of each CT, it is measured as negative current by CT_R, CT_T, and CT_{TANK}. The currents are transmitted from R and T conductor to tank, and then from tank to S phase conductor, because of the presence of coupling capacitances between the two conductors and between conductor and the tank. These discharge current path are depicted in Figure 3.12.

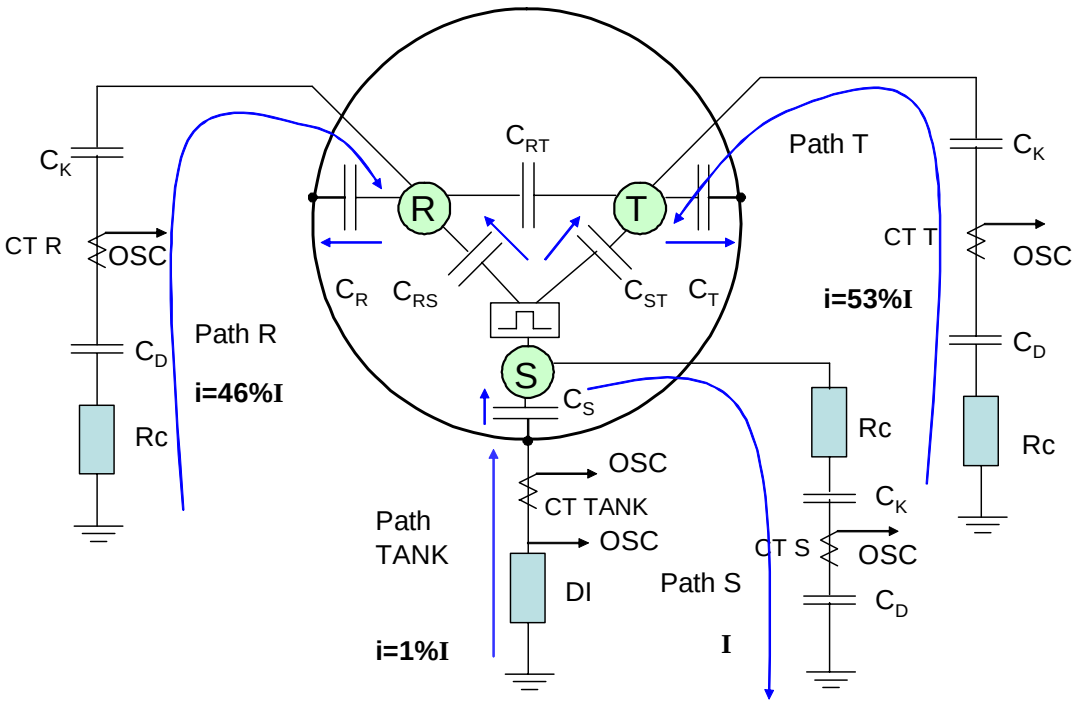

Figure 3.12 Equivalent circuit and path of PD current of S90 particle

The discharge current flowing in each phase was estimated based on the equivalent circuit and dominant frequency of discharge current. The frequency was estimated based on the rise time of PD current waveforms measured for particles attached on different positions. Average rise time (t_r) of PD current was 17.5 ns so that the dominant frequency of PD current can be determined by the relation f = 0.35/tr, giving f = 20 MHz.

If the current flowing in path S is I (high), the currents flowing in R, T, and tank paths are 0.46I (medium), 0.53I (medium), and 0.01I (low), respectively. These calculation results agree with the magnitude of discharge current resulting from the measurement in the term of magnitude level, although there are small differences in values.

3.6 Conclusions

PD characteristics in three-phase construction under three-phase voltage were investigated. The measurement system for observing discharge characteristics in three-phase construction was developed. PD from a particle on the different positions on the conductor and on the tank was observed. The conclusions are as follows.

1. Measuring PD signals only at the enclosure or on one of the phases of three phase construction will result in the position dependent sensitivity for partial discharges.
2. Partial discharge inception voltage of a particle adhered on different position differs depending on the particle position.
3. Phase where PD occurs at PDIV depends on particle position.
4. PD caused by a particle on one phase conductor is induced and detected on the other phase conductors.
5. Magnitude ratios of PD current flowing on each phase are unique for each particle on different positions. The ratio is constant and independent of magnitude of PD current pulse.
6. Polarity of PD current flowing on each phase depends on particle position.

Calibration and measurement results indicate that PD measurement on three phase construction must be conducted on three phases simultaneously to obtain measurement result of PD occurring in entire region with high sensitivity and to obtain information of the location of PD source. Experimental results indicate that

phase of applied voltage at PDIV and magnitude ratio of discharge current flowing on each phase provides information of the particle position on the cross section of three phase construction. Therefore, they can be considered as parameters for estimation of particle position on the cross section of three phase equipment.

References

1. S. Yanabu, H. Okubo, S. Matsumoto,“Metallic Particle Motion in Three-Phase SF_6 Gas Insulated Bus”, IEEE Transactions on Power Delivery Vol. PWRD-2, No. 1, January 1987.
2. Wielen, E.F. Steennis, and P.A.A.F Wouters,”Fundamental aspects of excitation and propagation of on-line PD signals in three-phase medium voltage cable systems,”, IEEE Trans. on DEI, vol 10, no4, pp. 678-688, Aug. 2003.
3. S. Yanabu, Y Murayama, and S. Matsumoto,”SF_6 Insulation and its Application to HV Equipment”, IEEE Transactions on Electrical Insulation, Vol. 26, No.3, pp 358-366, 1991.
4. G.V.N. Kumar, J.Amarnath, B.P. Singh, K.D. Srivastava,”Electric Field Effect on Metallic Particle Contamination in a Common Enclosure Gas Insulated Busduct”, IEEE Trans. on DEI, Vol 14, No. 2, pp. 334-340, Apr. 2007.
5. Kreuger, F.H, Samir Shihab, “Partial Discharge Measurement on Three-core Belted Power Cables”, IEEE Transactions on Power Delivery, Vol. 4, No. 2, April 1989
6. E. Harkink, F.H. Kreuger, P.H.F. Morshuis: “Partial Discharges in Three-core Belted Power Cables”, IEEE Transactions on Electrical Insulation, Vol. 24, No. 4, pp. 591-598, Aug. 1989.
7. R. Heinrich, S. Schaper, W. Kalkner, R. Plath, A. Bethge,”Synchronous Three-phase PD Detection on Rotating Machones”, XIIIth ISH, Netherlands 2003.
8. S.Schaper, W. Kalkner, R.Plath, H. Emanuel,”Synchronous Multi Terminal PD Detection on Power Transformer”, XIIIth ISH, Netherlands 2003.
9. W. Kalkner, A. Obralic, M. Kaufhold, R. Plath,”Investigation of PD-Pulse Propagation and Coupling between Three-phases of a Stator of a Rotating Machine”, XIVth ISH, Paper B-44, China, 2005.
10. W. Kalkner, A. Obralic, A. Bethge, R. Plath,”Synchronous 3-Phase Partial Discharge Detection on Rotating Machines”, XIVth ISH, Paper G-042, China, 2005.
11. A.M. Jafari, A. Akbari,”Multi-Source Partial Discharge Diagnosis in Three-phase High Voltage Devices”, XIVth ISH, Paper G-051, China, 2005.
12. Ronald Plath,”Multi-channel PD Measurement”, XIVth ISH, Paper J-04, China, 2005.

13. Akbari, A.M. Jafari, M. Kharezi,“Partial Discharge Localisation in Power Transformers with Delta Connected Windings”, XIVth ISH, Paper G-052, China, 2005.
14. D.B. Philips, R.G. Olsen, P.D. Pedrow,”Corona Onset as a Design Optimization Criterion for High Voltage Hardware”, IEEE Transaction on Dielectrics and Electrical Insulation Vol. 7 No. 6 pp. 744-751, December 2000.
15. N.H. Malik and A.H. Qureshi,”Calculation of Discharge Inception Voltage in SF_6-N_2 Mixtures”, IEEE Transaction on Electrical Insulation Vol. EI-14 No.2 pp. 70-76, 1979.

Chapter 4

Effects of Elliptical Nature of Rotating Electric Field on Partial Discharge Pattern in a Three-phase Construction

4.1 Introduction

Discharge investigations on single-phase power equipment have been well-established for many years. However, there are only a few reports on discharges in three-phase constructions such as three core belted power cable [1,2] and three-phase gas insulated switchgear (GIS) [3]. On the other hand, due to its compactness and low cost, application of three-phase equipment (three-phase in one tank) such as three-phase GIS and three-phase gas insulated bus (GIB), has been increasing. A three-phase in one-tank design has also been developed for 550 kV GIS [4]. Therefore, to improve diagnostics techniques in three-phase equipment, it is very important to develop a partial discharge (PD) measurement system and investigate PD characteristics in three-phase equipment.

The characteristics of PD under three-phase voltage, i.e., cross interference phenomena and phase angle dependence of PD occurrence on particle position have been reported previously [5,6]. It was explained that the phase angle dependence of PD occurrence is caused by the electric field characteristics in three-phase equipment. It can be expected that the PD characteristic will be different from that in single-phase equipment because the electric field in three-phase equipment is not linear, but rotates with power frequency. The electric field vector locus in three-phase construction is elliptical, although the shape differs locally.

In this chapter, the effects of the elliptical nature of the rotating electric field on PD distribution pattern are studied. It is known that PD distribution pattern is often used for PD diagnostics. A study on PD distributions is useful for

interpreting PD measurement results in three-phase equipment.

A simplified model of three phase GIS with air inside was used in this research. The electric field in the construction was analyzed and the discharge characteristics were observed. The experimental results showed that the phase widths where PD current pulses appeared, also called phase width δ_{PD}, were different depending on the elliptical nature of rotating electric field at the same applied voltage. The results also showed that the phase width δ_{PD} was also influenced by the applied electric field. These results were analyzed based on the relationship between the locus of the applied electric field and the critical electric field of air.

4.2 Model of Three-phase Equipment

A simplified model of three phase GIS with air inside was used in this research. It was composed of a tank model 150 mm in diameter, 300 mm in length, 2 mm in thickness, and three-phase conductors 25 mm in diameter. The electrode system was arranged to simulate three-phase electric field in three-phase equipment. The conductors were arranged in an isosceles triangle construction. The maximum voltage of three-phase transformer used for the experiment was 52 kV. The dimensions of the tank and the conductors were about one fifth of an actual 275 kV three-phase GIS. The layout and dimensions of the model are shown in Figure 4.1.

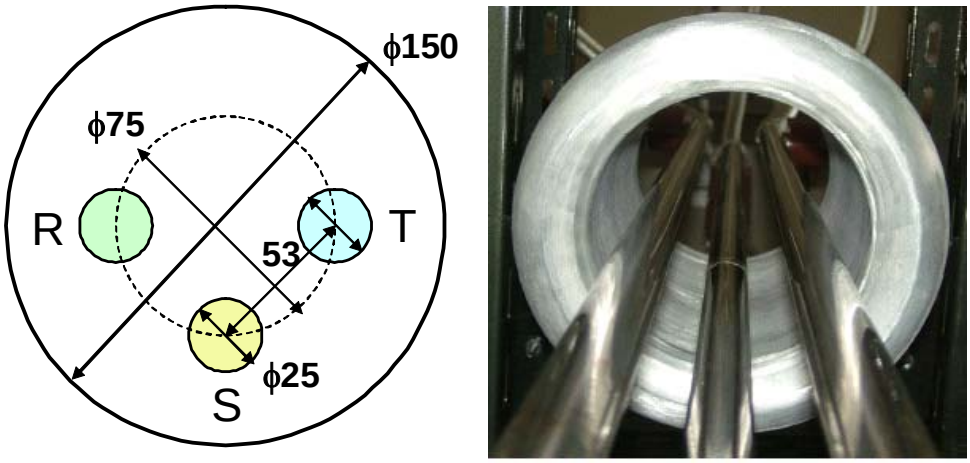

Fig. 4.1 Layout of simplified model of three-phase GIS

4.3 Electric Field Analysis

4.3.1 Electric Field inside Three-phase GIS without Particle

The electric fields inside the insulation of the construction were determined from a boundary element method simulation: along a circle among the phases and the tank, along vertical line starting from the bottom of the tank, along line connecting the centers of conductor phases, and around the conductor. The electric field calculation is two dimensional.

Figure 4.2 shows the change of electric field distribution with phase of applied voltage. The blue color in the figure reveals that the electric field intensity is the lowest, while the red color reveals that the electric field intensity is the highest.

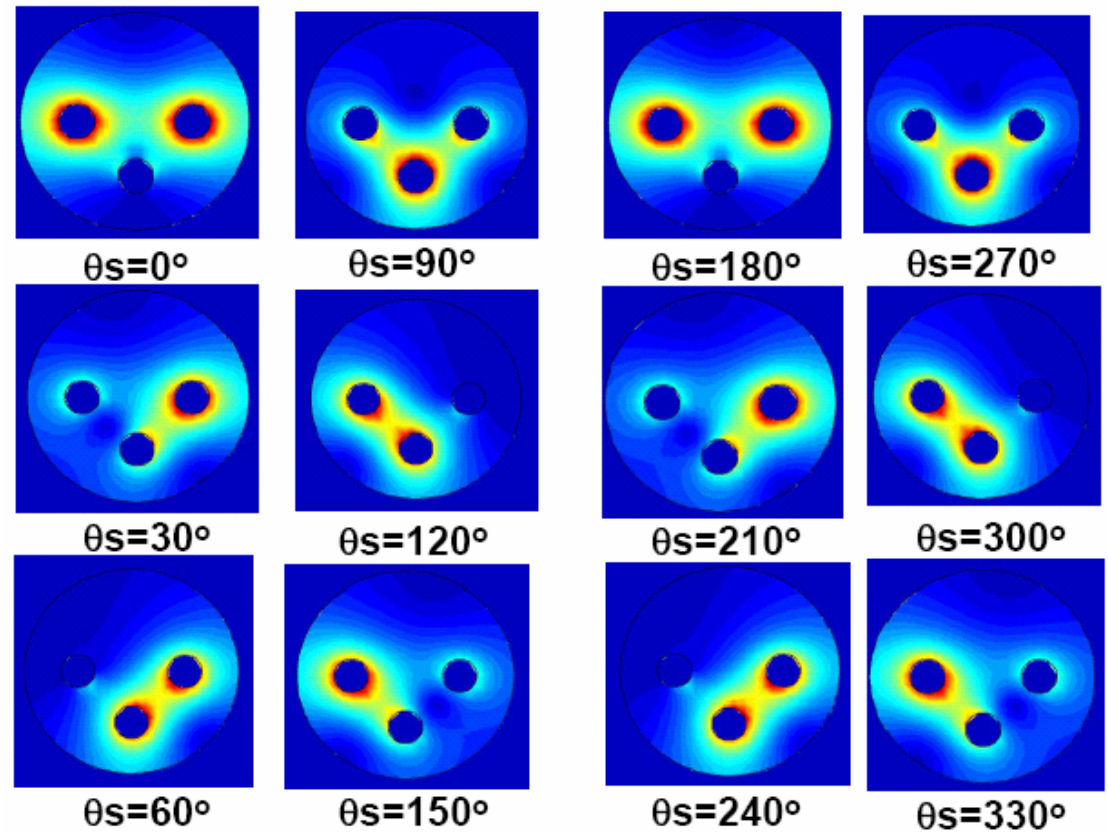

Figure 4.2 Change of electric field distribution with phase of applied voltage

The electric field distribution pattern varies with phase of applied voltage. Every a half cycle the pattern of electric field stress is repetitive.

Figure 4.3 shows the difference in electric field distribution between single-phase and three-phase equipment. The electric field distribution pattern in single-phase equipment is independent of phase of applied voltage, while one in three-phase equipment changes with the change of applied voltage.

Figure 4.4 shows the change in the pattern of the electric field vector at 5 mm below the centre of the tank (Point B in Figure 4.3) during one cycle of applied voltage. It seems that there are periodic changes in electric field distribution produced by three-phase voltage at any point. While the voltage phase varies from 0 to 2π, the electric field vector changes and rotates continuously.

Figure 4.5 shows the locus of the electric field vector at different points. Here, while the vector locus is elliptic, its shape varies locally. On the electrode surface the locus is linear because the electric field lines are vertical to the conductor surface. At some regions, for example at point A, the locus is elliptic. Meanwhile, at point B, which is 5 mm below the centre of the tank, the locus is truly circular. It is also found that the electric field vector locus between the phases and the tank is almost linear, resembling that in a single-phase configuration; while that between phases has variations: linear, elliptic, and circular.

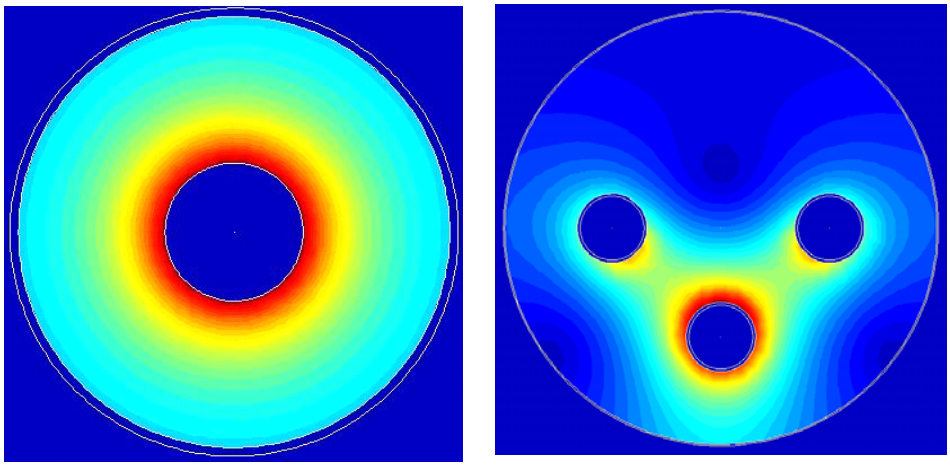

Single Phase Three Phase

Fig. 4.3 Electric field distribution inside single-phase equipment and three-phase equipment

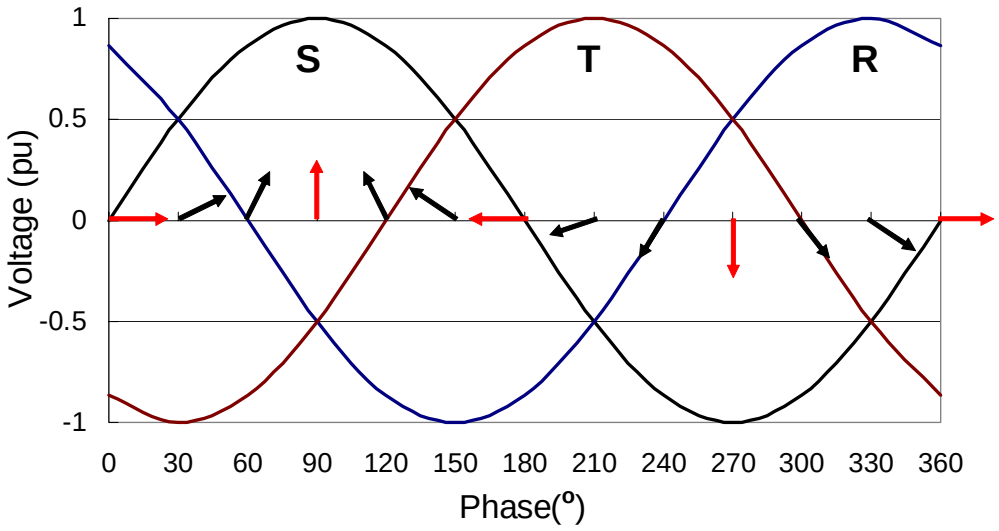

Fig. 4.4 Pattern of the electric field vector at 5 mm below the centre of the tank (B point in Figure 4.5) during one cycle of applied voltage

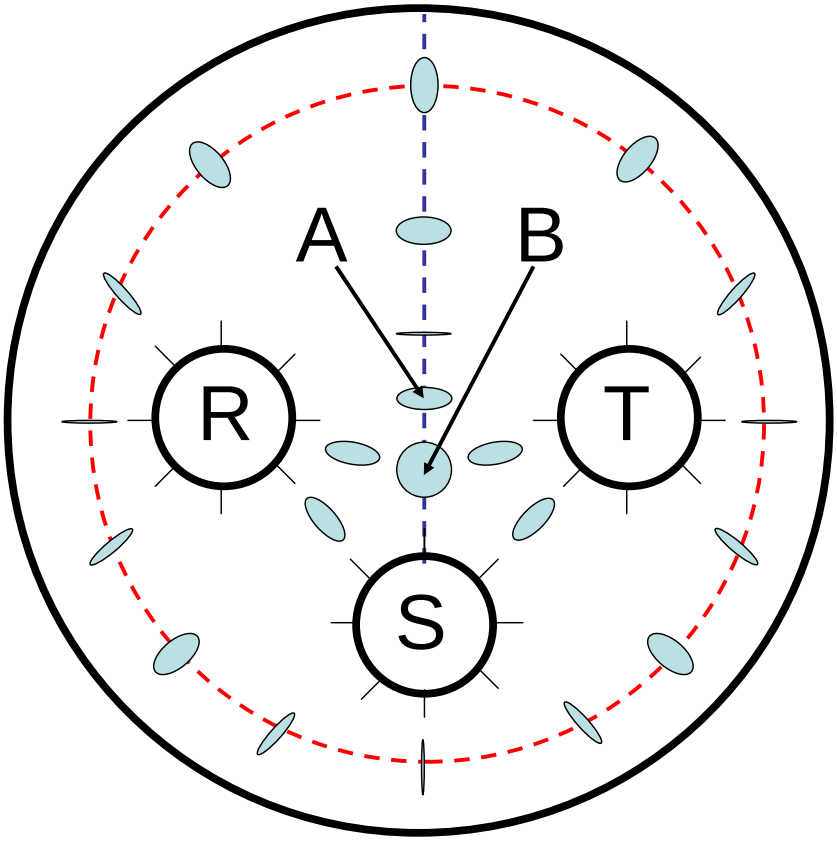

Fig. 4.5 Electric field vector loci in isosceles triangle arrangement of three-phase construction without particle

The rotating electric field at a certain position (x,y) can be described by four parameters: the maximum E_{max} (x,y) and minimum E_{min} (x,y) field strength, the phase angle of applied voltage θ_{max} (x,y) at maximum field E_{max} (x,y), and field direction ϕ_{max} (x,y) at maximum field [1]. These parameters are illustrated in Figure 4.6. δ_V in the figure is defined as the angle that designates the intersection width of the electric field vector locus and critical electric field circle.

The elliptical nature of rotating electric field is expressed as electric field ratio, η. It is defined as the ratio between the magnitudes of the elliptical field along the main axes,

$$\eta = E_{min} / E_{max} \quad (0<\eta<1) \qquad \text{.....(4.1)}$$

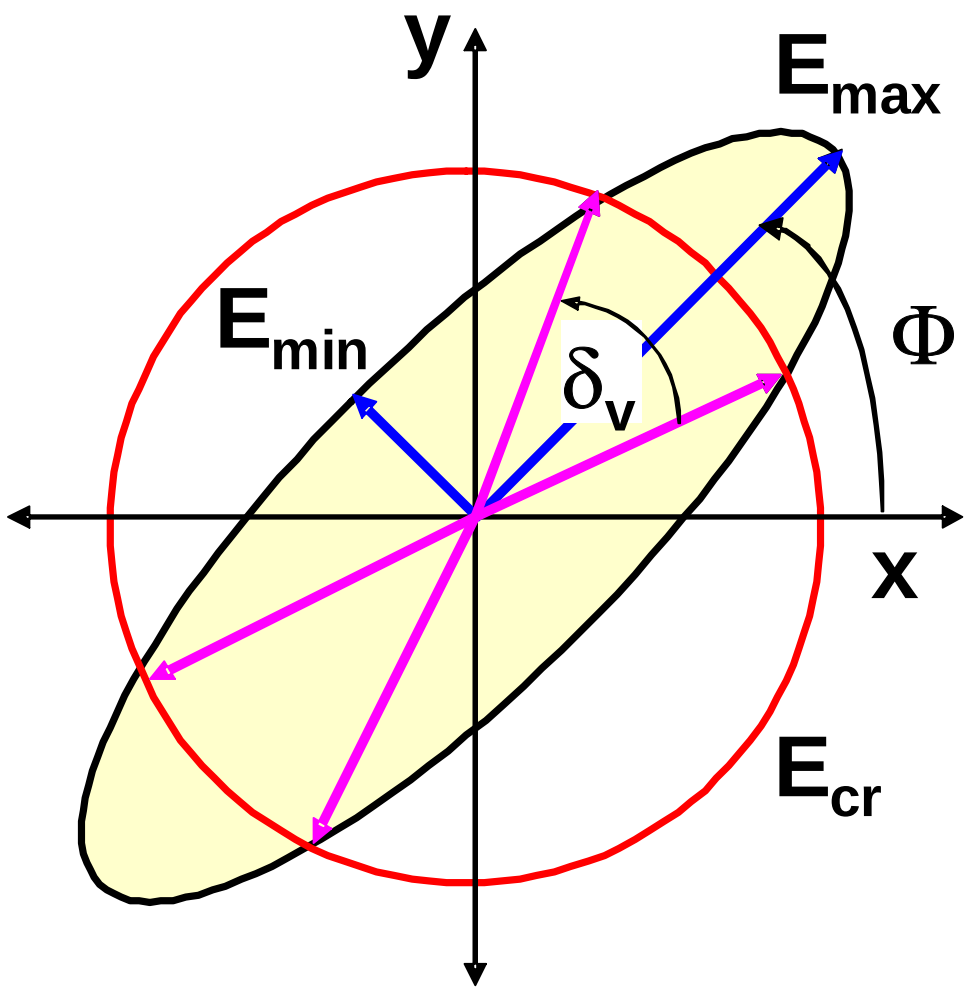

Fig. 4.6 Rotating electric field parameters

where:

E_{min}: minimum electric field intensity at a certain point during a cycle of applied voltage

E_{max}: maximum electric field intensity at a certain point during a cycle of applied voltage

4.3.2 Electric Field inside Three-phase GIS in the Presence of Particle

The background electric fields on the calculation points with and without particle were calculated to observe the effects of the presence of a particle on the electric field ratio η at the same points.

The diameter of a particle is 0.1 mm. The radius of the particle tip is 0.05 mm. Particles of 5 mm, 10 mm, 15 mm and 20 mm in length were laid at the S90 position to observe the effects of changes in electric field ratio η on PD distribution pattern. The particle position is shown in Fig. 4.7.

The electric field vector locus at the distances 0 mm (A), 5 mm (B), 10 mm (C), 15 mm (D), 20mm (E), and 25 mm (F) away from S conductor in the absence of particle are shown in Figure 4.8. The points are laid between S conductor and the center of three-phase GIS. If a point approaches the center of the cross section of the tank, the maximum electric field reduces; while the minimum electric field increases as shown in Figure 4.9.

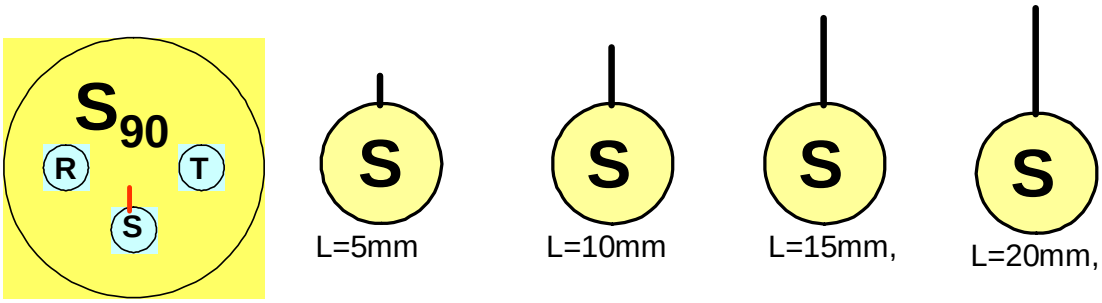

Fig. 4.7 Particle at S90 position with various lengths

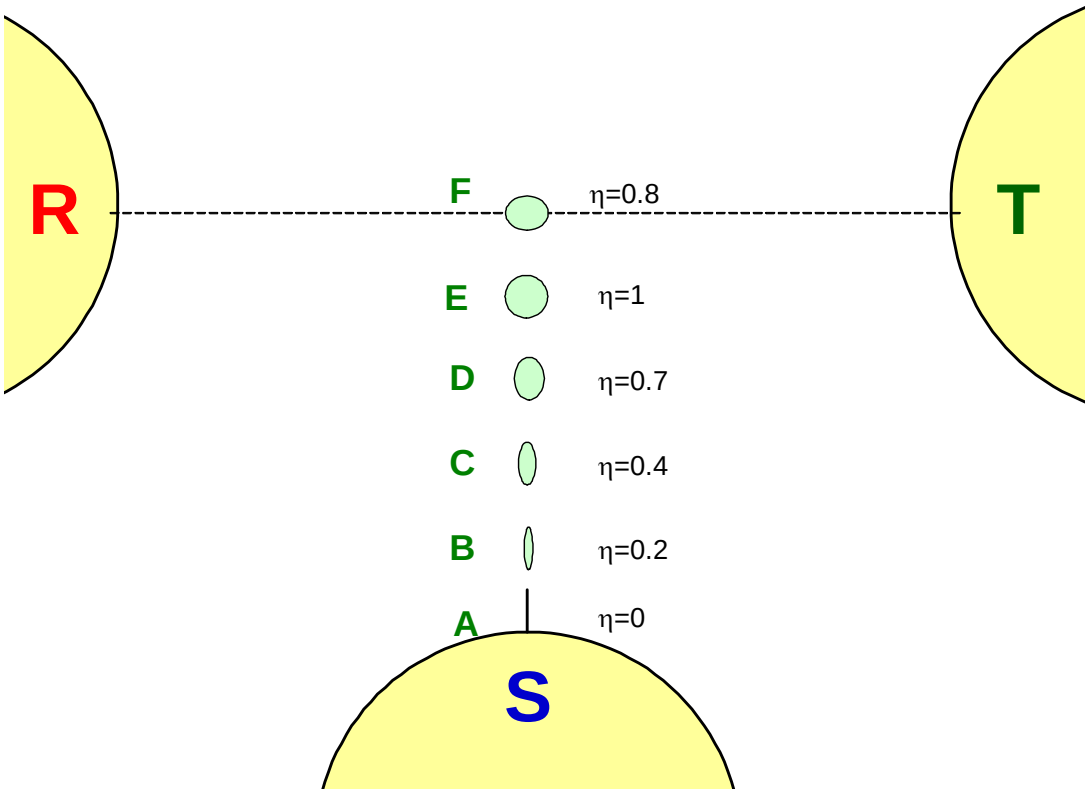

Figure 4.8 The electric field vector locus at the distances 0 mm (A), 5 mm (B), 10 mm (C), 15 mm (D), 20mm (E), and 25 mm (F) away from S conductor in the absence of particle.

The minimum and maximum electric fields are same at point E (20 mm from S conductor). The electric field vector locus changes from linear to circular when the points keep away from S conductor (point A) to the point 5 mm below the center of the three-phase construction (point E). The electric field ratio (η) changes from 0 until 1 from point A until E.

Fig. 4.10 shows minimum and maximum electric field from point B (5mm from S conductor) until point E (20mm from S conductor) in the presence of particle. The presence of particle increases significantly the maximum electric field on the particle tip, but its effect on minimum electric field is not significant. Therefore, the electric field ratio in the presence of particle is lower than one without particle as shown in Fig. 4.11..

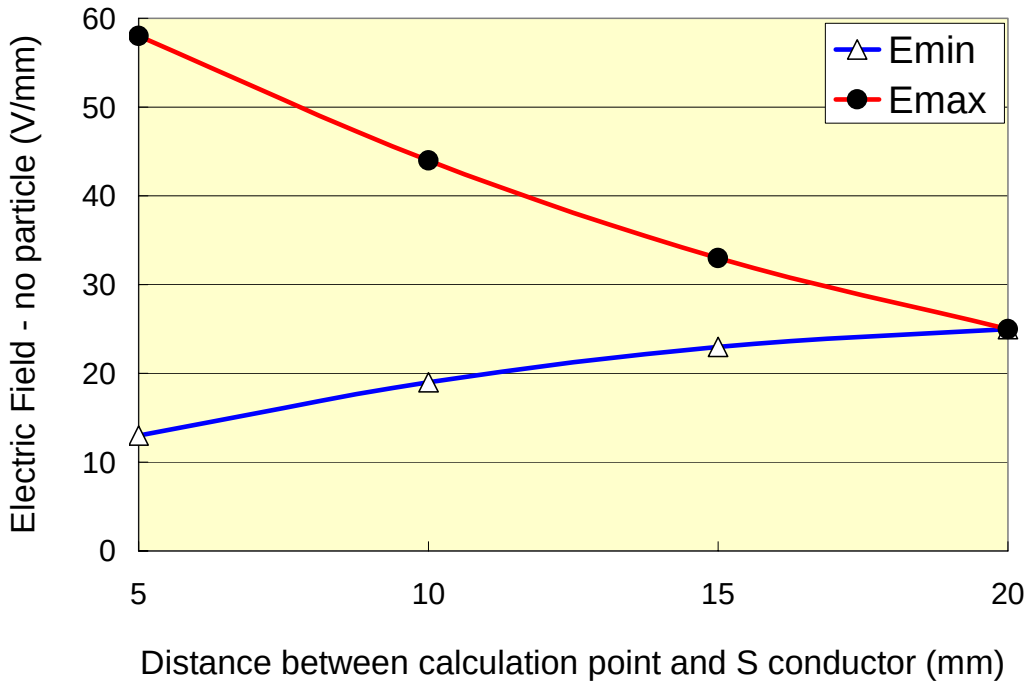

Fig. 4.9 Minimum and maximum electric field from point B (5mm from S conductor) until point E(20mm from S conductor) without particle

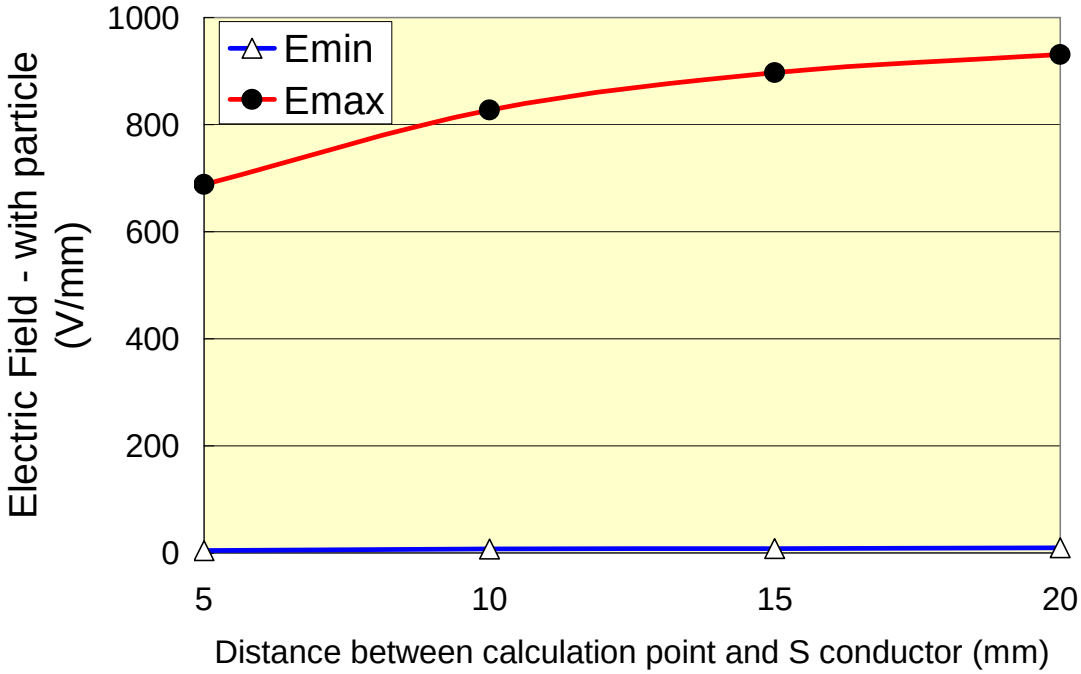

Fig. 4.10 Minimum and maximum electric field from point B (5mm from S conductor) until point E(20mm from S conductor) in the presence of particle

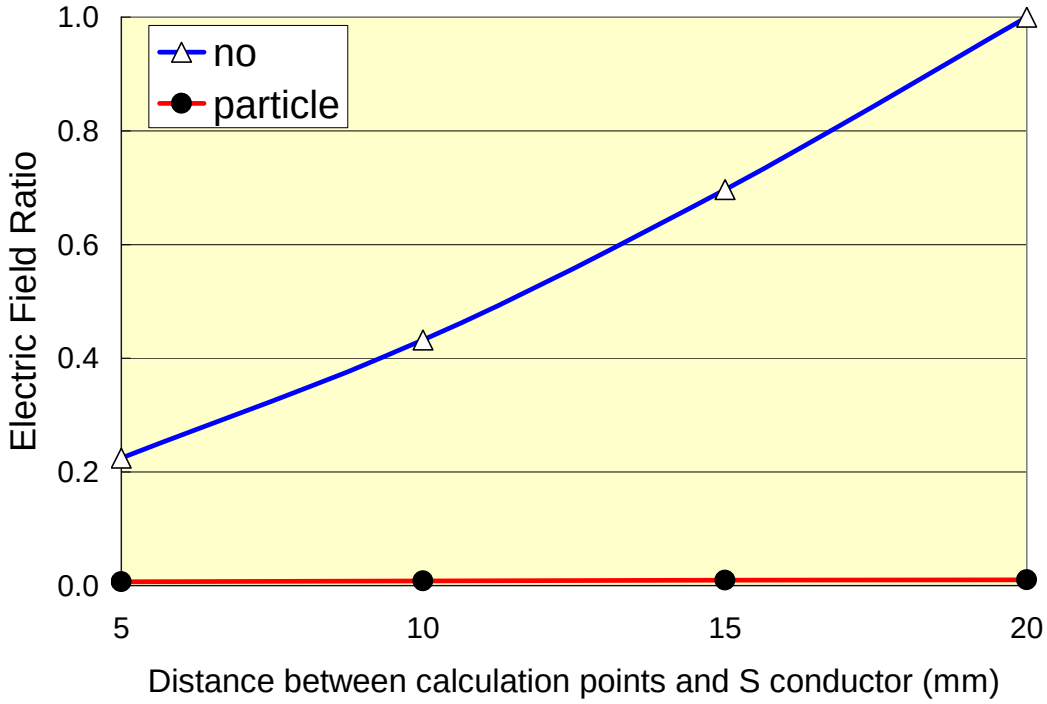

Fig. 4.11 Electric field ratio η from point B (5mm from S conductor) until point E(20 mm from S conductor)

4.4 Experiment

The experiment aims to clarify PD characteristics in the region having linear, elliptic, and circular fields of three-phase construction. In more specific terms, the experiment aims to clarify the effects of the elliptical nature of the electric field vector on the PD distribution pattern in a three-phase construction. Because the electric field vectors are different at different points, it is desired to understand the effect of the shape of the vector locus on discharge characteristics. Therefore, the particle model and position were designed so that the electric field ratio η on the particle tips was different. For each particle position and type, the discharge current pulse was observed at various values of applied voltage.

The experimental setup is same as explained in Chapter 2. The experiments were conducted in laboratory air. Because the particle is laid on S phase conductor, the highest PD signals are observed from the sensor connected to S phase conductor [6]. Thus, in this chapter we only analyze PD signals measured in CT_S.

4.5. Experimental Results

PD distribution pattern was observed in the term of phase width where PD pulses appear as shown in Figure 4.12. Phase width δ_{PD} where PD pulses appear is defined as the widest phase width of the sequence of PD pulses which appear in a cycle of applied voltage.

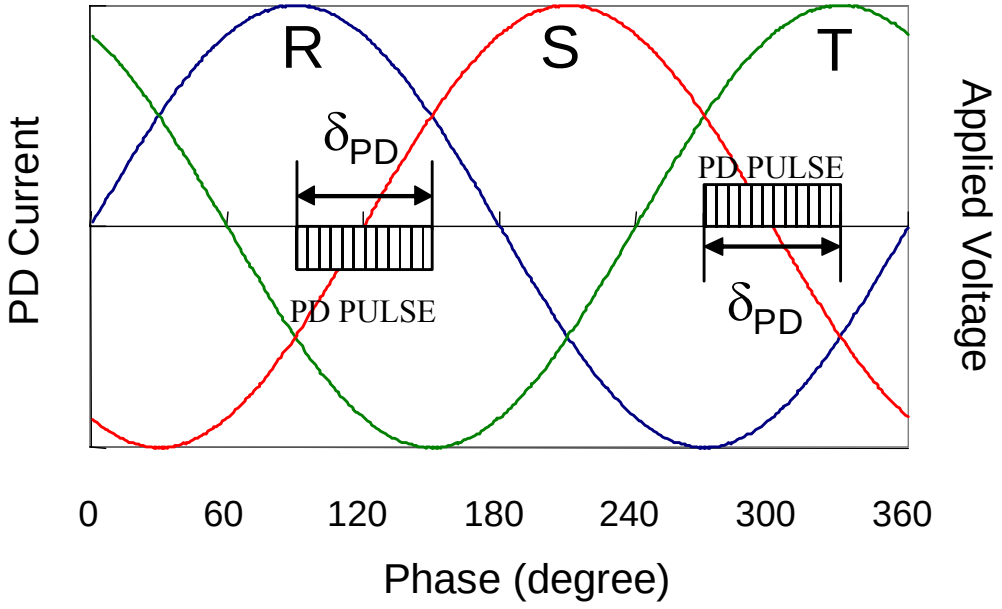

Fig. 4.12 Definition of Phase width δ_{PD} where PD pulses appear

4.5.1 Effects of Electric Field Ratio on PD Distribution Pattern

Effects of the electric field ratio η on PD pattern were observed at the same applied voltage.

Figure 4.13 shows PD distribution pattern of S90 L=10 mm and S90 L=15 mm particles at V=7.64 kV. The electric field ratio η on the particle tip of S90 L=10 mm and S90 L=15 mm particles were 0.008 and 0.009 respectively. The phase widths δ_{PD} are different: $\delta_{PD} = 109^0$ and 122^0 for S90 L=10 mm and S90 L=15 mm particles, respectively. These results indicate that the phase width δ_{PD} is influenced by electric field ratio η.

4.5.2 Effects of Applied Electric Field on PD Distribution Pattern

Figure 4.14 shows the PD distribution pattern of the S90 L=5mm particle for two values of applied voltage. It is obvious that δ_{PD} becomes wider as the applied voltage increases; i.e. at 7.64 kV, $\delta_{PD} = 77^0$ while at 10.18kV, $\delta_{PD} = 103^0$. These results indicate that the phase width δ_{PD} is also influenced by applied voltage Va, and hence by applied electric field Ea.

Figure 4.15 summarizes the results of PD measurements from S90 L=5 mm, 10 mm, 15 mm, and 20 mm particles on several values of applied voltage. The electric field ratio η on the particle tip is 0.007, 0.008, 0.009, and 0.01 for S90 L=5 mm, 10 mm, 15 mm, and 20 mm particles, respectively. The results shown in figure 4.13 reconfirm the previous results that the higher the electric field ratio η and the higher applied voltage are, the larger δ_{PD} is.

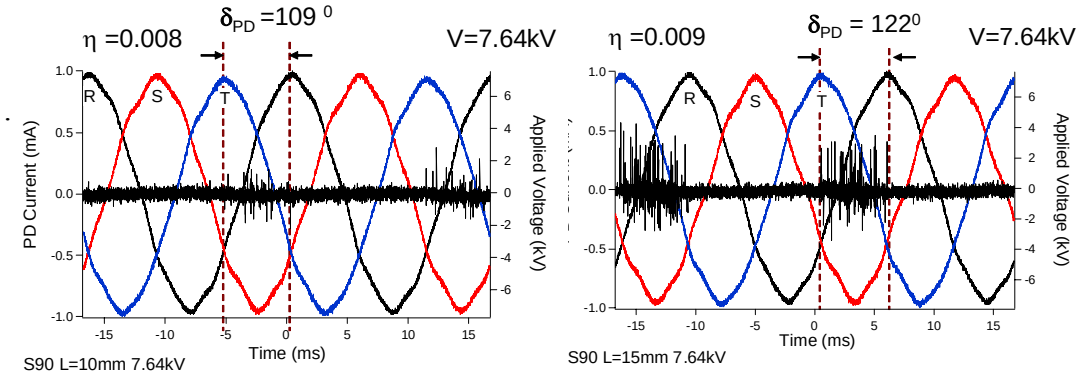

Fig. 4.13 PD pattern of S90 L=10 mm and L=15mm particles at V=7.64 kV

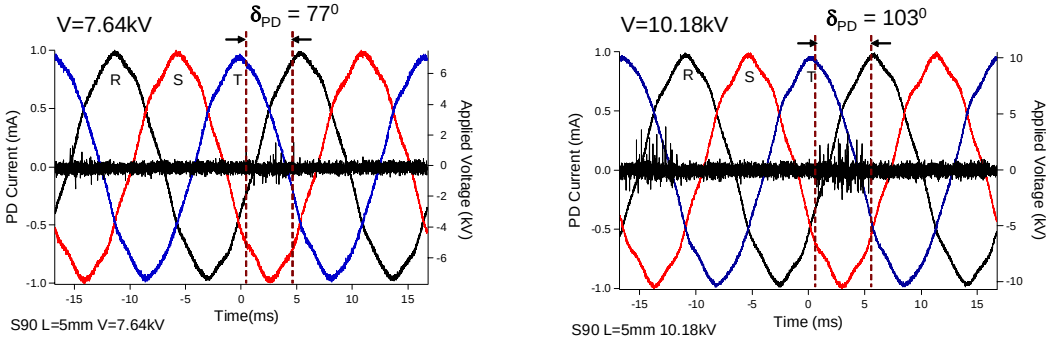

Fig. 4.14 PD pattern of S90 L=5 mm particle (η=0.007) at various applied voltage

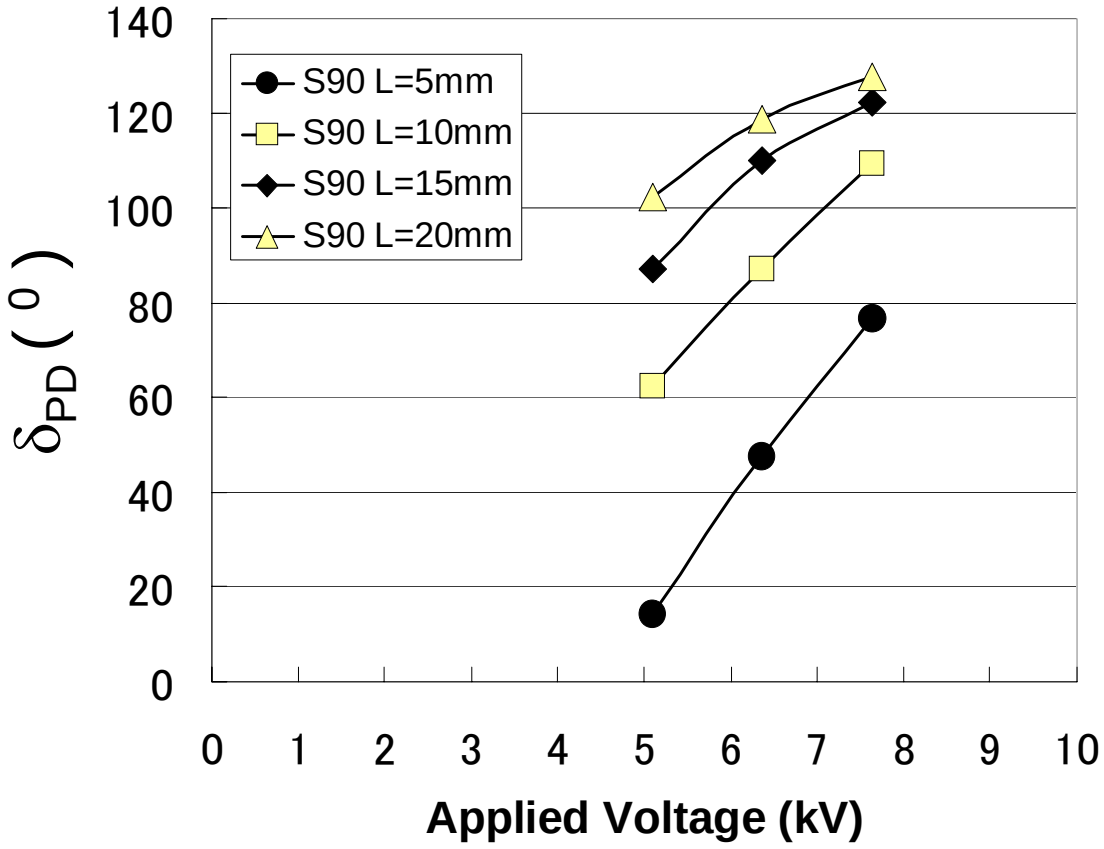

Fig. 4.15 Measurement results of phase width δ_{PD} resulted from S90 particles with various lengths

4.6 Discussion

4.6.1 Effects of Applied Electric Field on Phase Width δ_{PD}

The experimental results show that the phase widths δ_{PD} were different depending on the applied voltage Va. Because Va is proportional to the electric field inside the construction, the phase width δ_{PD} depends on the applied electric field Ea. These results were analyzed and explained from the electric field characteristics on the particle tip.

Figure 4.16 shows the absolute electric field on the particle tip of the S90 L=5 mm particle during a cycle for some values of Va. Here, it is assumed that PD occurs when the electric field in the insulation exceeds the critical electric field (E_{cr}). Because air is used as insulating gas inside the construction, E_{cr} = 3 kV/mm, which is designated by a dashed line.

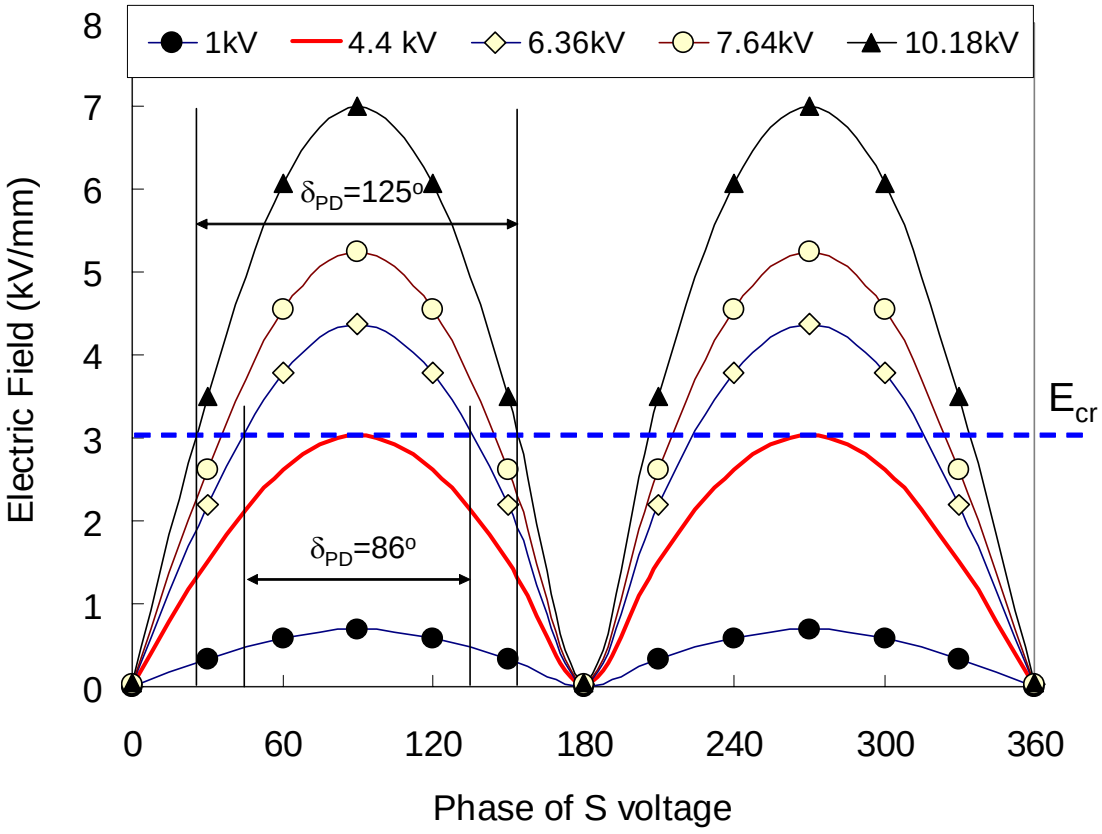

Fig. 4.16 Relation of electric field E and phase width δ_{PD} for S90 L=5mm particle

The intersection points between the electric field curve and the Ecr line express the beginning and the end of the phase angles of PD pulses appearances. Thus, phase width δ_{PD} can be estimated. This calculation method of δ_{PD} is called "**Calculation I**". At PDIV 4.4 kV, the intersection becomes a point, so PD is estimated to appear as a single pulse. At 6.36 kV, δ_{PD} is estimated to be 86°, while at 10.18 kV, δ_{PD} increases to 125°. It appears in Figure 4.16 that the higher Va is, and thus the higher Ea is, the wider δ_{PD} is.

4.6.2 Effects of Electric Field Ratio on Phase Width δ_{PD}

Based on the previous analysis, it seems that δ_{PD} is only influenced by maximum electric field E_{max}. However, the experimental results show that δ_{PD} were different depending on the electric field ratio η. This means that the electric field vector locus also contributes to δ_{PD}. These results were analyzed and

explained from the electric field characteristics in the three-phase construction.

At a certain position (x,y) inside the three-phase construction, the field is rotating with varying magnitudes, i.e, sinusoidal in two perpendicular directions without necessarily coinciding at zero crossings. Figure 4.17 illustrates the absolute electric field for three different positions during one cycle of applied voltage Va.

E_{max} at each position is the same, while the electric field ratio η is different, designated by η_1, η_2, and η_3, where $\eta_1 > \eta_2 > \eta_3$. Note that E_{cr} of air is designated by a dashed line.

It is apparent that for the same applied electric field E, δ_{PD} are different, where $\delta_{PD1} > \delta_{PD2} > \delta_{PD3}$. This indicates that η also influences δ_{PD}. It appears that for the same E_a, the higher η is, the larger δ_{PD} is.

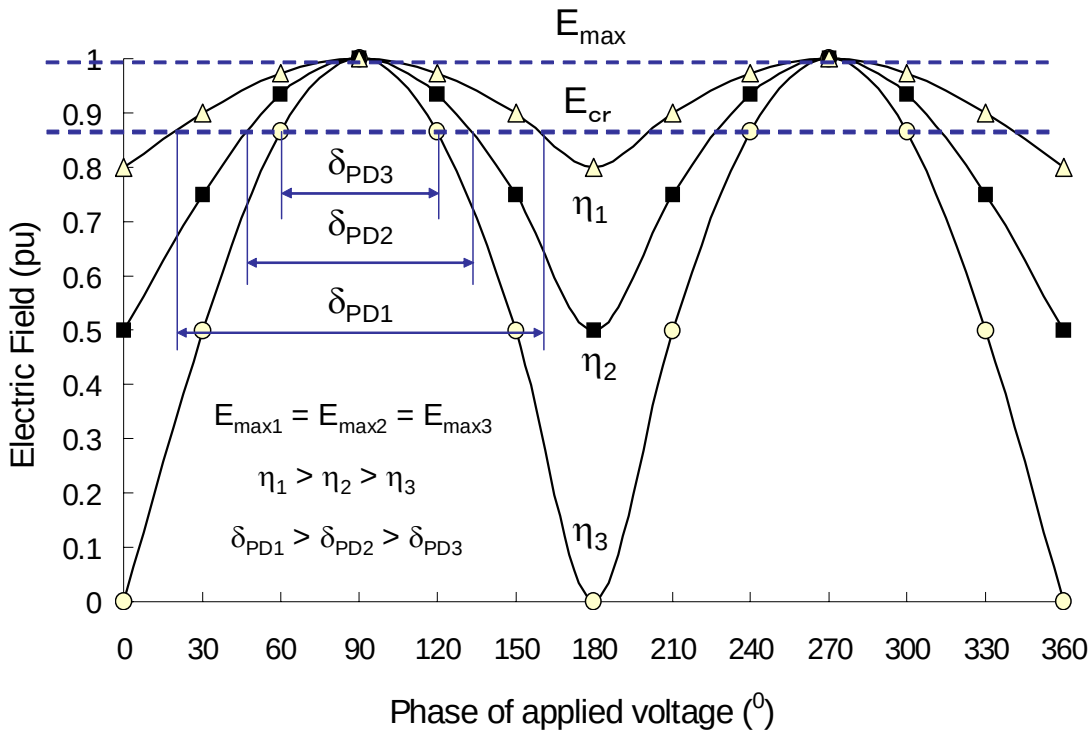

Fig. 4.17 Relation of electric field ratio η and phase width δ_{PD}

4.6.3 Relations among E, η, and δ_{PD}

The relations among E, η, and δ_{PD} are analyzed and explained from the relationship between the locus of the applied electric field E_a and the critical electric field E_{cr} of air.

At $E_{max} < E_{cr}$, PD does not occur. Under this condition, the electric field vector locus is inside the circle of E_{cr}. At $E_{max} \geq E_{cr}$, PD occurs. At $E_{max}=E_{cr}$, the electric field vector locus intersects the circle of E_{cr} at a point every half cycle. It is predicted that PD appears as a single pulse at PDIV. At $E_{max}>E_{cr}$, it is predicted that δ_{PD} becomes wider. On the other hand, the intersection line between the electric field vector locus and the circle of E_{cr}, and thus δ_V, becomes wider. Therefore, δ_V is considered to have a relation with δ_{PD} because the wider δ_V is, the wider δ_{PD} is.

However, δ_V is not equal to δ_{PD}, because the angular velocity of Va is not equal to the angular velocity of the electric field vector. The angular velocity of Va is constant, while the angular velocity of the electric field always changes.

Then, the δ_{PD} can be estimated as follows. The calculation method of δ_{PD} including the effects of electric field ratio is called as "**Calculation II**".

$$\delta_{PD} = (\Delta t/T) \times 360^0 \quad \text{(4.2)}$$

where Δt is the time duration of PD pulses appearance and T is period of power frequency. It is estimated as:

$$\Delta t = F / v_{avr} \quad \text{(4.3)}$$

where F is the length of the vector locus trajectory during PD, designated by F arch in Figure 4.16 (from Q to C to P), while v_{avr} is the average linear velocity of electric field vector movement. F is approximated as the sum of the length of the standing sides of isosceles triangle PCQ shown in Figure 4.18. δ_V is determined from the intersection of electric field vector locus and E_{cr} circle.

$$F \approx 2 \times \sqrt{(E_{cr} \sin(0.5\,\delta_v))^2 + (E_{max} - E_{cr} \cos(0.5\,\delta_v))^2} \quad \text{(4.4)}$$

and

$$\delta_v = 2 \tan^{-1} \sqrt{\frac{\eta^2 (E_{max}^2 - E_{cr}^2)}{(E_{cr}^2 - E_{min}^2)}} \quad \text{(4.5)}$$

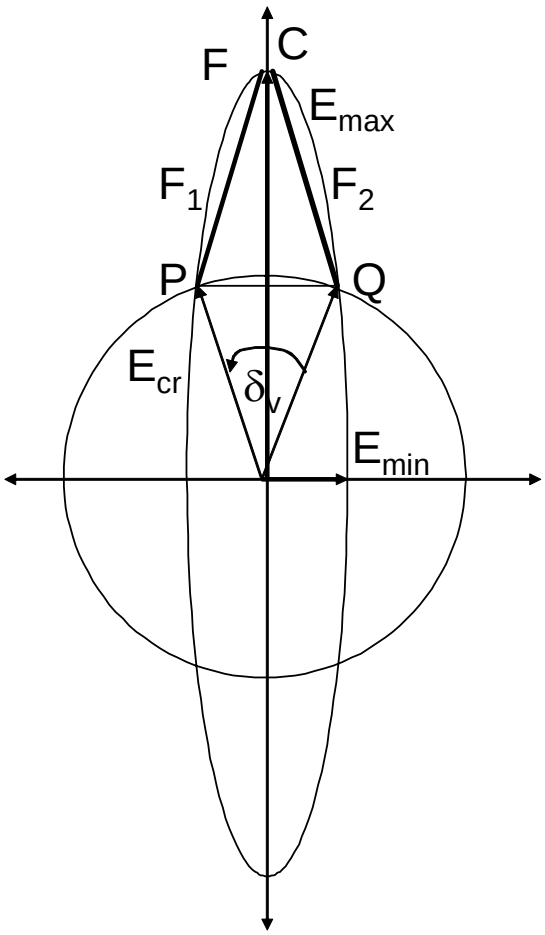

Fig. 4.18 Approximation of the length of F arch (QCP arch) as the sum of isosceles side F_1+F_2 of PCQ triangle

The linear velocity of electric field vector locus is estimated from the assumption that the areal velocity of the electric field vector locus is constant. This assumption is based on the fact that the electric field vector moves slowly in a high electric field area, but moves quickly in a low electric field area.

$$v_{avr} = v = \omega_{min} E_{max} = \omega_{max} E_{min} \quad \text{..... (4.6)}$$

The maximum angular velocity ω_{max} of electric field vector locus is estimated as change in the direction of the electric field vector with time at minimum electric field, i.e.

$$\omega_{max} = d\phi / dt \quad \text{.....(4.7)}$$

at $Ea = E_{min}$.

Finally, the relation between Emax, Ecr, η, and δ_{PD} is derived using equations (4.1) – (4.7). The result is:

$$\delta_{PD} \approx \frac{43.2 \times \sqrt{\left[(E_{cr} \sin (0.5\,\delta_v))^2 + (E_{max} - E_{cr} \cos (0.5\,\delta_v))^2 \right]}}{\omega_{max}\, E_{min}} \quad \text{.....(4.8)}$$

where:

$$\delta_v = 2 \tan^{-1} \sqrt{\frac{\eta^2 (E_{max}^2 - E_{cr}^2)}{(E_{cr}^2 - E_{min}^2)}} \quad \text{.....(4.9)}$$

Based on equations (4.8) and (4.9), it appears that δ_{PD} depends on η, Ea, the critical electric field E_{cr}, and the angular velocity ω of rotating electric field. Two conditions can be chosen for the calculation of δ_{PD} as follows.

a. ω is fixed at $\omega_{max} = 1/\eta$ and $\omega_{min} = 1$. This condition can be examined with $\omega_{max} = \omega_{min} = 1$ at $\eta = 1$, and $\omega_{max} = \infty$ at $\eta = 0$. The "Calculation II" method with this condition is called "**Calculation II A**". It enables us to describe the dependence of δ_{PD} on η and Ea.

b. ω is estimated by a precise calculation of the change in direction of electric field vector with time using equation (4.7). ω is approximated as: $\omega_{max} \approx \Delta\phi / \Delta t$ around $E = E_{min}$. The shorter Δt is, the better ω is. The calculation method II with this condition is called "**Calculation II B**".

At the fixed angular velocity of the rotating electric field, the dependence of δ_{PD} on η and Ea can be described. Figure 4.19 shows the relation among δ_{PD}, η, and E_{max}/E_{cr} for different values of E_{max}/E_{cr} at $\omega_{max} = 1/\eta$ and $\omega_{min} = 1$. It is clear from the figure that δ_{PD} depends on η and E_{max}/E_{cr}. For the same η, the higher Emax is, the wider δ_{PD} is. For the same Ea, the higher η is, the wider δ_{PD} is.

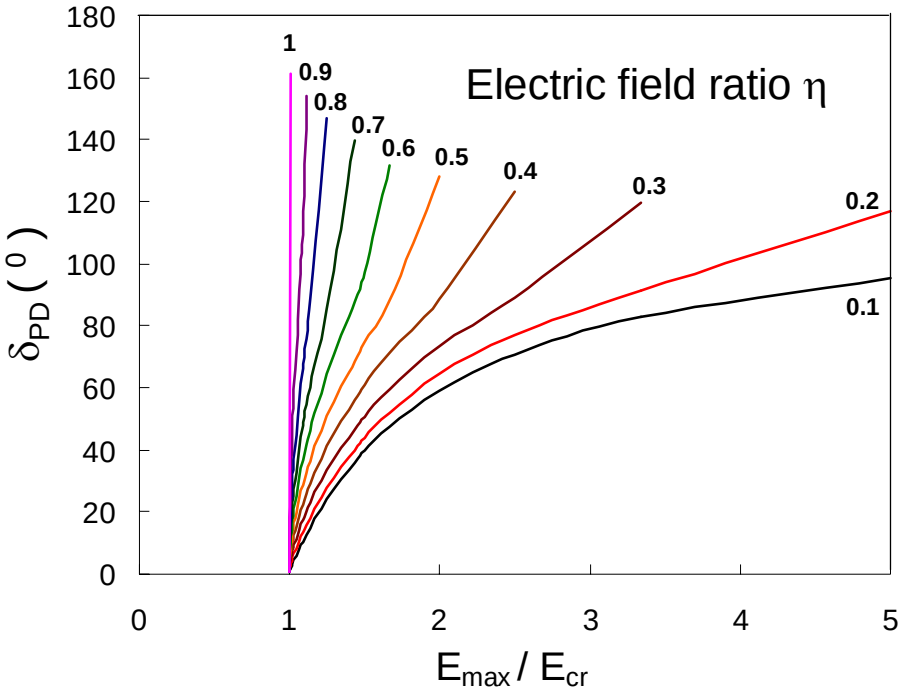

Fig. 4.19 Relation of electric field ratio η, applied electric field E_{max}/E_{cr}, and phase width δ_{PD} based on equation 4.8 and 4.9 for $\omega_{max} = 1/\eta$ and $\omega_{min} = 1$

Figure 4.20 shows a comparison between the experimental and calculation results for a S90 L=5 mm particle. As mentioned previously, the δ_{PD} calculation method as shown in Section 4.6.1 is called Calculation I. The δ_{PD} calculation method shown in Section 4.6.3 for $\omega_{max} = 1/\eta$ and $\omega_{min} = 1$ is called Calculation II A, while that for $\omega_{max} = d\phi/dt$ at $E = E_{min}$ is called Calculation II B. It is apparent from Figure 4.20 that the δ_{PD} obtained by these calculation methods are different from those obtained by the measurements. The differences may be caused by some simplifications in the calculation methods and parameters which are not considered in the calculation such as space charge behavior, sensitivity of PD measurement system, signal coupling mechanism between conductors and between the conductors and the tank, etc.

The calculation method II B gave the best fit with the measured results because the angular velocity in this method is estimated by a precise calculation of the change in direction of the electric field vector with time.

Although there are differences in values, the experiment and calculation results using the above methods show the same trend. Thus, the results indicate that the analysis methods (I, II A, and II B) may be considered for estimating PD distribution pattern, in the terms of δ_{PD}, in three-phase construction.

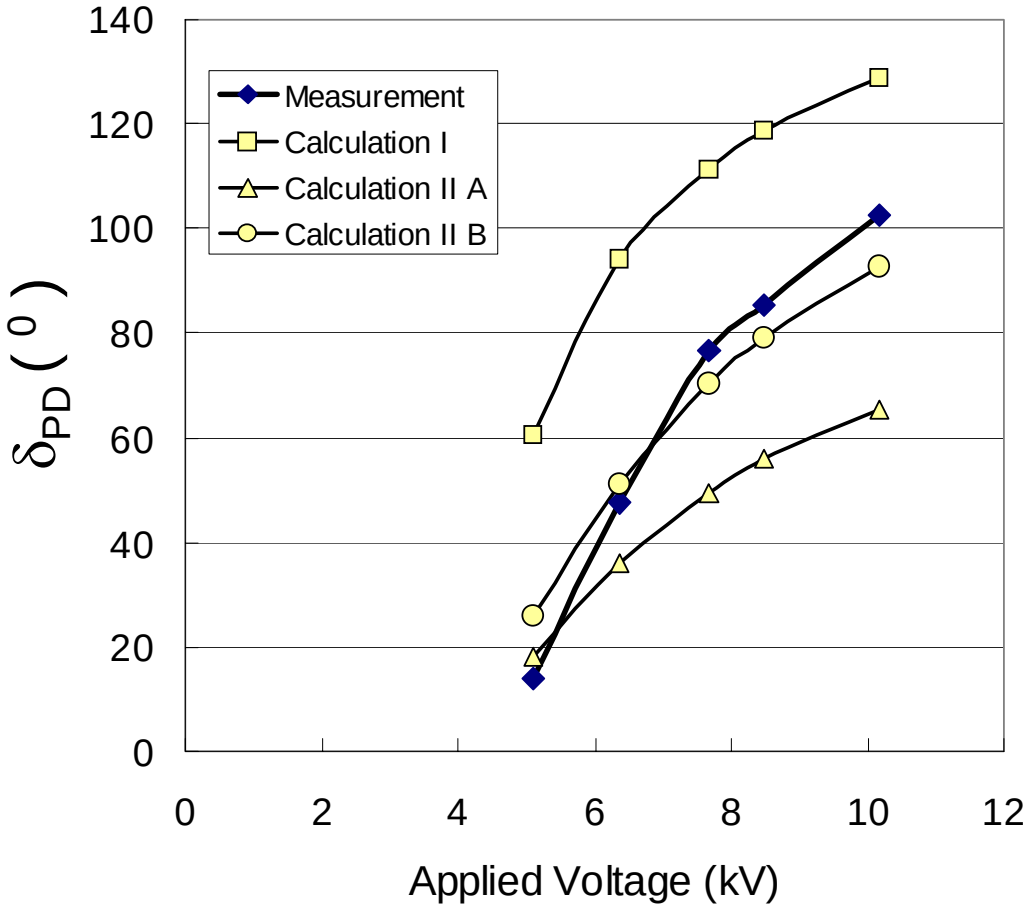

Fig. 4.20 Comparison between the experiment and calculation results for particle at S90 position with L=5 mm

4.7 Conclusions

The electric field in a three-phase construction of a simplified GIS model was analyzed. The effects of electric field ratio η of rotating electric field on PD distribution pattern in a three-phase construction were investigated. The following conclusions were drawn:

1. The electric field characteristics in a three-phase construction are as follows:
   a. The electric field rotates and changes continuously.
   b. The electric field vector locus is elliptic although the shape differs locally.
2. Electric field vector locus in the region between conductor and the enclosure is almost linear, resembling a single-phase construction; while ones between conductors have variations: linear, elliptic, circular.

3. The presence of a particle on the conductor increases the electric field while it reduces the electric field ratio η on the particle tip.
4. The rotating electric field influences PD distribution in the terms of phase width δ_{PD} where PD pulses appear and phase angle of applied voltage at PD occurrence.
5. The phase widths δ_{PD} differ depending on electric field ratio η and applied electric field Ea, and hence applied voltage Va.
   a. For the same Ea, the higher η is, the wider the δ_{PD} is.
   b. For the same η, the higher Ea is, the wider δ_{PD} is.
6. The effect of η and Ea on δ_{PD} can be estimated by considering E, E_{cr} of air, and the angular velocity of rotating electric field.

References

1. P.C.J.M. van der Wielen: “On-line Detection and Location of Partial Discharges in Medium-Voltage Power Cables”, *Doctoral Dissertation*, T.U. Eindhoven, (2005).
2. E. Harkink, F.H. Kreuger, P.H.F. Morshuis: “Partial Discharges in Three-core Belted Power Cables”, *IEEE Transactions on Electrical Insulation*, Vol. 24, No. 4, pp. 591-598 (1989).
3. S. Yanabu, H. Okubo, S. Matsumoto: “Metallic Particle Motion in Three-phase SF_6 Gas Insulated Bus”, *IEEE Transactions on Power Delivery*, Vol. PWRD-2, No. 1, pp. 1-6 (1987).
4. S. Yanabu, Y Murayama, and S. Matsumoto: “SF_6 Insulation and its Application to High Voltage Equipment”, *IEEE Transactions on Electrical Insulation*, Vol. 26, No.3, pp 358-366 (1991).
5. Umar Khayam, S. Ohtsuka, S. Matsumoto, M. Hikita:”Investigation of Partial Discharge Characteristics in Air from Artificial Defect under Three-phase Voltage”, *Korea Japan Symposium on Electrical Discharge and High Voltage Engineering*, pp. 100-103, Ansan, Korea (2005).
6. Umar Khayam, S. Ohtsuka, S. Matsumoto, M. Hikita: “Partial Discharge Measurement on Three-phase Construction”, 8th *International Conference on Properties and Application of Dielectric Material,,* Vol. 1, pp. 301-304, Bali, Indonesia (2006).

Chapter 5

Propagation Properties of Electromagnetic Wave Emitted by Partial Discharge in Three-phase Gas Insulated Switchgear using UHF Method

5.1 Introduction

Ultra high frequency (UHF) band signal of electromagnetic wave (EMW) emitted by partial discharge (PD) for PD diagnosis on gas insulated switchgear (GIS) has been investigated and applied for many years. However, there are mostly related to single-phase GIS. There are only a few reports on three-phase GIS. On the other hand, application of three-phase GIS and three-phase gas insulated bus (three-phase in one tank) has been increasing due to its compactness and low cost.

Recently, the special phenomena in three-phase equipment such as cross-interference phenomena, rotating electric field and its effect on PD characteristics, have been reported [1]. In those investigations, PD signals were measured by detecting impedance and current transformer. The particle metallic movement in three-phase GIS has been also simulated and investigated [2]. PD signals were measured by a tuning-type PD detector coupled to the isolated sheath conductor while particle motion was measured using ultrasonic detector. The investigation on PD detection in three-phase GIS using UHF method is still not adequate. The existing reports are mainly related to sensitivity verification of UHF method [3,4].

Based on the above view points, the investigation on PD detection on three-phase GIS using UHF method was conducted. There are some matters which must be considered in the diagnosis of three-phase GIS. First, the possibility of application of single phase detection method in three-phase GIS. It needs to be investigated whether single-phase PD detecting device be able to cover special phenomena in three-phase GIS. The detection capability and the level of erroneous in amplitude and location determination must be also investigated. Second, the PD characteristics (frequency and phase spectrum) from

different type sources at different positions. Third, the propagation and resonance characteristics of EMW emitted by PD in the three-phase GIS. These matters are investigated in this dissertation. In this chapter, the frequency spectrums of EMW signal emitted by PD from a particle at different positions in three-phase GIS is reported. The propagation and resonance characteristics of EMW emitted by PD in the three-phase GIS are studied based on the frequency spectrums.

This chapter deals with PD detection on three-phase gas insulated switchgear (GIS) using UHF method. A simplified model of three-phase GIS with SF_6 gas inside is used. A particle was adhered on different positions on the conductor and on the tank to produce PD. Electromagnetic wave (EMW) induced by PD was measured with UHF sensors. Frequency spectrums of EMW signals excited by PD from a particle in different position were observed.

5.2 Experiment

The particles were put on S45 to produce PD in the phase-phase region and S270 and E270 to produce PD in the phase-tank region. The model, the experiment setup, and PD sources have been explained in Chapter 2. GIS Model II and the measurement system II were used in the experiment. The particles were put on S45 to produce PD in the phase-phase region and S270 and E270 to produce PD in the phase-tank region.

5.3 Experimental Results

5.3.1 PDIV, BDV, and Measurement Points

Fig. 5.1 shows the breakdown voltage (BDV) and PD inception voltage (PDIV) of S45 and E270 particles for 0.1, 0.2, and 0.3 MPa. It is shown that the PDIV and BDV of E270 particle was higher than ones of S45 particle. The effect of the gas pressure on PDIV and BDV was observed. The higher the pressure was, the higher the PDIV was. At 0.2 and 0.3 MPa BDV was not achieved for both particles because the limitation of the applied voltage. The measurement points (MP) were the points between PDIV and BDV or the maximum voltage: 16 kV, 24 kV, 32 kV, and 36 kV.

5.3.2 Frequency spectrum of EMW emitted by PD

Fig. 5.2 shows frequency spectrum of EMW emitted by discharge for S45, E270, and S270 particles at gas pressure p=0.3 MPa and applied voltage Va=36 kV.

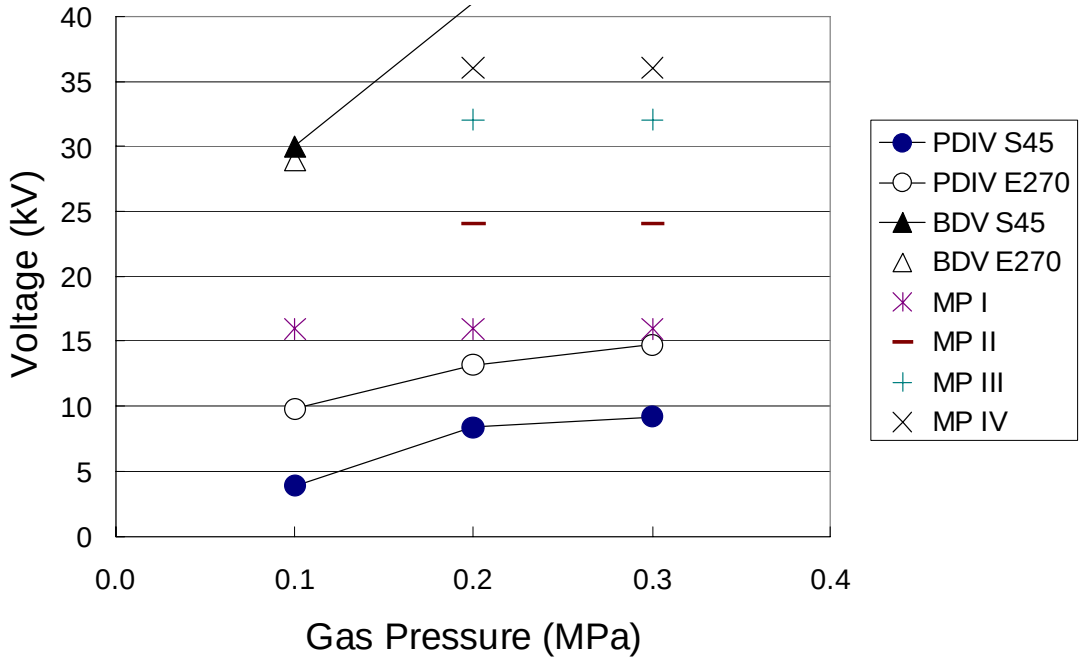

Fig. 5.1 PDIV, BDV and measurement points

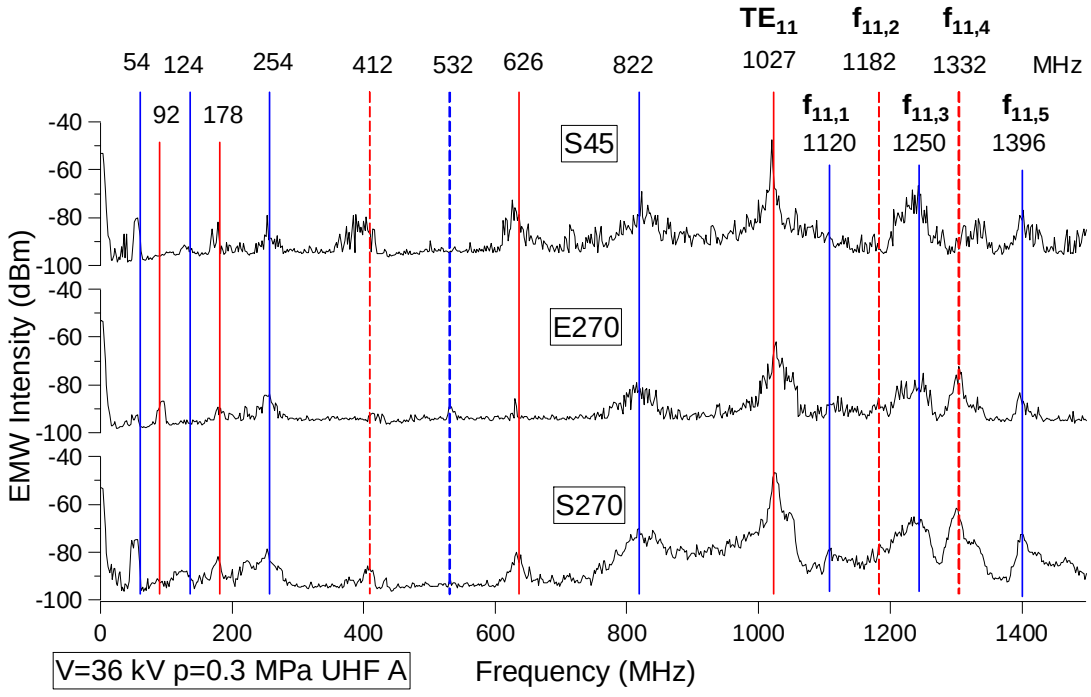

Fig. 5.2 Experimental results: frequency spectrum of EMW signals emitted by PD from S45, E270, and S270 particles

There are many peaks in the frequency spectrum. For E270 particle, the peak frequencies appear at 15 frequencies: 54, 92, 124, 178, 254, 412, 532, 626, 822, 1027, 1120, 1182, 1250, 1332, and 1396 MHz. The most dominant frequencies (f_d) are 1018 MHz, 1027 MHz, and 1025 MHz for S45, E270, and S270 particles, respectively. It also appears that there is no significant difference in the peak frequencies of frequency spectrums from these particles.

5.3.3 Phase spectrum of EMW emitted by PD

Phase spectrums are acquired by fixing the central frequency of band-path filter at frequency where maximum value is detected in frequency spectrum. Fig. 5.3 – Fig. 5.5 show phase spectrum of EMW emitted by PD measured with UHF A for S270, E270, and S45 particles at gas pressure p=0.3 MPa and applied voltage Va=16 kV.

There are two mountains of phase spectrum in a cycle. θ_{PD} is defined as phase of single-phase voltage or S applied voltage at the middle point of larger mountain in PD phase spectrum measured in the experiment. θ_{PD} is shown as dashed line in Fig. 5.3-5.5 and the next figure. $\theta_{PD} = 60^0$, 240^0, and 100^0 for S270, E270, and S45 particles, respectively.

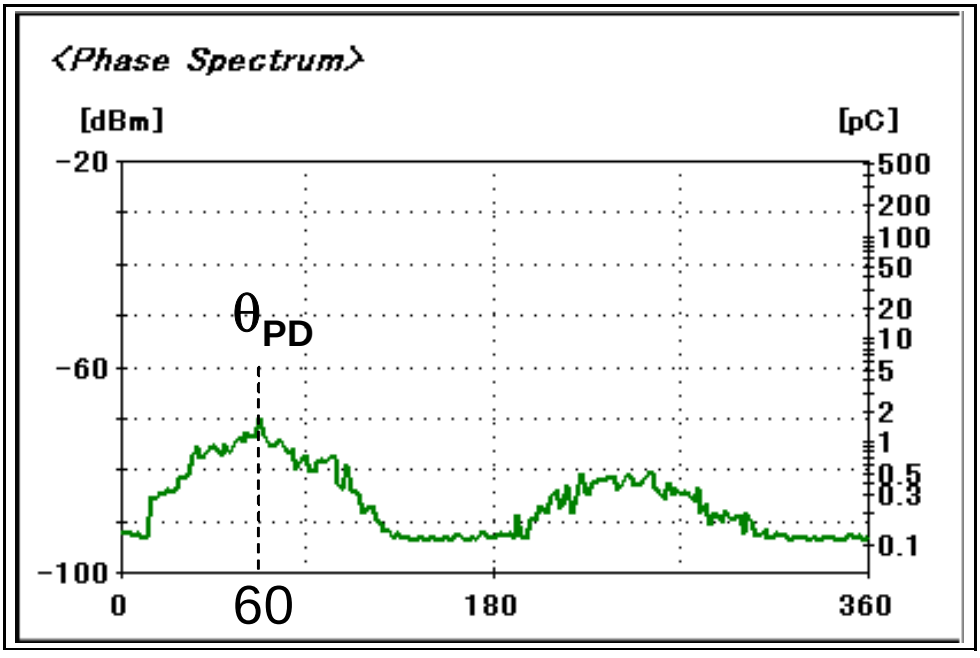

Fig. 5.3 Frequency and phase spectrum of EMW emitted by PD for S270 particle (p=0.3 MPa, Va=16 kV)

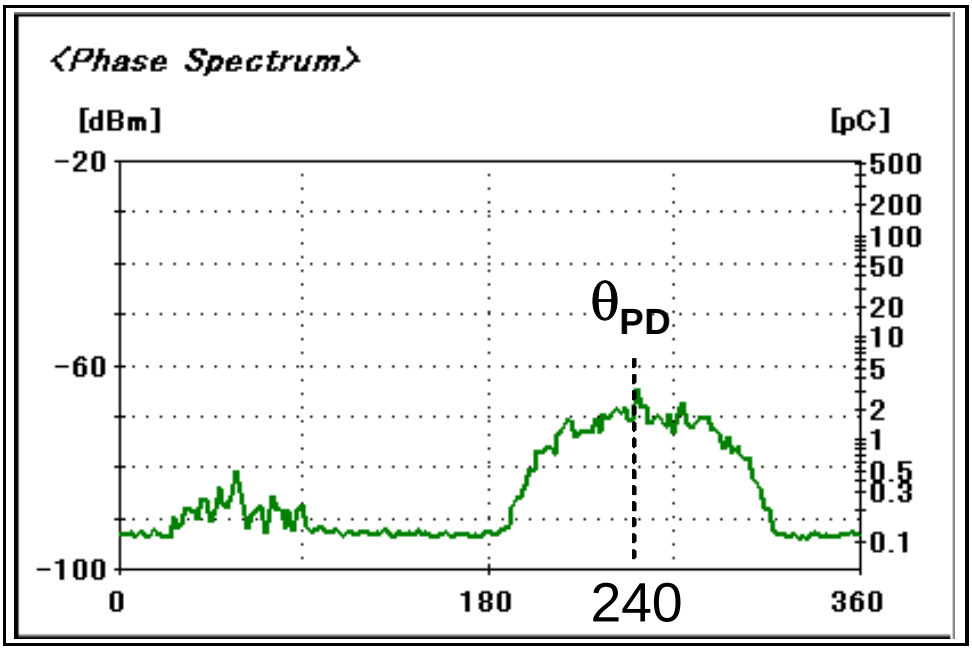

Fig. 5.4 Frequency and phase spectrum of EMW emitted by PD for E270 particle (p=0.3 MPa, Va=16 kV)

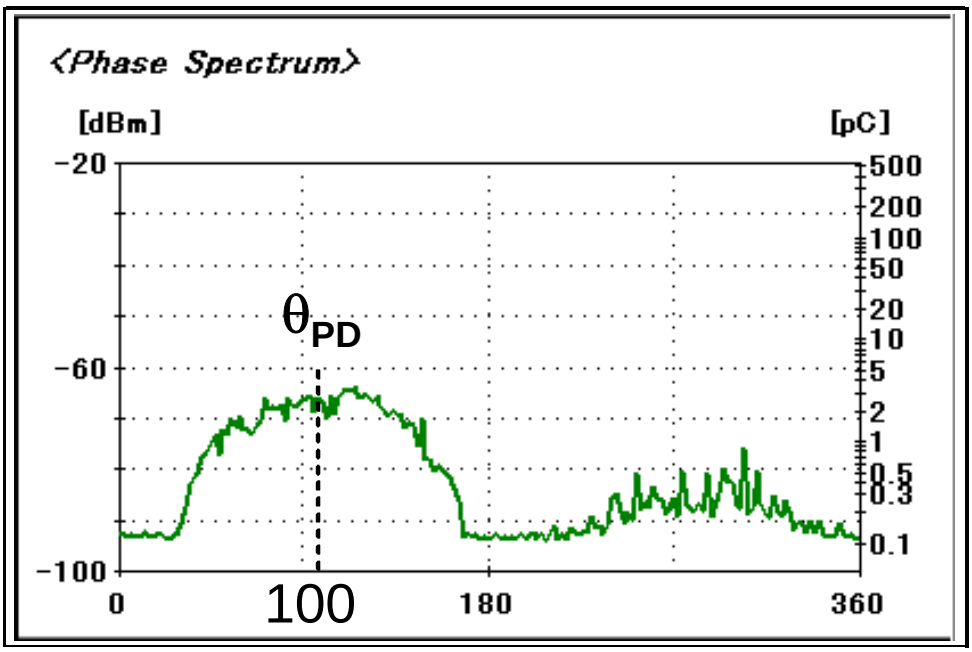

Fig. 5.5 Frequency and phase spectrum of EMW emitted by PD for S45 particle (p=0.3 MPa, Va=16 kV)

5.3.4 Diagnosis Results of PDM Device

Phase spectrums are acquired by fixing the central frequency of band-path filter at frequency where maximum value is detected in frequency spectrum. A measured signal is compared with the reference waveforms stored in a personal computer. The reference waveform is obtained from single-phase GIS. At the first stage, actual PD and external noise signals are classified by means of phase patterns. Then, through the neural network, one reference waveform is selected to identify the PD cause. PDM provide synchronization facility so that the phase of PDM power source and the phase of experiment power source can be synchronized. Moreover, PDM also provide phase shift setting facility so that phase of PD pattern may be shifted. First, phase shift β was set at $\beta = 0^0$.

Fig. 5.6 summarizes diagnosis results of PDM based on EMW signals measured with UHF A when a particle at S45, E270, or S270 position was attached in GIS model. Diagnosis is success if a protrusion is detected as protrusion. Success rate ρ means presentation of success diagnosis results to all diagnosis results.

It is found that success rate ρ is 69%, 6%, and 1% for S45, E270, and S270 particles, respectively. ρ for particles on HVC / tank in the phase-tank region (S270 and E270) is very low.

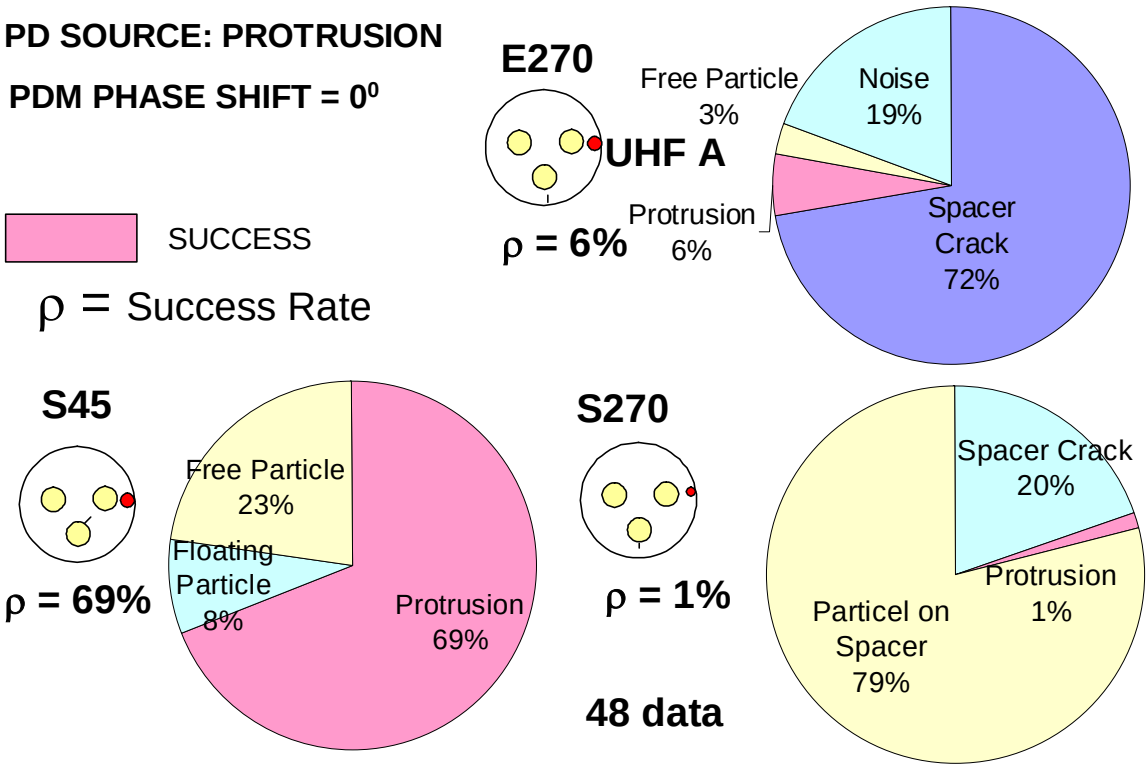

Fig. 5.6 PD diagnosis results by PDM

5.4 Discussion

5.4.1 Frequency spectrum of EMW signal and EMW propagation in GIS

As shown in Fig. 5.2, there are many peaks in the frequency spectrum. Frequency spectrum of EMW emitted by PD describes EMW propagation characteristics inside GIS. At low frequency conditions where the wavelength is long compared to the diameter of the structure, the wave propagation is TEM wave. At higher frequencies, thus shorter wavelength, more complex configuration becomes possible: TE and TM modes. The electromagnetic waves in TE_{mn} and TM_{mn} modes can not exist at frequencies below the cutoff frequency (f_c). The characterization and identification of each mode is very useful to understand PD phenomena in GIS. Generally, the peaks in the frequency spectrum excited by PD describe cutoff frequencies (f_c) and resonant frequencies (f_r) of each mode [7].

5.4.1.1 The most dominant frequency (f_d) and the cutoff frequency (f_c)

Let's analyze the most dominant frequency of the frequency spectrum shown in Fig. 5.2 by estimation of cutoff frequency of each mode in three-phase GIS. In the calculation of cutoff frequency, the models as shown in Fig. 5.7 are examined. The model A approximates f_c considering only tank A, while the model B approximates f_c considering only tank B. For each model, there are three types calculation: I, II, III.

Model I considers the actual three-phase GIS structure. Model II approximates f_c using single phase formula of f_c, with the single phase conductor radius equal to one of three-phase conductor radius. Model III is same with model II, with the single-phase conductor radius equal to the radius of the circle connecting three-phase conductors. The special formula of cutoff frequency f_c for three-phase GIS has not been derived yet. Therefore, the calculation of cutoff frequency f_c of three-phase GIS will be estimated with the formula for single-phase GIS.

The cutoff frequency f_c for single-phase GIS, with the outer radius of the conductor r_i and the inner radius of the tank be r_o, can be estimated by these formulas [7,8]:

$f_c = c / \lambda_c$

TM_{mn} wave:

$\lambda_c = 2 (r_o - r_i) / n$ for (m=0,1,…, n=1,2,…)

TE_{mn} wave:

$\lambda_c = \pi (r_o + r_i) / m$ for (m=1, 2, …, n=1)

$\lambda_c = 2 (r_o - r_i) / (n-1)$ for (m=1, 2, …, n=2,3,…) (5.1)

Since the model is three-phase lumped buses and not in coaxial cylindrical shape, this analytical equation can not be applied strictly speaking. However, because the equivalent r_i is a small value with respect to r_o, that much large error may not occur even by assuming a similar form with single-phase bus.

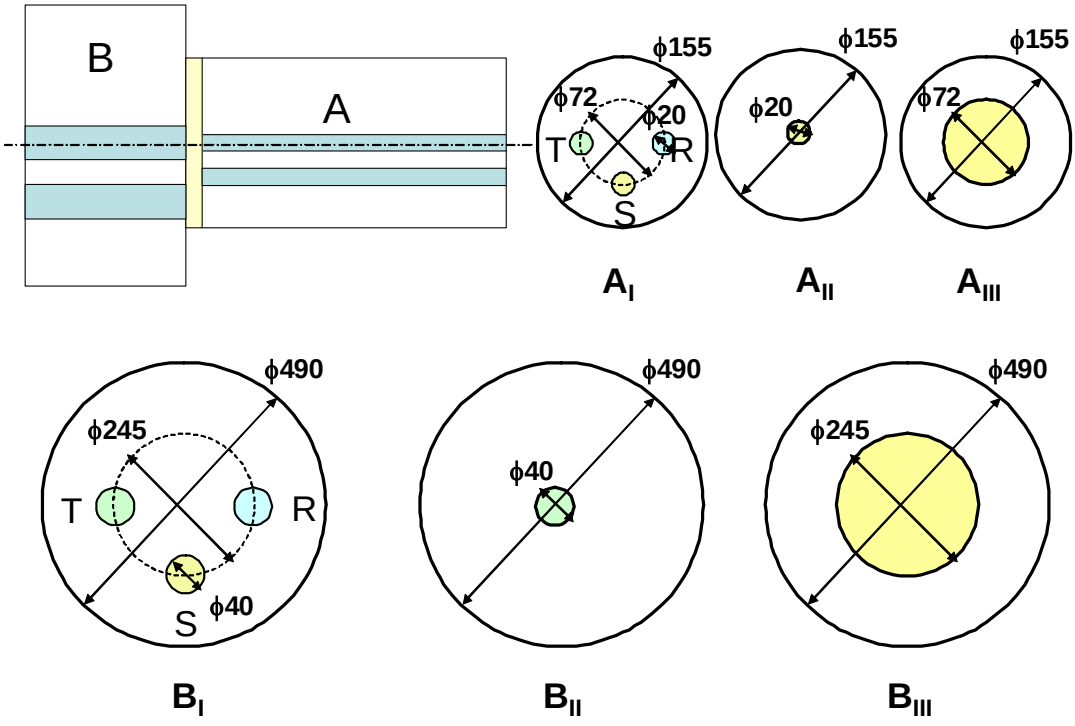

Fig 5.7 Model for calculation of cutoff frequencies

Table 1 contains the calculation results of TE_{11} mode for A_{II}, A_{III}, B_{II}, and B_{III} model and the comparison with the frequency dominant of frequency spectrum resulted from the measurement.

Table 1 Cutoff frequency f_c (calculation results) and dominant frequency f_d(measurement results)

METHODE	f_c CALCULATION (MHz)				f_d MEASUREMENT (MHz)		
MODEL	A_{II}	A_{III}	B_{II}	B_{III}	S45	E270	S270
TE_{11}	**1,092**	842	361	265	**1,018**	**1,027**	**1,025**

It appears that only f_c TE_{11} of A_{II} model be close to f_d. As mentioned previously, model A_{II} only considers the small tank and approximates f_c using single phase formula of f_c, with the single phase conductor radius equal to one of three-phase conductor radius. This result indicates that formula of f_c for single-phase GIS may be used for the f_c calculation on three-phase GIS. This result also indicates the most dominant frequency f_d of the frequency spectrum emitted by PD can be attributed to TE_{11} mode with cutoff frequency of 1018 MHz, 1027 MHz, and 1025 MHz for S45, E270, and S270 particles, respectively.

5.4.1.2 Frequency above the most dominant frequency

Let's discuss the peaks in the frequency spectrum at frequency above cutoff frequency of TE_{11} mode until 1.5 GHz. TEM and higher order TE and TM modes propagating through the GIS are partly absorbed in, and partly reflected and transmitted at discontinuities. Standing wave occurs which result in a measurable pattern of resonance frequencies. Supposing the cavity length to be L, the p-th resonance frequency $f_{mn,p}$ of the TE_{mn} mode can be expressed by the following equation [7]:

$$f_{mn,p} = \sqrt{f_{c,mn}^2 + \left(\frac{pv}{2L}\right)^2} \tag{5.2}$$

where $f_{c,mn}$ is the cutoff frequency of the TE_{mn} mode and v is the velocity of light.

The resonance frequencies of TE_{11} mode in tank A calculated using model A_{II} are $f_{11,1}$=1108 MHz, $f_{11,2}$=1155 MHz, $f_{11,3}$=1228 MHz, $f_{11,4}$=1325 MHz, and $f_{11,5}$=1439 MHz. The resonance frequencies of TE_{21} mode and other higher modes are more than 2 GHz. Thus, there are 5 resonant frequencies between f_c and 1.5 GHz. As shown in Fig. 5.2, there are 5 peaks between f_c and f=1.5 GHz. Therefore, the peaks in the range of f_c until 1.5 GHz of frequency spectrum may be attributed to resonance frequency of TE_{11} mode.

5.4.1.3 Frequency below the most dominant frequency

As shown in Fig. 5.2, there are some peaks in the frequency spectrum below the cutoff frequency. These peaks may be generated by resonance frequency of TEM mode. The resonance in the tank B may also give contribution on the peaks frequencies since the f_c TE_{11}= 361 MHz and f_c TE_{21}=721 MHz in the tank B.

5.4.2 Comparison of EMW signals emitted by PD between single-phase and three-phase GIS

Finite difference time domain (FDTD) simulation was conducted to examine the effect of the number of the conductors on the EMW signal waveform and the cutoff frequency of TE_{11} mode. The validity of an analytical result by FDTD has been proven [9]. The GIS model size in the simulation was the same as the size of tank A or the small tank in the experiment model. Two different models A_I and A_{II} were simulated. The model size, particle, and sensor position for single-phase (A_{II} model) and three-phase GIS (A_I model) are shown in Fig. 5.8 and Fig. 5.9 respectively. Position of sensors and particle location are same with in the experiment. The pulse input was Gaussian pulse with pulse width 1 ns.

Fig. 5.10 and Fig. 5.11 show the simulation results of Fast Fourier Transform (FFT) of EMW signals emitted by PD of a particle on the tank (E270) measured with UHF A, B, and D, for three-phase GIS and single-phase GIS models, respectively. It is found that there are many peaks in the frequency spectrum. The vertical lines in the figures represent cut-off frequency of TE_{11}, TE_{21}, and TE_{31} modes of EMW signals in three-phase GIS model. The horizontal lines at -40 dBm in the figures are used for the comparison purpose of EMW signals magnitude.

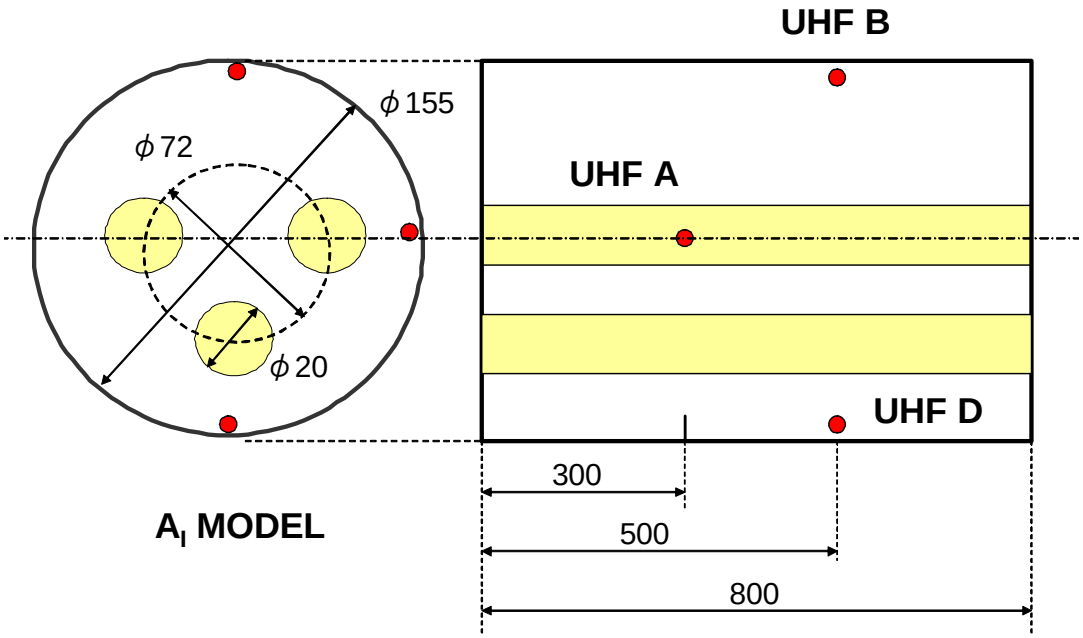

Figure 5.8 FDTD model of three-phase GIS (A_I model)

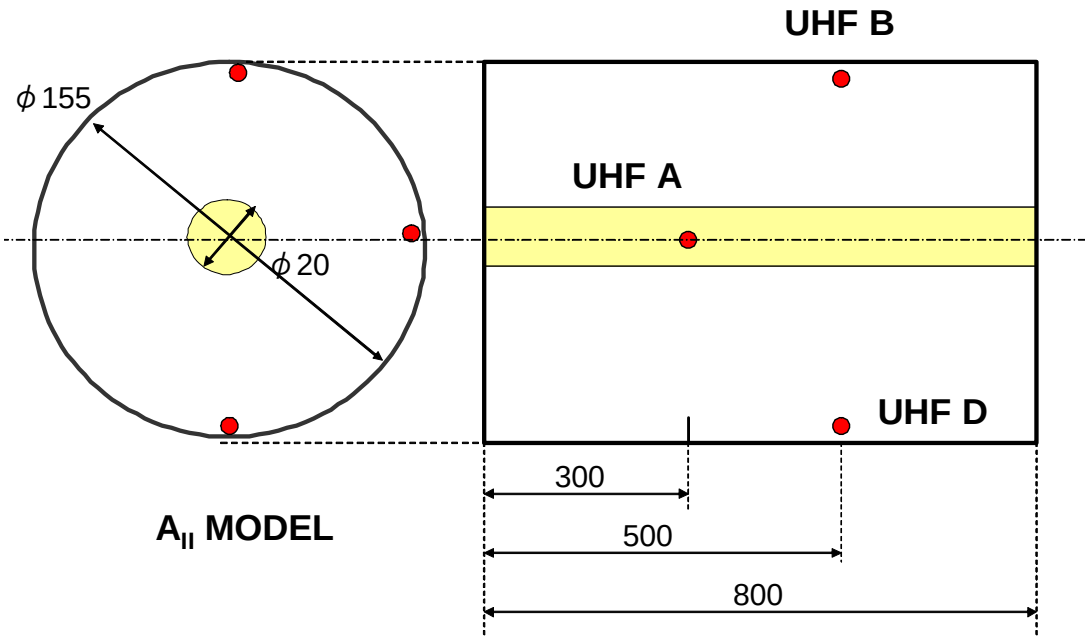

Figure 5.9 FDTD model of single-phase GIS (A_{II} model)

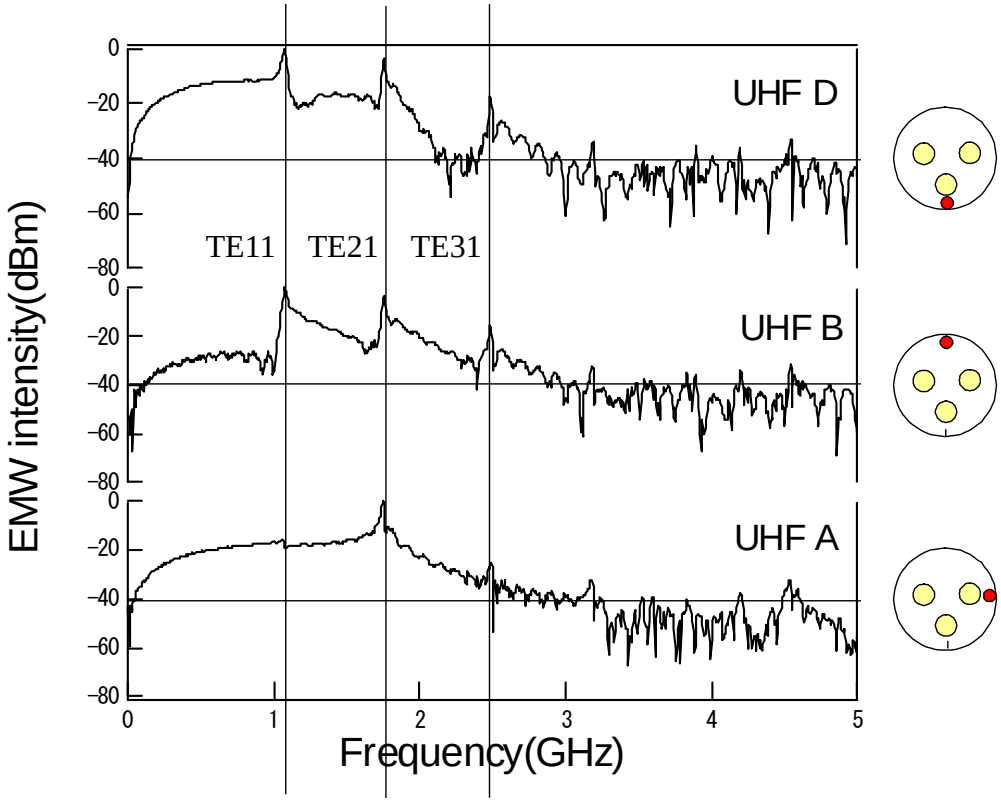

Figure 5.10 Simulation results of EMW signals emitted by PD of E270 particle inside three-phase GIS.

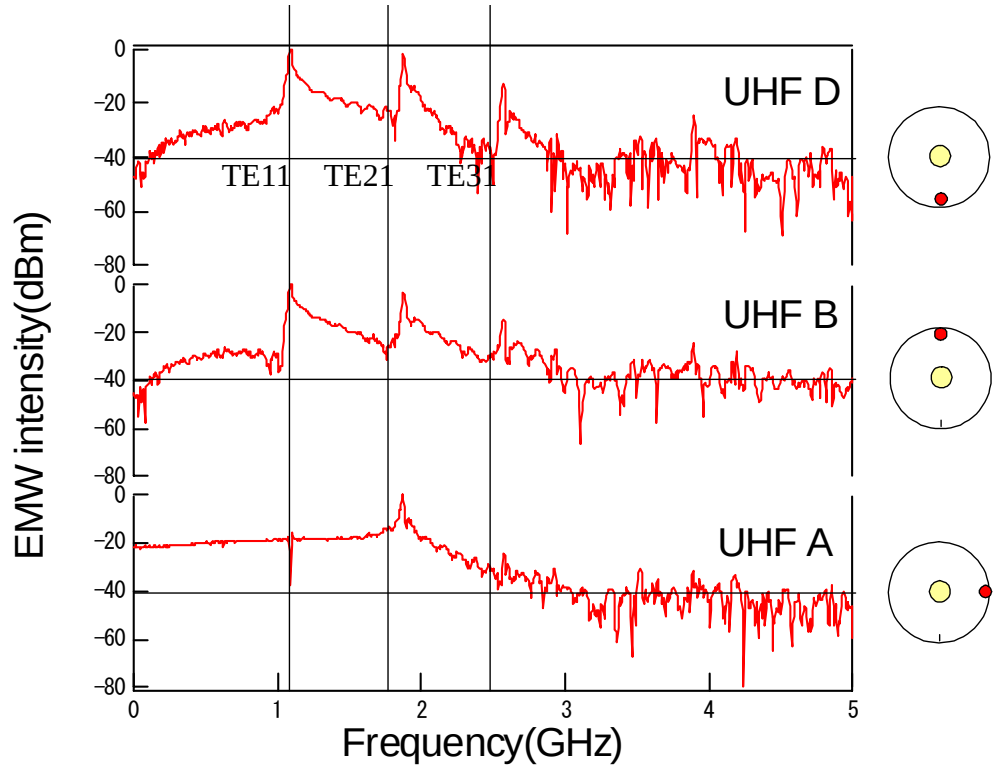

Figure 5.11 Simulation results of EMW signals emitted by PD of E270 particle inside single-phase GIS.

Some facts are observed in Fig. 5.10 and 5.11. The cutoff frequencies of TE_{11} modes measured with all sensors in the single phase and three-phase GIS models are almost same, around 1 GHz. It confirms the previous calculation in sub chapter 5.4.1 that the cutoff frequency of three-phase GIS can be estimated from the single-phase formula. This significance of this finding in terms of application is in selecting center frequency for phase spectrum measurement.

However, there is a little difference in the cut off frequency of EMW signals measured with all sensors between single-phase and three-phase GIS model mainly for the cutoff frequencies above f_c of TE_{11} mode. The difference is found to be the shifting of f_c to lower value for three-phase GIS. Figure 5.12 shows comparison of f_c obtained from calculation using equation 5.1, measurement, and FDTD simulation.

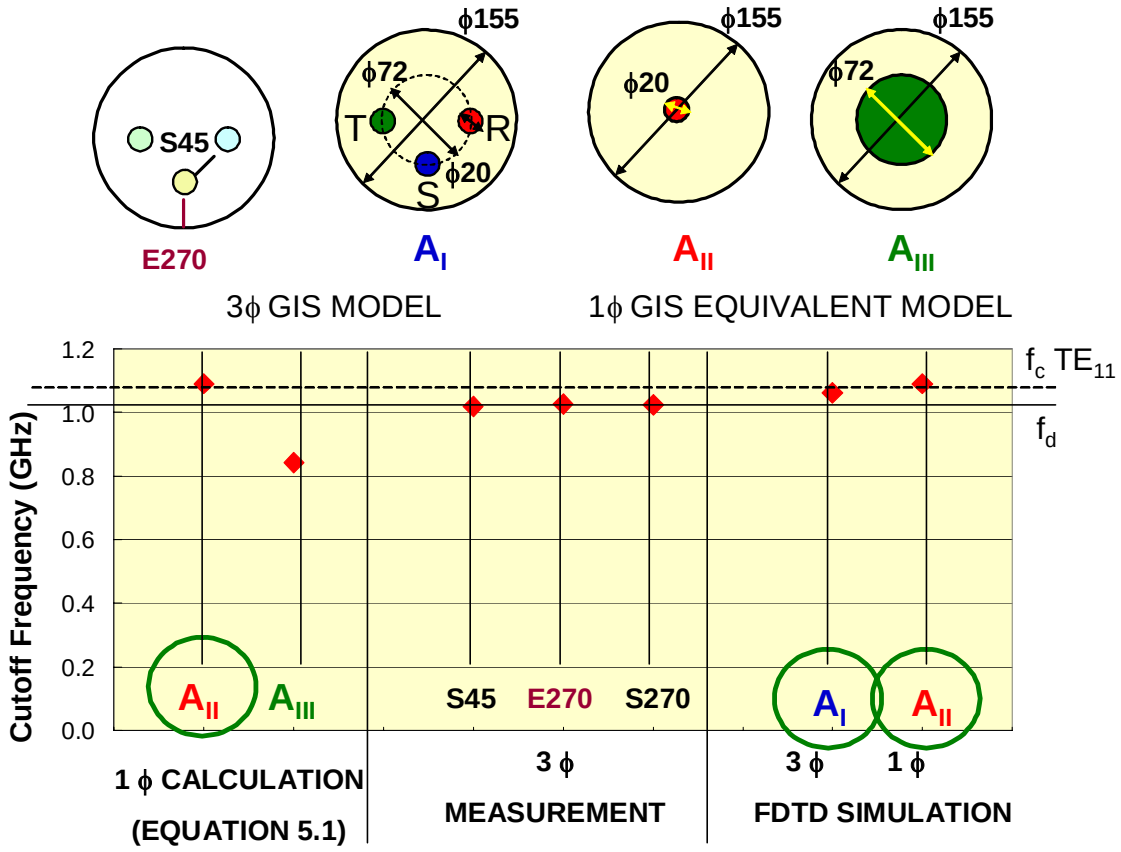

Fig. 5.12 Comparison of cut off frequency resulted
from calculation using equation 5.1, measurement, and FDTD simulation

The difference in cut off frequency f_c between single-phase and three-phase GIS is discussed as follows. Because f_c 3-phase is lower than f_c 1-phase, the cutoff wavelength λ_c of three-phase GIS is longer than λ_c of single-phase GIS based on equation 5.1. Based on equation 5.2, the λ_c is proportional to the radius of the tank r_o and the conductor r_i of GIS. Because both the radius of the tank and the conductor is same in three-phase GIS and single-phase GIS model, the different in wavelengths λ_c is caused by the difference in the number of conductor inside the tank. The effect of the number of conductor can be estimated by introducing one equivalent conductor inside three-phase GIS tank with radius r_i equal to certain equivalent radius r_{ieq} which may be calculated using equation 5.1 and 5.2. The radius equivalent is predicted larger than the radius of single phase conductor ($r_{ieq} > r_i$) based on equation 5.2. The calculation results are summarized in Table 5.2.

Table 5.2
The calculation results of equivalent radius of three-phase conductor

Parameter	1Φ	3Φ
f_c TE_{11} (MHz)	1090	1030
λ_c TE_{11}(m)	0.29	0.36
r_o (mm)	77.5	77.5
r_i (mm)	10	23.5

It is found that equivalent radius of three-phase GIS is 2.3 times larger than the radius of single-phase conductor (r_{ieq} = 2.3 r_i). Therefore, the presence of three conductors can be considered as increase in radius equivalent r_{ieq} of three-phase conductor which reduces the cutoff frequency f_c.

5.4.3 Comparison of EMW signals emitted by PD between particle on phase-phase and phase-tank regions

Figure 5.13 shows simulation results of frequency spectrum of EMW signal emitted by PD measured with UHF A for S45 particle (a particle on the phase-phase region (P-P)) S270 particle (a particle on the phase-tank region (P-T)). The differences in EMW signals between particle on phase-phase region (P-P) and phase-tank region (P-T) can be observed. TE11 mode appears clearly at S45 (P-P), while it almost diminishes at S270 (P-T). It is considered that the

electric field of TE11 mode of S270 particle has no direction to sensor UHF A. It is found that in general EMW intensity of particle on the phase-phase (P-P) region is higher than one of particle on the phase-tank (P-T) region mainly in the region $f<f_c$ TE_{11} and $f>f_c$ TE_{31}. The electric field intensity of S45 particle is higher than S270 because the electrode gap of S45 particle is smaller than one of S270 particle.

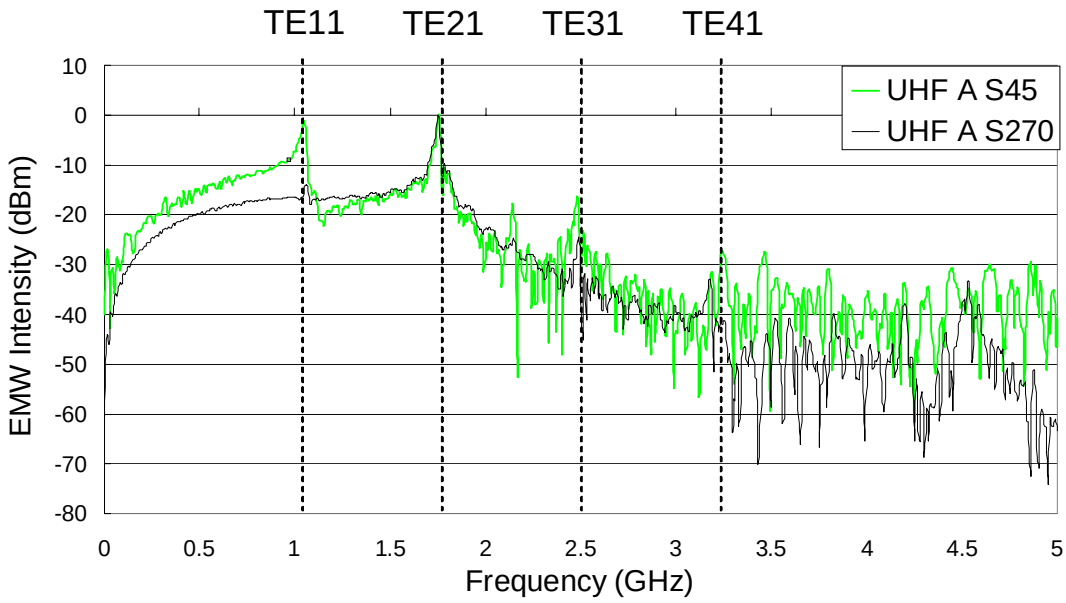

Figure 5.13 Simulation results of EMW signals emitted by PD of S45 and S270 particles inside three-phase GIS.

5.4.4 Discussion on PDM Diagnosis Results

It is found that success rate ρ is 69%, 6%, and 1% for S45, E270, and S270 particles, respectively. ρ for particles on HVC / tank in the phase-tank region (S270 and E270) is very low. It may be caused by the error in phase recognition of PD pattern. Note that the reference waveform in PDM is obtained from single-phase GIS data base. In single-phase GIS PD caused by protrusion always occurs at the peak of applied voltage [10] while in three-phase GIS there is dependence of phase where PD pulse occurs on particle position [1].

By trial and error, the phase shift $\beta=150^0$ results in the better diagnosis result of S270 and E270 particles, but no improvement in diagnosis result of S45 particles as shown in Table 5.3.

Table 5.3 Success rate ρ of PD diagnosis by PDM
at phase shift $\beta=0^0$ and $\beta=150^0$

PARTICLE POSITION			ρ at $\beta=0^0$	ρ at $\beta=150^0$
S45	P-P	HVC	69%	51%
S270	P-T	HVC	1%	99.5%
E270	P-T	TANK	6%	98.2%

These results are explained as follows. Fig. 5.14 shows electric field on the particle tip of S45, S270 and E270 particles at 1 kV during one cycle of S phase voltage. $\theta_{s\ max}$ is defined as the phase angle of S applied voltage when the electric field on the particle tip achieves maximum value. PD pulse sequence of protrusion appears around $\theta_{s\ max}$ [10]. $\theta_{s\ max}$ is shown as solid line in Fig. 5.14.

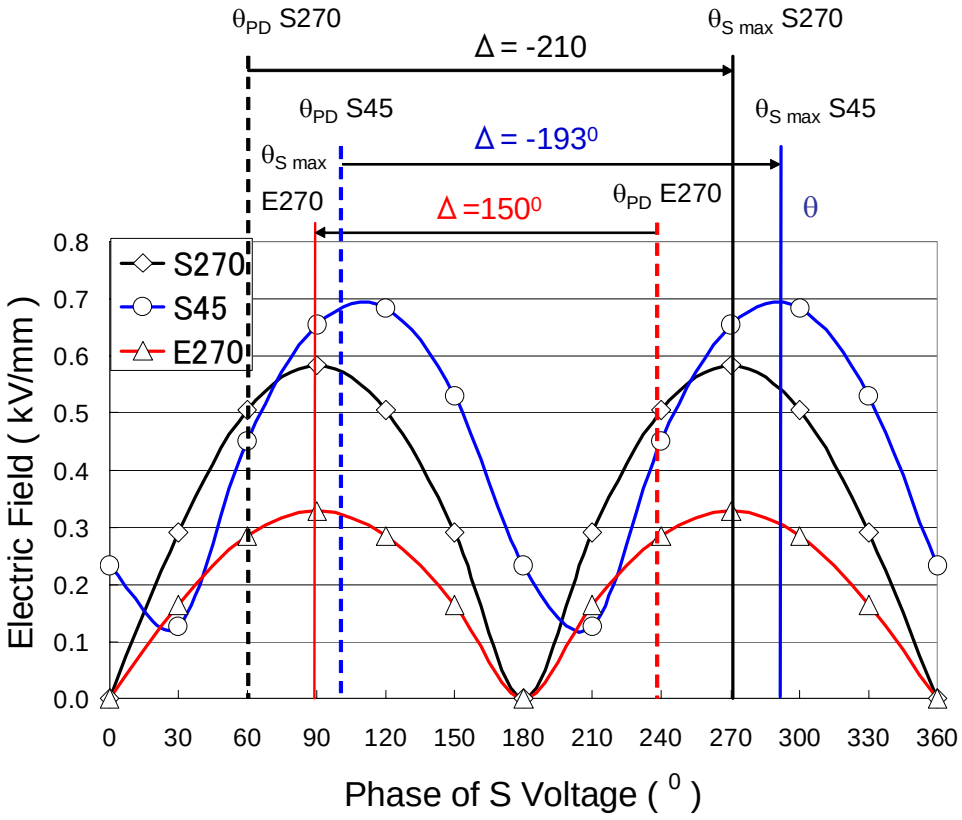

Fig. 5.14 Electric field on the tip of S270, S45, and E270 particles

Δ is defined as the phase differences between $\theta_{s\,max}$ and θ_{PD}. It is found that in a cycle of S applied voltage $\theta_{s\,max} = 113^0$ and $\theta_{s\,max} = 293^0$ for S45, while $\theta_{s\,max} = 90^0$ and $\theta_{s\,max} = 270^0$ for S270 and E270. It is estimated that $\Delta = 150^0$ or $\Delta = -210^0$ for S270 and E270, while $\Delta = -193^0$ or $\Delta = 167^0$ for S45. Therefore, setting of phase shift $\beta = 150^0$ in PDM gave success diagnosis for S270 and E270 but it still gave erroneous diagnosis result for S45 particle. Based on the electric field calculation above, the best phase shift setting for S45 particle is estimated to be $\beta = -193^0$ or $\beta = 167^0$.

In actual situation, the particle position is unknown, so that the proper phase shift β can not be determined. Therefore, PD data base resulted from different PD types at different positions inside three-phase GIS is needed to achieve correct diagnosis results. More ever, modification in PD diagnosis algorithm is needed because three-phase PD data base may be more complicated than single-phase one. These matters need further investigation.

5.5 Conclusions

We investigated partial discharge in three-phase GIS using UHF method. Frequency spectrums of EMW signals emitted by PD on different positions were observed. The results are summarized as follows.

There are many peaks in the frequency spectrum of EMW signals emitted by PD. Cutoff frequency of EMW in three-phase GIS can be estimated from the cutoff frequency formula for single-phase GIS. The most dominant frequency in frequency spectrum can be attributed as cutoff frequency of TE_{11} mode. The peaks in the frequency spectrum between cutoff frequency and 1.5 GHz can be attributed as resonance frequencies of TE_{11} mode. The peaks in the frequency spectrum below cutoff frequency may be attributed as resonance frequency of TEM mode and the influence of the bigger tank.

The main difference in frequency spectrum between three-phase and single-phase GIS was found to be the shifting of f_c to lower value for three-phase GIS. It was also found that the presence of three conductors can be considered as increase in an equivalent radius of three-phase conductor by a factor of 2.3. Frequency spectrums were influenced by GIS structure (three-phase or single-phase) and particle position (phase-phase or phase-tank; HVC or tank).

Application of single-phase PDM device in three-phase GIS gave some erroneous in diagnosis results. The error may be caused by error in phase

recognition of PD pattern. The change in phase shift β setting in PDM device based on the phase angle of applied voltage at maximum electric field on the particle tip gave better diagnostics.

References

1. Umar Khayam, T. Ishitobi, S. Ohtsuka, S. Matsumoto, M. Hikita: “Effect of Elliptical Nature of Rotating Electric Field on Partial Discharge Pattern in a Three-phase Construction”, IEE of Japan Trans., Vol. 127, No.9, 2007, pp. 524-530.
2. S. Yanabu, H. Okubo, S. Matsumoto: “Metallic Particle Motion in Three-phase SF6 Gas Insulated Bus”, IEEE Transactions on Power Delivery Vol. PWRD-2, No. 1, January 1987, pp. 1-6.
3. T. Hoshino, H. Koyama, S. Maruyama, and M. Hanai: ”Comparison of Sensitivity between UHF Method and IEC 60270 Standard for on-site Calibration in Various GIS”, 15th International Symposium on High Voltage Engineering, Slovenia, 2007, paper T7-264.
4. M. Knapp, R.Feger, K. Feser:”Application of The CIGRE Sensitivity Verification for UHF PD Detection in Three-Phase GIS”, 11th International Symposium on High Voltage Engineering, London, 1999, Vol. 5, pp. 82-85.
5. Hitachi Engineering and Services Co. Ltd: “Portable Type of PDM Device”.
6. M.D. Judd, O. Farish: “High Bandwidth Measurement of Partial Discharge Current Pulses”, ISEI Paper of IEEE Vol. 2, June 1998, pp 436-439.
7. H. Muto, M. Doi, H. Fuji, M. Kamei: ”Resonance Characteristics and Identification of Modes of Electromagnetic Waves Excited by Partial Discharges in GIS”, Electrical Engineering in Japan, Vol. 131, No. 2, 2000, pp. 1-11.
8. H. Imagawa, K. Emoto, H. Murase, H. Koyama, S. Wakabayashi, T. Sakakibara, E. Haginomori: ”Frequency Domain Discussions on PD Signal Propagation Characteristics in GIS”, Electrical Engineering in Japan, Vol. 133, No. 3, 2000, pp. 9-17.
9. S. Ohtsuka, M. Onomoto, T. Teshima, S. Kaneko, S. Okabe, M. Hikita,”Influence of GIS Tank Size on First Incoming PD Induced Electromagnetic Wave in Terms of Risk Assessment of GIS”, IEEJ Transaction on Power and Energy, Vol. 124-B, No. 11, pp. 1365-1372, 2004.
10. S. Meijer, E. Gulski, J.J. Smith,”Pattern Analysis of Partial Discharges in SF_6 GIS”, IEEE Trans. on DEI, Vol.5 No. 6, pp. 830-842, 1998.

Chapter 6

Concluding Remarks

Discharge characteristics in single-phase equipments are a well-known and well-established art; however, those in three-phase equipment are far less understood. On the other hand, due to its compactness and low cost, application of three-phase equipment (three-phase in one tank) such as three-phase gas insulated switchgear and three-phase gas insulated bus has been increasing. Therefore, to improve diagnostics techniques in three-phase equipment, it is very important to understand partial discharge (PD) characteristics in three-phase equipment.

Three-phase equipment differs from single-phase equipment in two aspects: configuration and applied voltage. In this dissertation, effects of these differences on electric field, PD, and electromagnetic wave (EMW) emitted by PD in three-phase gas insulated system (GIS) were studied. This dissertation contains the investigation results of PD and EMW emitted by PD in three-phase GIS.

The experiment setup and the measurement system were constructed. There are two types of three-phase GIS model used in the experiment. The first model was simplified model of three-phase GIS with open tank and air insulation at atmospheric pressure. The investigation was emphasized on the effect of three-phase configuration and three-phase applied voltage on electric field and PD characteristics. A particle was put on different positions on the tank or on the conductor. Coupling capacitors were installed on each phase. PD signals induced on the tank were measured with detecting impedance while ones induced on three-phase conductors were measured by current transformer (10 kHz-250 MHz). PD signals were observed by a four-channel oscilloscope (300 MHz, 2.5GSa/s). The second model was three-phase GIS model with closed tank and SF_6 gas insulation at atmospheric and higher pressure up to 0.3 MPa. The investigation was emphasized on the propagation properties of EMW emitted by PD in three-phase GIS. EMW emitted by PD were measured with ultra high frequency (UHF) sensors (0-1.5GHz) and observed by oscilloscope (1.5GHz, 8GSa/s) and PD monitoring (PDM) device (9 kHz – 1.5GHz). Diagnostic of PD source is also performed by PDM.

6.1 Results

Results on the effects of the presence of three-phase conductors and three-phase voltage on PD characteristics are as follows. Measuring PD signals only at the enclosure or on one of the phases of three phase conductor resulted in the position dependent sensitivity for PDs. PD inception voltage (PDIV) of a particle adhered on different position differed depending on the particle position. Phase angle θ of applied voltage Va where PD occurs at PDIV also depended on particle position. PD caused by a particle on one phase conductor was induced and detected on the other phase conductors. Magnitude ratios of PD current flowing on each phase were found to be unique for each particle on different positions. The ratio was constant and independent of magnitude of PD current pulse. Polarity of PD current flowing on each phase depended on particle position.

Electric field inside the three-phase GIS model with and without particle was analyzed. In three-phase construction and under three-phase applied voltage, the electric field rotates and changes continuously. The electric field vector locus is elliptic although the shape differs locally. In the region between conductor and the enclosure, it is almost linear, resembling a single-phase construction; while one between conductors has variations: linear, elliptic, circular. The elliptical nature of electric field vector locus at certain point was defined as electric field ratio, η. It was defined as ratio between maximum Emax and minimum electric field Emin at that point. The presence of a particle on the conductor increased the electric field while it reduced η on the particle tip.

The rotating electric field influences PD distribution in the terms of phase width δ_{PD} where PD pulses appear and θ at PD occurrence. δ_{PD} was found to differ depending η and applied electric field Ea, and hence Va. For the same Ea, the higher η is, the wider δ_{PD} is. For the same η, the higher Ea is, the wider δ_{PD} is. The effect of η and Ea on δ_{PD} can be estimated by considering Ea, critical electric field of air E_{cr}, and angular velocity ω of rotating electric field. θ at PDIV was influenced by the field direction at Emax.

Using the second model, EMW propagation characteristics were examined from frequency spectrum of EMW signal measured by PD measurement system. In addition, it was also analyzed by finite difference time domain (FDTD) method. There are many peaks in the frequency spectrum of EMW signals emitted by PD. Cut off frequency f_c of each mode in three-phase GIS was estimated from the f_c formula for single-phase GIS. The most dominant frequency in frequency

spectrum can be attributed to f_c of TE11 mode. The peaks in the frequency spectrum between fc and 1.5 GHz were attributed as resonance frequencies of TE11 mode. The peaks in the frequency spectrum below f_c may be attributed as resonance frequency of TEM mode and the influence of the bigger tank. The main difference in frequency spectrum between three-phase and single-phase GIS was found to be the shifting of f_c to lower value for three-phase GIS. It was also found that the presence of three conductors can be considered as increase in an equivalent radius of three-phase conductor by a factor of 2.3. Frequency spectrums were influenced by GIS structure (3 phase or 1 phase) and particle position (phase-phase or phase-tank; HVC or tank).

6.2 New Findings in terms of Academic

In terms of academic outcome from this dissertation, the special characteristics of electric field, PD, and EMW emitted by PD in three-phase equipment were found in this study. Namely, the special characteristics, which are different with ones in single phase equipment, are rotating electric field, cross-interference phenomena, position dependent sensitivity for PDs, the dependence of applied voltage phase at PD occurrence on particle position, the dependence of magnitude of PDIV on particle position, the dependence of PD pattern on electric field ratio η, the shift of cutoff frequency to lower value. The development of PD diagnostic device for three-phase equipment should consider these special characteristics of three-phase GIS.

6.3 Practical Significance of the Presence Work

The practical significances of these finding in term of practical application are as follows. PD detection on three phase equipment should be conducted on three phases simultaneously to obtain measurement result of PD occurring in entire region with high sensitivity and to obtain information of the PD source location. Phase angle of applied voltage at PDIV and magnitude ratio of discharge current flowing on each phase provides information of the particle position on the cross section of three phase construction. They can be considered as parameters for estimation of particle position on the cross section of three phase equipment. PD diagnostic device for three-phase equipment should provide simultaneous three-phase PD measurement system and data base of PD from different source and different location in three-phase equipment. Application of single-phase PD

diagnostic device to three-phase equipment needs data base of PD in three-phase equipment and modification in diagnostics algorithm.

Acknowledgment

Bismillahir rahmaanir rahiim.

In the Name of **Allah**, The Most Gracious, The Most Merciful. Praise be to **Allah**, The Lord of the worlds.

Firstly, the author would like to express his thank to Ministry of Education, Culture, Science and Technology of Japan (**Monbukagakusho**) for granting him a scholarship during his study in Japan.

The author would like to express his great thank to his Adviser, **Dr. Masayuki Hikita**, Professor of Kyushu Institute of Technology for his inspiring guidance, encouragement, discussion and advice during this work and in preparing and completing this dissertation.

The author is greatly indebted to Dr. Shinya Ohtsuka, Associate Professor of Kyushu Institute of Technology for his encouragement and helpful discussion during this study.

The author is deeply indebted to Dr. Satoshi Matsumoto, Professor of Shibaura Institute of Technology, for his encouragement, discussion and inspiring guidance through the course of this work..

The author would like also to express his great pleasure and special thanks to Japan AE Power Systems Corporation and Hitachi Engineering and Services for contributing a collaboration research with Kyushu Institute of Technology by providing GIS model, PDM device, and financial support.

The author would like to give his great appreciation to Dr. Nobuko Otaka and Dr. Masanori Tsukushi, the person in charge of Japan AE Power Systems Corporation, and Dr. Yoshiki Takehara, the person in charge of Hitachi Engineering and Services for all their valuable discussion and helpful comment to succeed this research.

The author is greatly indebted to Dr. Ken Kimura, Dr. Hisatoshi Ikeda, Dr. Mengu Cho, Dr. Mitani, Dr. Hideo Hirose, Professors of Kyushu Institute of Technology for their encouragement and helpful discussion in completing this dissertation.

The author is deeply grateful to the staffs of Prof Hikita`s Laboratory, Ms. Yotsui, Ms. Iwahori, Ms. Fujimoto, and Ms. Koyama for their helps.

The author would like to express his great thank to the present and previous members of Prof. Hikita`s Laboratory, especially Dr. Yanuar Zulardiansyah Arief, Dr. M. Kamarol bin M. Jamil, Mr. Toshihisa Abe, Mr. Toshio Ishitobi, Mr. Yuu Nishiuchi, Mr. Omori and Mr. Takashi Teshima for their helps and eager discussions.

The author is greatly indebted to **Dr. Suwarno** and Dr Isnuwardianto, Professors of Bandung Institute of Technology for their recommendation and encouragement.

The author would like to express his thank to staffs of Electrical Engineering Department of Bandung Institute of Technology, Indonesia for their support during his study in Japan.

The author gives his thank to his wife **Ira Artilia,** Doctor of Dental Surgery, his son Muhammad Ibrahim Rasyid, his daughters Salma Hanim Rafifa and Syarifa Rania Maryam, who gave spirit and so many joyful times when the author went back home after hard works at the laboratory, for their do’a, love, support, and encouragements.

The author expresses his thank to his mother **Siti Ruhani**, his father **Soekardjo**, his brother Ir. Arif Sambodo, and his sister Evi Sri Restuwati for their do’a, love, support, and encouragements.

Finally, the author expresses his thank to everybody who was important in this study that the author could not mention personally one by one.

Kitakyushu, March 2008

Umar Khayam

List of Publications

Journal

1. Effect of Elliptical Nature of Rotating Electric Field on Partial Discharge Pattern in a Three Phase Construction

   IEEJ Transactions on Fundamentals and Material A Vol. 127 No. 9, pp. 524-530, Sep. 2007

   Authors: **Umar Khayam**, Toshio Ishitobi, Shinya Ohtsuka, Satoshi Matsumoto, Masayuki Hikita

Best Paper Presentation Award

2. Investigation of Partial Discharge Characteristics in Air from Artificial Defect under Three Phase Voltage

   Proceeding of 2005 Korea Japan Joint Symposium on Electrical Discharge and High Voltage Engineering, paper PA-2, pp. 100-103, Ansan, KOREA, Nov. 3-4, 2005.

   Authors: **Umar Khayam**, Shinya Ohtsuka, Satoshi Matsumoto, Masayuki Hikita

International Proceedings

3. Measurement and Analysis of Frequency Spectrums of Electromagnetic Wave Signals Emitted by Partial Discharges in Three-phase Gas Insulated Switchgear using UHF Method

   Proceeding of 2007 Japan Korea Joint Symposium on Electrical Discharge and High Voltage Engineering, paper 16A-a3, pp. 7-10, Tokyo, JAPAN, Nov. 15-17, 2007.

   Authors: **Umar Khayam**, Y. Nishiuchi, S. Ohtsuka, M. Hikita, N. Otaka, T. Matsuyama, Y. Kobayashi, Y. Takehara

4. Effect of Foreign Particle on Rotating Electric Field and Partial Discharge Characteristics in Three-phase Construction

   Proceeding of 15th International Symposium on High-Voltage Engineering, ISH 2007, Paper 502, Ljubljuna, SLOVENIA, Aug. 27-31, 2007.

   Authors: **Umar Khayam**, Toshio Ishitobi, Shinya Ohtsuka, Satoshi Matsumoto, Masayuki Hikita

5. Effect of Eccentricity of Rotating Electric Field on Partial Discharge Pattern in Three Phase Construction

   Proceeding of 2006 Asian Conference on Electrical Discharge, ACED 2006, paper P1-15, Sapporo, JAPAN, Oct. 16-19, 2006.

   Authors: **Umar Khayam**, Toshio Ishitobi, Shinya Ohtsuka, Satoshi Matsumoto, Masayuki Hikita

6. Partial Discharge Distribution Pattern in Three Phase Electric Field

   Proceeding of 2006 Japan Korea Joint Session on Annual Conference of Fundamental and Material Society IEEJ, paper JK2-8, pp. 34, Kumamoto, JAPAN, August 21-22, 2006.

   Authors: **Umar Khayam**, Toshio Ishitobi, Shinya Ohtsuka, Satoshi Matsumoto, Masayuki Hikita

7. Partial Discharge Measurement on Three Phase Construction

   Proceeding of IEEE International Conference on Properties and Application of Dielectric Material, ICPADM 2006, Vol. 1, paper K-4, pp.301-304, Bali, INDONESIA, June 26-30, 2006.

   Authors: **Umar Khayam**, Shinya Ohtsuka, Satoshi Matsumoto, Masayuki Hikita

8. Investigation of Partial Discharge Characteristics in Air from Artificial Defect under Three Phase Voltage

   Proceeding of 2005 Korea Japan Joint Symposium on Electrical Discharge and High Voltage Engineering, paper PA-2, pp. 100-103, Ansan, KOREA, Nov. 3-4, 2005.

Authors: **Umar Khayam**, Shinya Ohtsuka, Satoshi Matsumoto, Masayuki Hikita

National Proceedings

9. Application of Single-phase PD Diagnostic Device in Three-phase GIS

   Proceeding of the 2008 Annual Meeting of Institute of Electrical Engineers of Japan, Vol. 6, paper 6-187, pp. 318-319, Fukuoka, JAPAN, March, 19-21, 2008.

   Authors: **Umar Khayam**, Y. Nishiuchi, S. Ohtsuka, M. Hikita, N. Otaka, T. Matsuyama, Y. Kobayashi, Y. Takehara

10. Examination of Electromagnetic Wave Propagation Characteristic in Cylinder Waveguide by FD-TD Method

    Proceeding of 2007 Joint Conference of Electrical and Electronics Engineers in Kyushu, Paper 03-1P-07, pp. 150, Okinawa, JAPAN, Sep. 17-18, 2007. (in Japanese)

    Authors: Yu Nishiuci, **Umar Khayam**, Shinya Ohtsuka, Masayuki Hikita

11. PD Distribution Pattern in High Eccentricity of Rotating Electric Field in Three-phase Construction

    Proceeding of the 2007 Annual Meeting of Institute of Electrical Engineers of Japan, Vol. 6, paper 6-259, pp. 424, Toyama, JAPAN, March 16-18, 2007.

    Authors: **Umar Khayam**, Toshio Ishitobi, Shinya Ohtsuka, Satoshi Matsumoto, Masayuki Hikita

12. Effect of Eccentricity of Rotating Electric Field on Partial Discharge in Three-phase GIS

    Proceeding of 2006 Joint Conference of Electrical and Electronics Engineers in Kyushu, paper 01-2A-12, pp. 212, Miyazaki, JAPAN, Sep. 28-29, 2006. (in Japanese)

    Authors: Toshio Ishitobi, **Umar Khayam**, Shinya Ohtsuka, Satoshi Matsumoto, Masayuki Hikita

13. Crosstalk Phenomena caused by Partial Discharge in Three Phase Construction

    Proceeding of The 2006 Annual Meeting of Institute of Electrical Engineer of Japan, Vol. 1, paper 1-048, pp. 61, Yokohama, JAPAN, March 15-17, 2006.

    Authors: **Umar Khayam**, Shinya Ohtsuka, Satoshi Matsumoto, Masayuki Hikita

14. Investigation of Partial Discharge Characteristics in Air from Artificial Defect in Conductor under Three Phase Voltage

    Proceeding of 2005 Joint Conference of Electrical and Electronics Engineers in Kyushu, paper 02-2A-10, pp. 101, Fukuoka, JAPAN, Sep. 29-30, 2005.

    Authors: **Umar Khayam**, Shinya Ohtsuka, Satoshi Matsumoto, Masayuki Hikita

APPENDIX I

DESIGN AND CONSTRUCTION OF EXPERIMENT SYSTEM I

1

Construction of Experiment System

- Design
- Order
- Test of equipment individually
- Assemble experimental equipment
- Write procedure of turning on and turning off experimental equipment
- Test: protection circuit; applied voltage
- PD Calibration
- Free corona Test
- Make artificial defects

2

Design (1)

SAFETY, ACCURACY, SENSITIVITY

- Rating of equipment
- Electric field stress (electric field calculation)
- One point grounding
- Suppression of Noise

3

Design (2)

- Experiment circuit design
- Lay Out of experimental equipment
- Power supply
- Electrode for experiment
- PD measurement system
- Protection circuit
- Grounding circuit
- Artificial Defects

4

Experimental Circuit

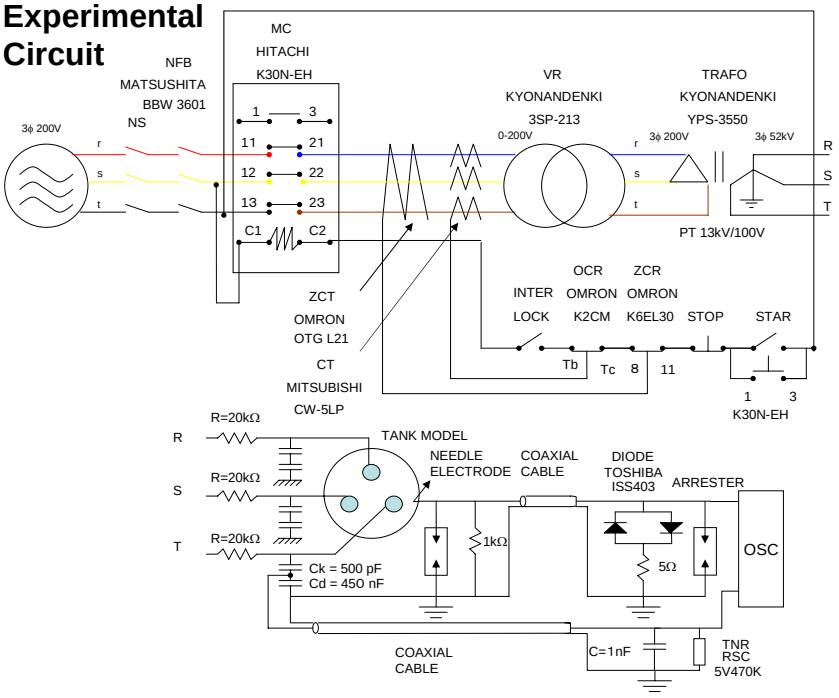

5

Equipments

Equipment	Maker	Type	Specification
CB (遮断器)	松下電工	BBW 3601	3P,60 A
IL (インターロック)	omron	Z-15GNJ55	
MC (電磁接触器)	日立産機	K30N-EPH	200 V,11 kW
ZCR (零相継電器)	omron	K6EL-30	
ZCT (零相変流器)	omron	OTG-L21	50 A
OCR (過電流継電器)	omron	K2CM-Q2LAV	
CT (変流器)	三菱電機	CW-5LP	50/5 A
VR (電圧調整器)	京南電機	3SP-213	200/0～240 V
TR (試験用変圧器)	京南電機	YPAS-3550	200 V/52 kV
Rk (制限抵抗)	KOA	PSO5	100 W,20 kΩ
Ck (カップリングコンデンサ)	TDK	FD-36AU	500 pF
Cd (分圧用コンデンサ)	nichicon		450 nF
Rd (検出抵抗)	KOA	RW1/2	1 kΩ

6

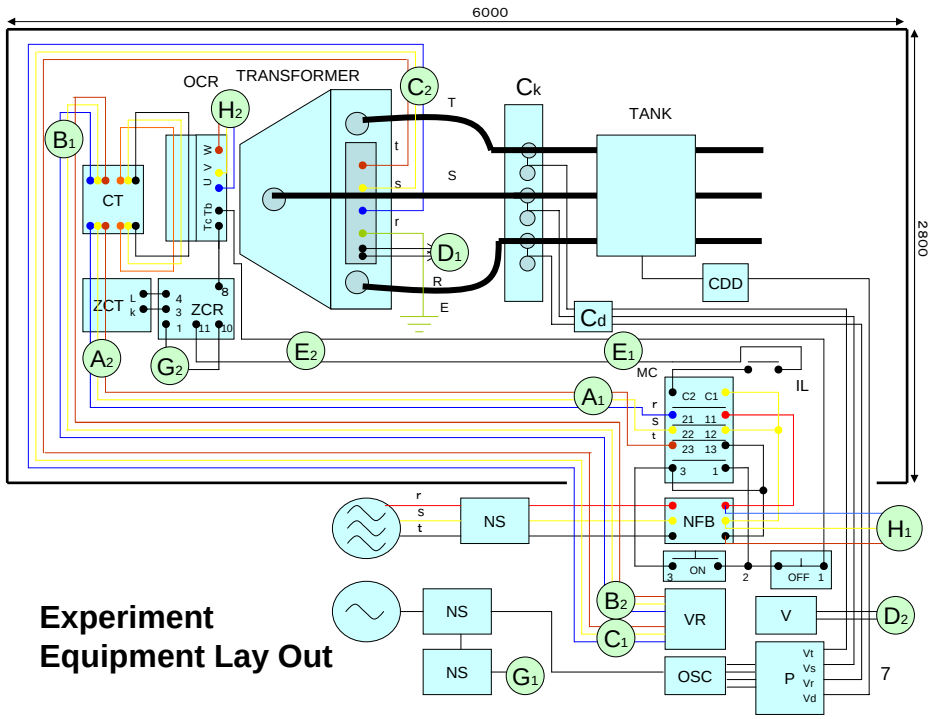

Experiment Equipment Lay Out

PHOTOGRAPH OF EXPERIMENT EQUIPMENT I

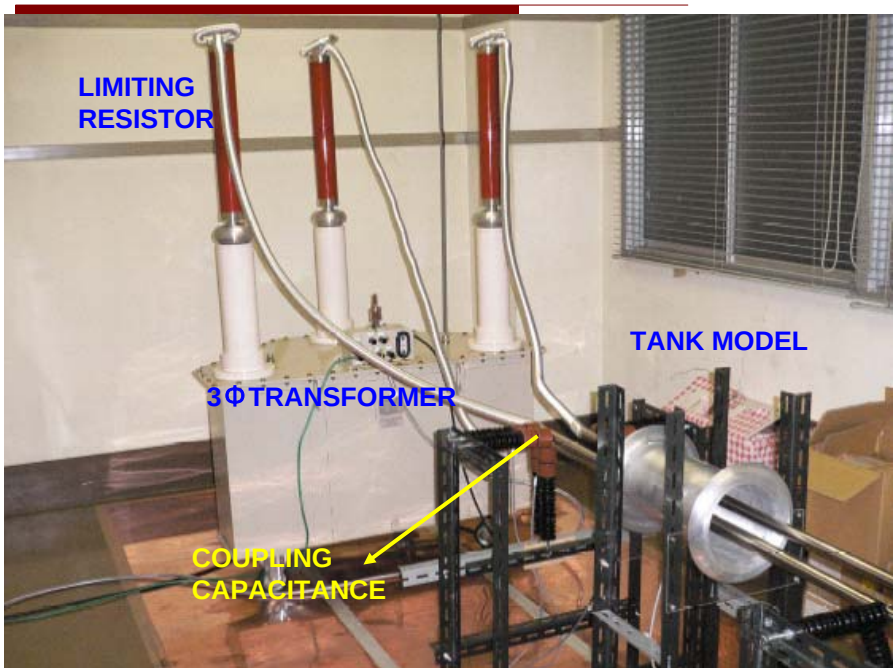

9

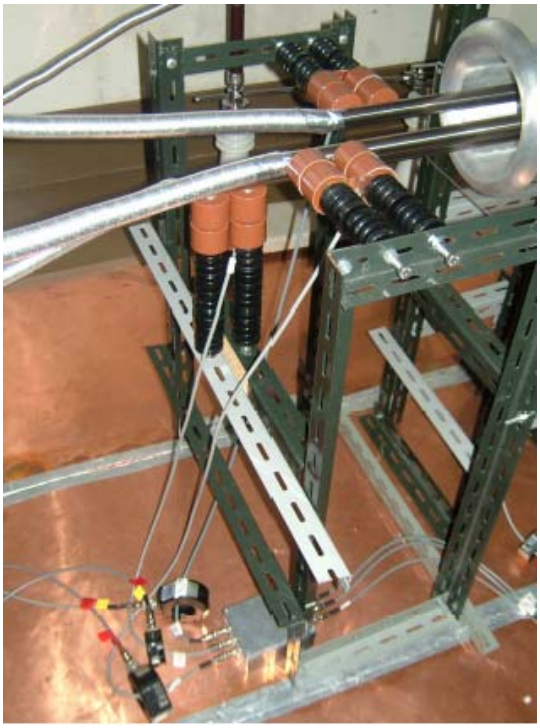

10

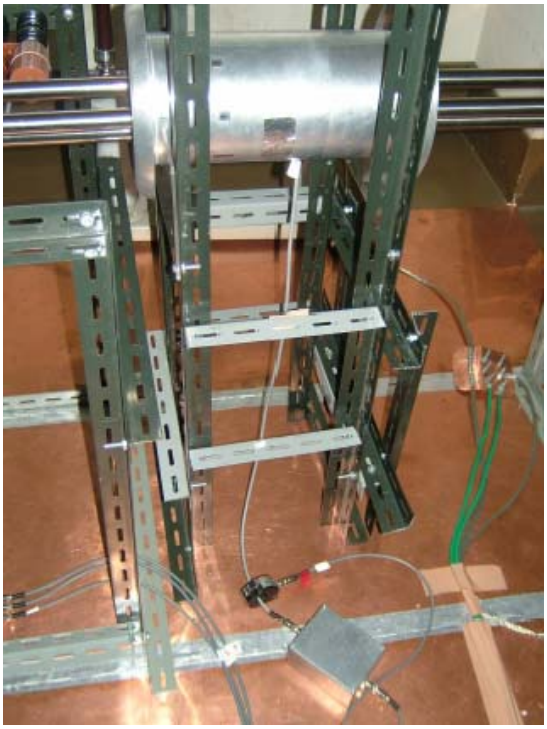

11

The power supply for experiment

Capacity : 3 phase, 5 KVA
Input voltage : 200 V
Output voltage : 30 kV (52 kV L-L)
Output current : 55 mA
Frequency : 60 Hz
P.T : 30 kV / 150 V
Corona : 30 kV / 10 pC
Rating : 30 parts
Connection : Δ / Y
Weight : 700 ∽ 750 kg
Manufacture : 京南電機株式会社

12

Photograph of Equipment

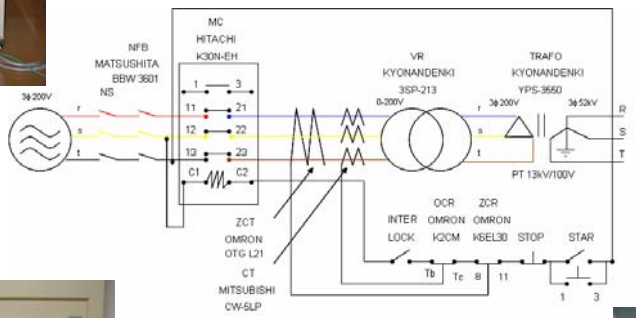

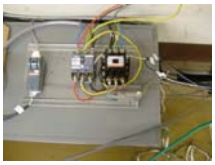

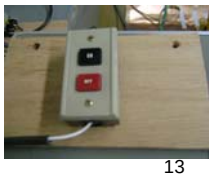

13

Photograph of Equipment

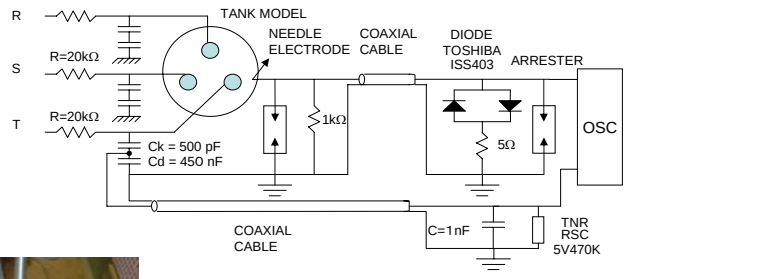

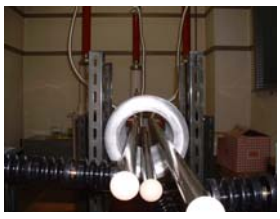

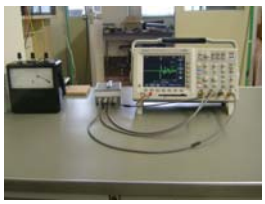

14

Lay Out of 3 Phase Tank

Max testing voltage: 52 kV
Air inside

Real GIS: 275 kV
SF6 gas inside

Size of Tank:
1/5 of real GIS

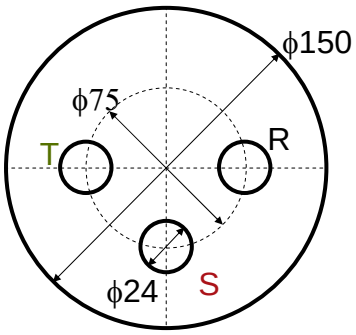

3ϕ model tank

15

THREE-PHASE GIS MODEL I

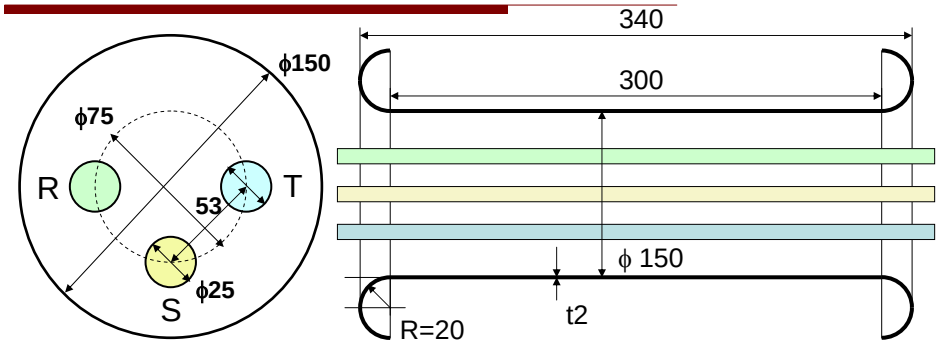

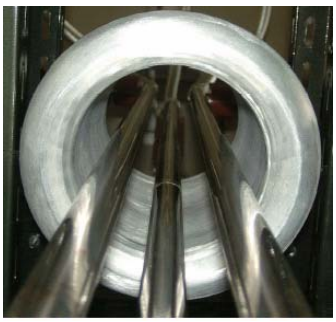

TANK DESIGN

Material: Aluminum

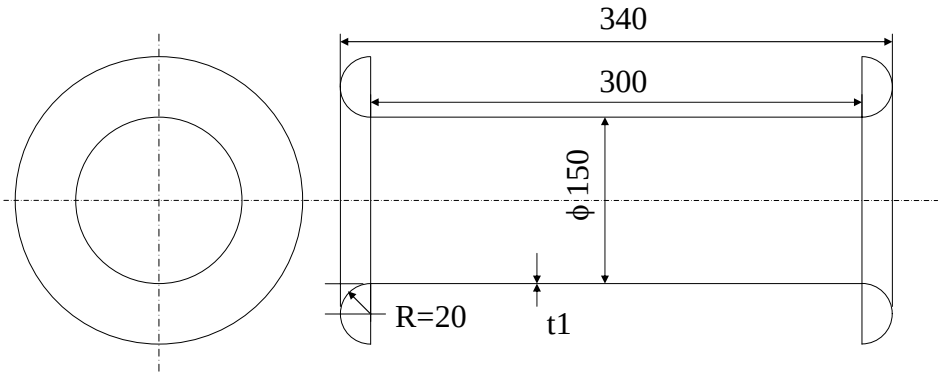

Figure 4 Tank Design

17

TANK SUPPORTER

Material: Acrylic

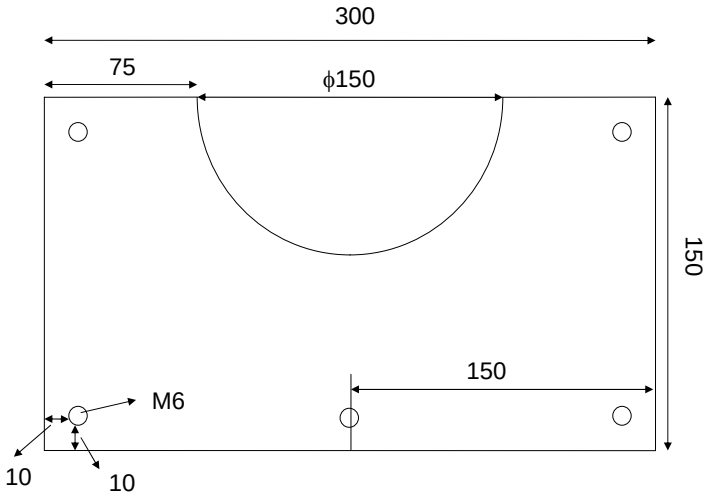

18

Conductor Arrangement

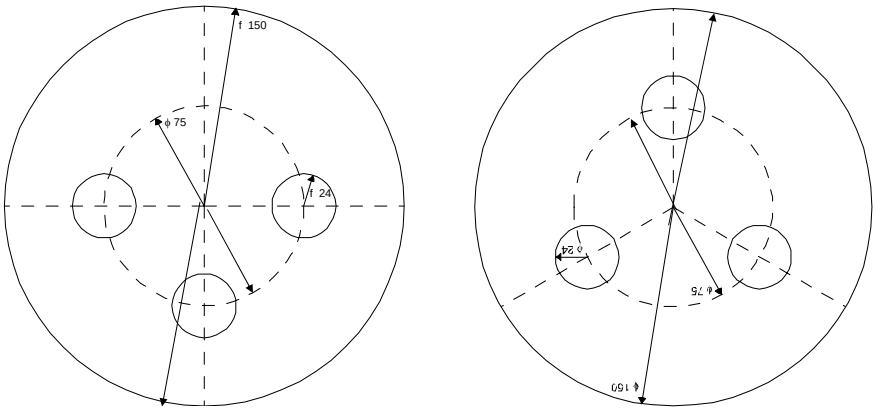

(a) Equilateral triangle (b) Isosceles triangle

19

CONNECTION BETWEEN CONDUCTOR AND CAPACITOR

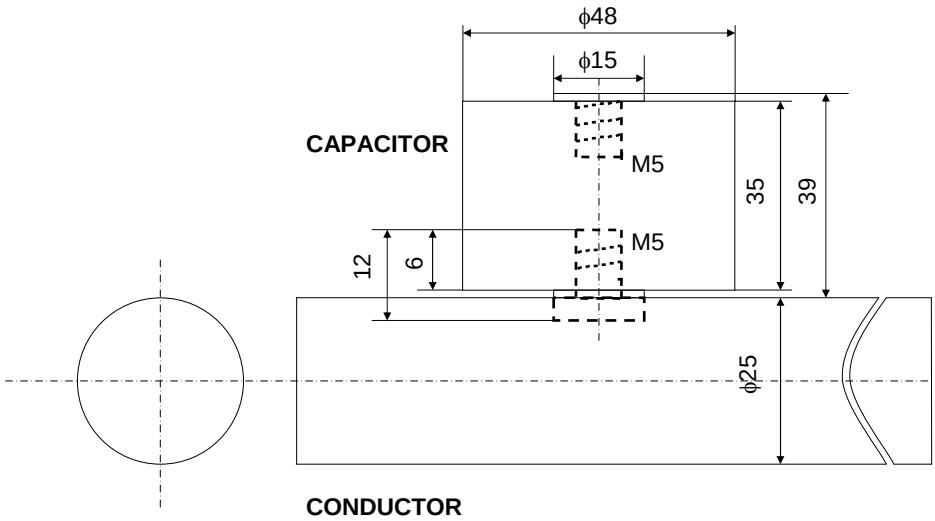

20

TOOL FOR CONDUCTOR POSITION SETTING 1

Material: Acrylic

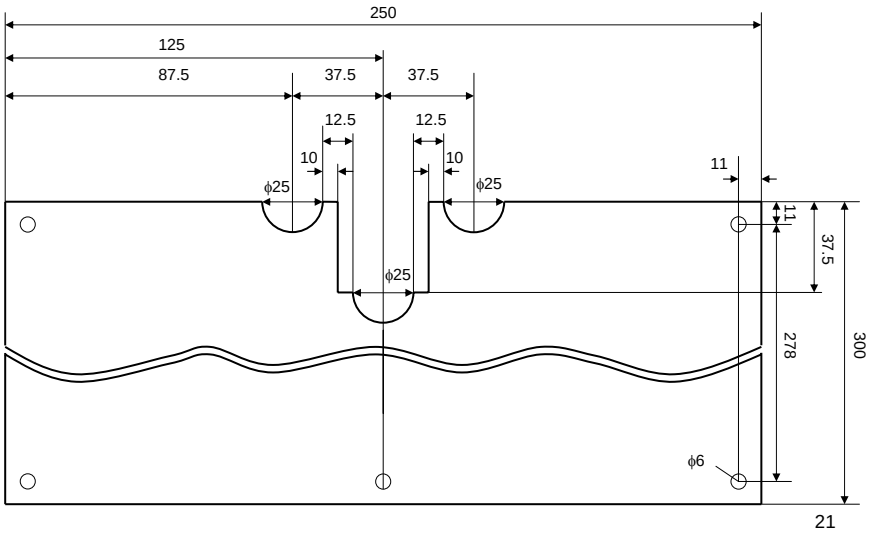

TOOL FOR CONDUCTOR POSITION SETTING 2

Material: Acrylic

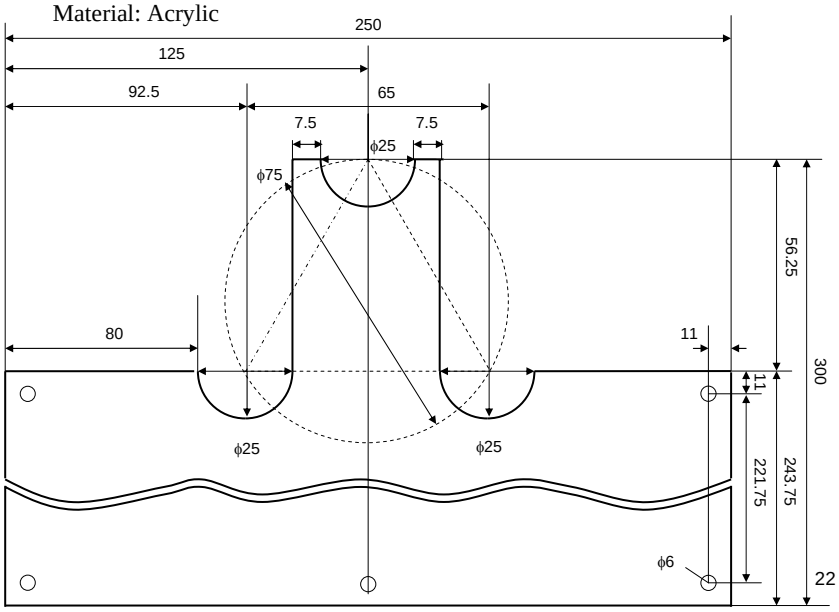

CONDUCTOR SUPPORTER 1

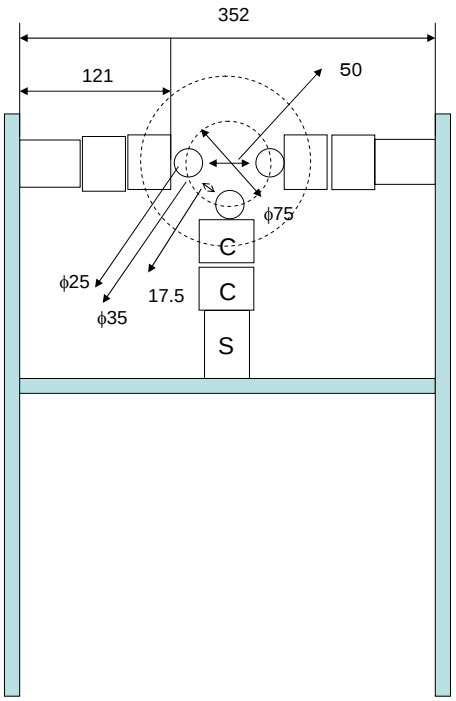

23

CONDUCTOR SUPPORTER 2

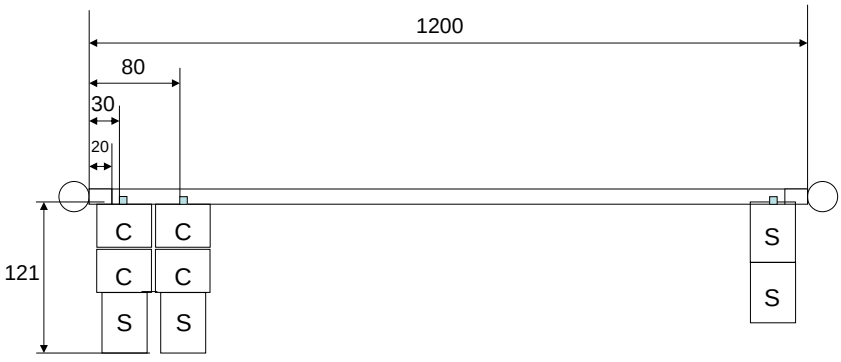

24

Material: Aluminum

Screw M12
Pitch 1.75
Length 27

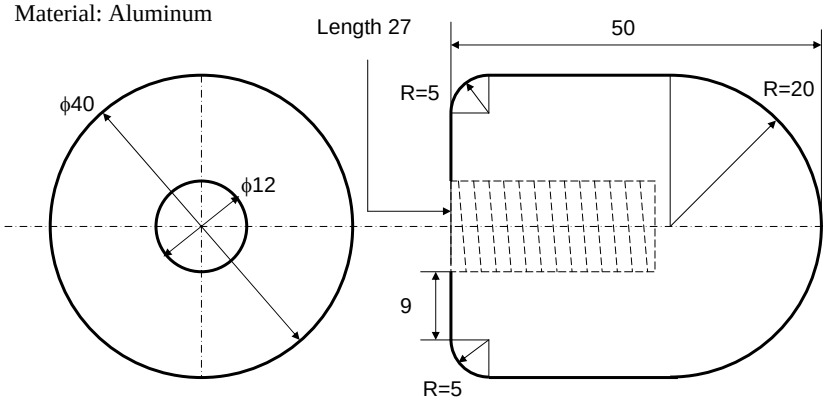

END ELECTRODE FOR LIMITING RESISTOR

材料	Aluminum
数量	3
所属	匹田研究室
氏名	ウマルハヤム

25

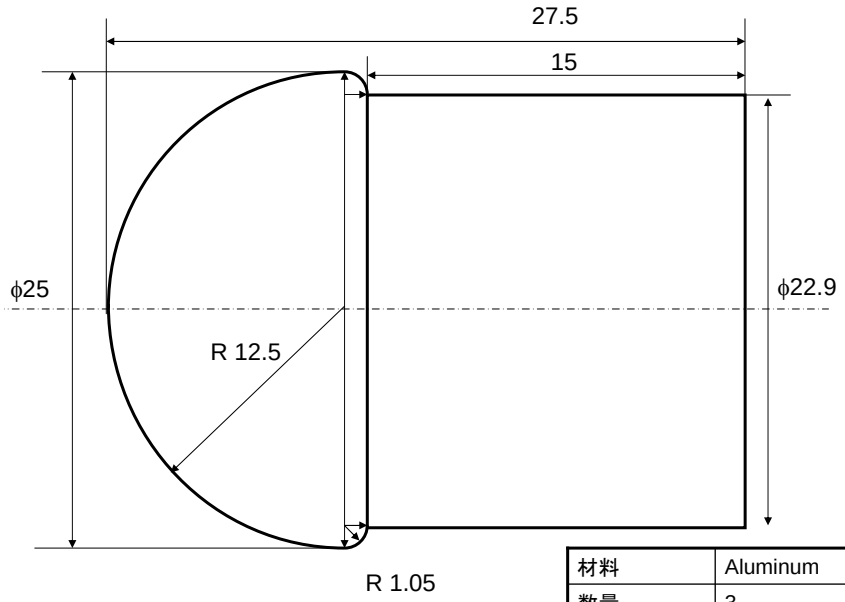

END ELECTRODE FOR CONDUCTOR

Material: Aluminum

材料	Aluminum
数量	3
所属	匹田研究室
氏名	ウマルハヤム

26

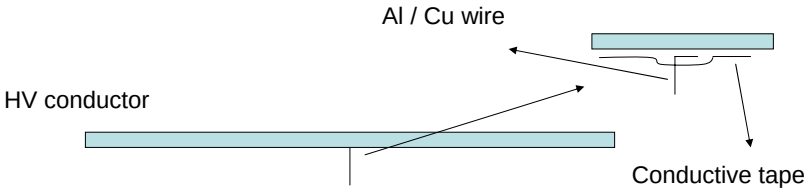

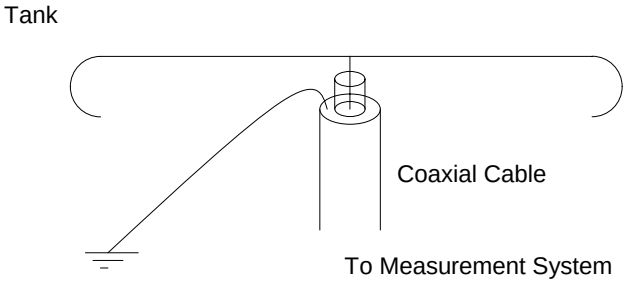

Protrusion on HV Conductor

27

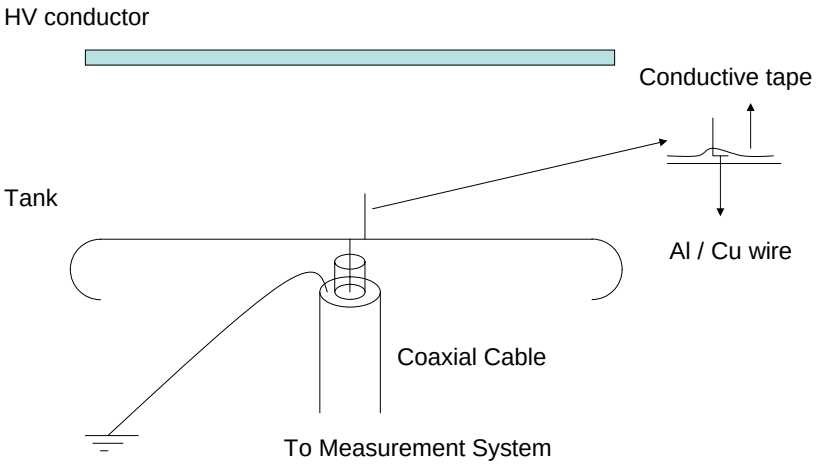

Protrusion on Tank

28

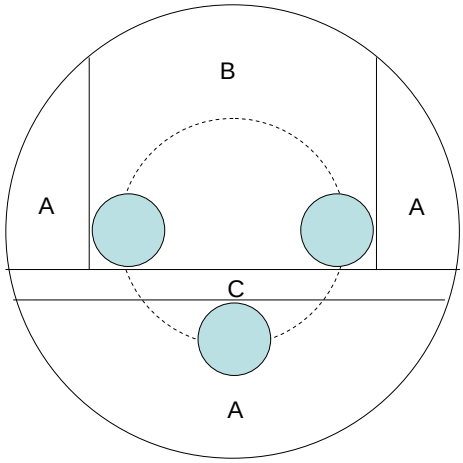

Method for Supporting of Floating Metallic Particle

29

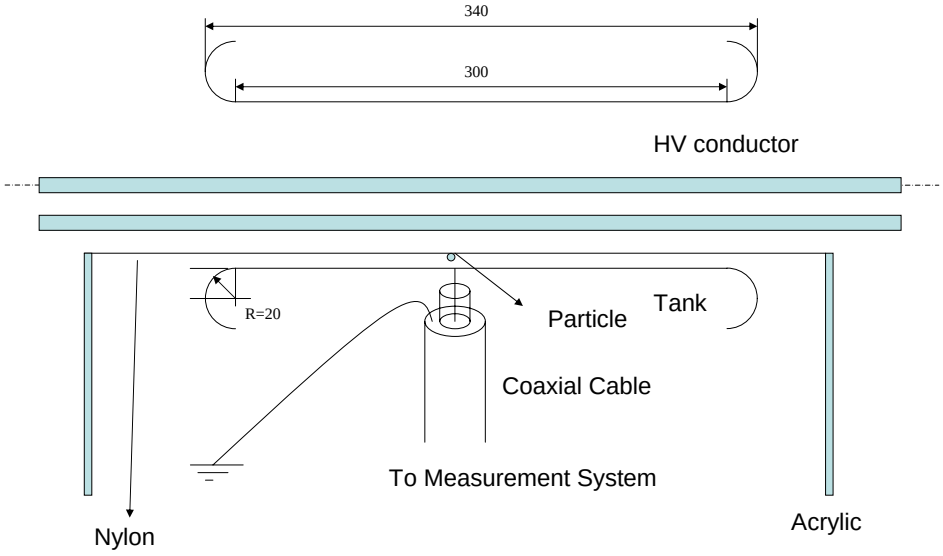

Method for Supporting of Floating Metallic Particle A

30

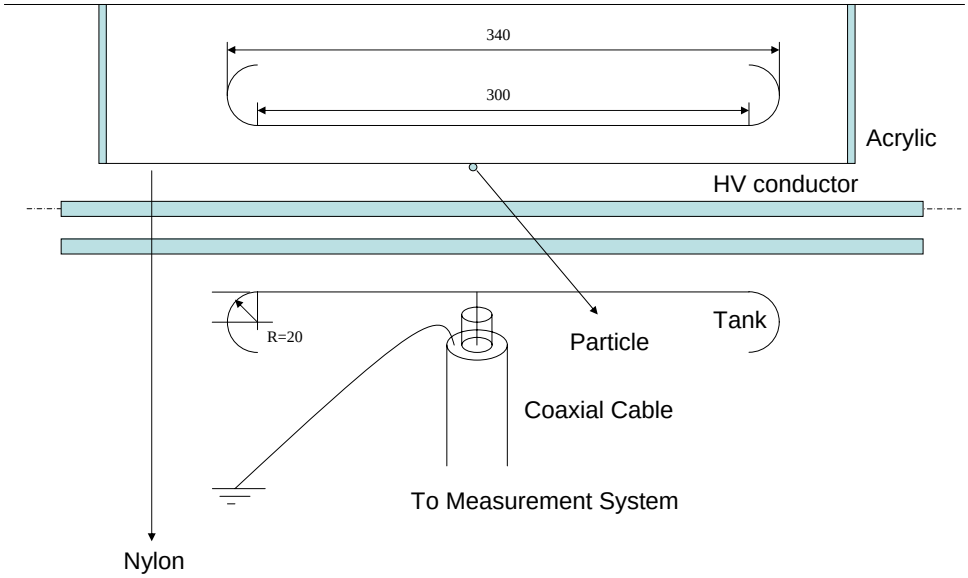

Method for Supporting of Floating Metallic Particle B

31

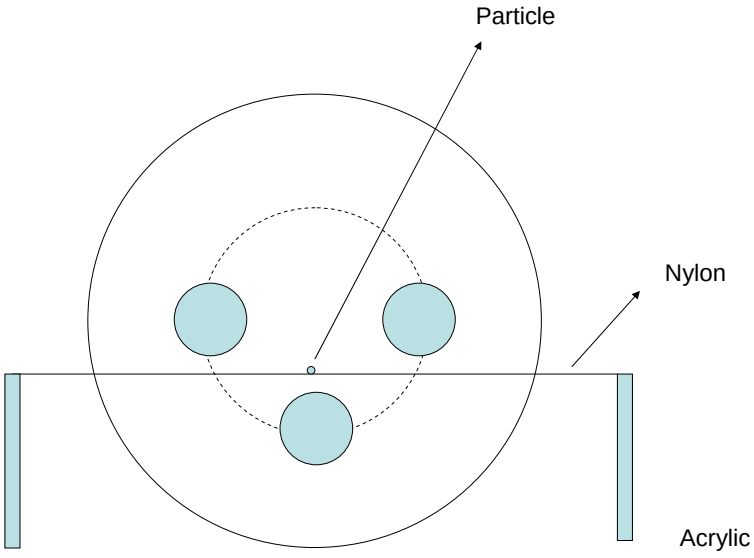

Method for Supporting of Floating Metallic Particle C

32

Short Circuit Current

L-L

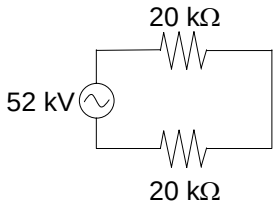

L-G

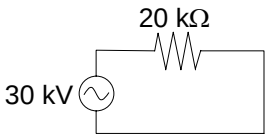

Secondary Side

$$I_2 = \frac{52000[V]}{40000[\Omega]} = 1.3[A] \quad < \quad I_2 = \frac{30000[V]}{20000[\Omega]} = 1.5[A]$$

Primary Side

$$I_1 = 1.5[A] \times \frac{52000[V]}{200[V]} = 390[A]$$

33

Zero Current Relay (ZCR)

- Balance Condition

  $I_R + I_S + I_T = 0$

- Unbalance Condition

  $I_R + I_S + I_T = I \neq 0$

ZCR works if $I \geq 30$ mA

34

Over Current Relay

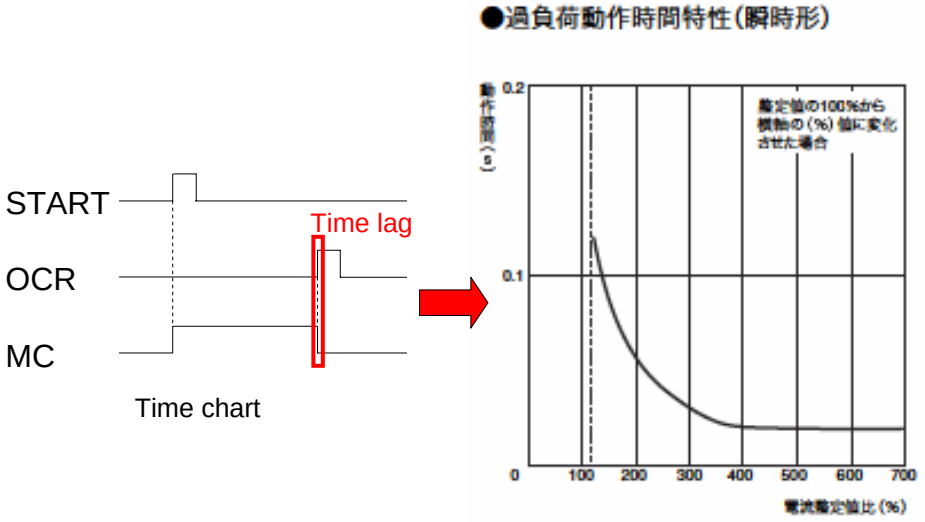

35

Rating current of cable is 30 A
Over relay current is set at 8 A

115 % (9.2 A)	0.12 sec (7.2 cycle)
400 % (32 A)	0.02 sec (1.2 cycle)

36

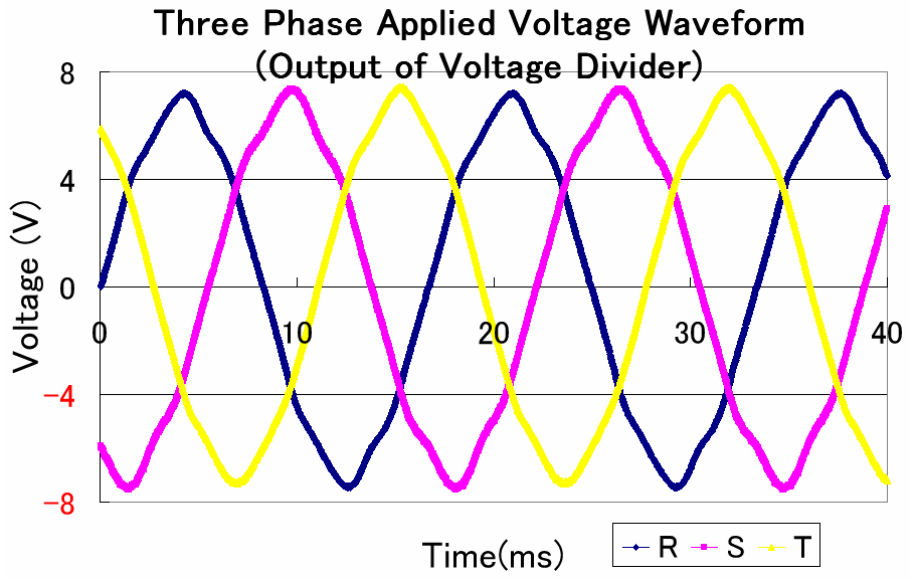
Three Phase Applied Voltage Waveform
(Output of Voltage Divider)
Voltage (V)
8
4
0
−4
−8
0
10
20
30
40
Time(ms)
R
S
T

37

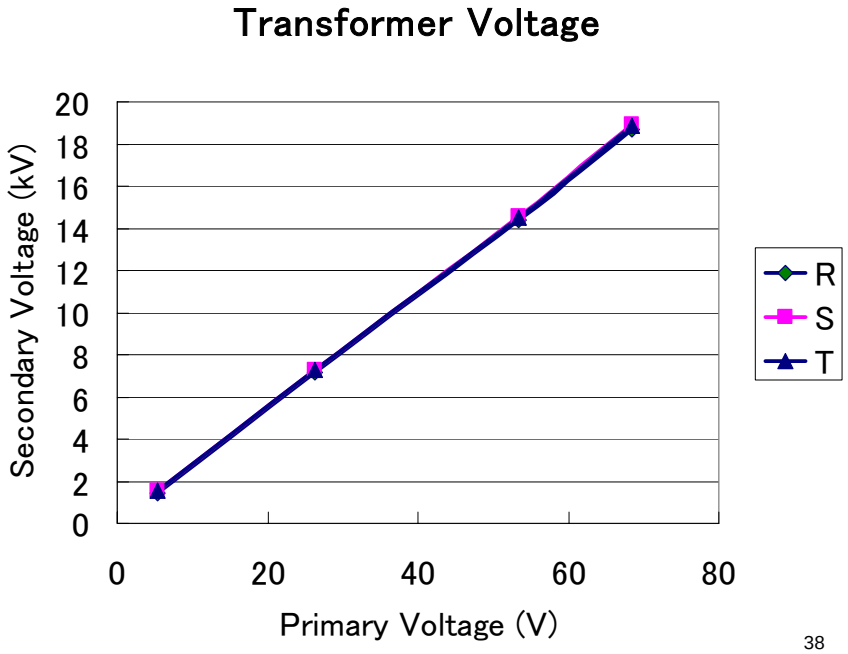
Transformer Voltage
Secondary Voltage (kV)
20
18
16
14
12
10
8
6
4
2
0
0
20
40
60
80
Primary Voltage (V)
R
S
T

38

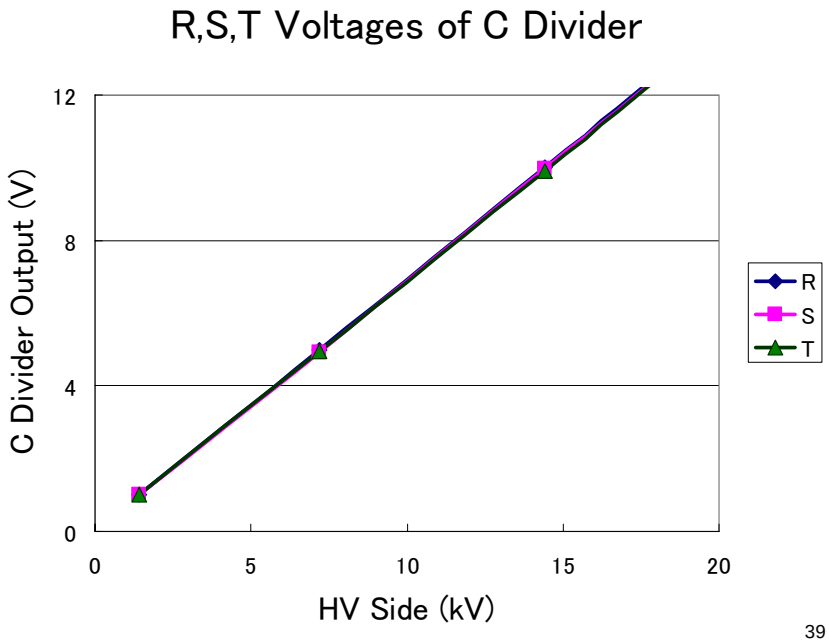

39

Calibration of PD Measurement

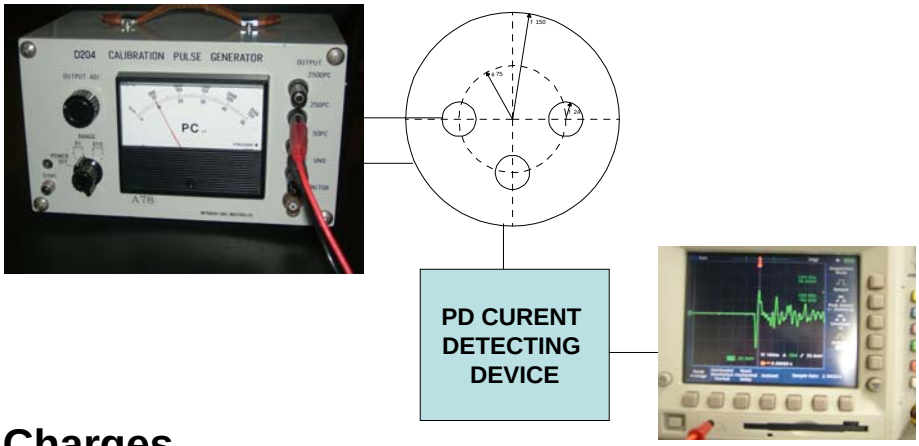

Charges (pC) → **Voltage (V)**

40

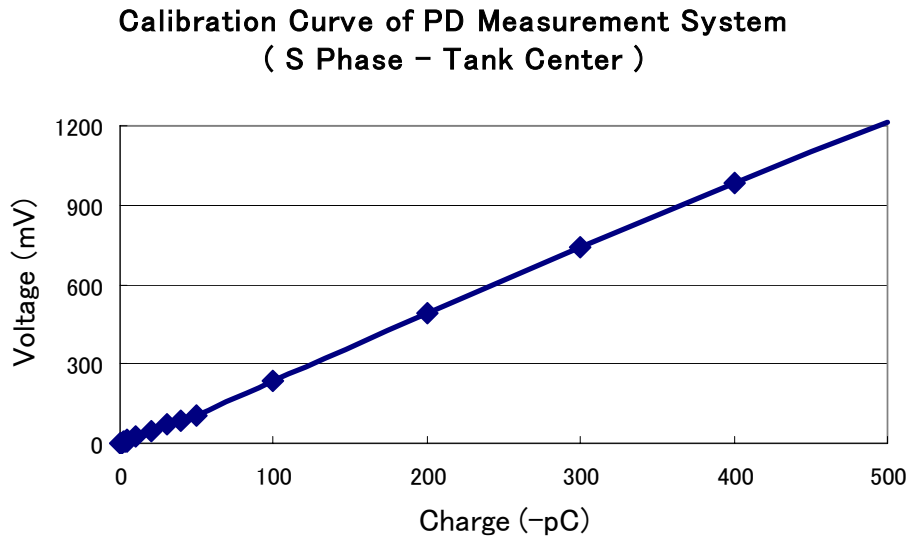

41

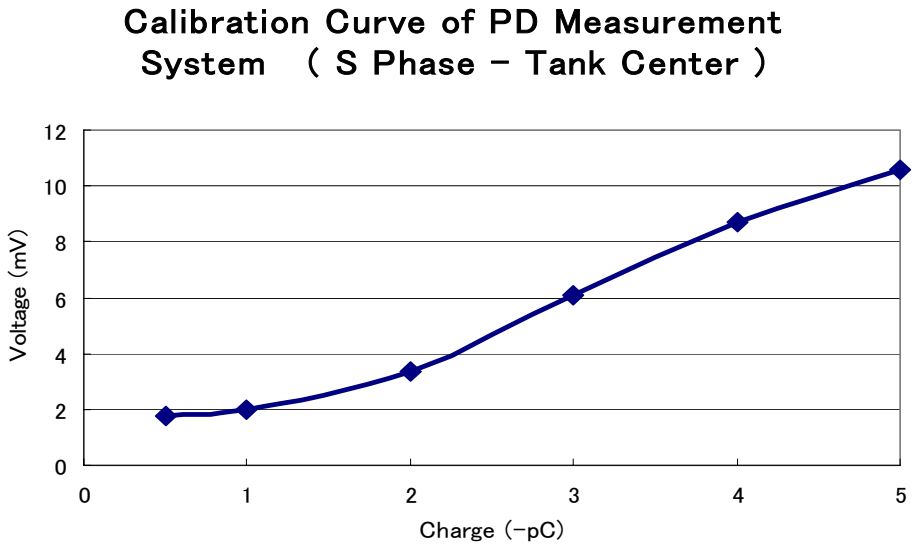

PD Measurement Sensitivity: 2 pC

42

APPENDIX II CALIBRATION

CALIBRATION PURPOSE:

- To verify the relation between the reading of the PD detector (mV) and injected charge (pC)

- To verify sensitivity of measurement systems in some PD positions.

43

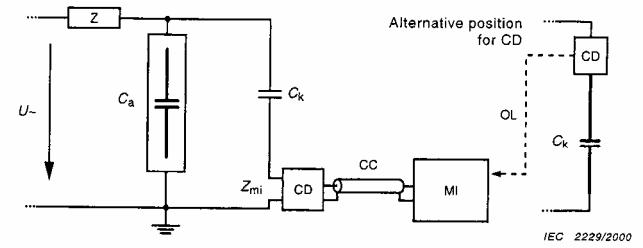

Figure 1a – Coupling device CD in series with the coupling capacitor

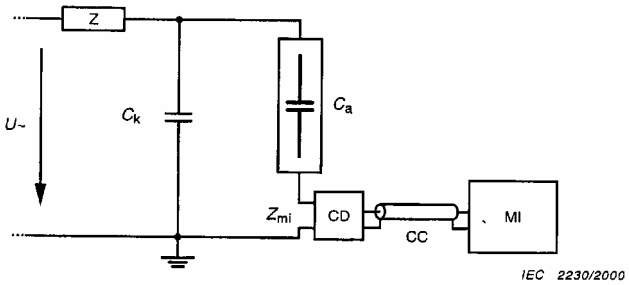

Figure 1b – Coupling device CD in series with the test object

Components

$U_{\sim}$	high-voltage supply
Z_{mi}	input impedance of measuring system
CC	connecting cable
OL	optical link
C_a	test object
C_k	coupling capacitor
CD	coupling device
MI	measuring instrument
Z	filter

Figure 1 – Basic partial discharge test circuits

44

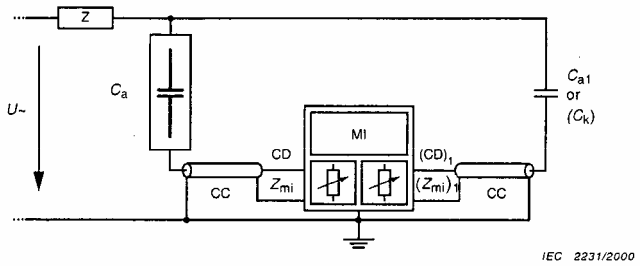

Figure 1c – Balanced circuit arrangement

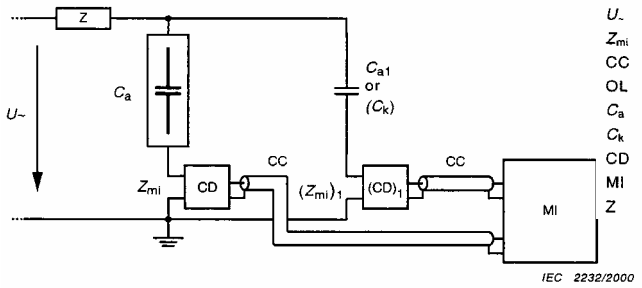

Figure 1d – Polarity discrimination circuit arrangement

Components

$U_\sim$	high-voltage supply
Z_{mi}	input impedance of measuring system
CC	connecting cable
OL	optical link
C_a	test object
C_k	coupling capacitor
CD	coupling device
MI	measuring instrument
Z	filter

Figure 1 – Basic partial discharge test circuits

45

PD Measurement System A (DI)

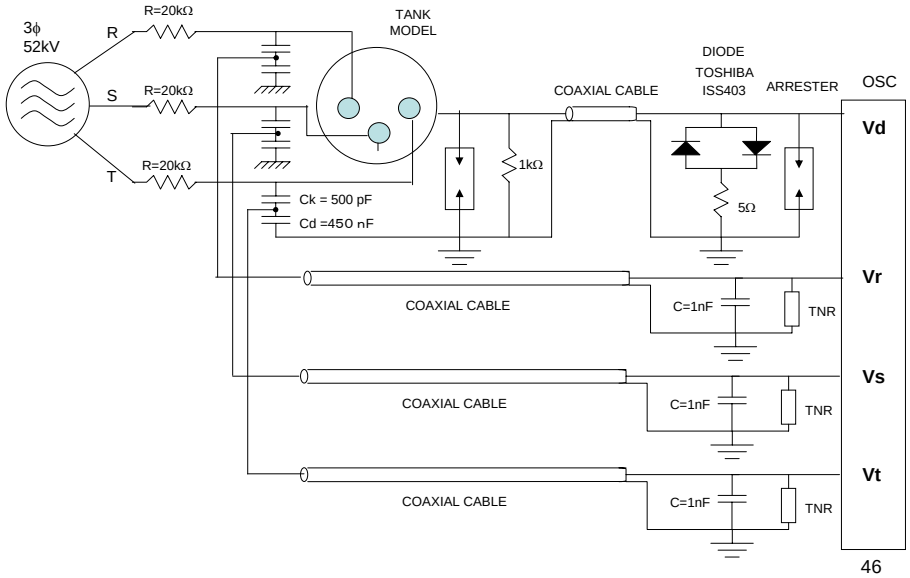

46

PD Measurement System B (CT)

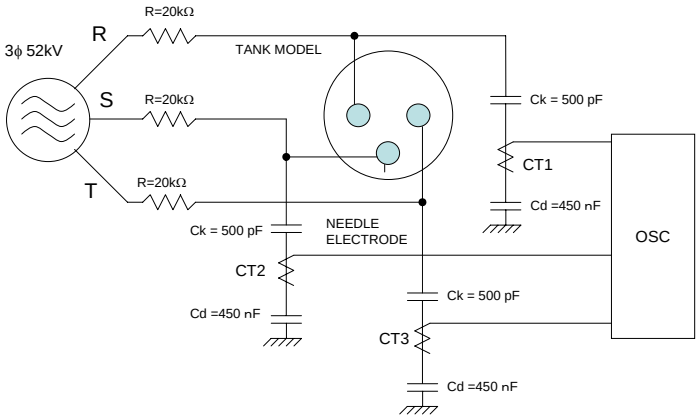

47

PD Measurement System C (ZC)

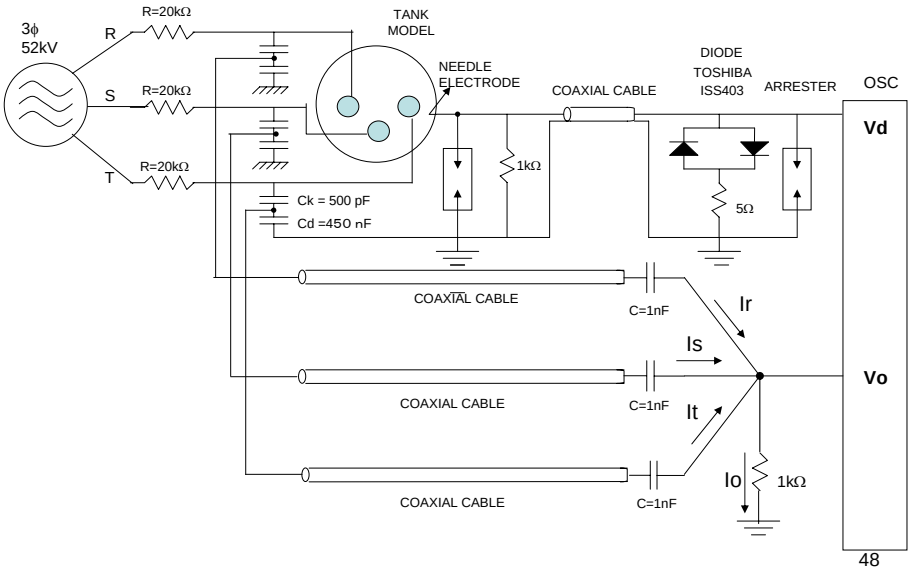

48

PD MEASUREMENT SYSTEM D (A+B)

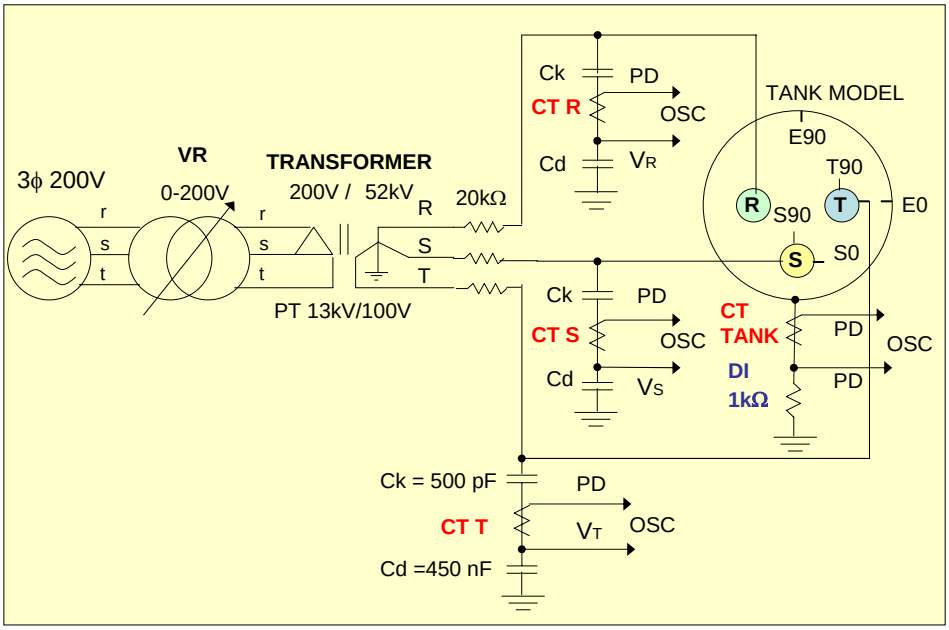

Calibration Circuit

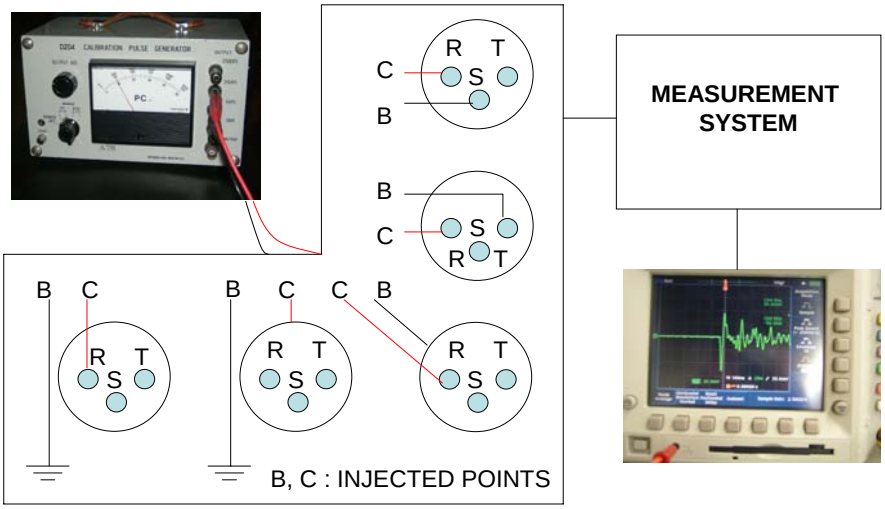

50

Positive Charge

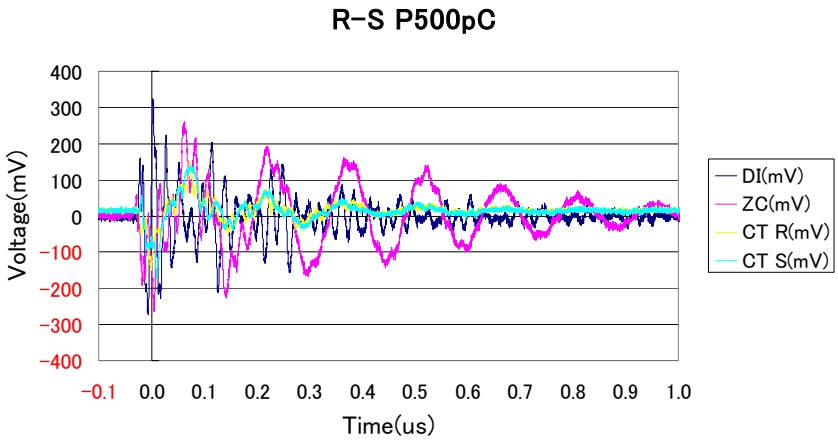

51

Negative Charge

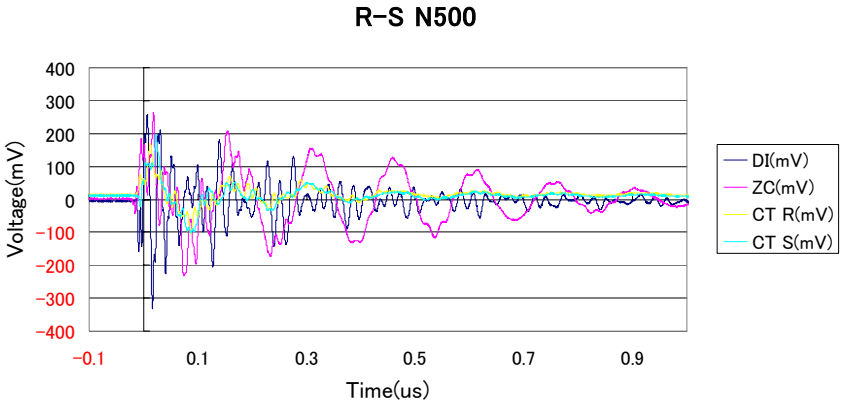

52

Calibration Curve A

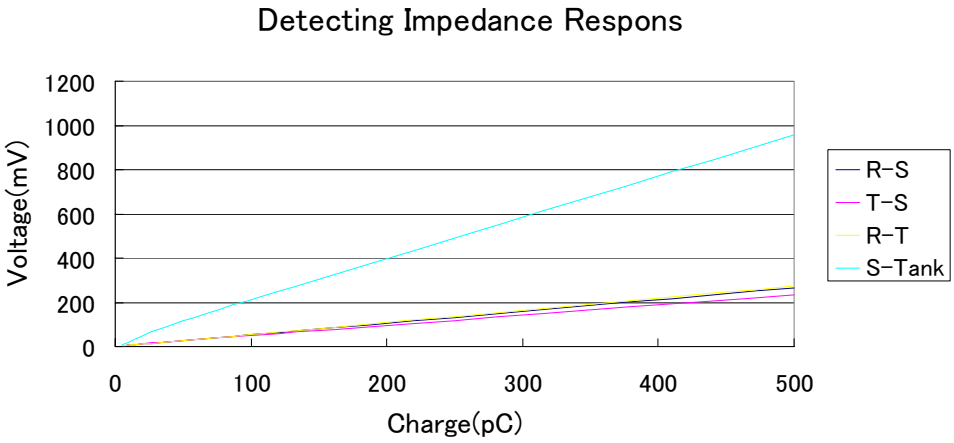

53

Calibration Curve B

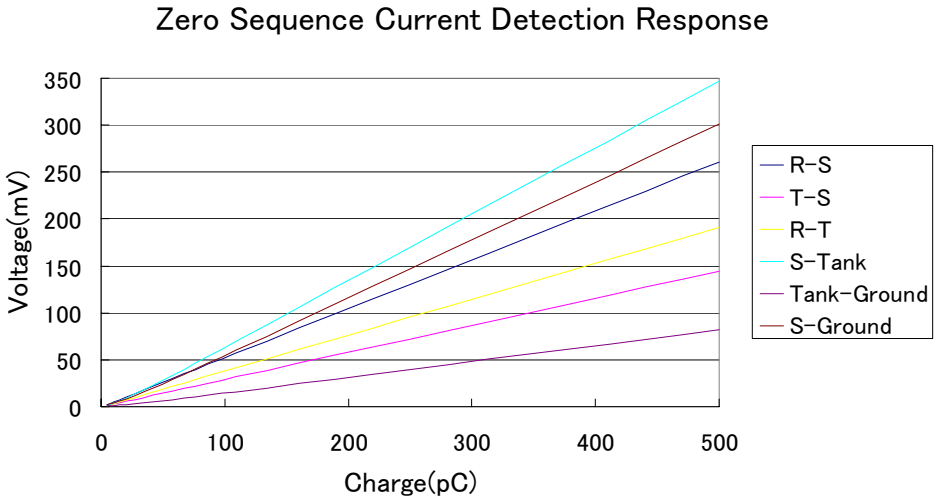

54

Calibration Curve Cr

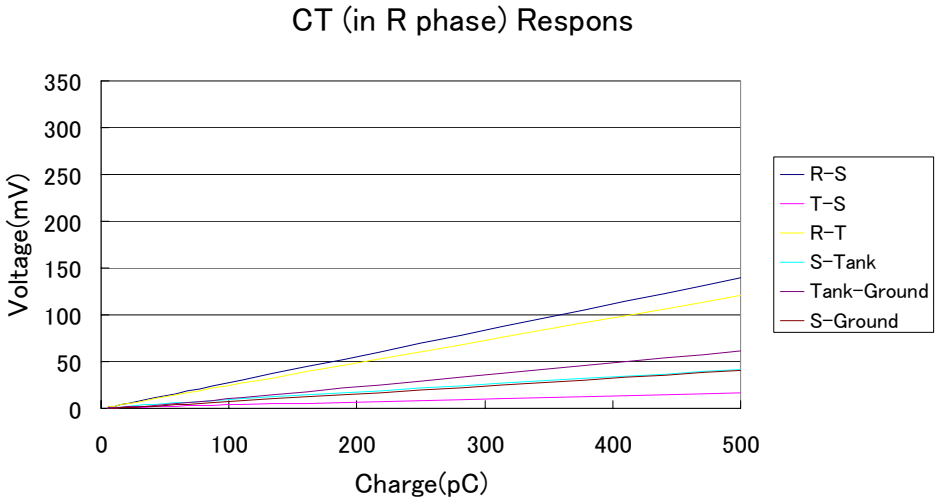

55

Calibration Curve Cs

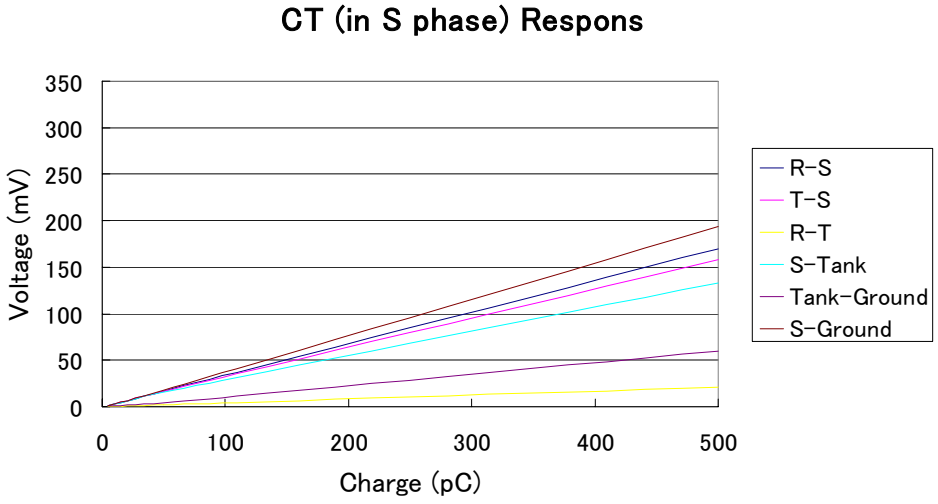

56

DETECTING IMPEDANCE SENSITIVITY

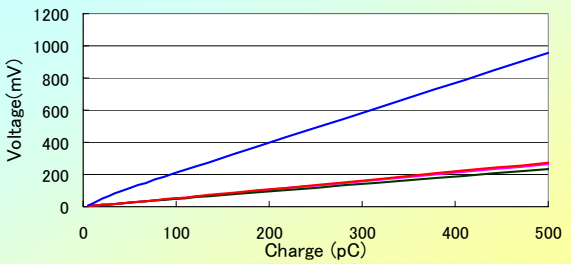

CIRCUIT D

DETECTING IMPEDANCE

High sensitivity for discharge occurring between phase and tank

CTs SENSITIVITY

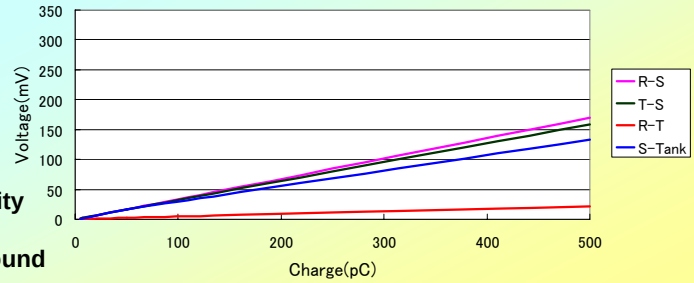

CTs

High sensitivity for discharge occurring around S phase

57

CLASSIFICATION OF AMPLITUDE LEVEL OF PD CURRENT MEASURED BY CT

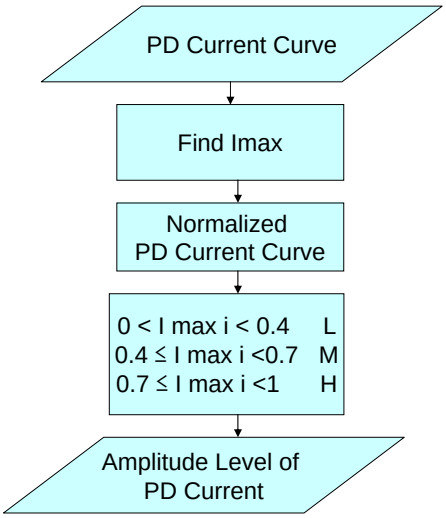

CIRCUIT D

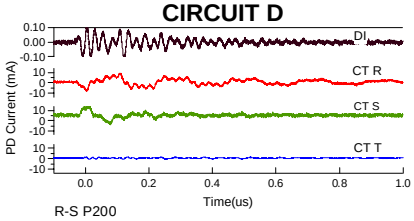

Imax = I max CT S = 9.28 mA

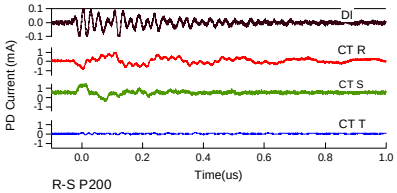

Imax CT R =0.89 H

Imax CT S =1 H

Imax CT T =0.12 L

R-S P200 H, H, L

58

CIRCUIT D

Table Circuit Sensitivity

Injecting Points	Amplitude Level of Discharge Current			
	R=1kΩ / CT	CT R	CT S	CT T
R-Tank	**H**	**H**	L	L
S-Tank	**H**	L	**H**	L
T-Tank	**H**	L	L	**H**
R-S	L	**H**	**H**	L
R-T	L	**H**	L	**H**
S-T	L	L	**H**	**H**

We may distinguish discharge positions based on magnitude of discharge current flowing in every phase

59

CIRCUIT D

Table Polarity and Amplitude Level of Discharge Current

No	Injected Points	Charge	Conductor Polarity			Discharge Current			
			R	S	T	DI	CTR	CTS	CTT
1	R-S	+	+	-		+	H-	H+	L-
2	R-S	-	-	+		-	H+	H-	L+
3	R-T	+	+		-	+	H-	L+	H+
4	R-T	-	-		+	-	H+	L-	H-
5	T-S	+		-	+	+	L-	H+	H-
6	T-S	-		+	-	-	L+	H-	H+
7	R-Tank	+	+			+	H-	L+	L+
8	R-Tank	-	-			-	H+	L-	L-
9	S-Tank	+		+		+	L+	H-	L+
10	S-Tank	-		-		-	L-	H+	L-
11	T-Tank	+			+	+	L+	L+	H-
12	T-Tank	-			-	-	L-	L-	H+
13	R-G	+	+			+	H-	L-	L+
14	S-G	+		+		+	L-	H-	L+
15	T-G	+			+	+	L+	L-	H-
16	Tank-G	+				+	L-	L-	L-

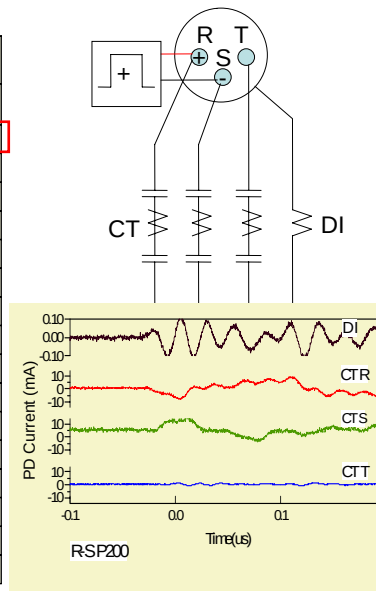

60

APPENDIX III

PD MEASUREMENT RESULT
(GIS MODEL I)

61

EXPERIMENTAL SETUP I

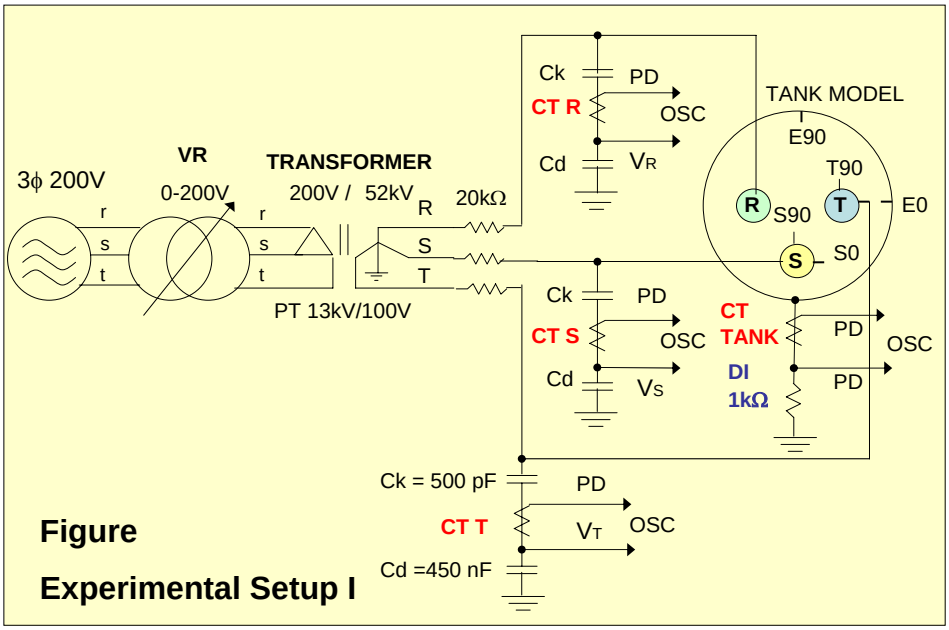

Figure

Experimental Setup I

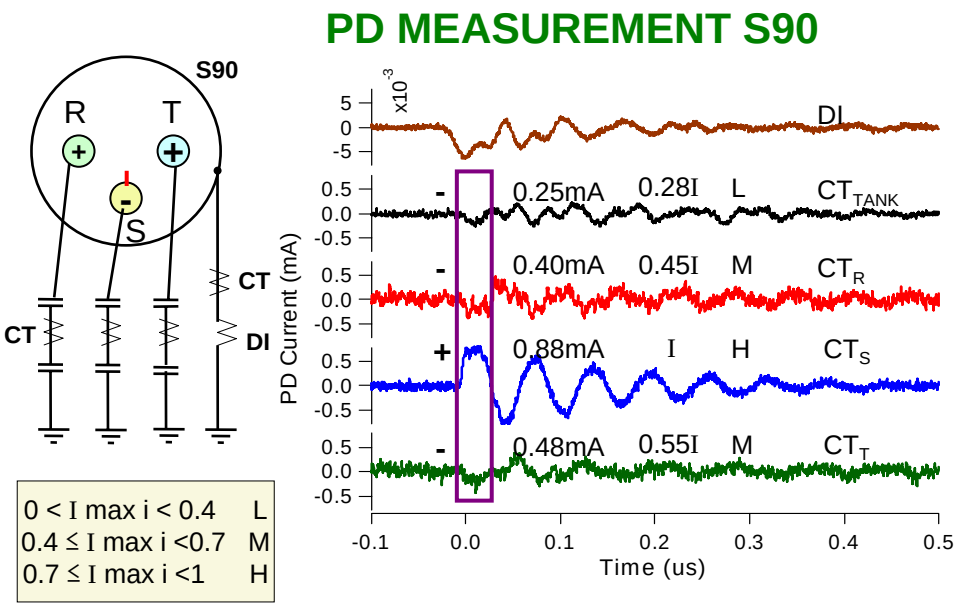

Fig. 1 PD Current Waveform measured for S90 defect 63

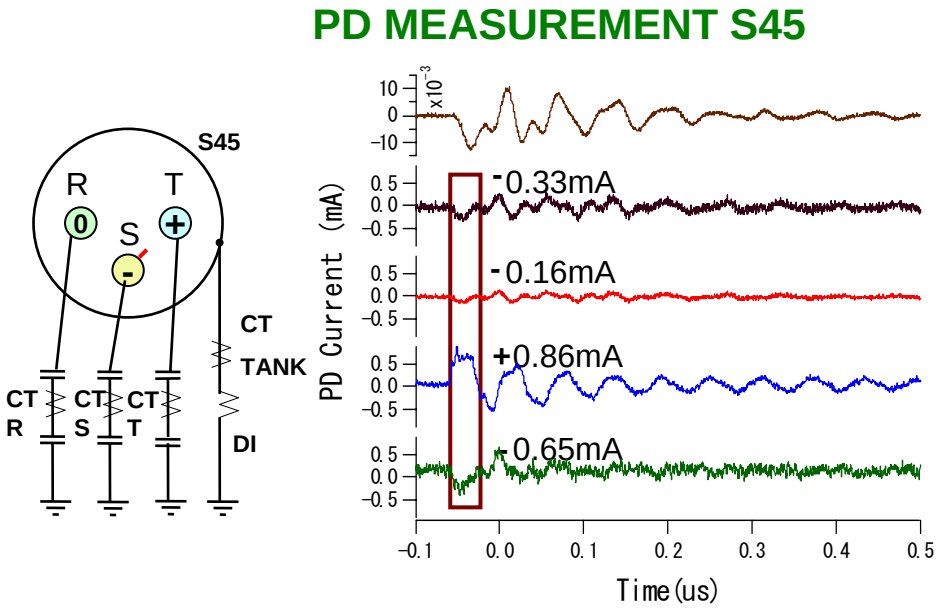

Fig. 2 PD Current Waveform measured for S45 defect 64

PD MEASUREMENT S270

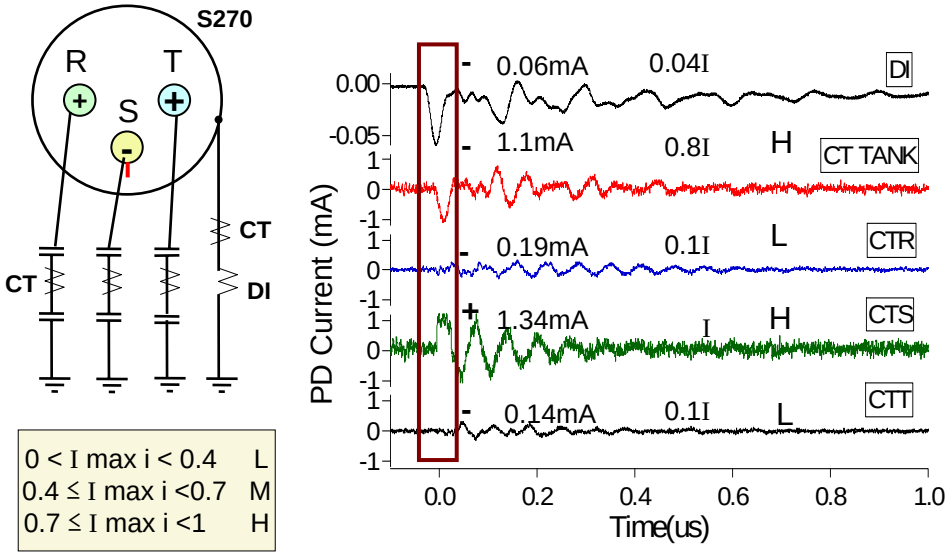

Fig. 3 PD Current Waveform measured for S270 defect 65

PD MEASUREMENT S180

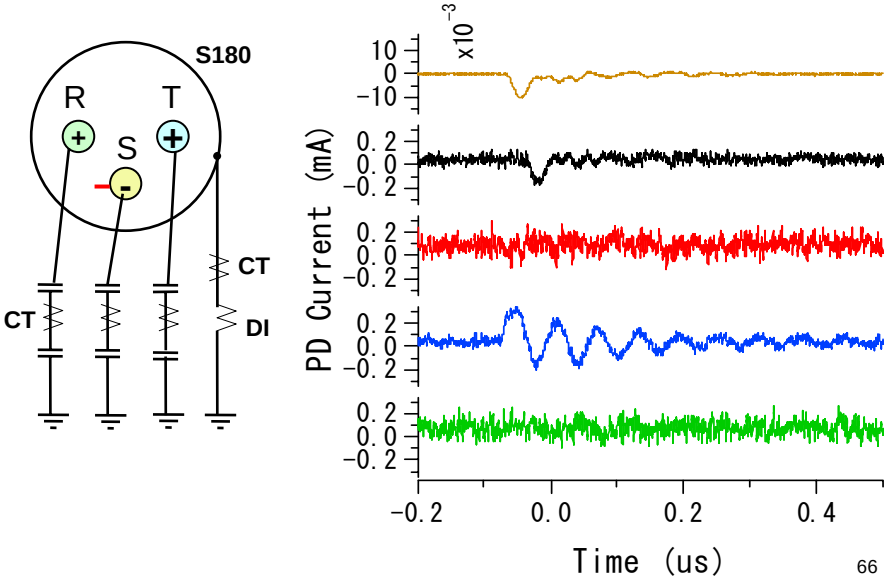

66

PD MEASUREMENT T90

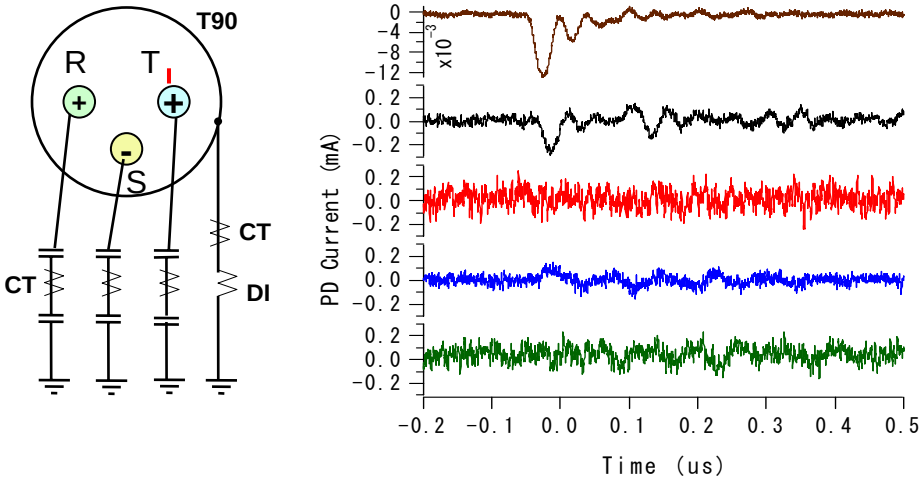

67

PD MEASUREMENT T45

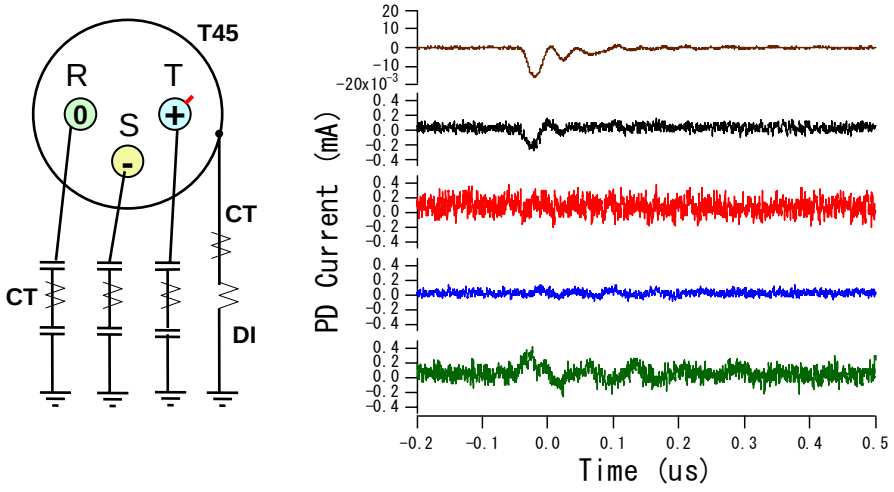

68

PD MEASUREMENT T225

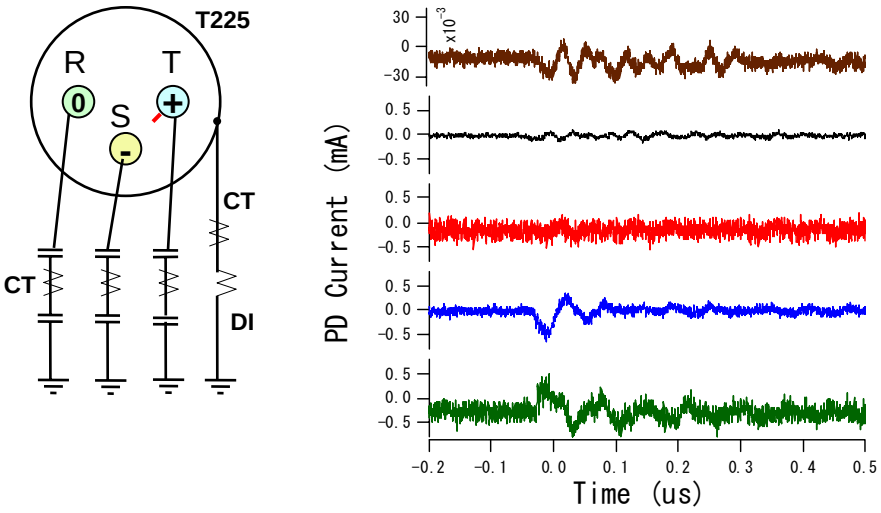

69

PD MEASUREMENT T180

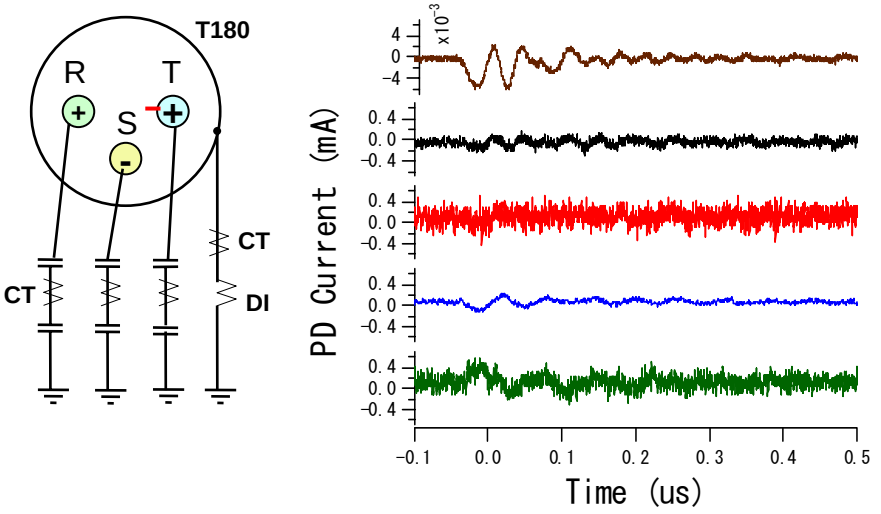

70

PD MEASUREMENT T135

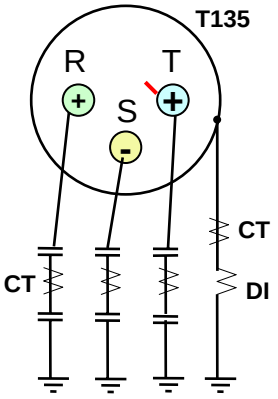

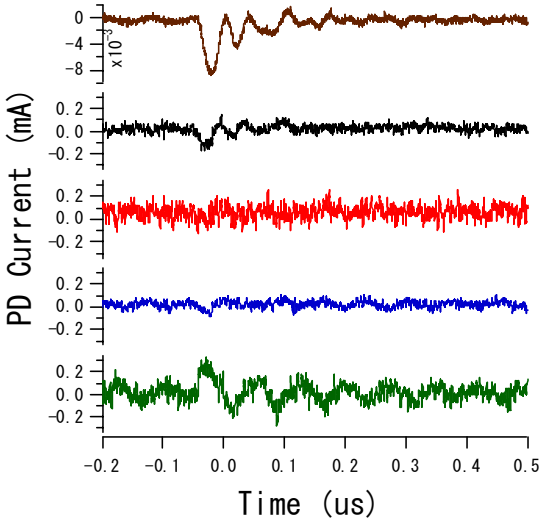

71

PD MEASUREMENT R45

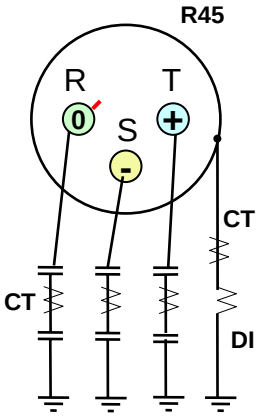

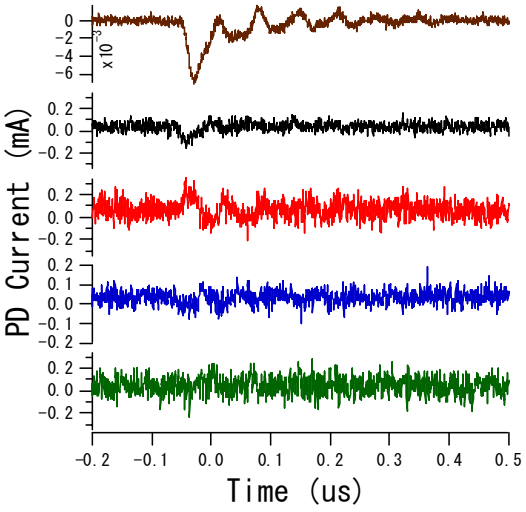

72

PD MEASUREMENT R0

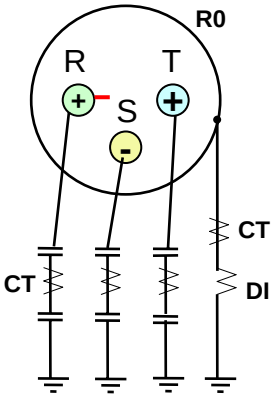

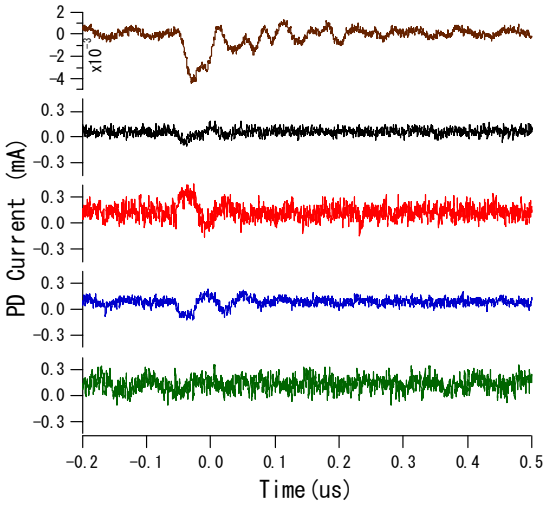

73

PD MEASUREMENT R315

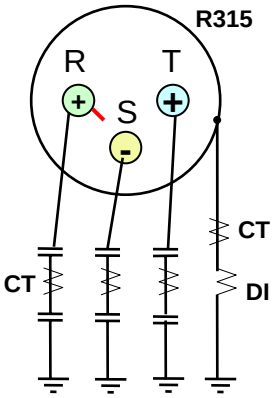

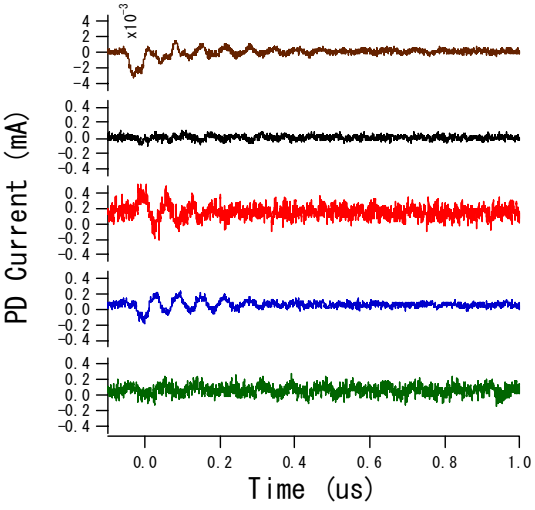

74

PD MEASUREMENT R270

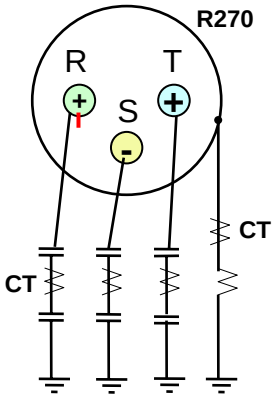

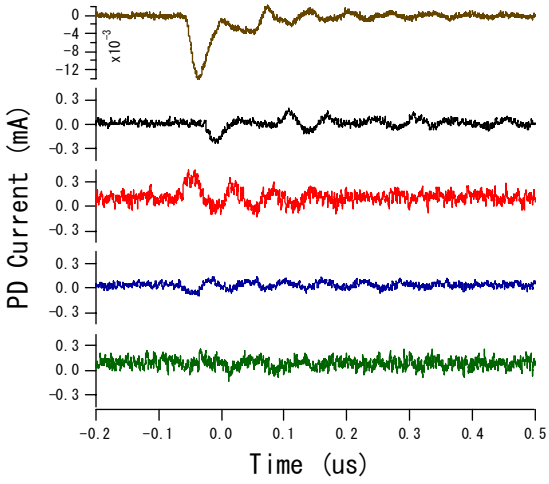

75

PD MEASUREMENT R225

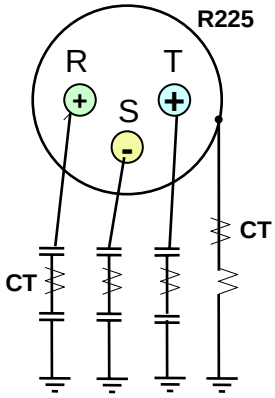

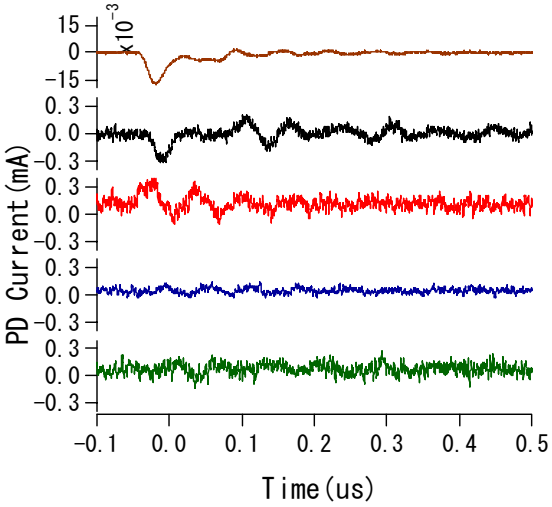

76

PD MEASUREMENT R135

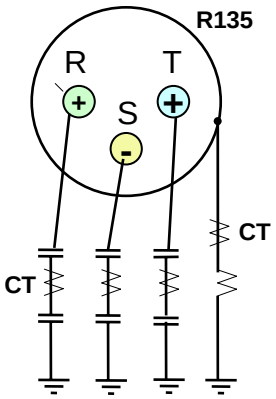

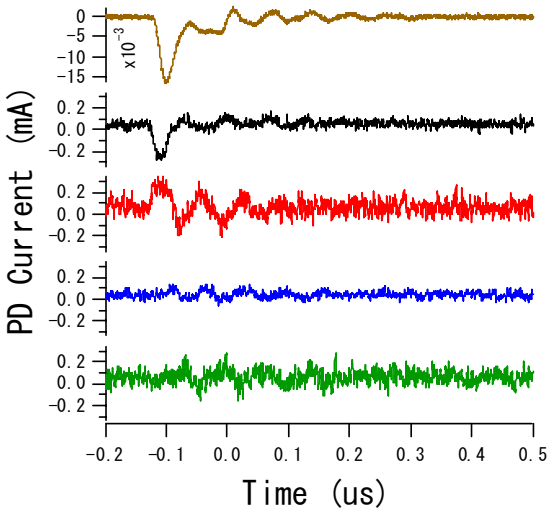

77

PD MEASUREMENT E0

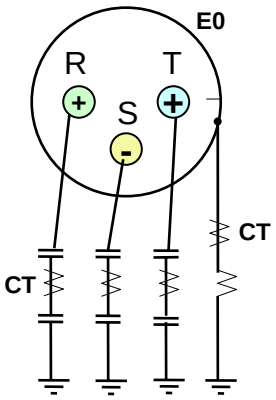

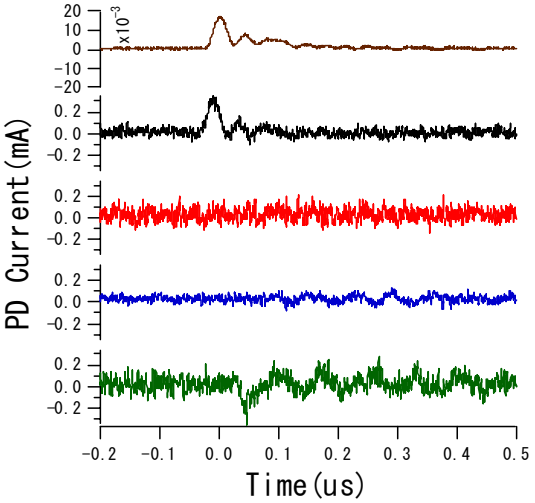

78

PD MEASUREMENT E270

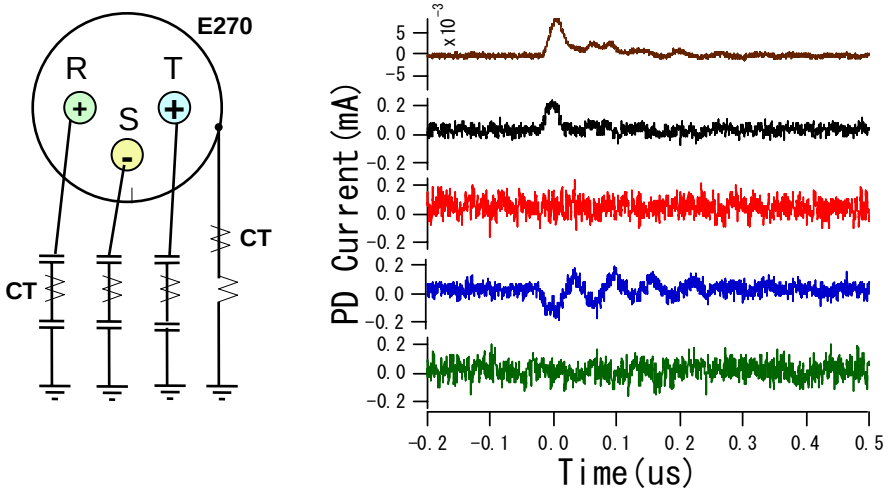

79

PD MEASUREMENT E180

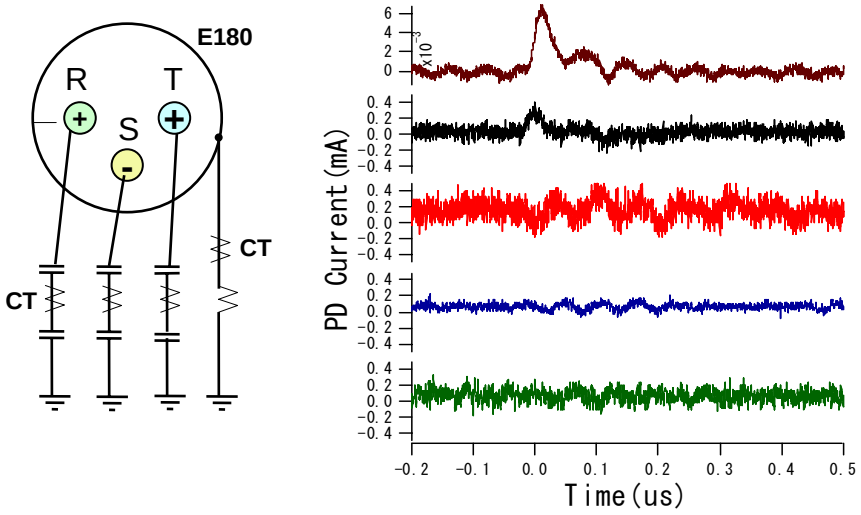

80

APPENDIX IV

PD MEASUREMENT RESULT II
(GIS MODEL I)

PD MEASUREMENT DATA:

1. Frequency Spectrum of PD Current
2. ϕ, q, n pattern
3. PD current waveform
4. Light emission of PD

PARTICLE POSITION:

1. Floating F2;
2. S45,
3. S90

81

The **PURPOSE** of the present experiment
Investigation of PD characteristics in the region having high eccentricity

82

PARTICLE POSITION OBSERVATION POINTS

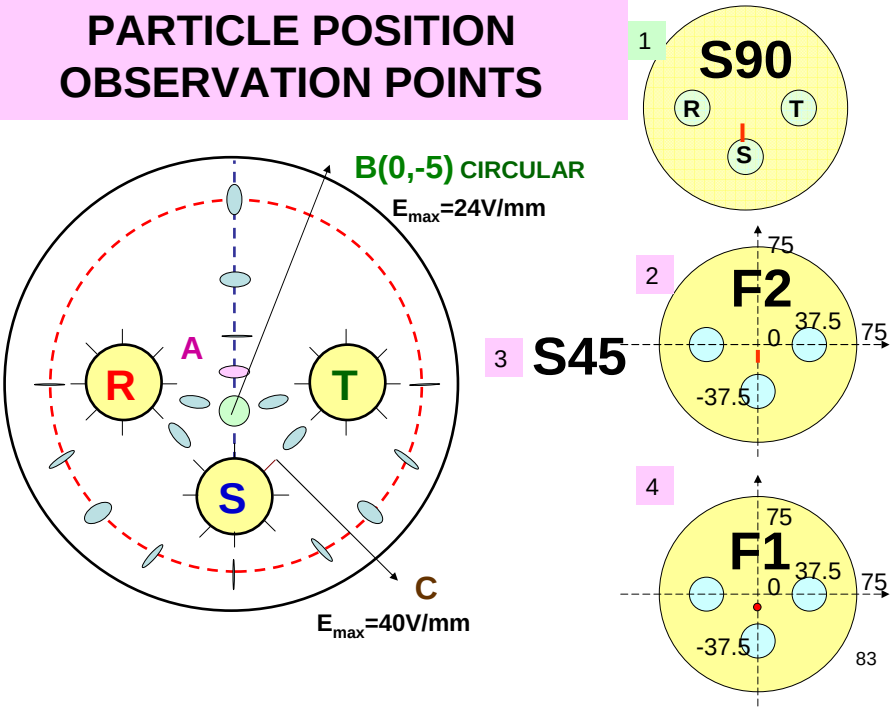

EXPERIMENT SETUP

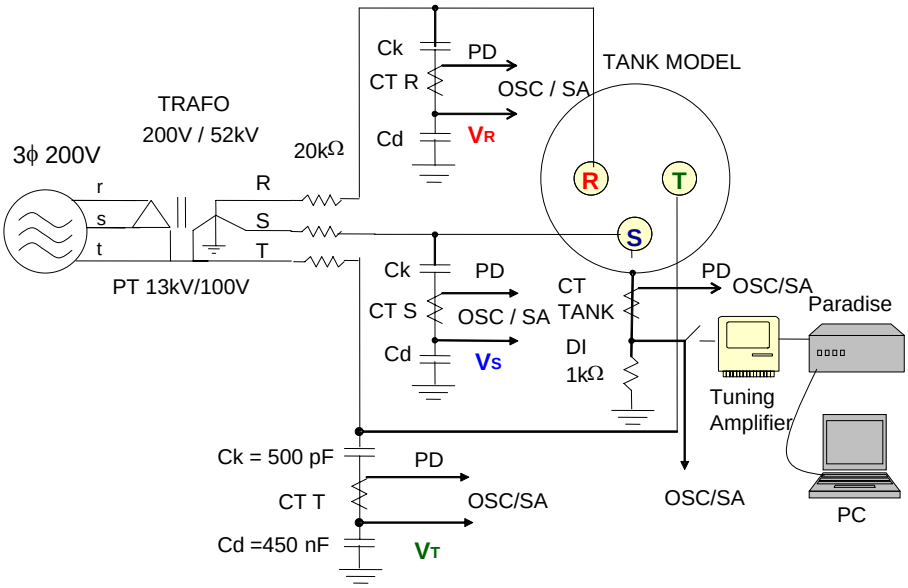

DEFECT POSITION AND CALCULATION POINTS (FLOATING F2)

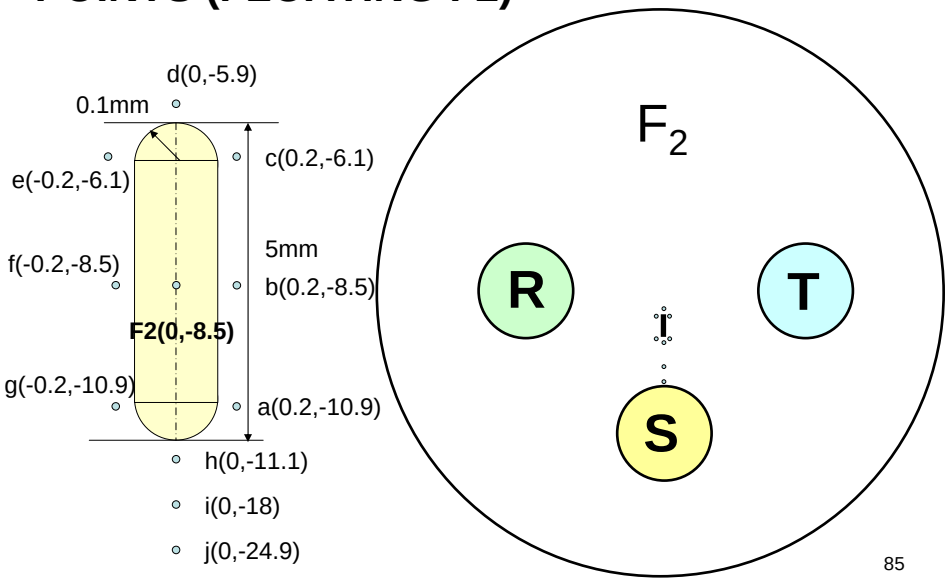

85

1. Spectrum Frequency of Id F2

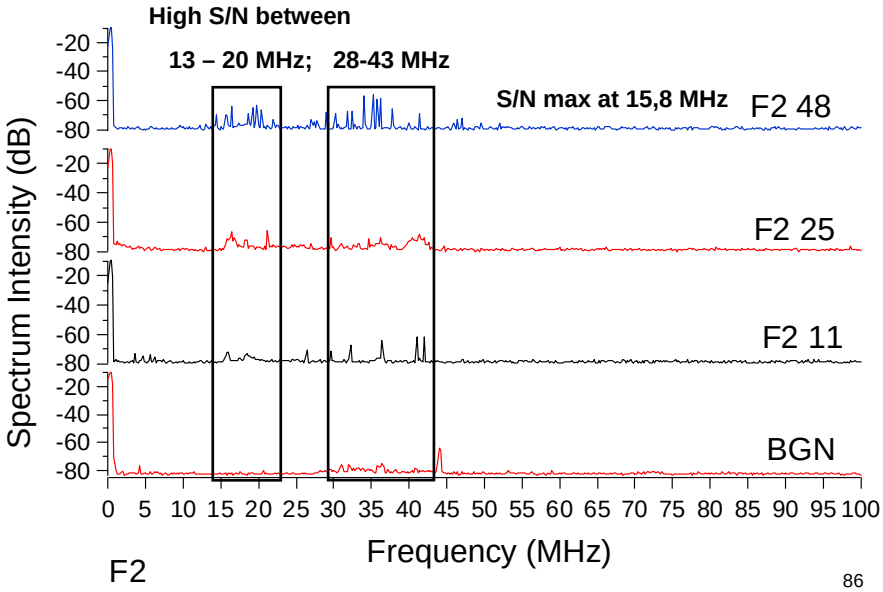

86

2. PD PATTERN F2

There is a little difference in Δ between OSCILLOSCOPE and PARADISE results

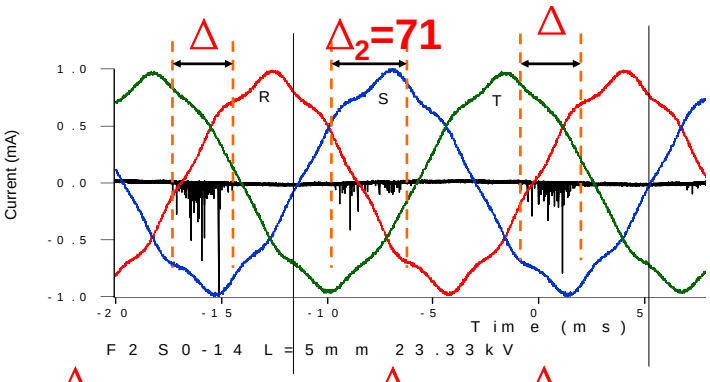

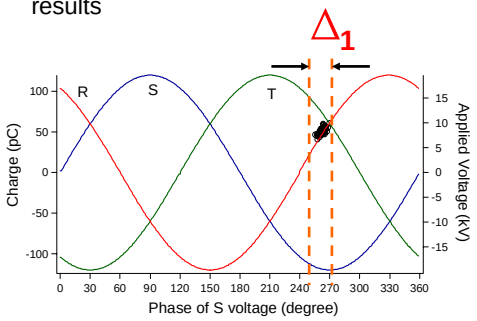

$\Delta_1 = 15^o$

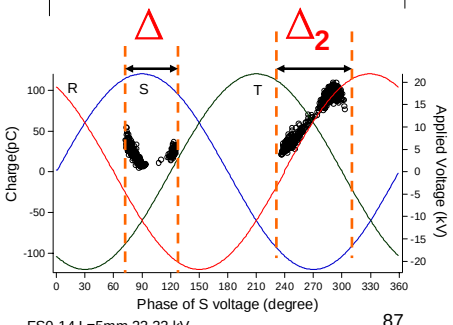

$\Delta_2 = 66^o$

87

Change of PD waveform with applied voltage F2

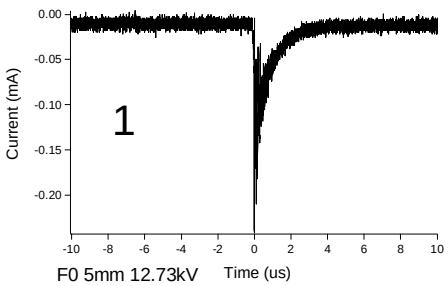

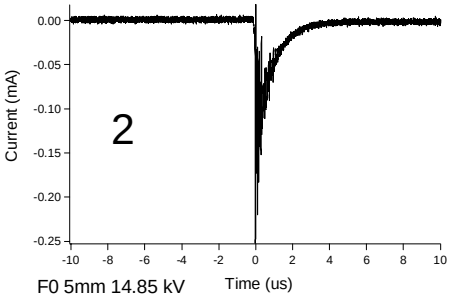

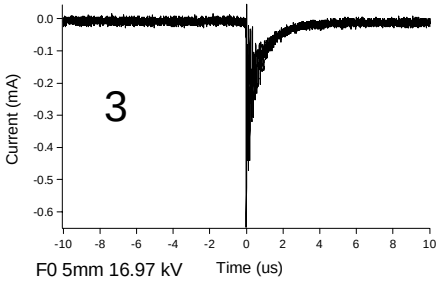

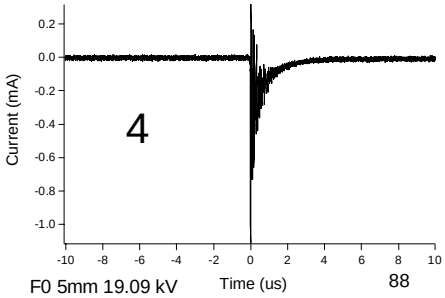

88

Light emissions of PD F2

1

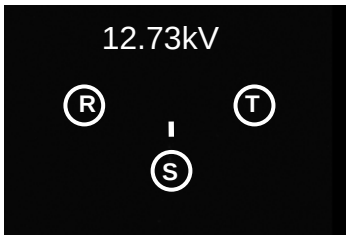

2

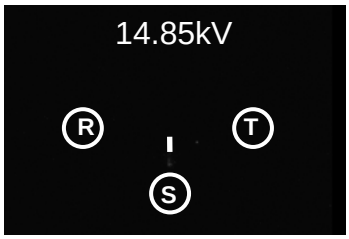

3

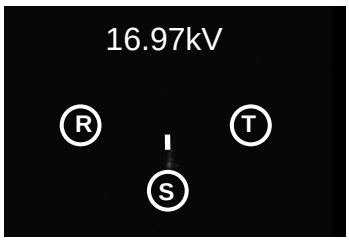

4

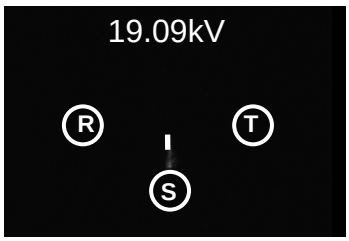

The light emission appears on the conductor 1, 2, 3

The light emission appears on the particle 4

89

DEFECT POSITION AND EXPERIMENT RESULTS (S45)

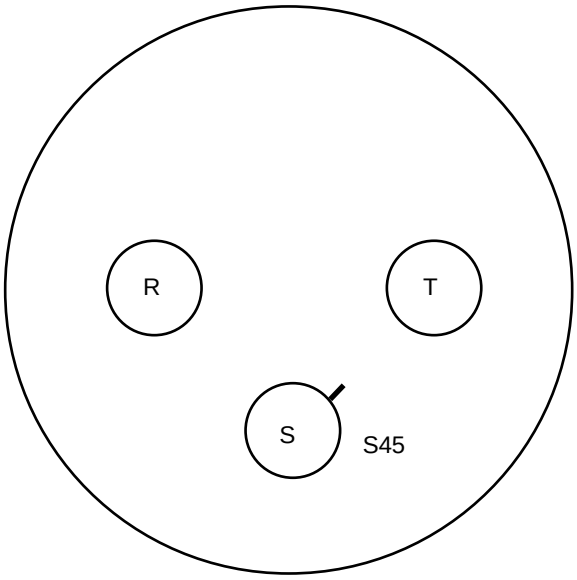

90

1. PD waveform S45

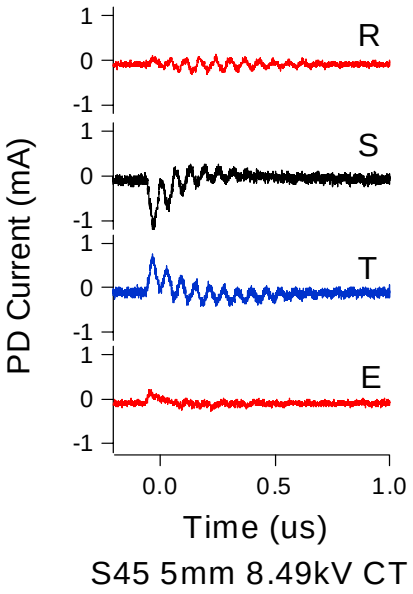

S45 5mm 8.49kV CT

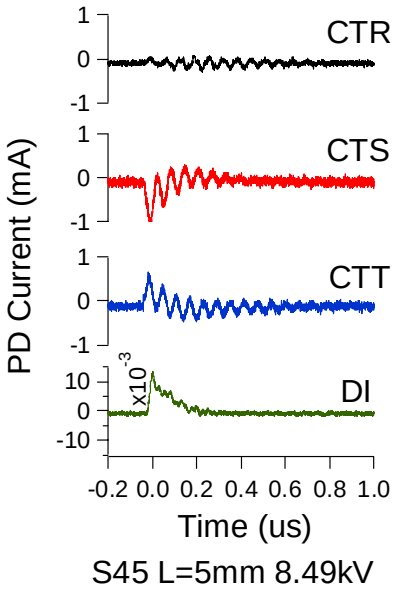

S45 L=5mm 8.49kV

91

Phase dependence S45

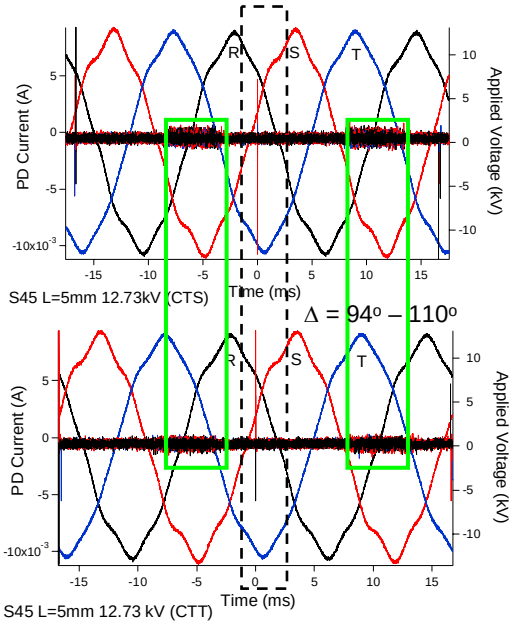

PD pulses consist of sequences of small pulses and single big pulse

PD Measurement using **CTS and CTT** gave same results in the term:

- Phase width where PD pulses appears
- Phase of PD occurrence

Δ = 94º – 110º

ϕ = around S240 or R0

92

S45

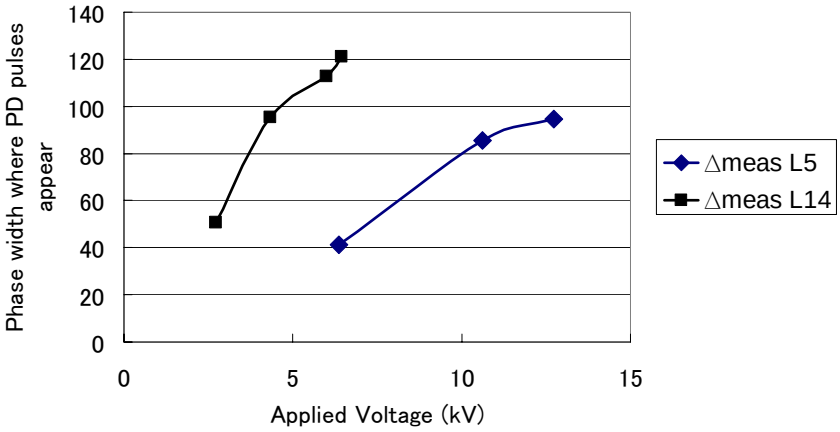

93

Φ, q, n pattern S45 at f=15.8 MHz

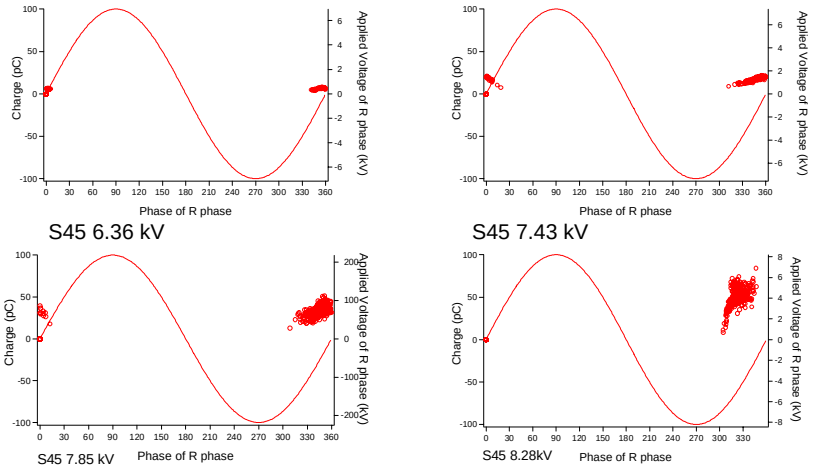

94

Φ, q, n pattern S45 at f = 15.8 MHz

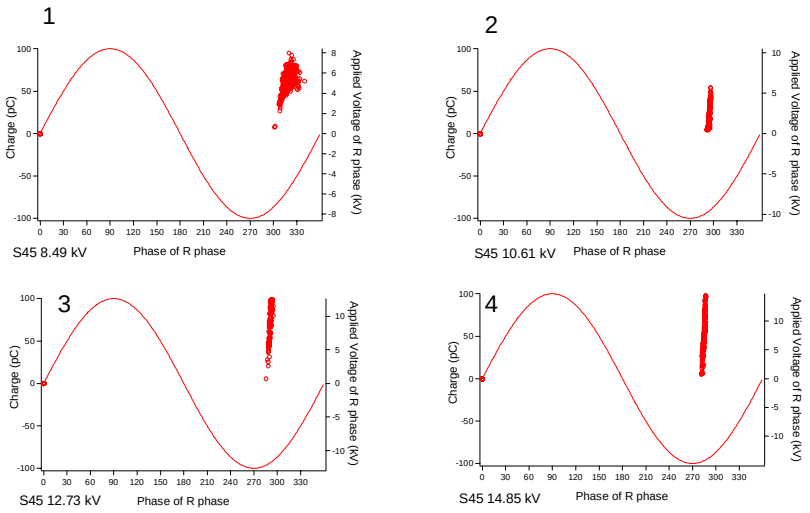

95

Change of PD waveform with applied voltage S45

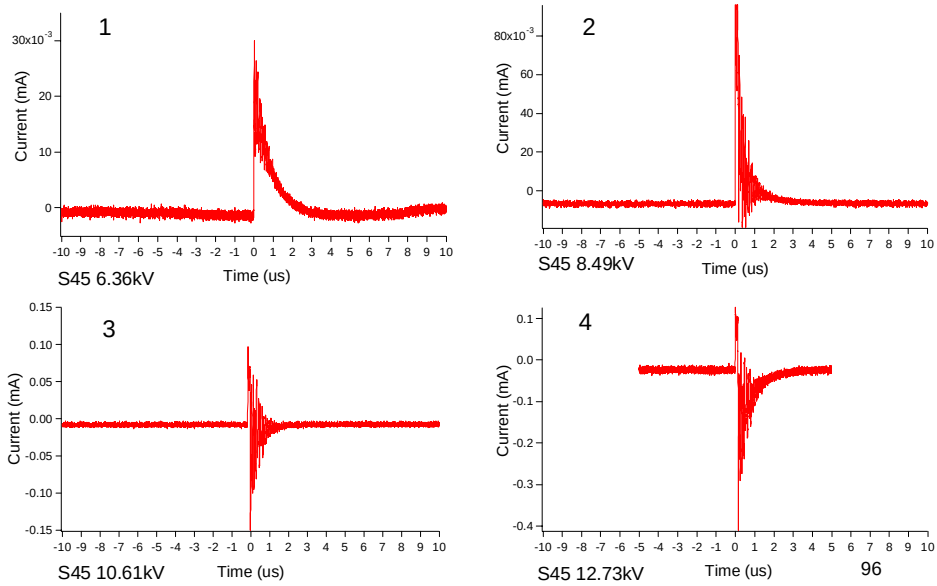

96

Light emissions of PD S45

1

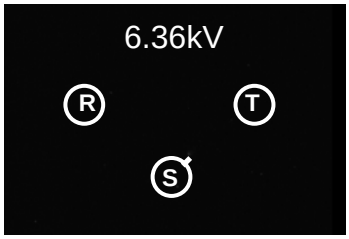

2

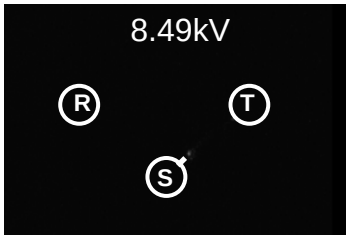

3

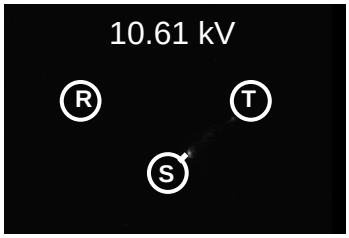

4

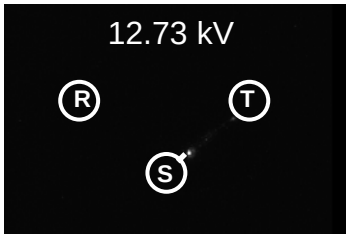

The change in PD waveform is related to the change in PD mechanism

When the light emission appears in the other electrode, the waveform change

97

Light emissions of PD S45

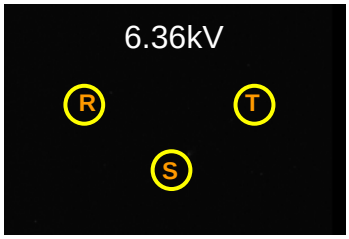

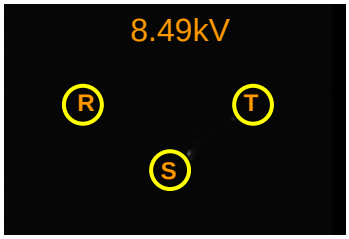

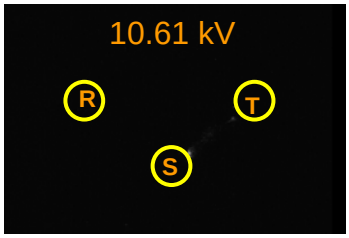

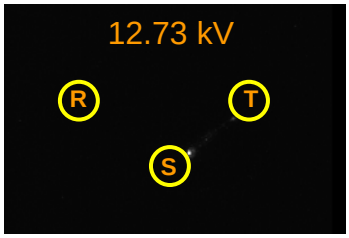

98

DEFECT POSITION AND EXPERIMENT RESULTS (S90)

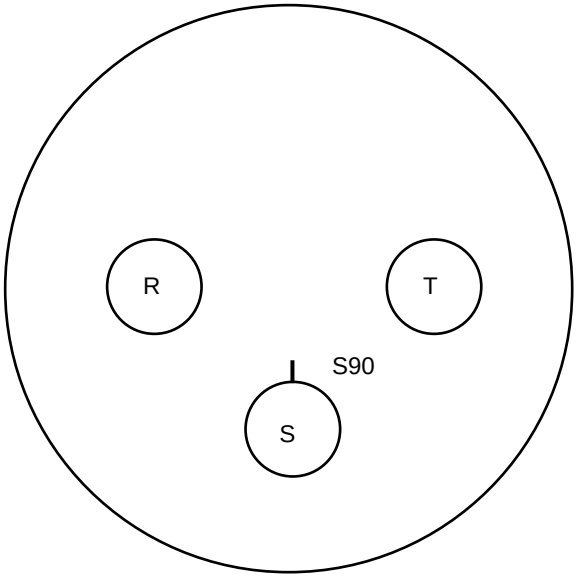

99

Spectrum Frequency of Id

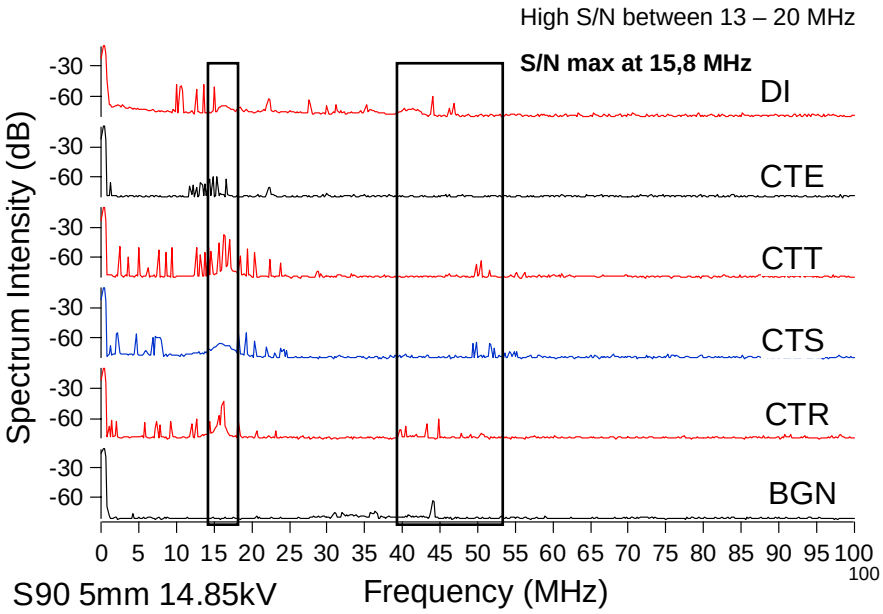

100

DEFECT POSITION AND CALCULATION POINTS (S90)

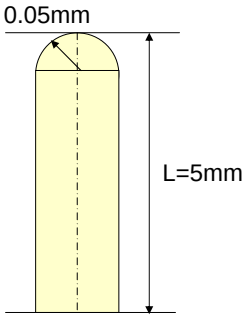

a(0.56,-20.05)	a(0.56,15.05)	a(0.56,10.05)	a(0.56,5.05)
b(0,-19.9)	b(0,-14.9)	b(0,-9.9)	b(0,-4.9)
c(-0.56,-20.05)	c(-0.56,15.05)	c(-0.56,10.05)	c(-0.56,5.05)
d(0,-5)	d(0,-5)	d(0,-5)	d(0,-5)
e(0,0)	e(0,0)	e(0,0)	e(0,0)

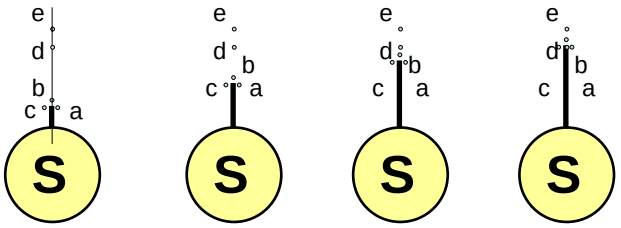

L=5mm L=10mm L=15mm L=20mm

101

S90 measurement

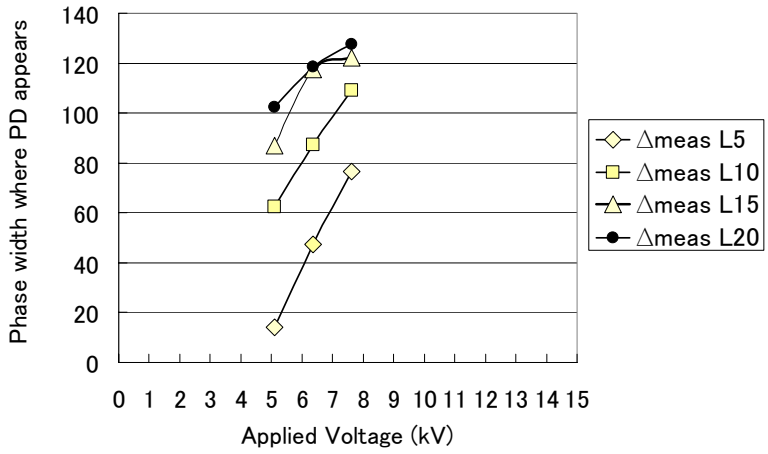

102

APPENDIX V

DESIGN AND CONSTRUCTION OF EXPERIMENTAL SYSTEM II

103

SKETCH OF THREE-PHASE GIS MODEL

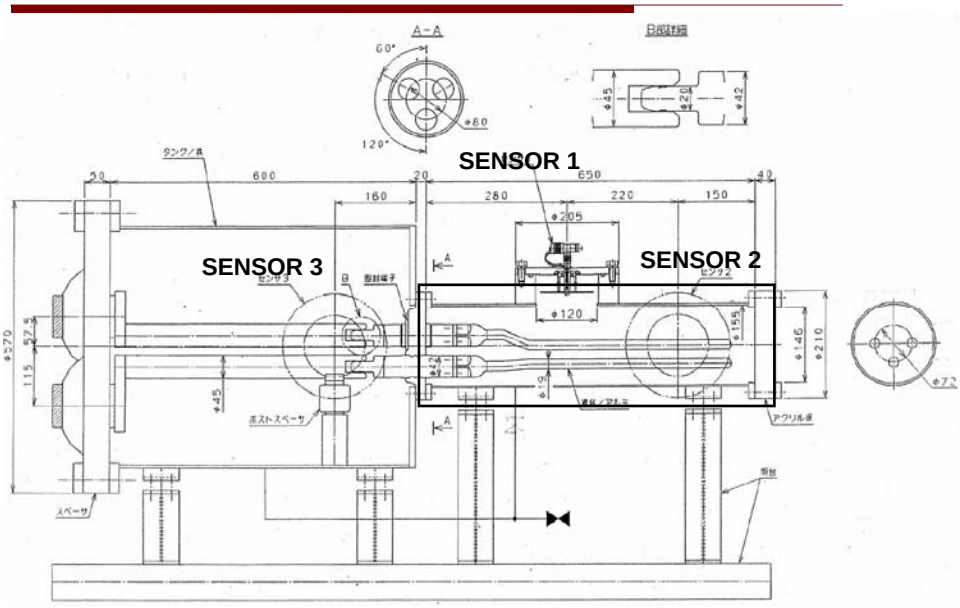

Figure 1 Sketch of 3-phase GIS model

104

THREE-PHASE GIS MODEL II

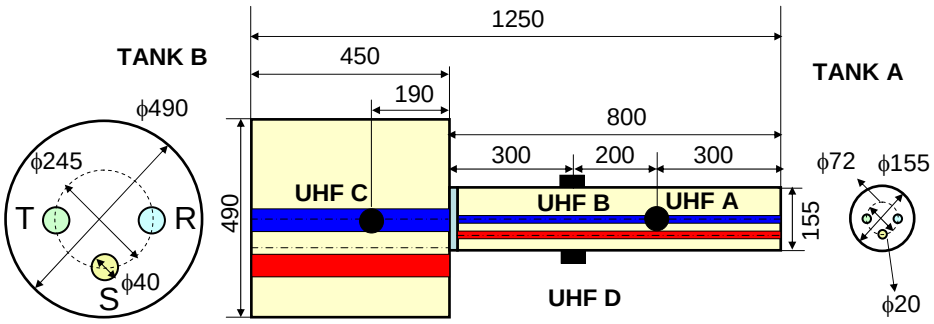

Figure 2 Lay out of three-phase GIS Model

105

EXPERIMENTAL SETUP II

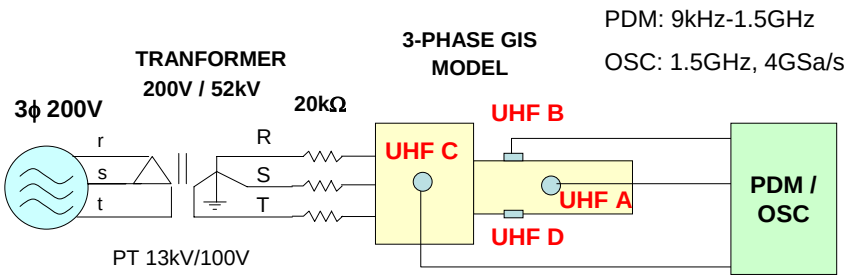

Figure 3 Equivalent Circuit of Experimental Equipment

106

PHOTOGRAPH OF EXPERIMENTAL EQUIPMENT II

1:5 SIZE OF

275kV THREE-PHASE GIS MODEL

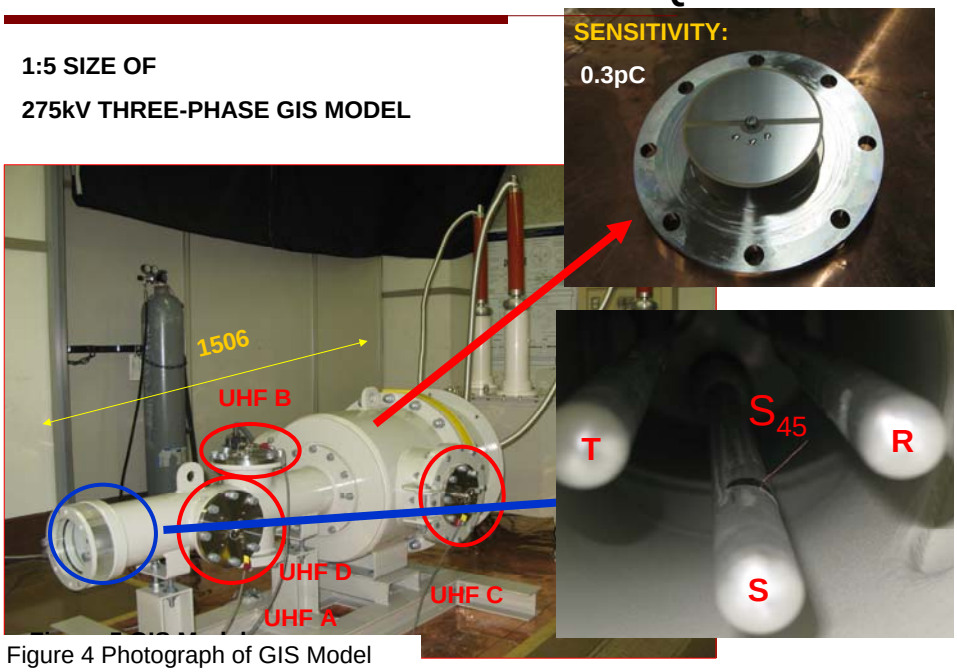

Figure 4 Photograph of GIS Model

LAYOUT

A. 3相変圧器
B. 3相GIS MODEL
C. COOPER SHEET
D. SF_6 GAS TUBE
E. PUMP
F. GAS PIPE 1
G. GAS PIPE 2
H. GAS OUTLET
K. CABLE DUCT

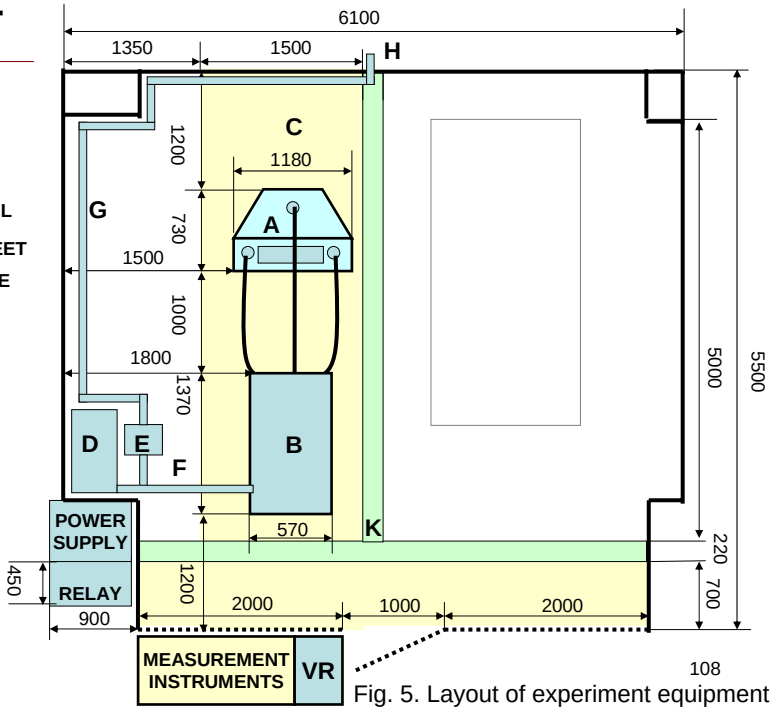

Fig. 5. Layout of experiment equipment

DIAGRAM OF POWER SUPPLY, CONTROL AND PROTECTION EQUIPMENT

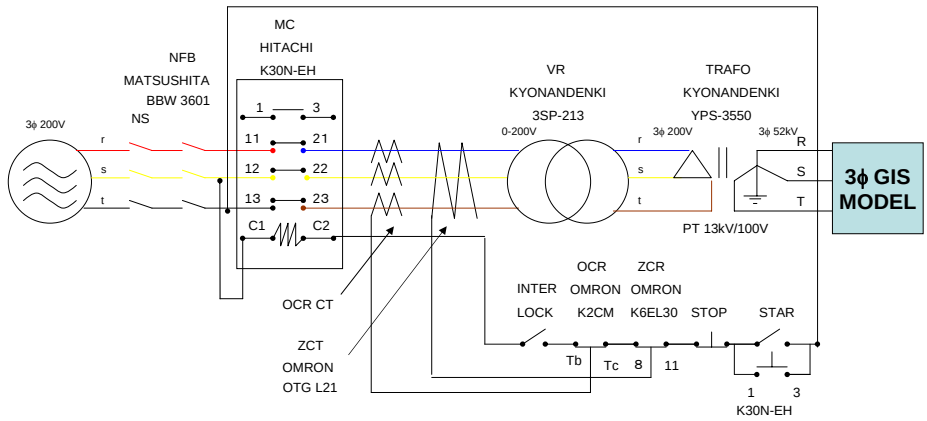

Figure 6 Three Phase Equivalent Circuit of Experimental Circuit

109

OPERATION SEQUENCES OF CONTROL AND PROTECTION SYSTEM

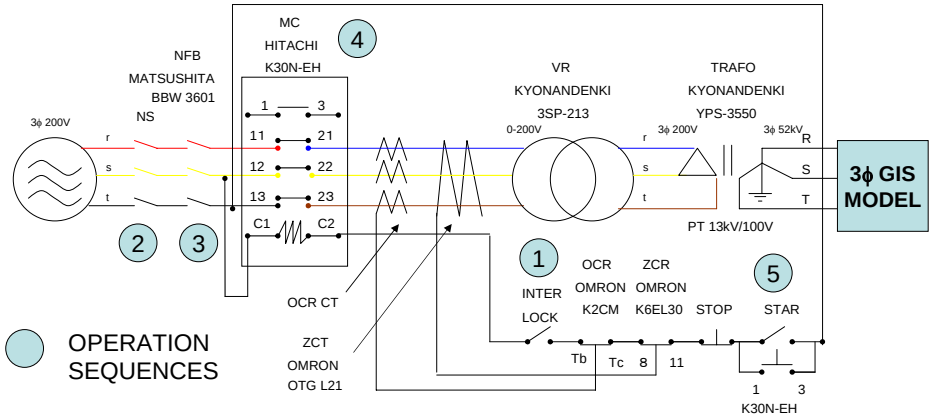

Figure 7 Three Phase Equivalent Circuit of Experimental Circuit and Operation Sequences

110

CALCULATION OF SHORT CIRCUIT CURRENT

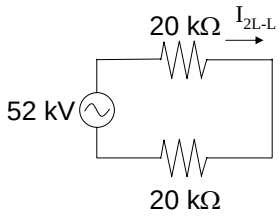

a. Line-Line

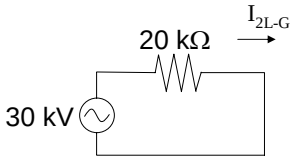

b. Line-Ground

Figure 8 Equivalent Circuit of Secondary Side of Experimental Circuit at Short Circuit Condition

Secondary Side $I_{2_{L\text{-}L}} = \frac{52000[V]}{40000[\Omega]} = 1.3[A]$ < $I_{2_{L\text{-}G}} = \frac{30000[V]}{20000[\Omega]} = 1.5[A]$

Primary Side $I_1 = 1.5[A] \times \frac{52000[V]}{200[V]} = 390[A]$

111

SETTING OF OVER CURRENT RELAY

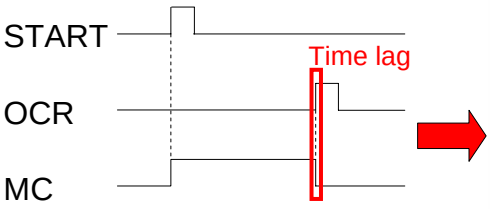

Figure 9 Time chart of OCR operation

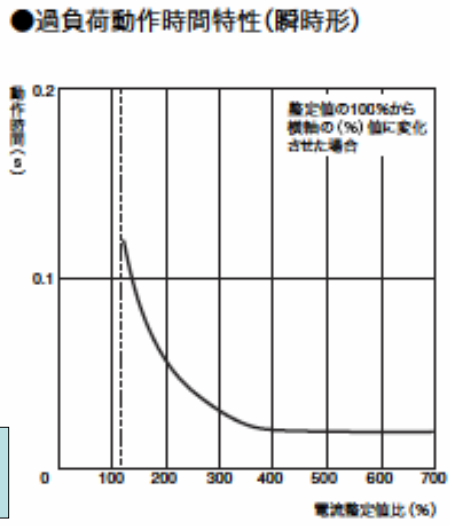

Figure 10 Current time characteristic of OCR

Rating current of cable is 30 A
Over current relay is set at 8 A

115 % (9.2 A) 120ms (7.2 cycles)
400 % (32 A) 20ms (1.2 cycles)

112

Zero Current Relay (ZCR)

- Balance Condition

  $I_R + I_S + I_T = 0$

- Unbalance Condition

  $I_R + I_S + I_T = I \neq 0$

ZCR works if $I \geq 30$ mA

Figure 11 ZCR Relay

113

VACUUM EVACUATION AND GAS SUPPLY SYSTEM

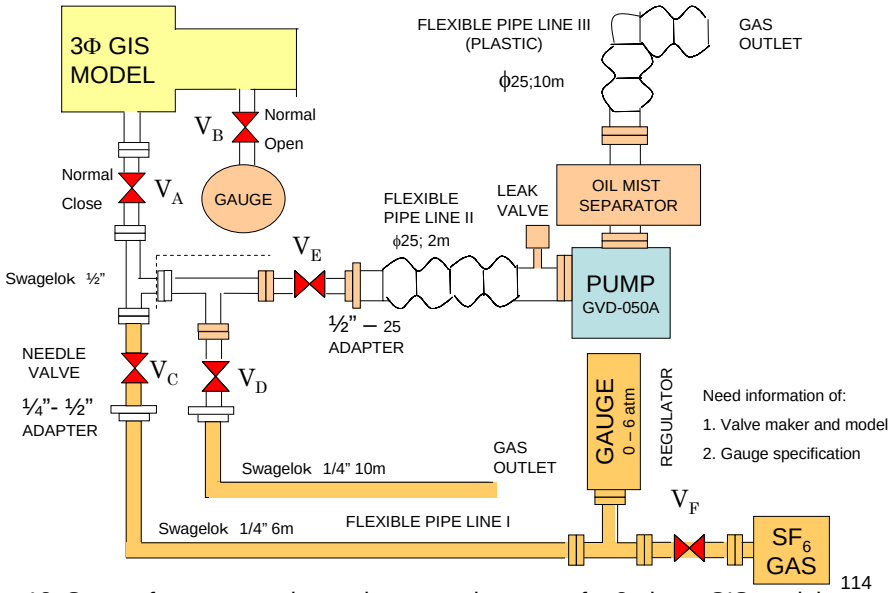

Fig. 12. Setup of gas evacuation and gas supply system for 3-phase GIS model

114

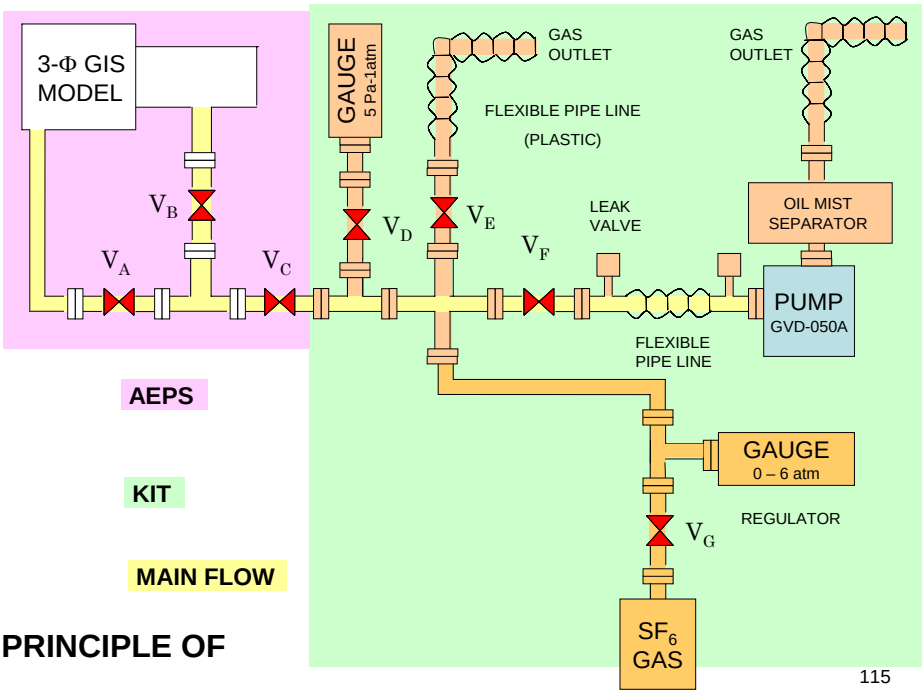

115

PRINCIPLE OF

VACUUM EVACUATION AND GAS SUPPLY SYSTEM

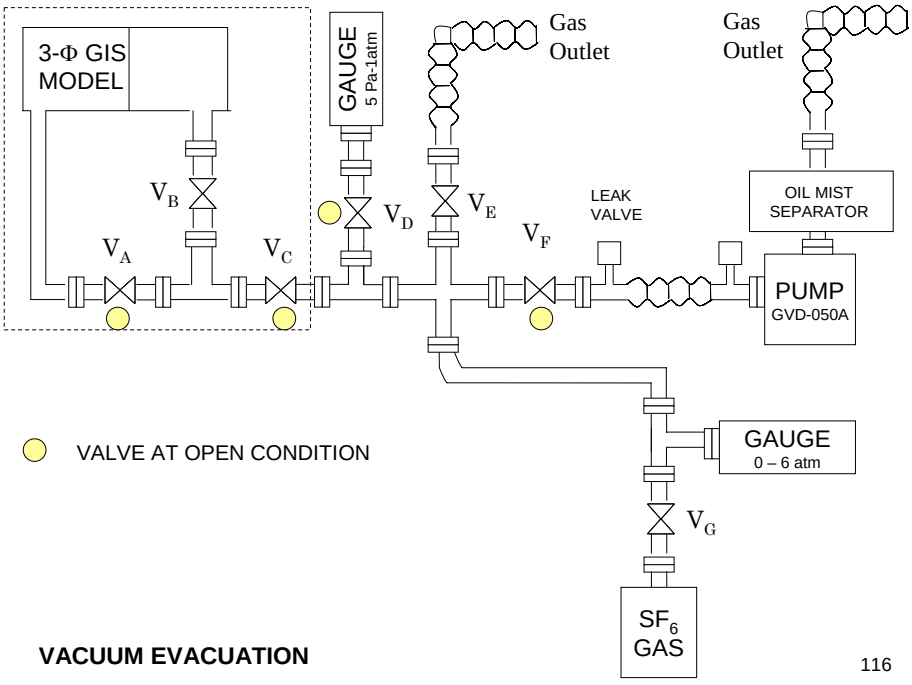

VACUUM EVACUATION

116

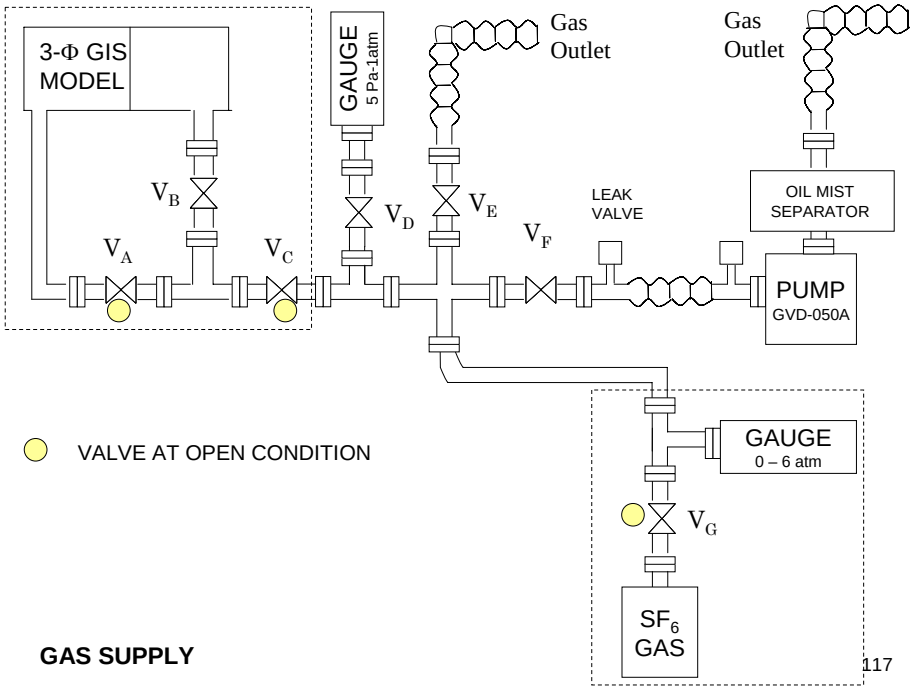

GAS SUPPLY

117

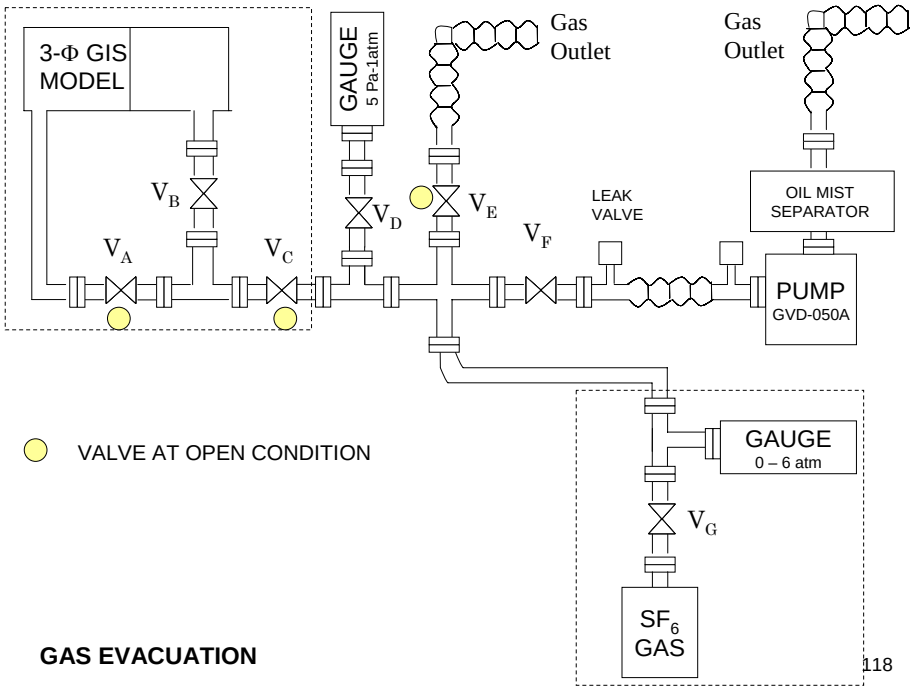

GAS EVACUATION

118

GAS / AIR EVACUATION

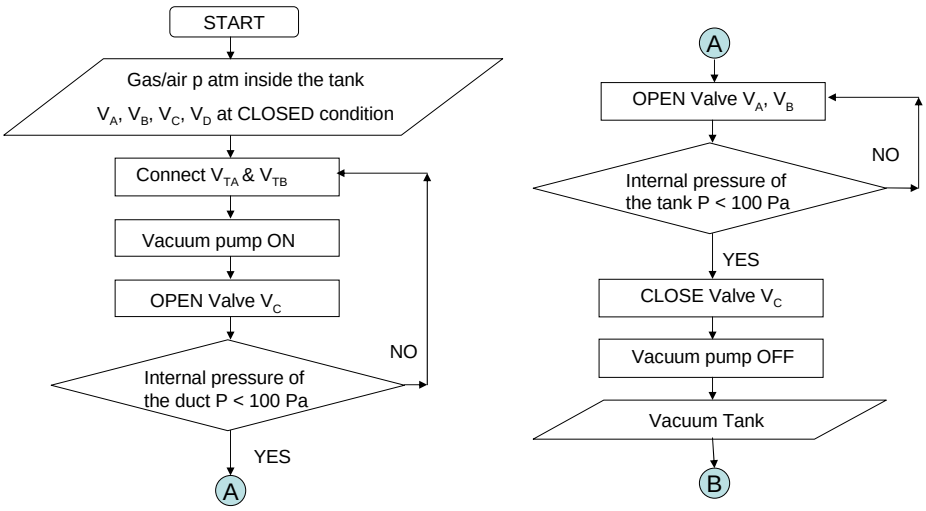

Flowchart of gas / air evacuation

119

SF_6 GAS SUPPLY

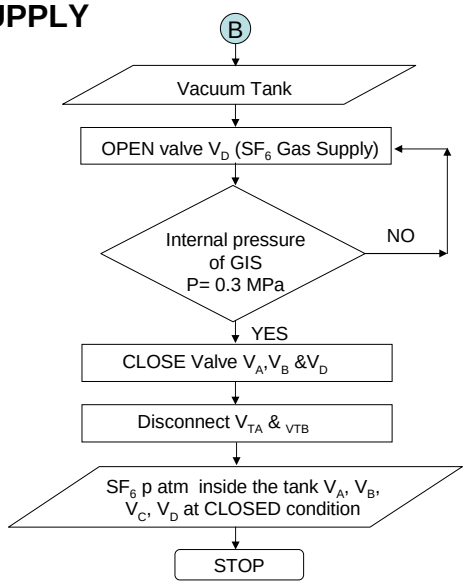

Flowchart of gas supply

120

APPENDIX VI

DATA OF EXPERIMENTAL RESULTS OF GIS MODEL II

121

EXPERIMENT- PDIV TEST

- Particle S45 L=20mm;
- Gap length g =11mm

- At p=1 atm, PDIV=24 kV
  No breakdown until 36 kV

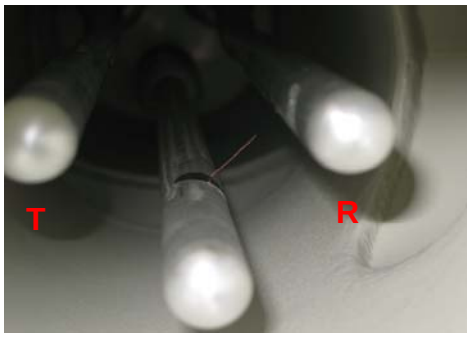

- At p=3 atm, 2.5 atm, 2 atm, 1.5 atm,
  PD did not occur until 36 kV (70% Vmax)

The gap length was reduced until about 5 mm

122

PARTICLE POSITION AND NOTATION

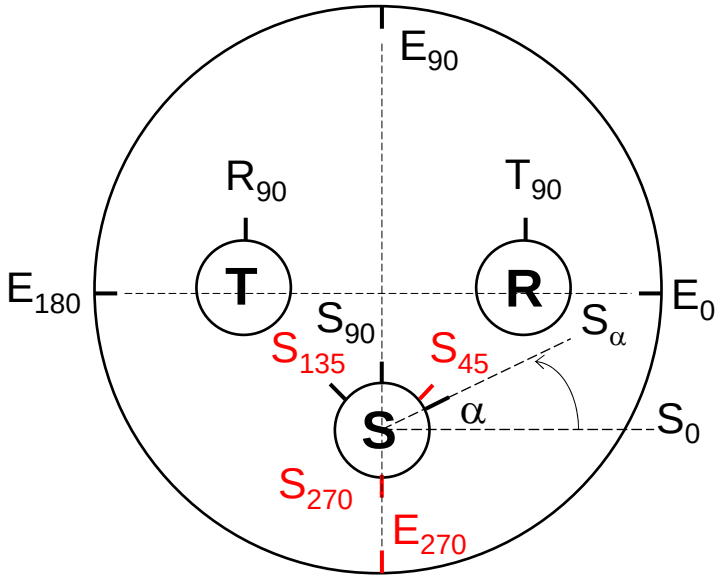

123

Figure 1 Particle Position and Notation

Table 1 Type and shape of particles

Particle Type	Particle on HVC	Particle on the tank
Position	S45, S135, R225, S90 (phase-phase) R0,S270 (phase-phase)	E270 (phase-tank)
Diameter (mm)	0.1	0.1
Length (mm)	27	27
Gap Length (mm)	4	4.5
Material	copper	copper

124

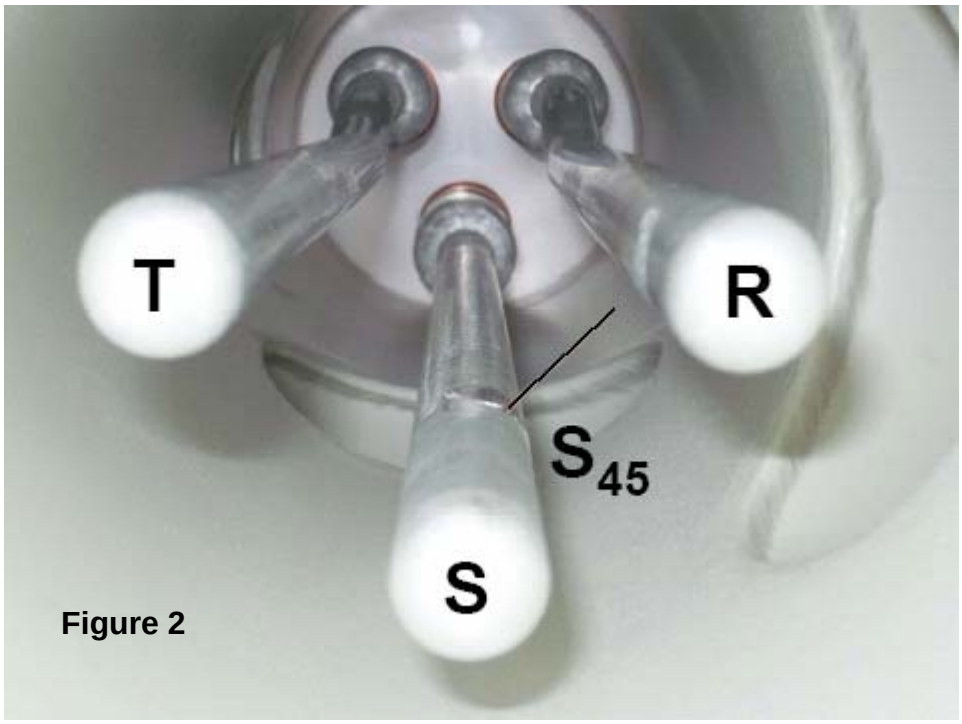

Figure 2

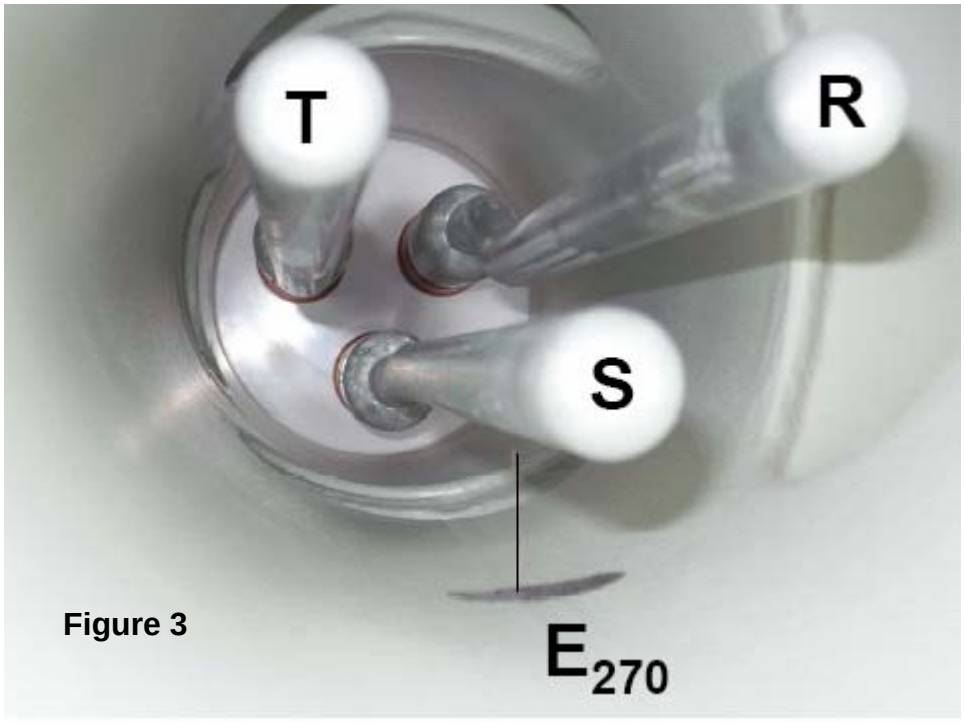

Figure 3

Figure 4

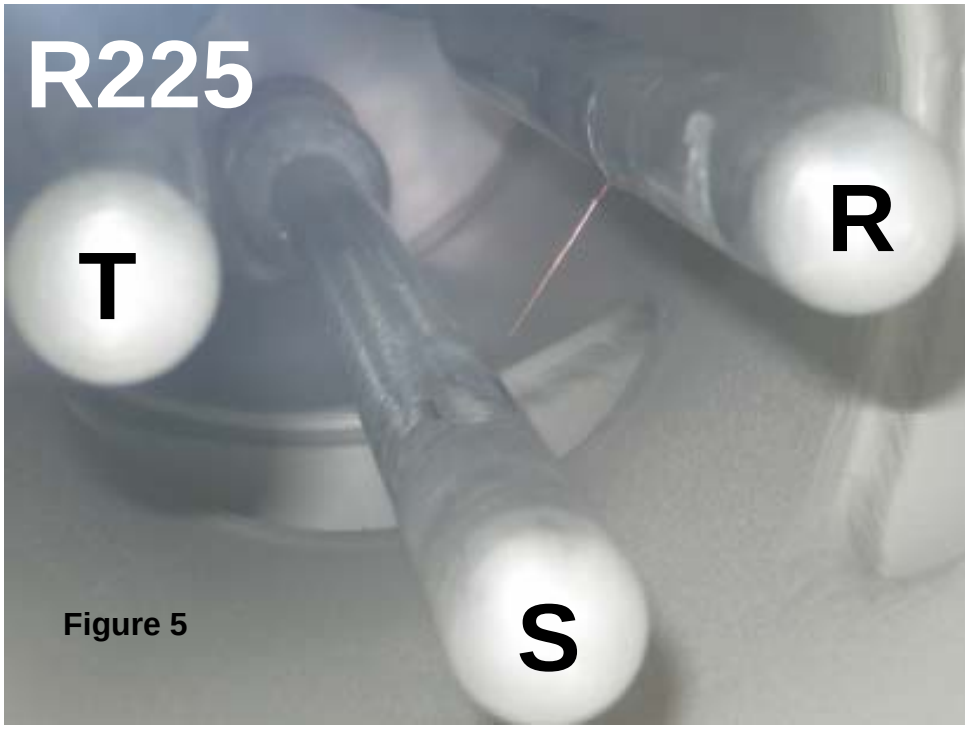

Figure 5

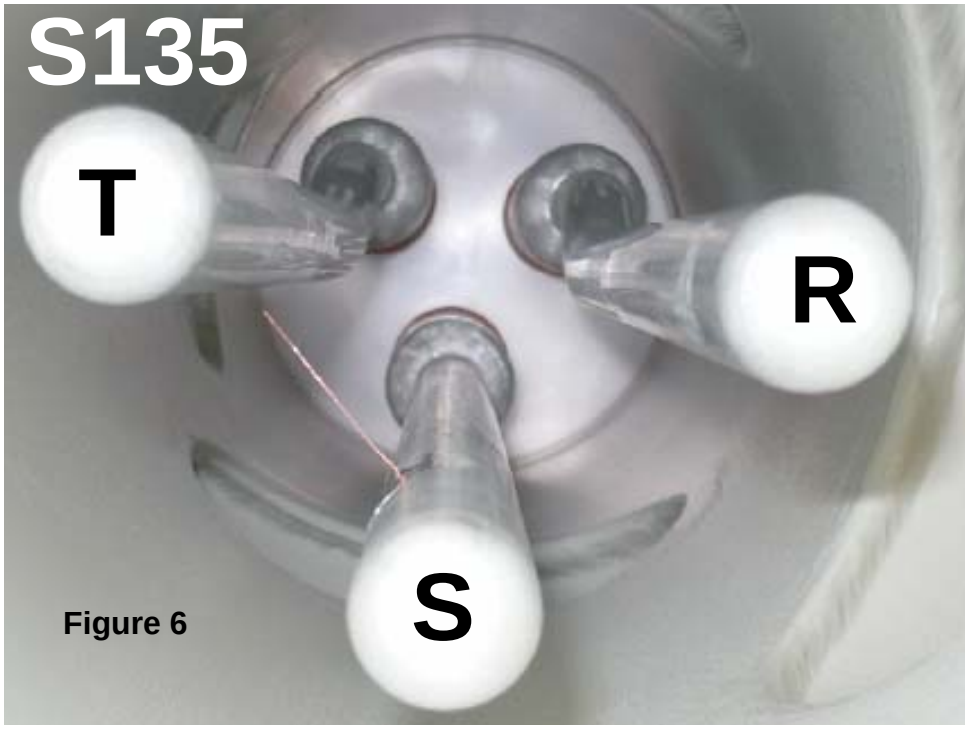

Figure 6

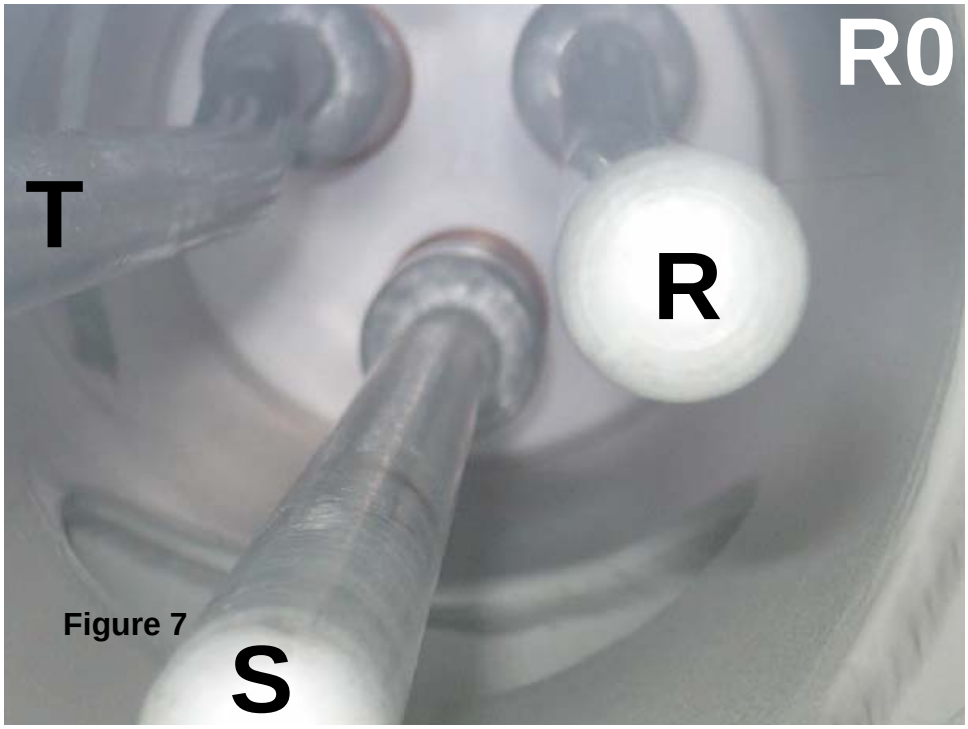

Figure 7

DEFINITION 1: EMW magnitude (Vpp)

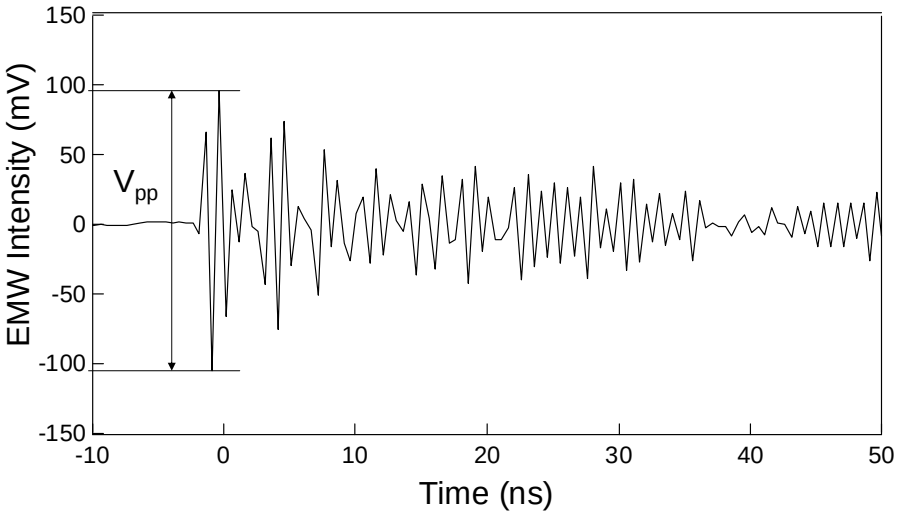

Figure 8 Definition of peak to peak voltage (Vpp) 131

DEFINITION 2: EMW signal duration (t)

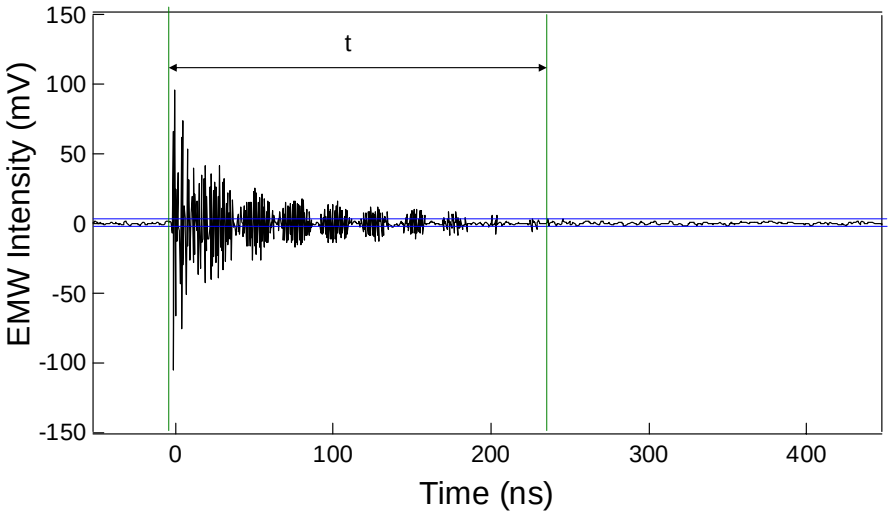

Figure 9 Definition of EMW signal duration (t) 132

PDIV

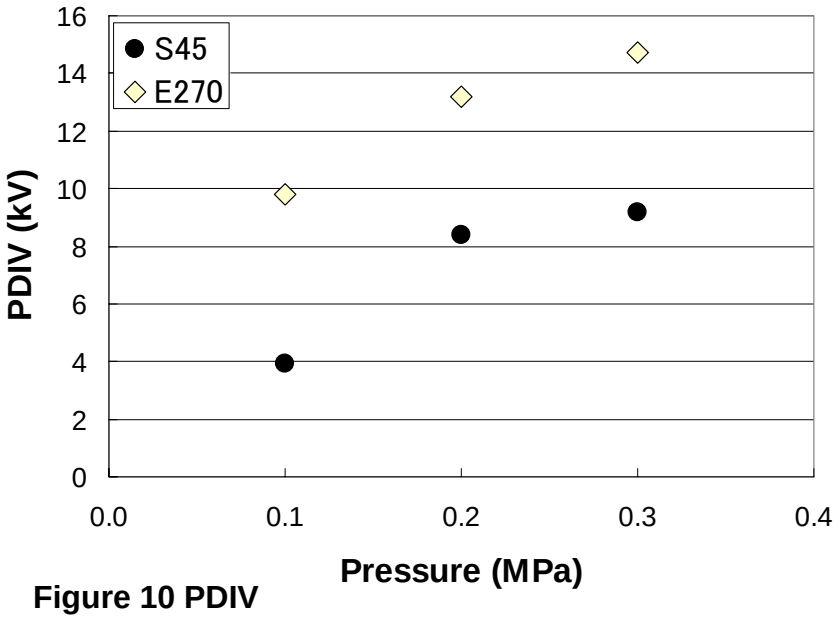

Figure 10 PDIV

133

MEASUREMENT POINTS (MP)

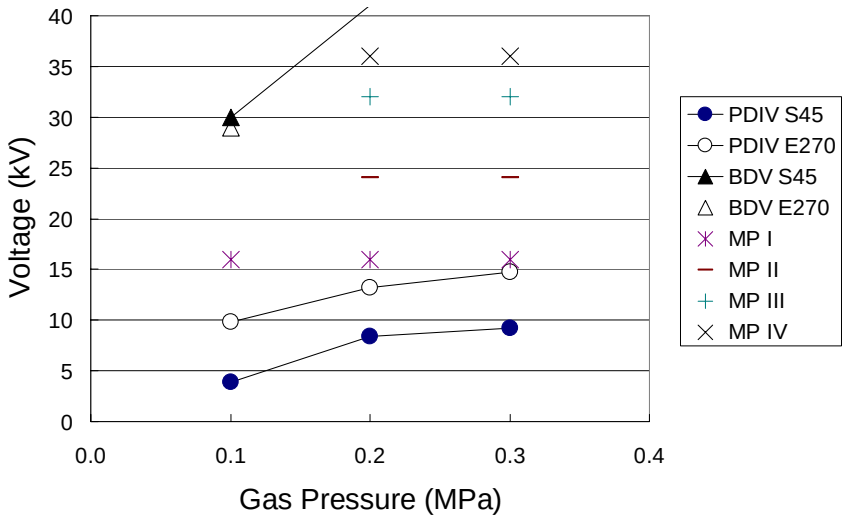

Figure 11 Measurement Points

134

EXPERIMENTAL RESULTS: OBSERVATION OF EMW SIGNALS IN TIME DOMAIN

135

Effect of particle position on EMW signals

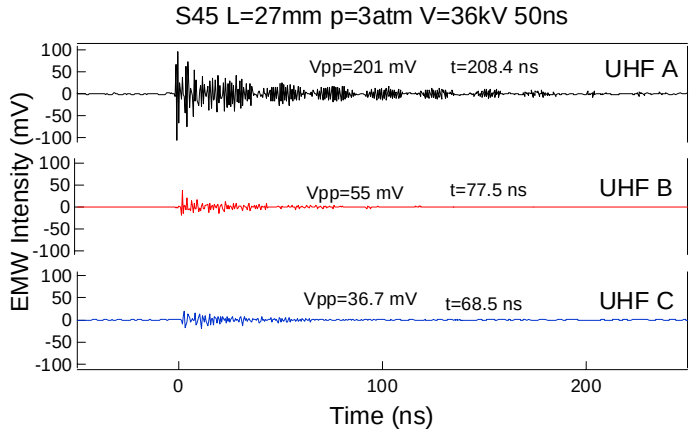

Figure 12 EMW induced by PD on S45 particle

136

Effect of sensor position on EMW signals

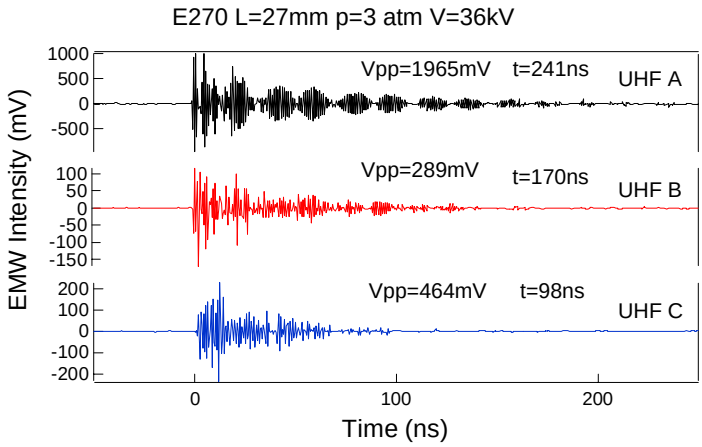

Figure 13 EMW induced by PD on E270 particle

137

Time differences of PD detected in each sensor

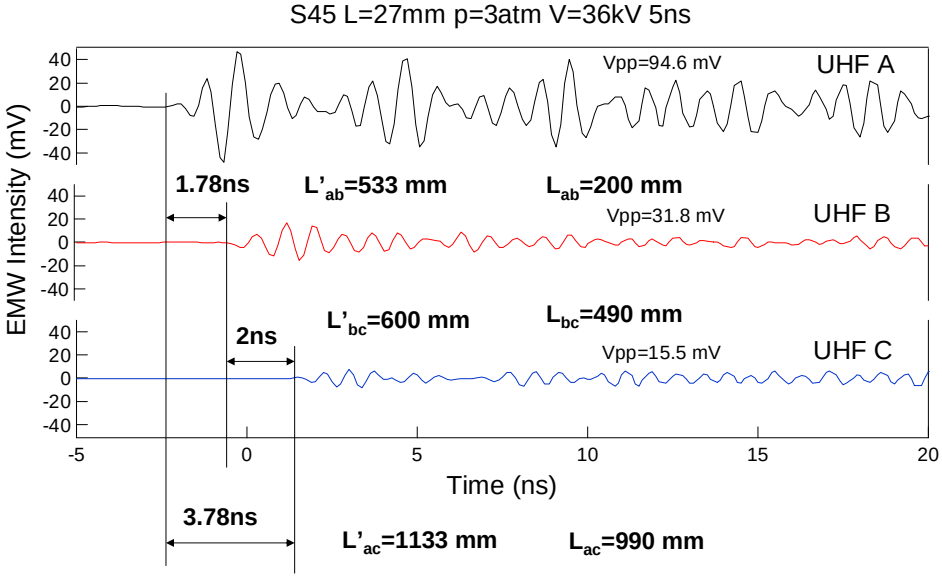

Figure 14 EMW induced by PD on S45 particle

138

Effect of particle position on EMW signals

- S45 p1, p2, p3 16kV, 36kV, UHF A
- E270 p1,p2, p3 16 kV, 36kV, UHF A

Effect of particle position on EMW:

waveform,

magnitude (Vpp), $Vpp_{S45} < Vpp_{E270}$

duration (t), $t_{S45} < t_{E270}$

139

Effect of sensor position UHF A, UHF B, UHF C on EMW signals

- S45 p3 36kV, UHF A,UHF B, UHF C
- E270 p3 36kV, UHF A,UHF B, UHF C

For S45:

EMW Magnitude $V_{pp\,A} > V_{pp\,B} > V_{pp\,C}$

EMW Duration $t_A > t_B > t_C$

For E270:

EMW magnitude $V_{pp\,A} > V_{pp\,C} > V_{pp\,B}$

EMW Duration $t_A > t_B > t_C$

140

Effect of applied voltage on EMW signals

Data: S45 p=1atm, V=4kV, 8kV, 12kV, 16kV

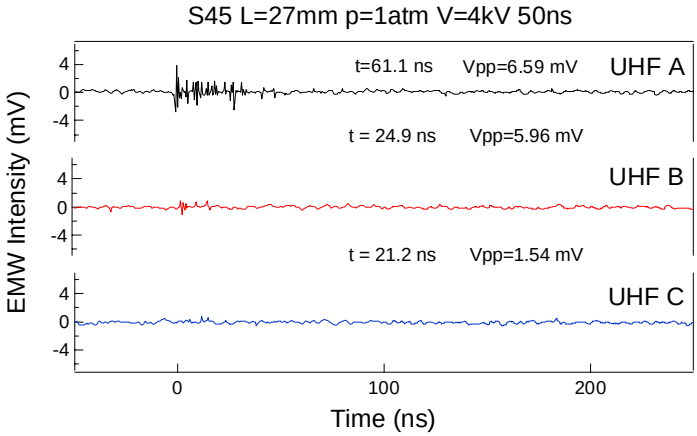

Figure 15 EMW induced by PD on S45 particle

141

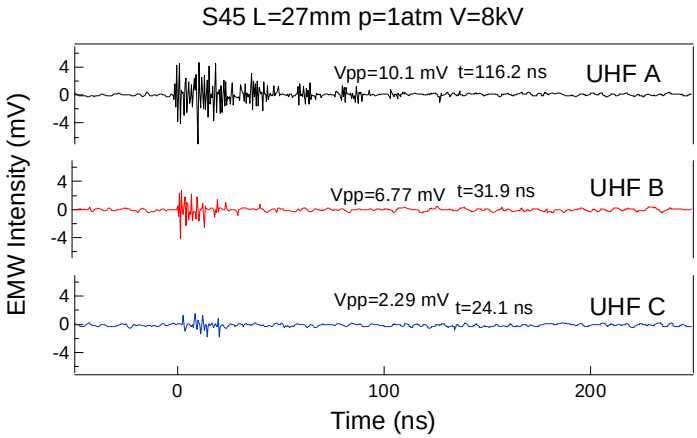

Figure 16 EMW induced by PD on S45 particle

142

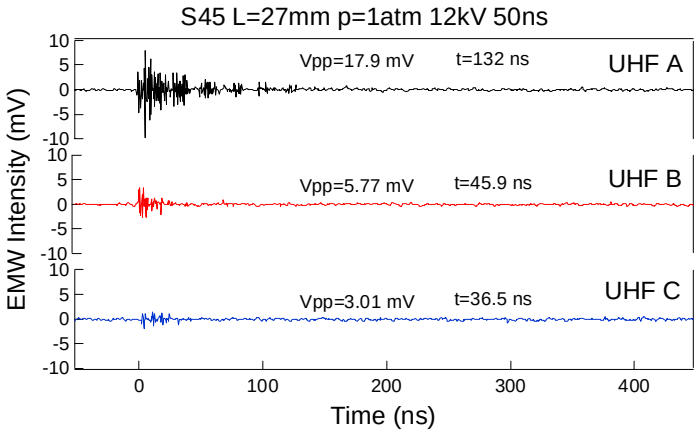

Figure 17 EMW induced by PD on S45 particle

143

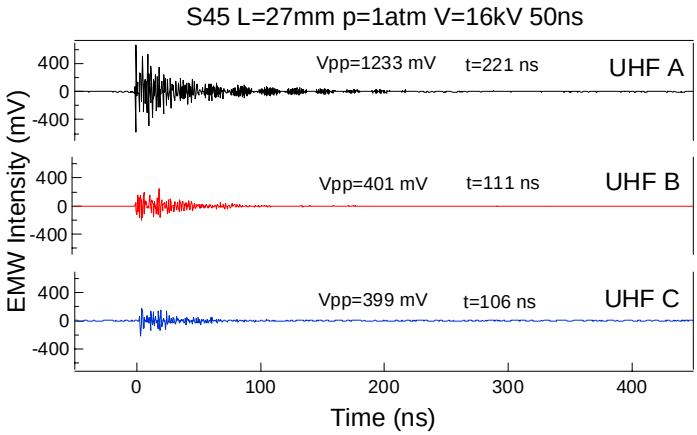

Figure 18 EMW induced by PD on S45 particle

144

Effect of V on Vpp
Vpp vs V (S45, p=0.1 MPa)

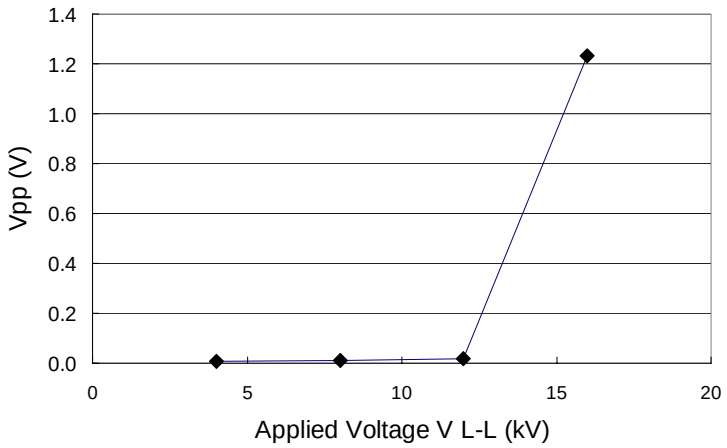

Figure 19 Effect of applied voltage on Vpp (S45 particle)

The higher V, the higher PD activity is, the lower Vpp is

145

Effect of gas pressure p on EMW signals

Data: S45 V=16kV p = 1 atm, 2 atm, 3 atm

S45 L=27mm p=1atm V=16kV 50ns

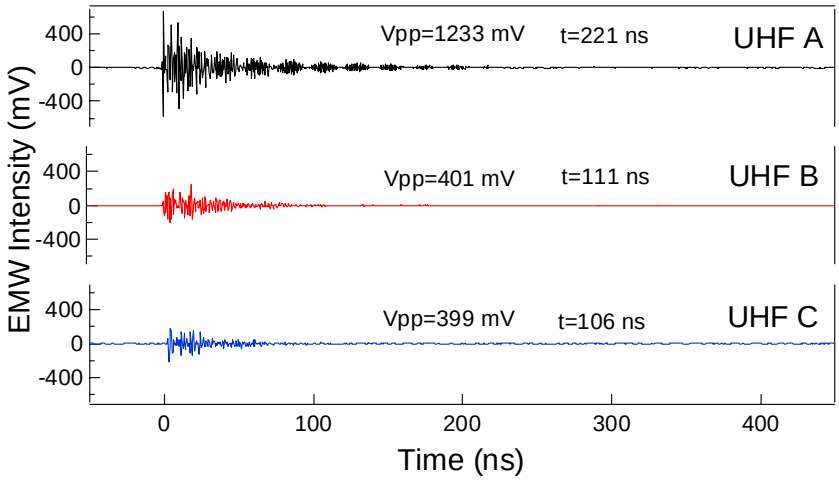

Figure 20 EMW induced by PD on S45 particle

146

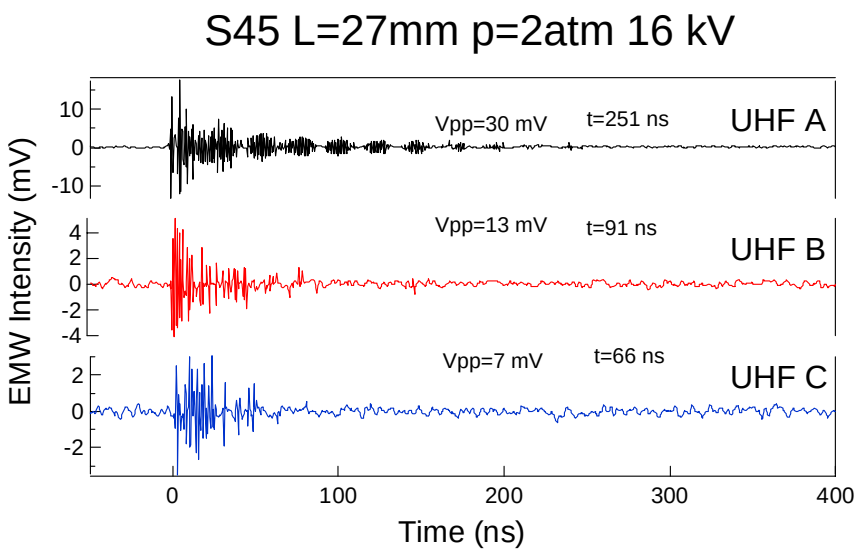

Figure 21 EMW induced by PD on S45 particle

147

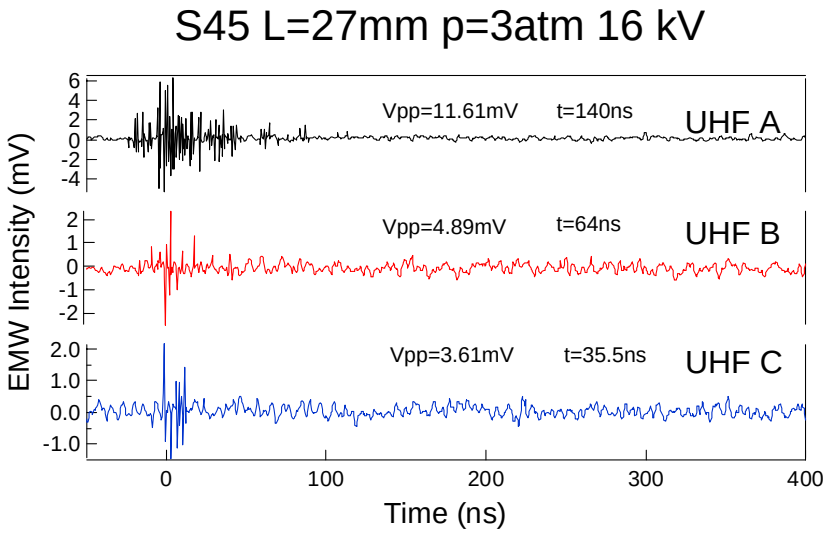

Figure 22 EMW induced by PD on S45 particle

148

Effect of p on Vpp
Vpp vs p (S45, V=16 kV)

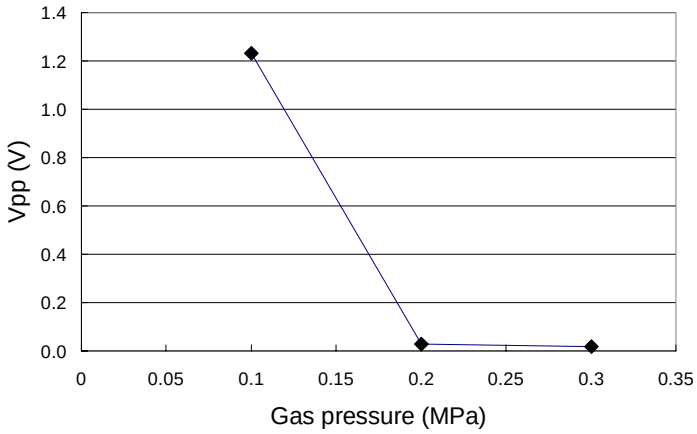

Figure 23 Effect of gas pressure on EMW magnitude

The higher p, the lower PD activity is, the lower Vpp is

149

CONCLUSION

1. Effect of PARTICLE POSITION on EMW:
   - magnitude (Vpp), Vpp S45 < Vpp E270
   - duration (t), t S45 < t E270

2. Effect of SENSOR POSITION on EMW
   - For S45: EMW Magnitude $V_{pp\,A} > V_{pp\,B} > V_{pp\,C}$
     EMW Duration $t_A > t_B > t_C$
   - For E270: EMW magnitude $V_{pp\,A} > V_{pp\,C} > V_{pp\,B}$
     EMW Duration $t_A > t_B > t_C$

3. Effect of APPLIED VOLTAGE on EMW
   - The higher V, the higher PD activity is, the lower Vpp is

4. Effect of GAS PRESSURE on EMW
   - The higher p, the lower PD activity is, the lower Vpp is

150

EXPERIMENTAL RESULTS OBSERVATION OF FREQUENCY AND PHASE SPECTRUM

151

Frequency and Phase Spectrum of S45 particle

Data PDM S45

1 atm UHF A: 16kV
2 atm UHF A: 16 24 36 kV
3 atm UHF A: 12 16 24 32 36 kV

1atm 16kV: UHF A,B,C

152

1 atm

153

S45 27mm 1 atm UHF A 16 kV

2 atm

155

S45 27mm 2 atm UHF A 16 kV 156

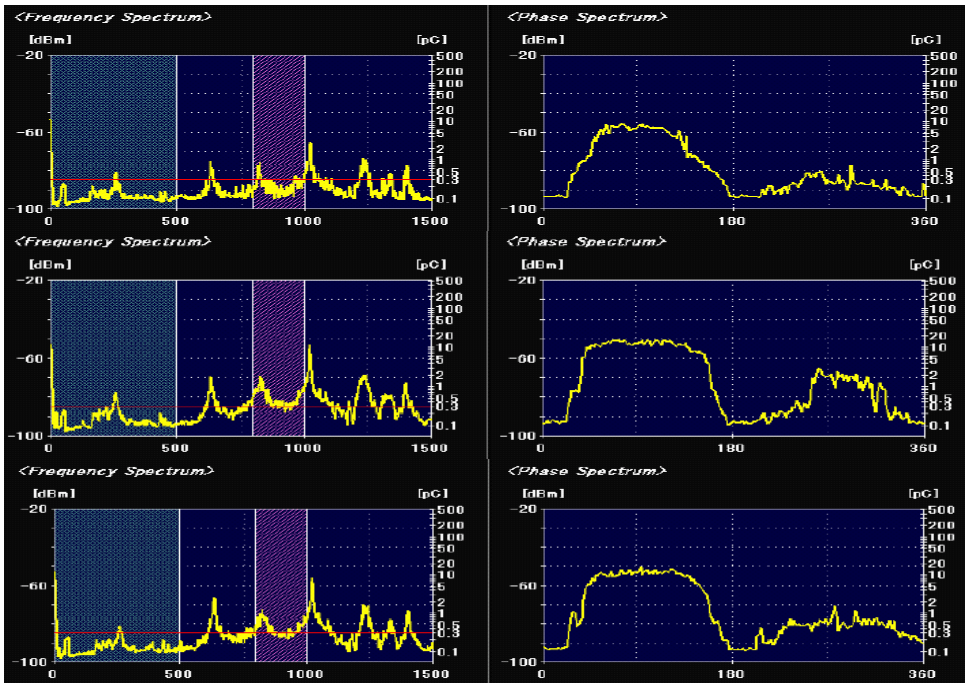

S45 27mm 2 atm UHF A 24 kV 157

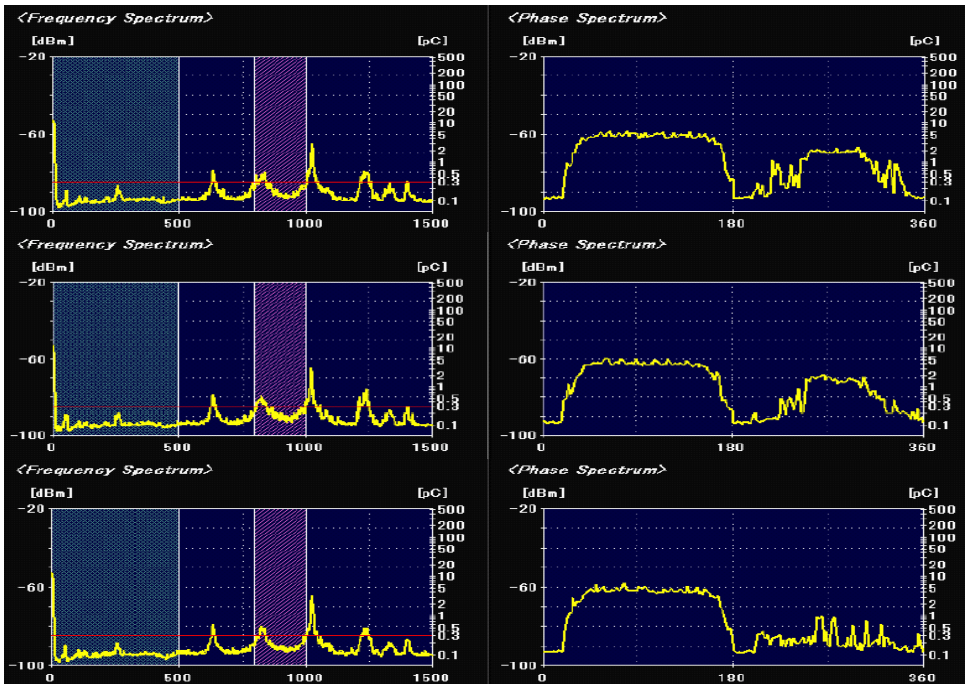

S45 27mm 2 atm UHF A 36 kV 158

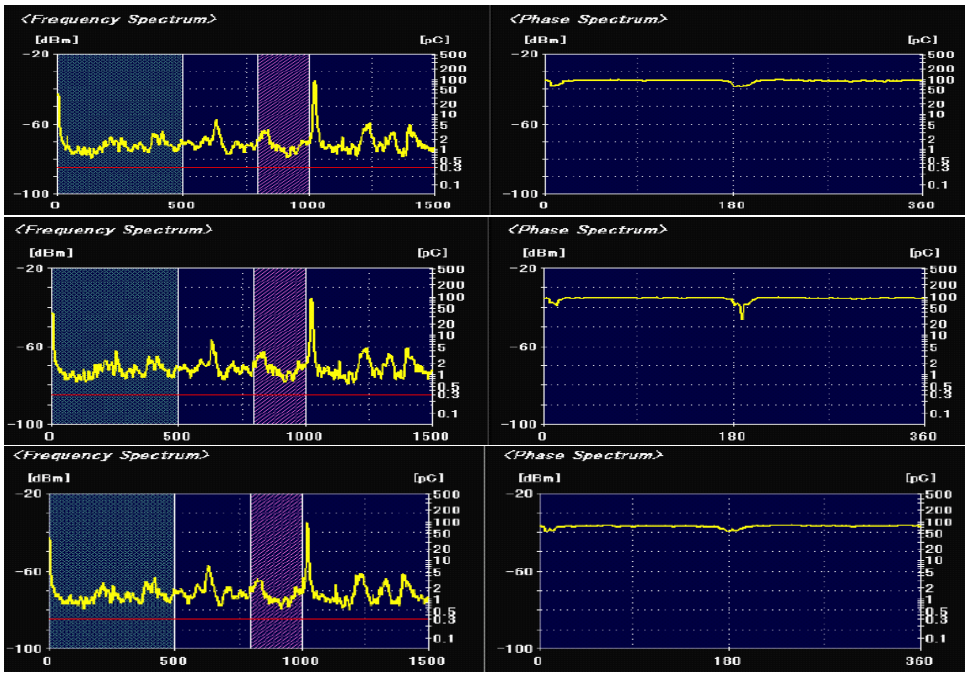

3 atm

159

S45 27mm 3 atm UHF A 12 kV 160

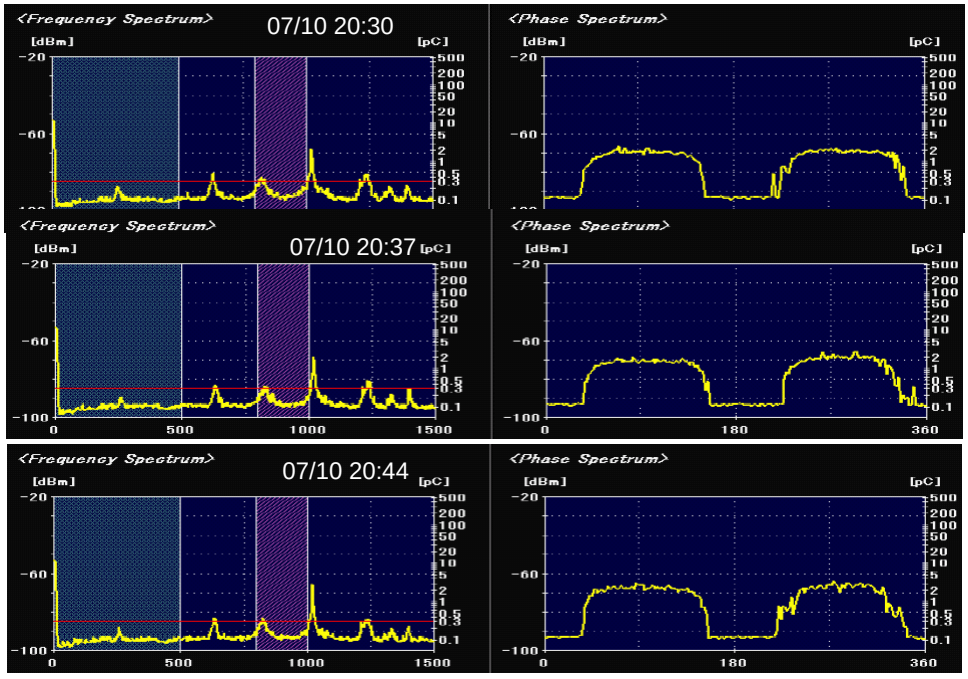

S45 27mm 3 atm UHF A 16 kV 161

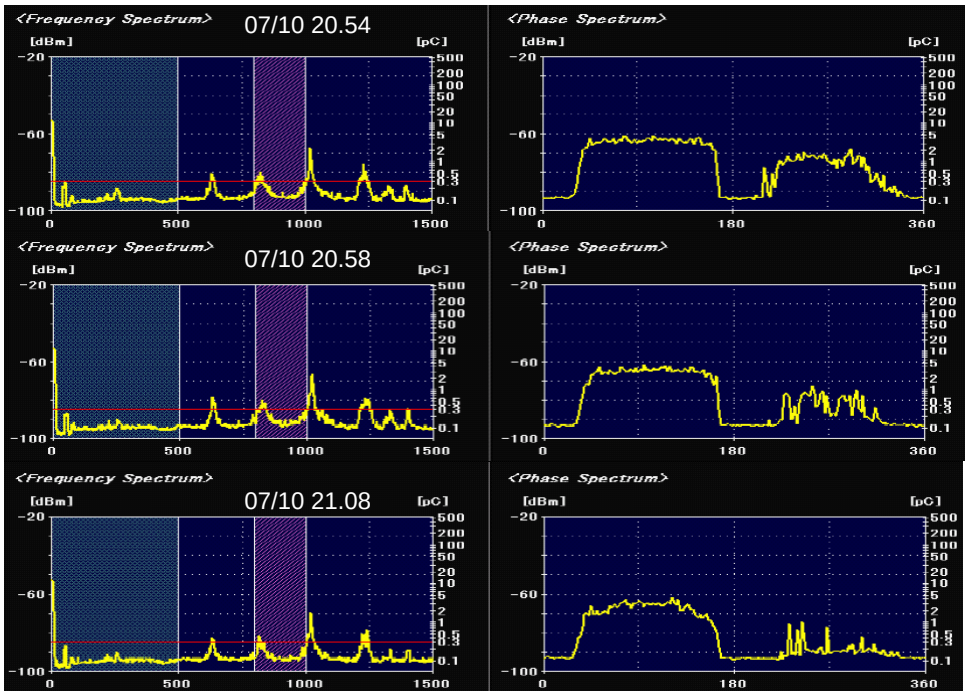

S45 27mm 3 atm UHF A 24 kV 162

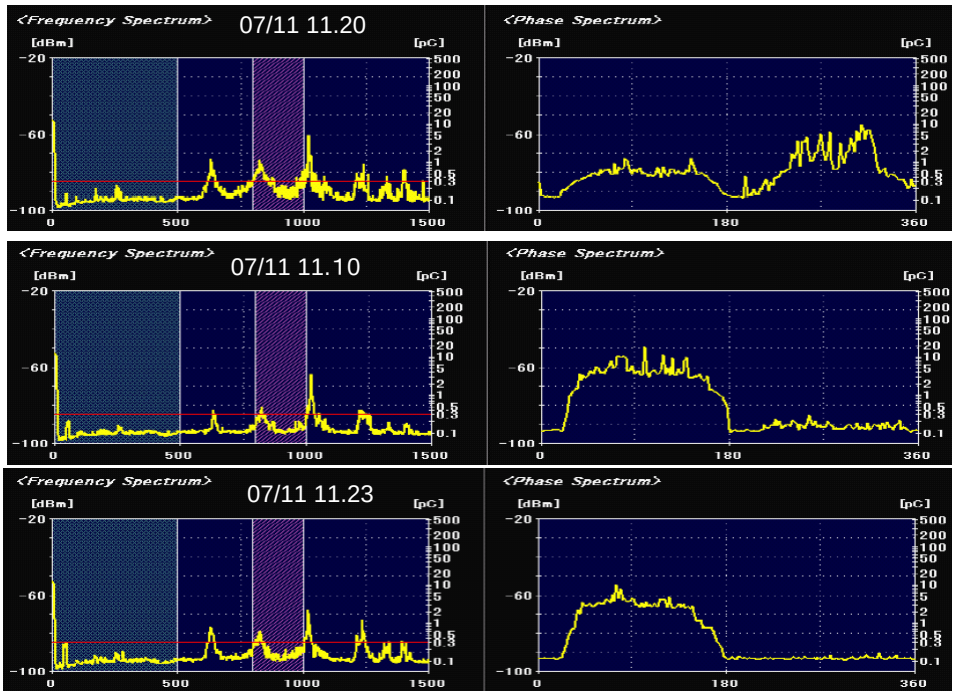

S45 27mm 3 atm UHF A 32 kV 163

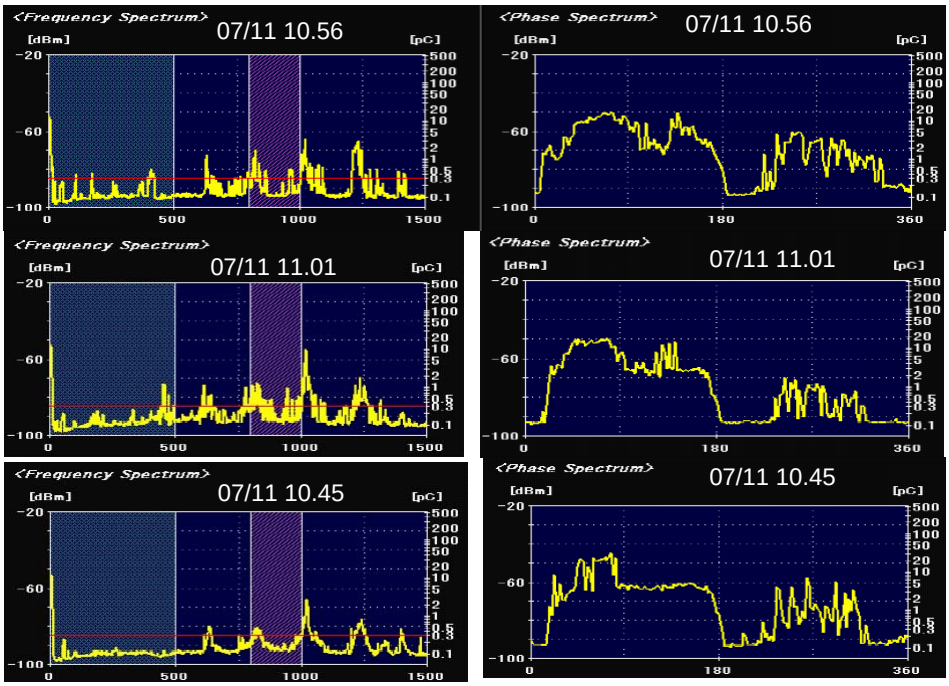

S45 27mm 3 atm UHF A 36 kV 164

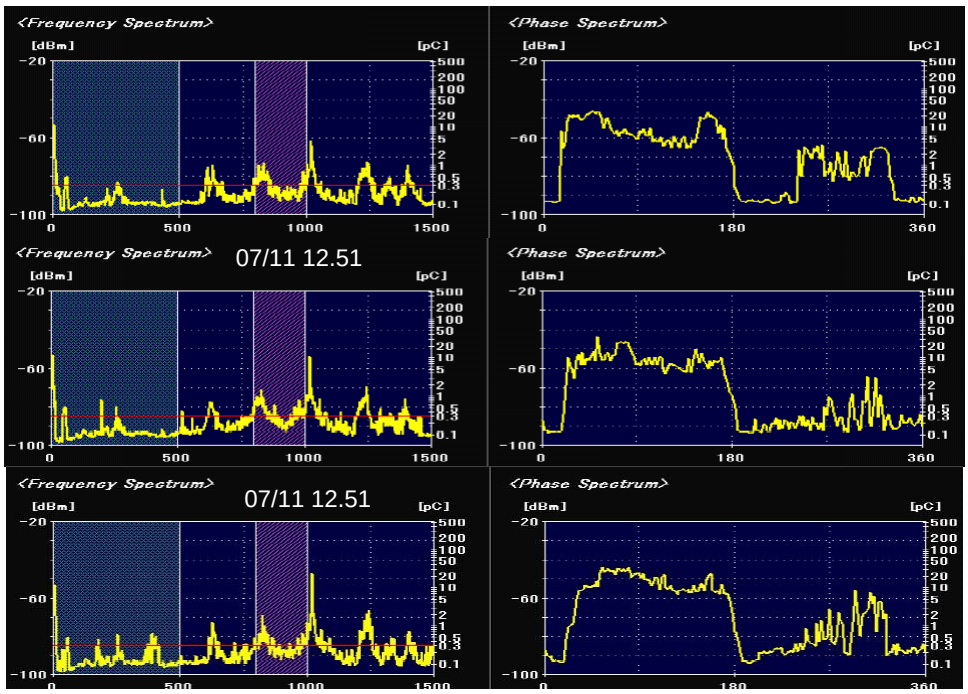

UHF A vs UHF B vs UHF C

165

S45 27mm 1 atm UHF A 16 kV 166

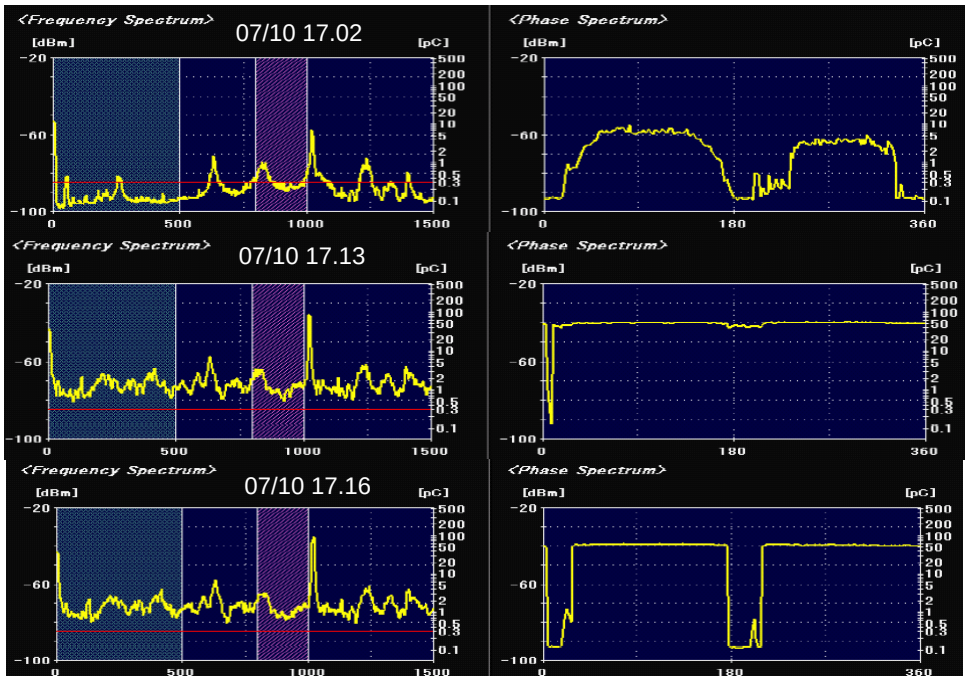

S45 27mm 1 atm UHF b 16 kV 167

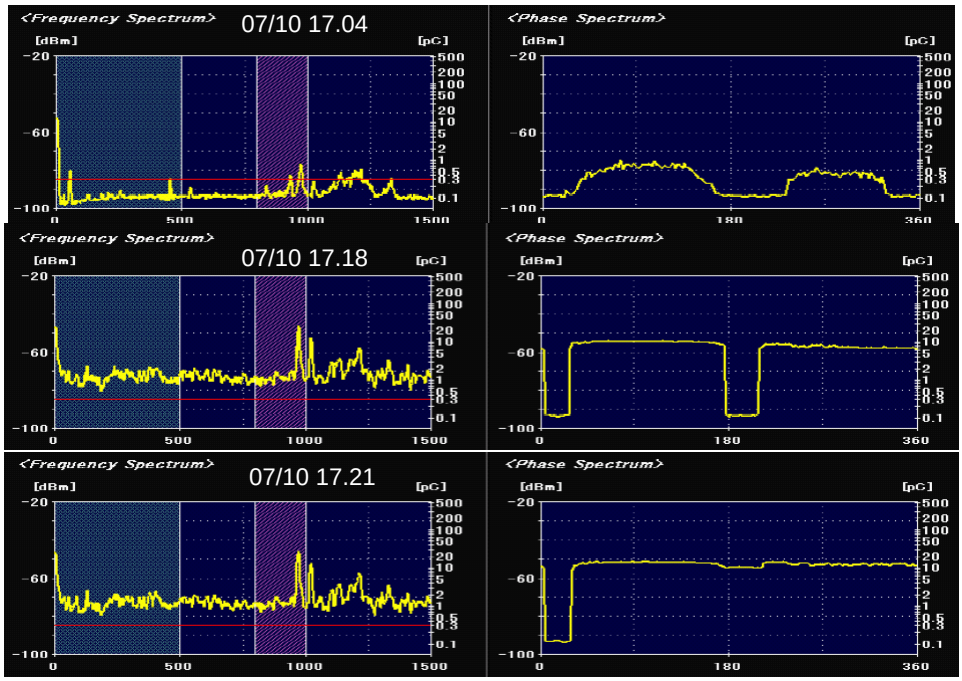

S45 27mm 1 atm UHF c 16 kV 168

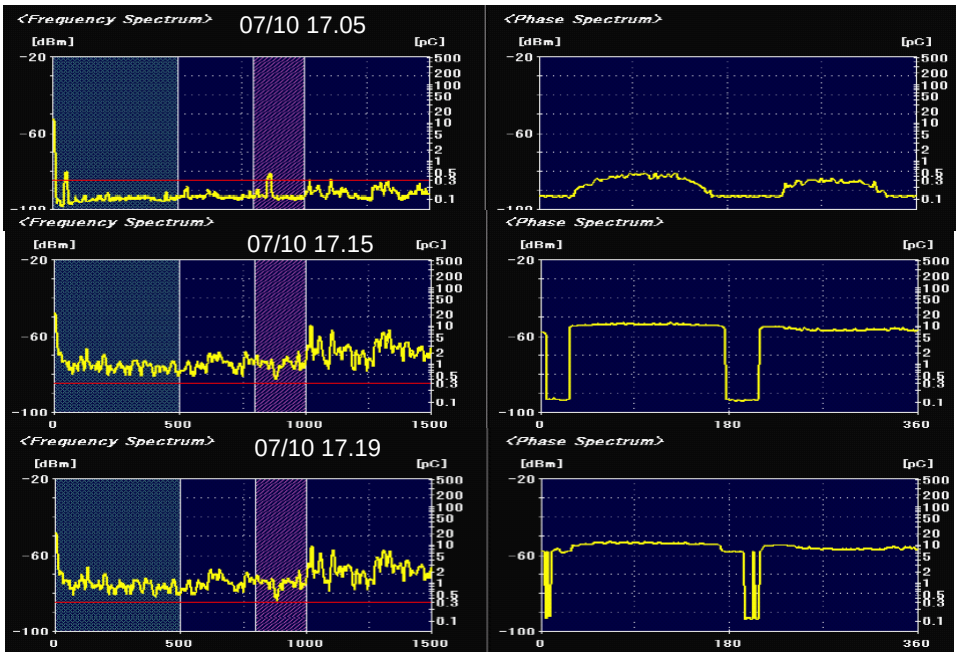

S45 27mm 1 atm UHF A 16 kV (1) 169

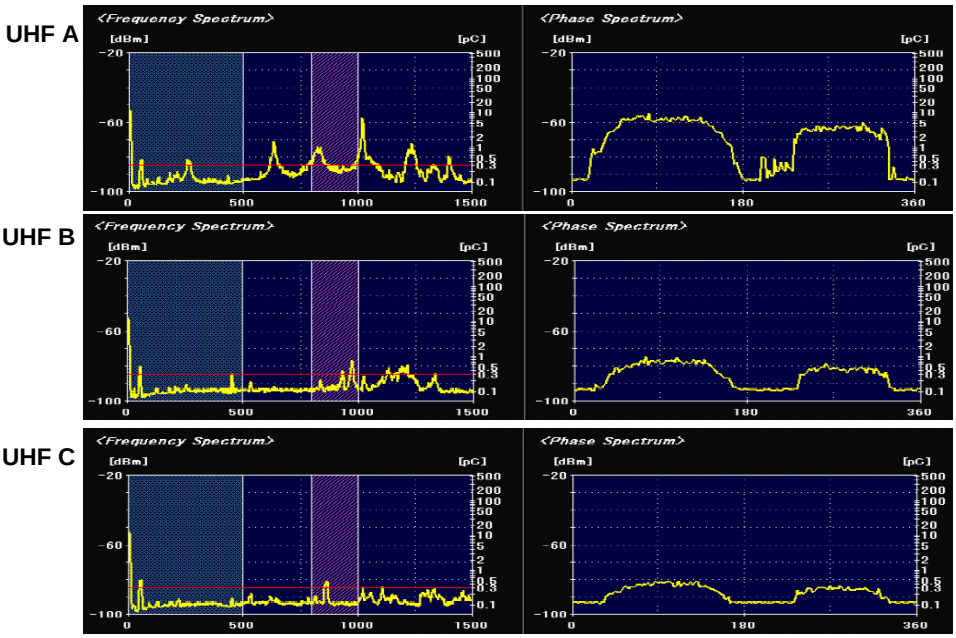

S45 27mm 1 atm UHF A 16 kV (2) 170

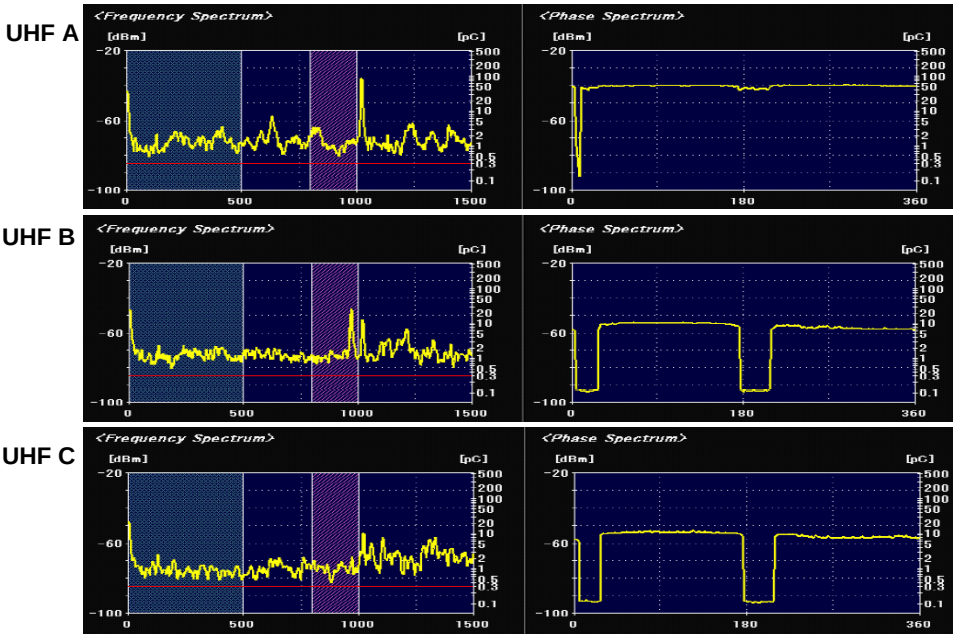

S45 27mm 1 atm UHF A 16 kV (3) 171

UHF A

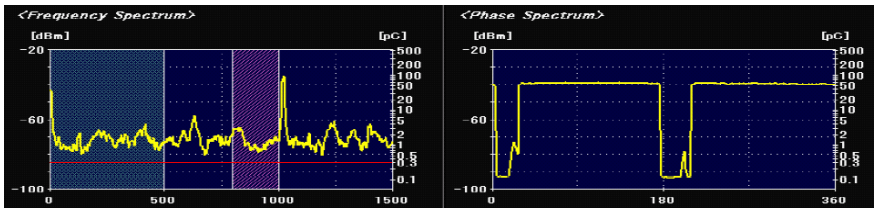

UHF B

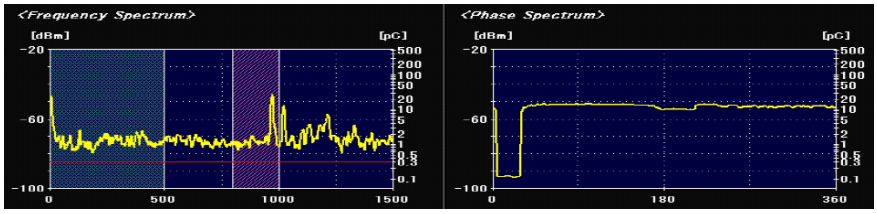

UHF C

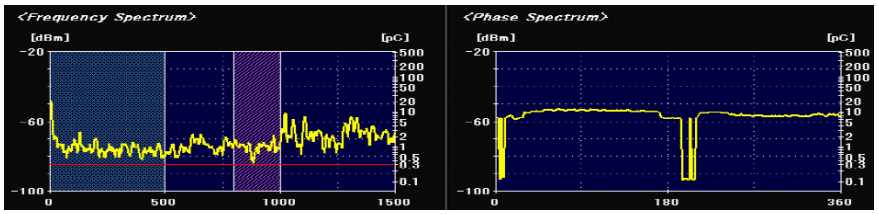

172

Effect of applied voltage on frequency and phase spectrum of PD (S45 UHF A)

173

Effect of applied voltage on frequency and phase spectrum of PD (S45 UHF A 1 atm)

16 kV

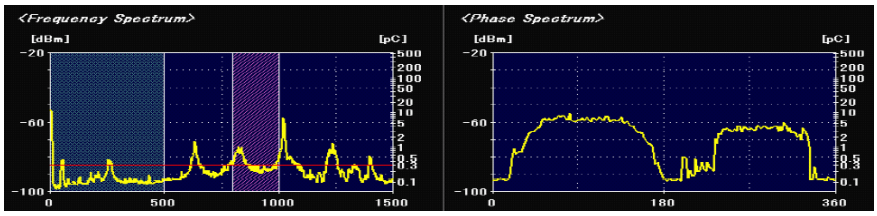

24 kV

breakdown

36 kV

breakdown

174

Effect of applied voltage on frequency and phase spectrum of PD (S45 UHF A 2 atm)

175

16 kV

24 kV

36 kV

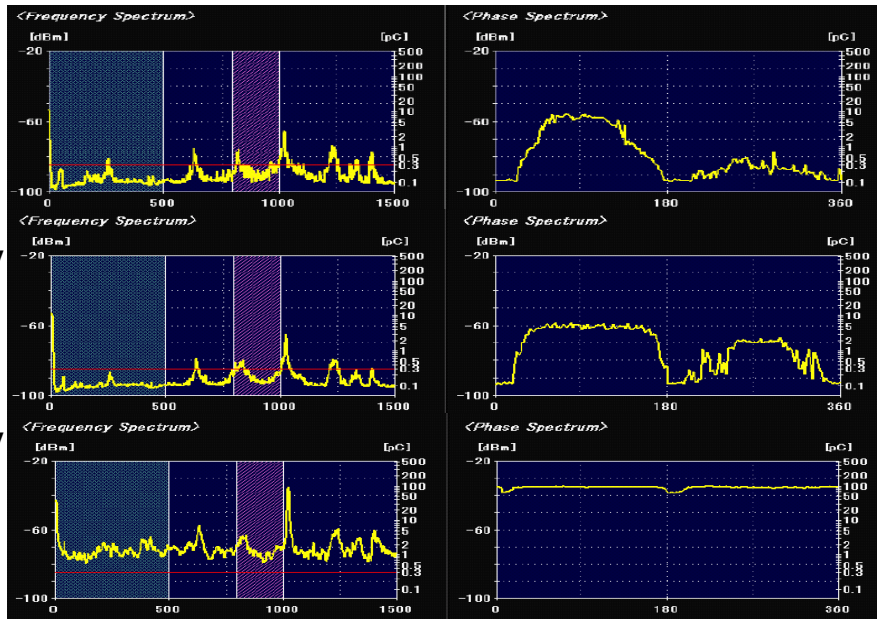

Effect of applied voltage on frequency and phase spectrum of PD (S45 UHF A 3 atm)

176

16 kV

24 kV

36 kV

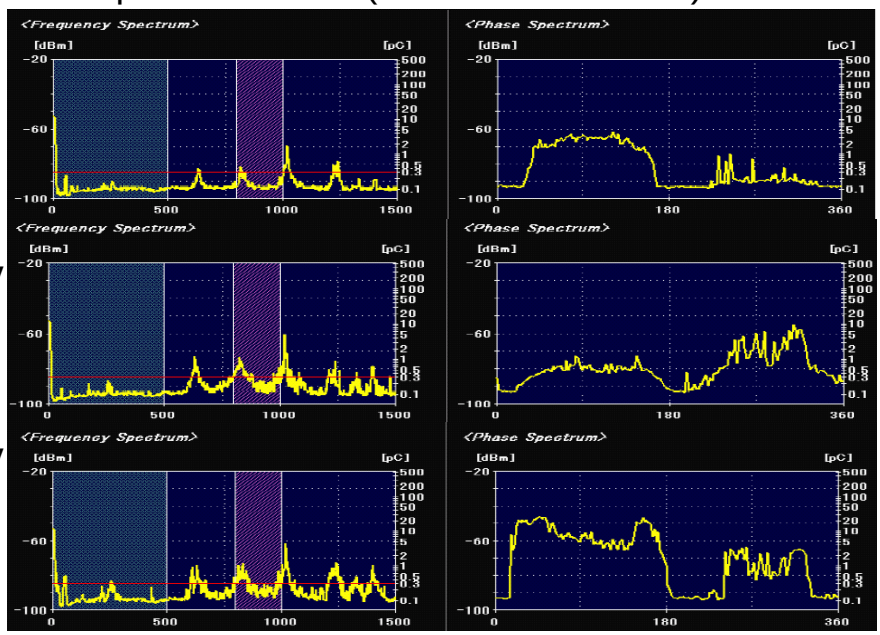

Effect of gas pressure on frequency and phase spectrum of PD (S45 UHF A)

177

Effect of gas pressure on frequency and phase spectrum of PD (S_{45} UHF A 16kV) 178

1 atm

2 atm

3 atm

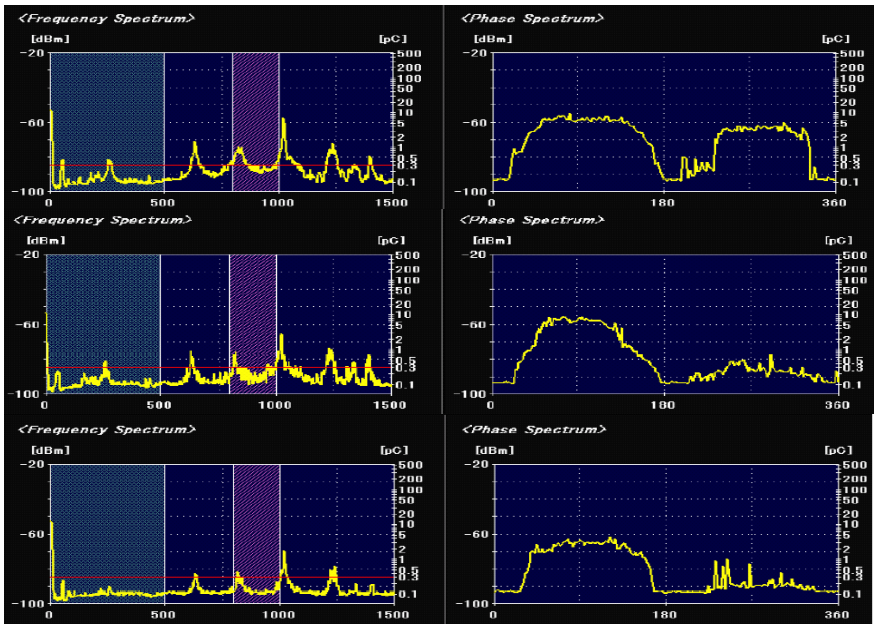

Effect of gas pressure on frequency and phase spectrum of PD (S45 UHF A 24kV)

179

1 atm

breakdown

2 atm

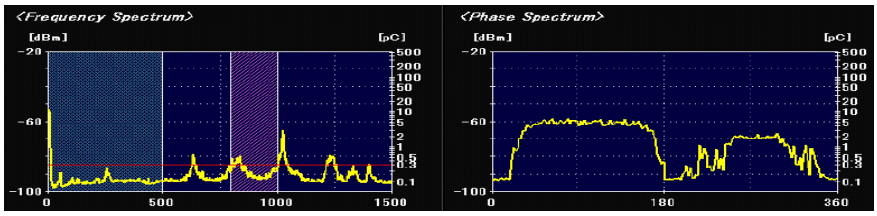

3 atm

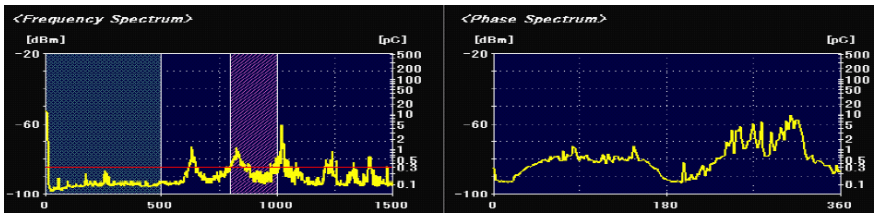

Effect of gas pressure on frequency and phase spectrum of PD (S45 UHF A 36kV)

180

1 atm

breakdown

2 atm

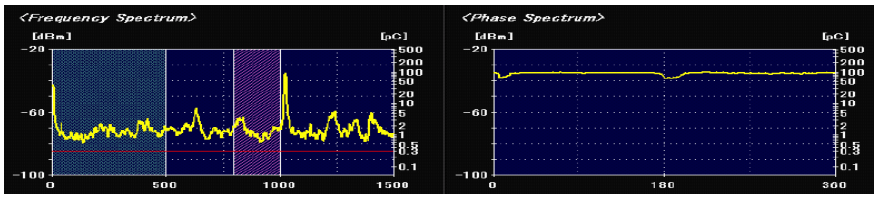

3 atm

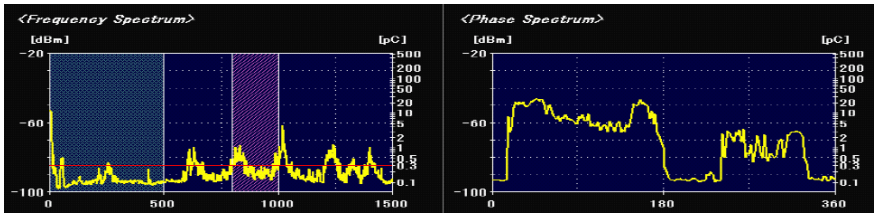

Frequency and Phase Spectrum of E270 Particle

Data PDM E270

1 atm UHF A: 16,24,36 kV
2 atm UHF A: 16, 24, 36 kV
3 atm UHF A: 16, 24, 36 kV

1atm 16kV: UHF A,B,C

181

1 atm

182

E270 27 mm **1atm 16** kV UHF A

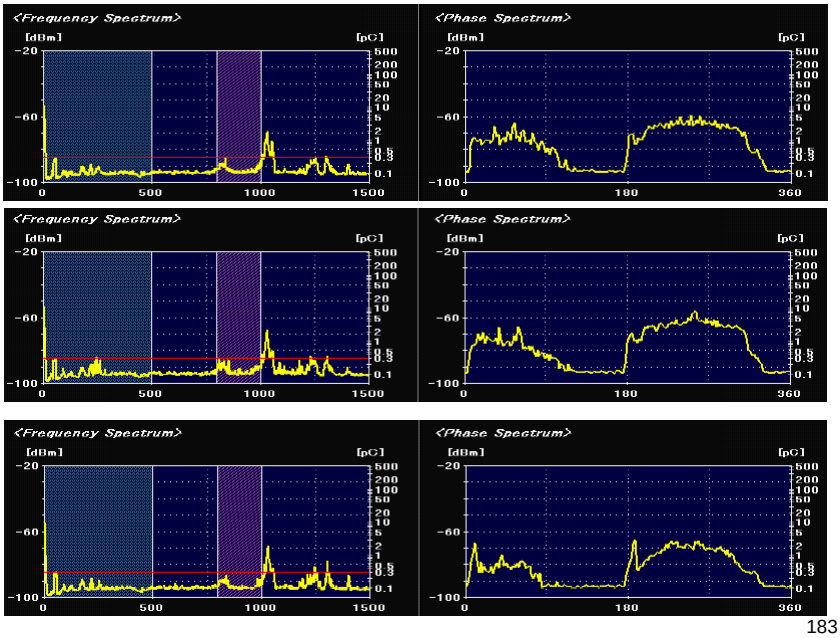

183

E270 27 mm 1atm **24** kV UHF A

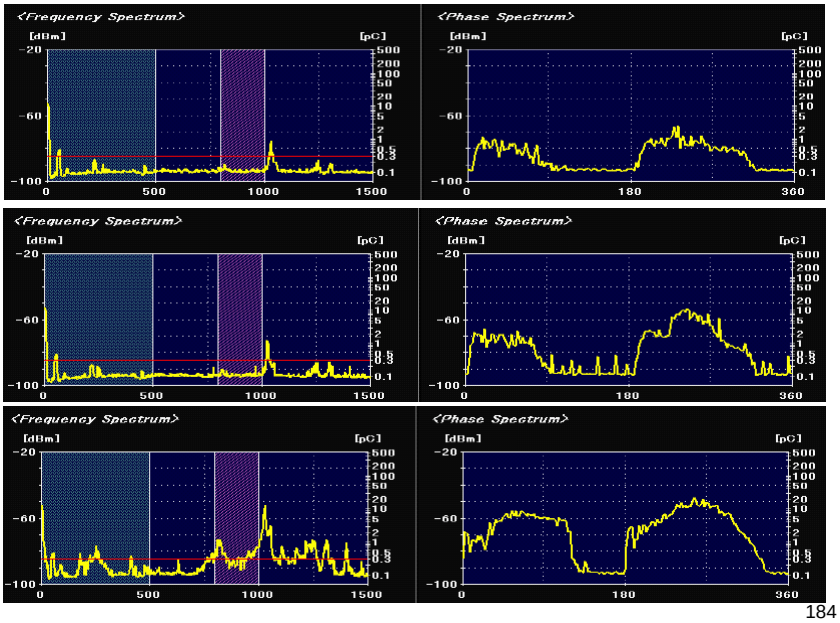

184

2 atm

185

E270 27 mm **2atm 16 kV** UHF A

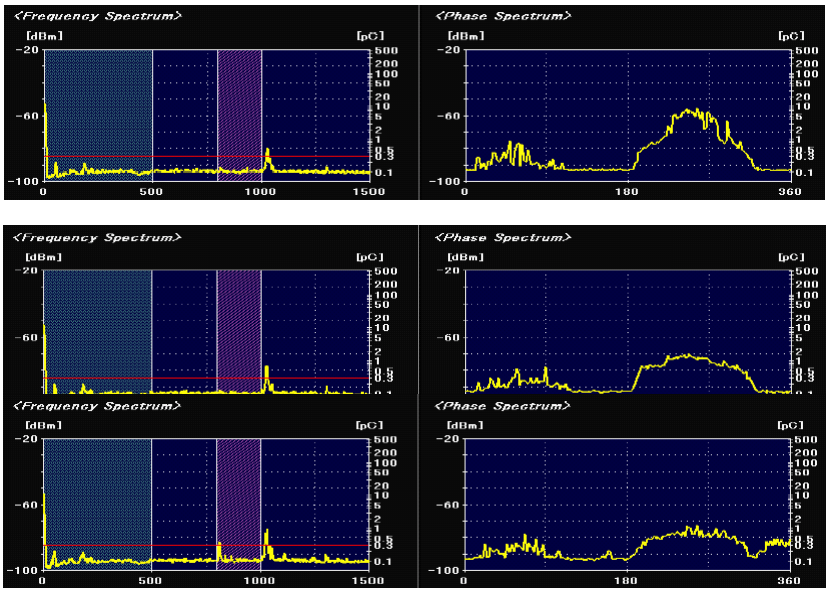

186

E270 27 mm 2atm **24** kV UHF A

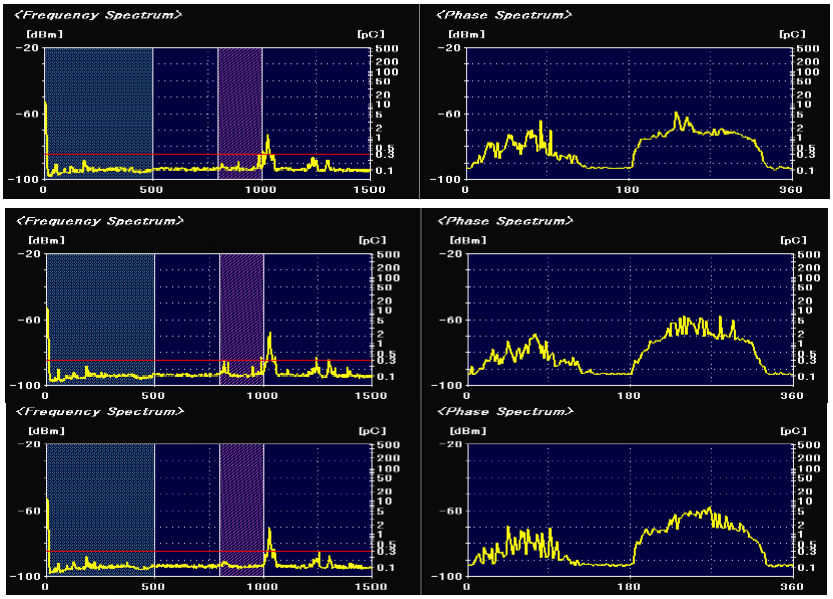

187

E270 27 mm 2atm **36** kV UHF A

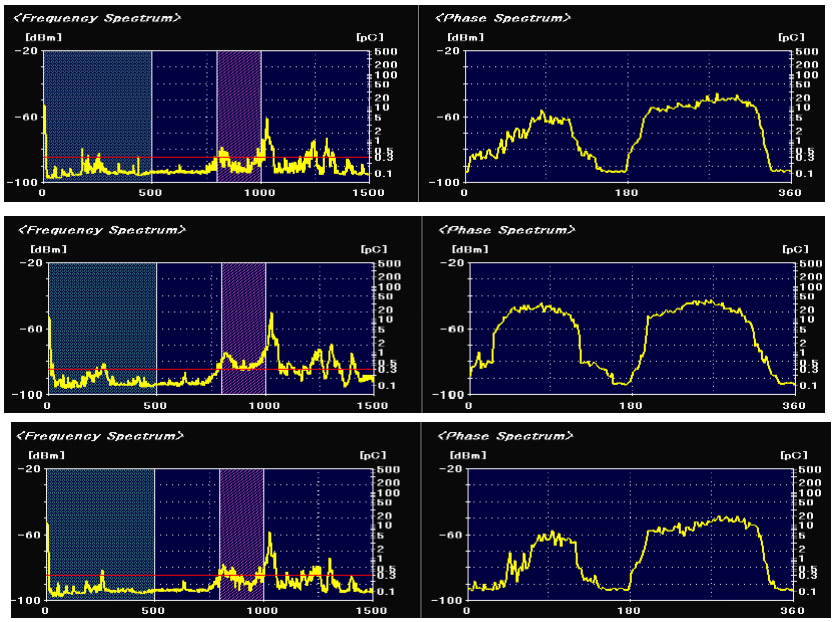

188

3 atm

189

E270 27 mm **3atm 16** kV UHF A

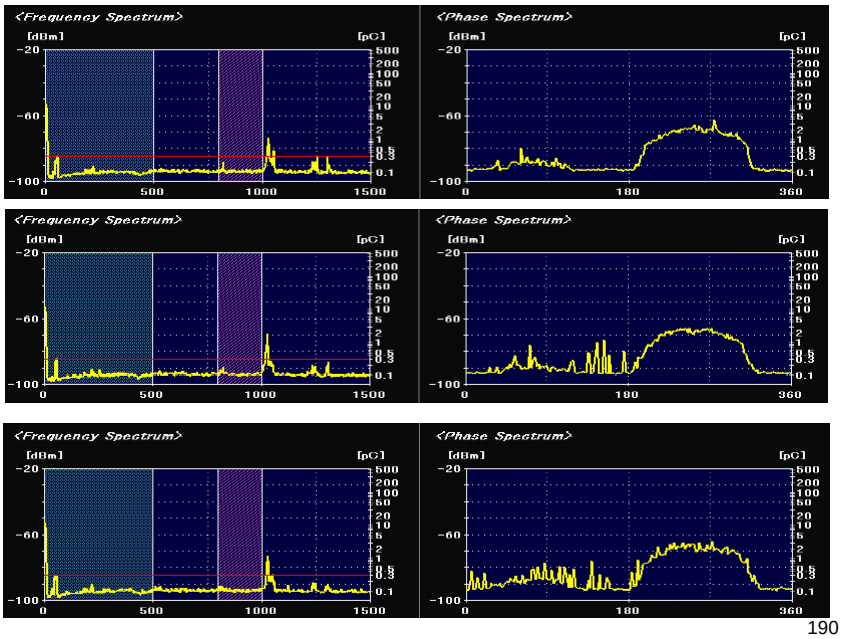

190

E270 27 mm 3atm **24** kV UHF A

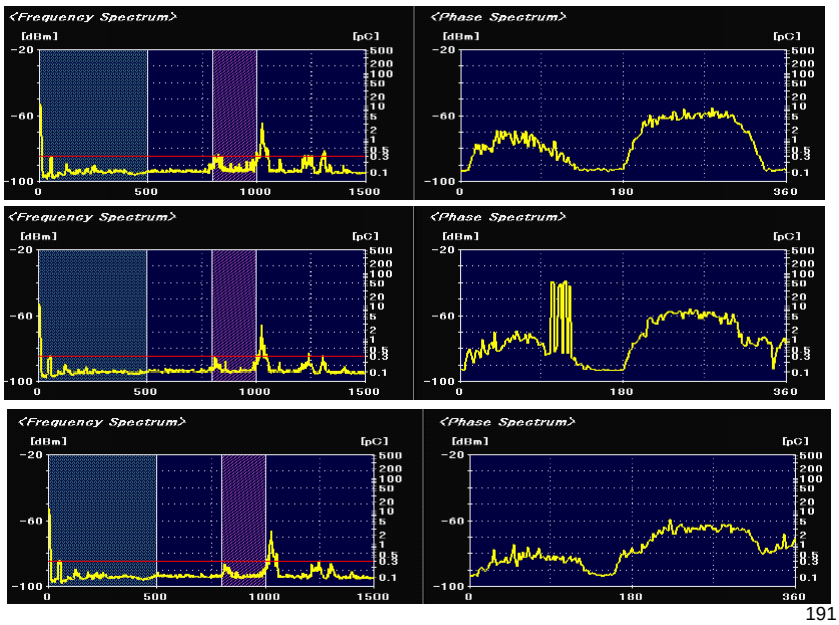

191

E270 27 mm 3atm **36** kV UHF A

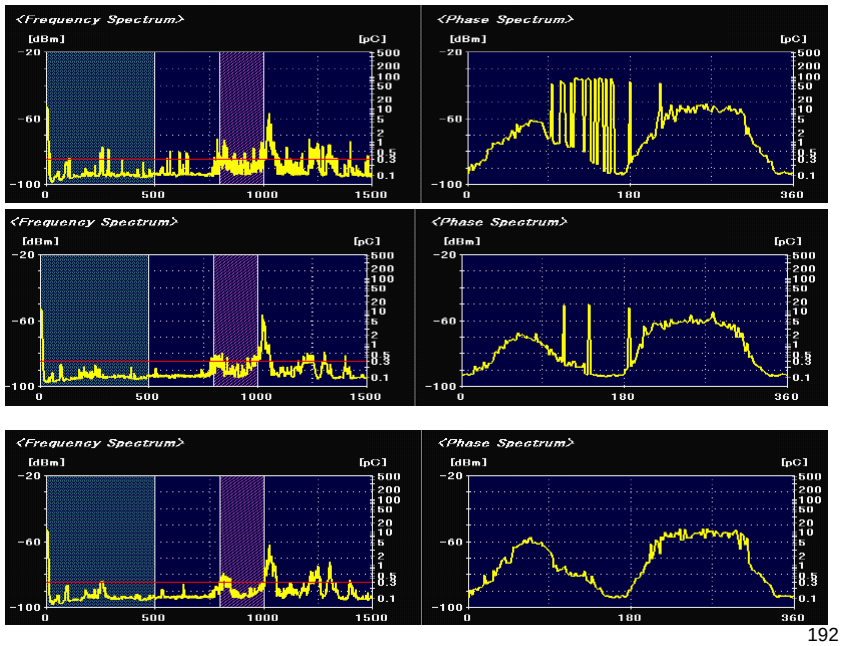

192

Effect of applied voltage on frequency and phase spectrum of PD (E_{270} UHF A)

193

Effect of applied voltage on frequency and phase spectrum of PD (E_{270} UHF A 1 atm)

16 kV

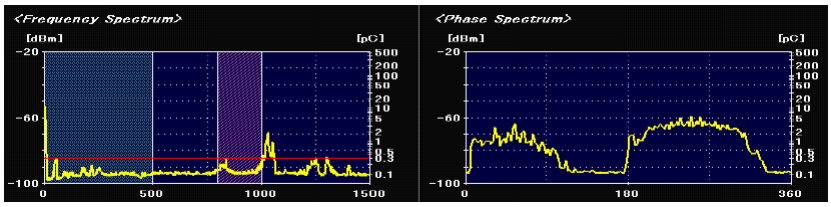

24 kV

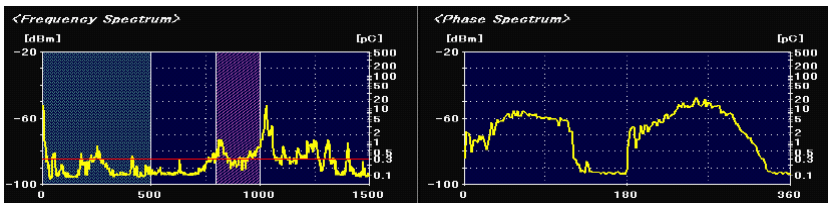

36 kV

Breakdown

194

Effect of applied voltage on frequency and phase spectrum of PD (E270 UHF A 2 atm)

195

16 kV

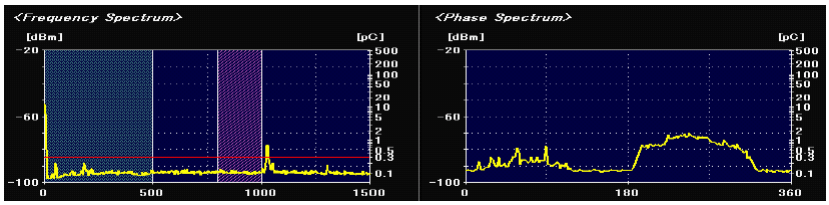

24 kV

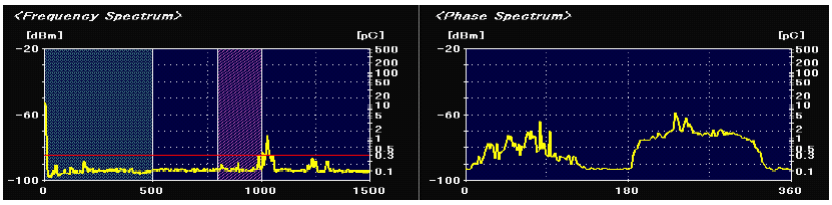

36 kV

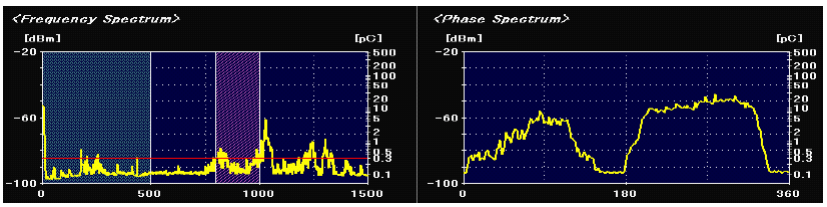

Effect of applied voltage on frequency and phase spectrum of PD (E_{270} UHF A 3 atm)

196

16 kV

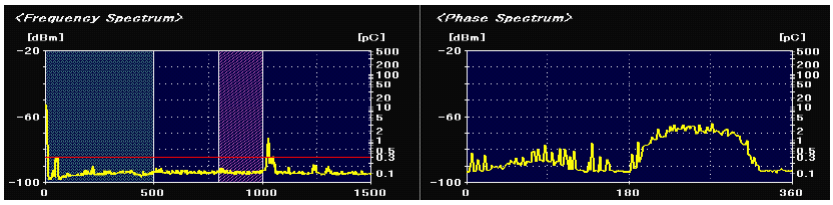

24 kV

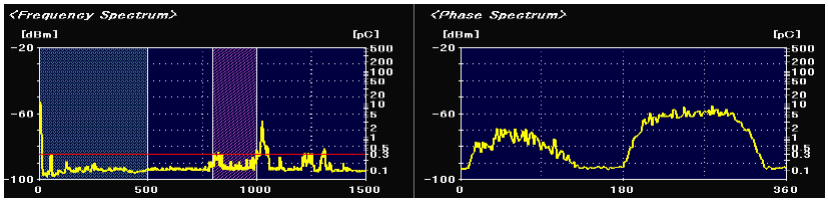

36 kV

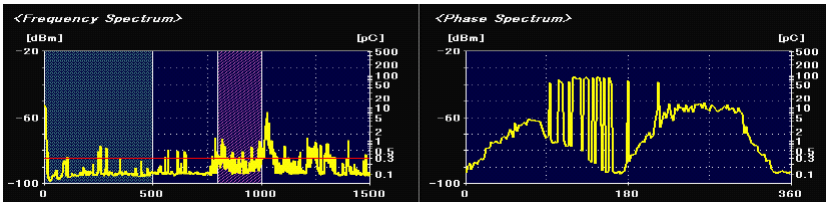

Effect of gas pressure on frequency and phase spectrum of PD (E_{270} UHF A)

197

Effect of gas pressure on frequency and phase spectrum of PD (E_{270} UHF A 16kV)

198

1 atm

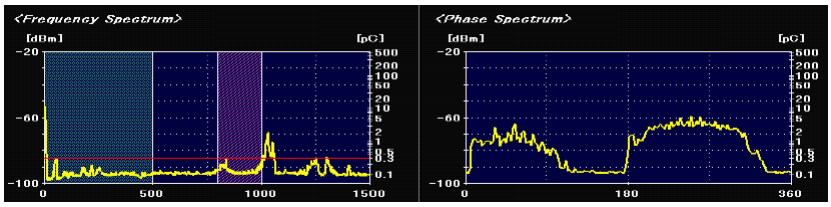

2 atm

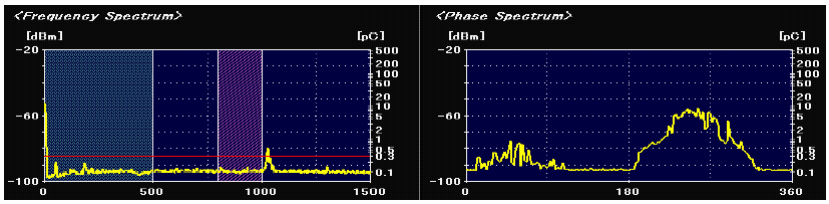

3 atm

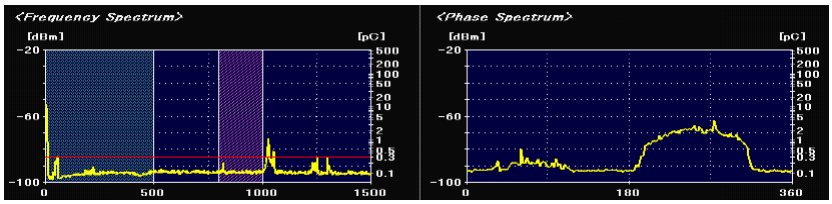

Effect of gas pressure on frequency and phase spectrum of PD (E270 UHF A 24kV)

199

1 atm

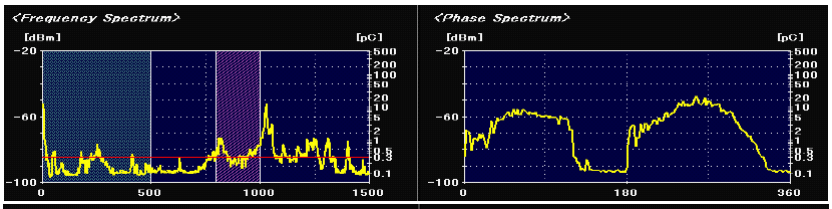

2 atm

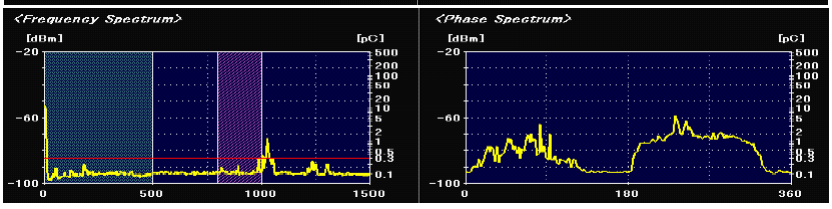

3 atm

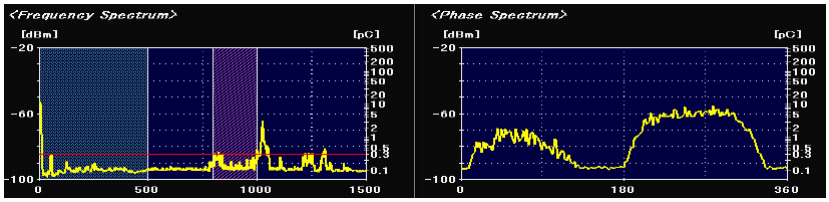

Effect of gas pressure on frequency and phase spectrum of PD (E270 UHF A 36kV)

200

1 atm

Under PDIV

2 atm

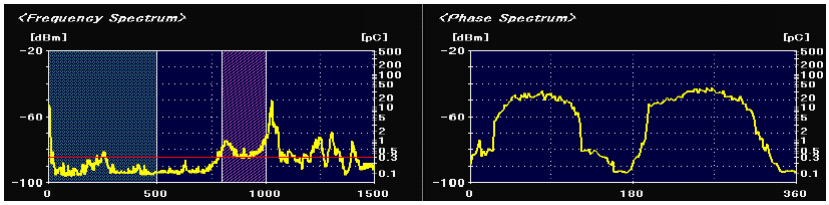

3 atm

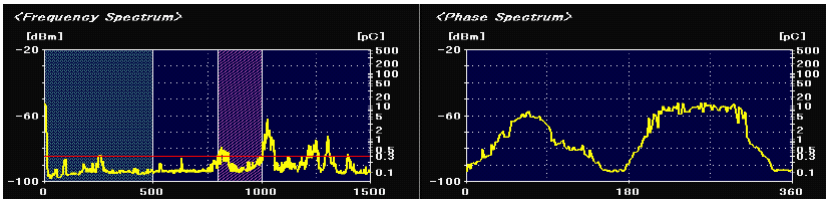

S45とS135の比較(UHF A)

S45 16kV 3atm UHF A　Protrusion → Protrusion

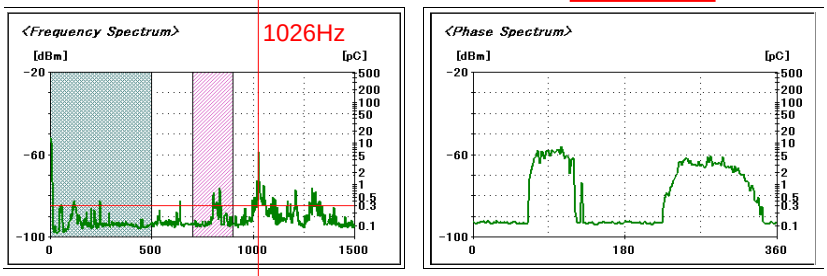

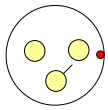

S135 24kV 3atm UHF A　Protrusion → Particle on Spacer

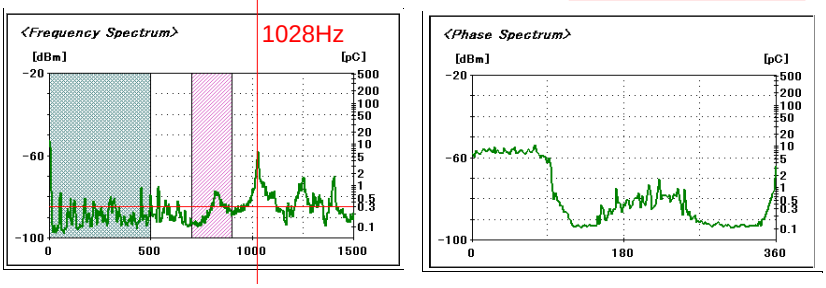

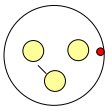

201

S45とR225の比較(UHF A)

S45 16kV 3atm UHF A　Protrusion → Protrusion

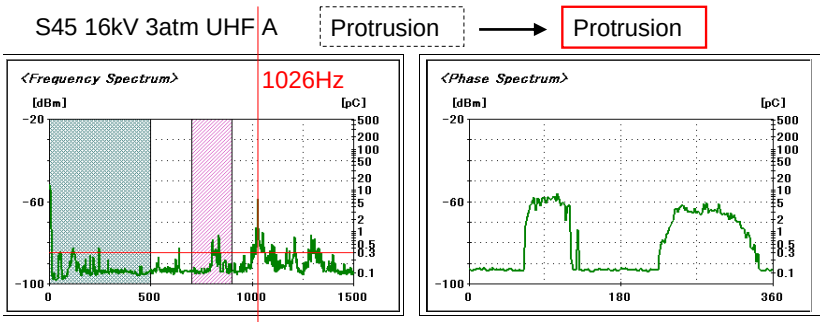

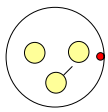

R225 16kV 3atm UHF A　Protrusion → Protrusion

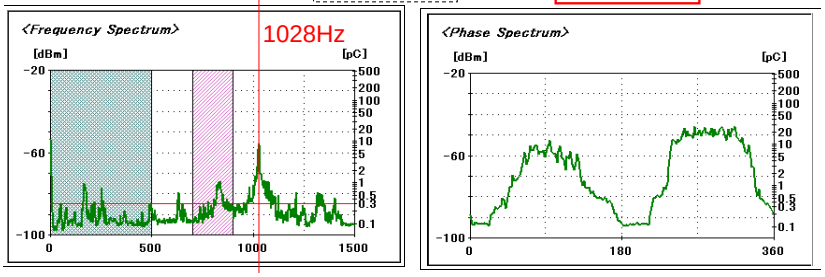

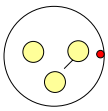

202

S45とS135の比較(UHF B)

S45 16kV 3atm UHF B　Protrusion → Protrusion

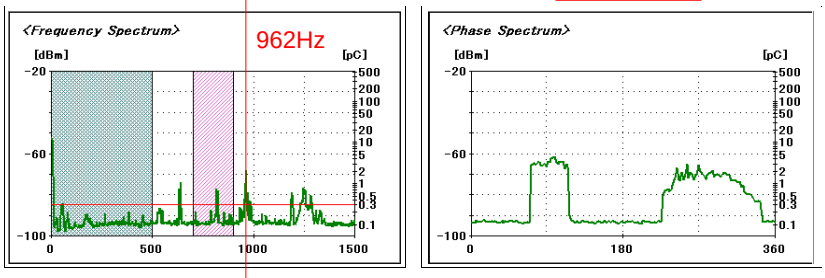

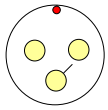

S135 16kV 3atm UHF B　Protrusion → Particle on Spacer

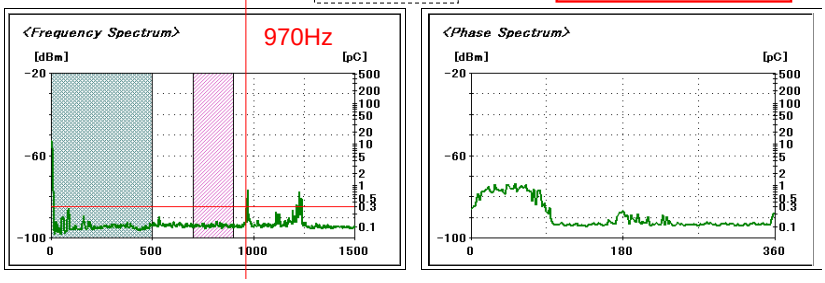

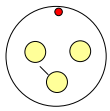

203

S45とR225の比較(UHF B)

S45 16kV 3atm UHF B　Protrusion → Protrusion

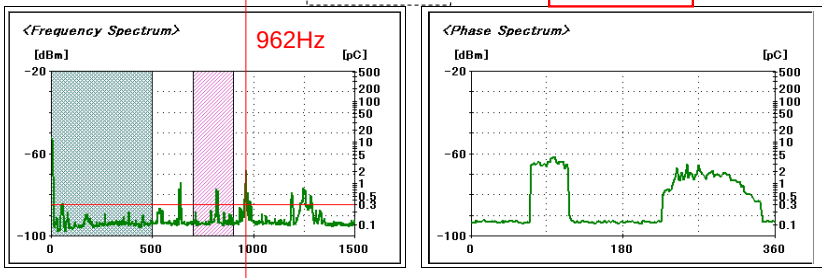

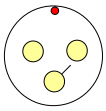

R225 16kV 3atm UHF B　Protrusion → Protrusion

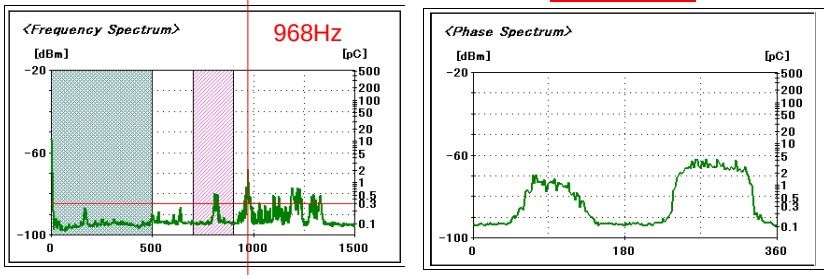

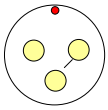

204

S270(UHF BとUHF Dの比較)

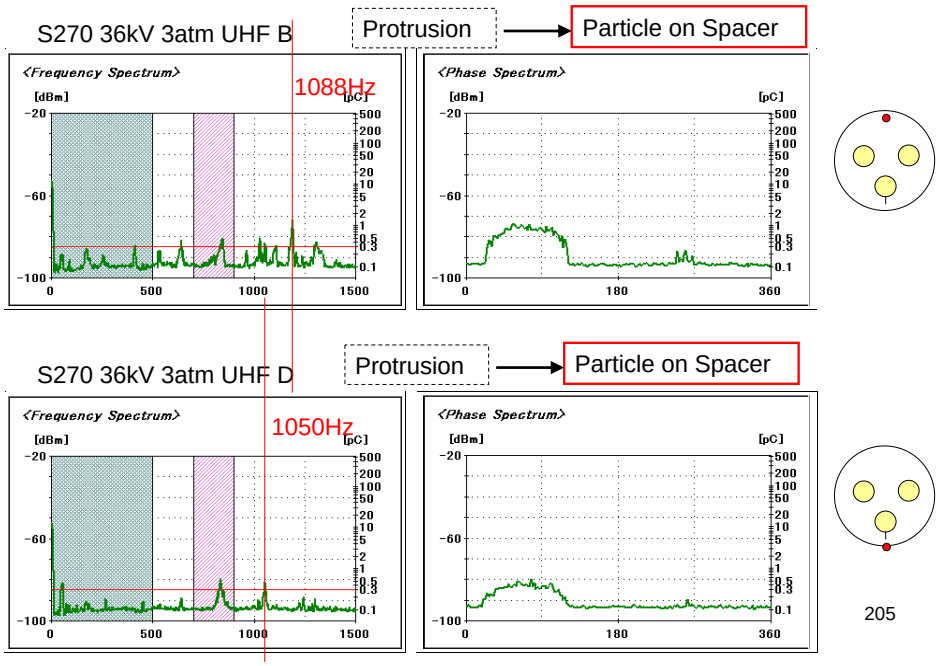

S270とR0の比較(異物とセンサの位置が近い場合)

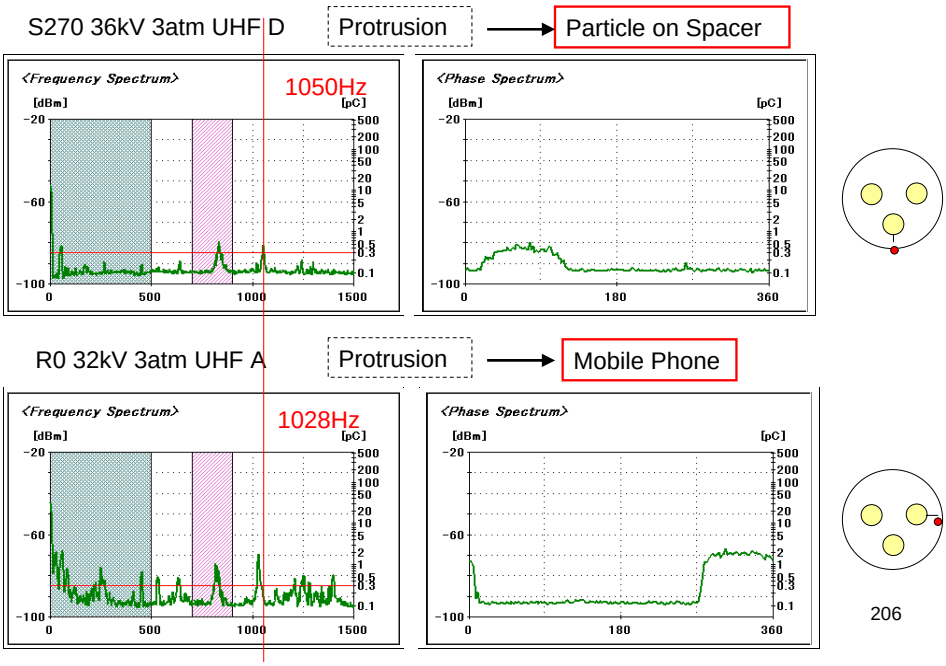

S270とR0の比較(UHF A)

S270 36kV 3atm UHF A　Protrusion → Spacer Crack

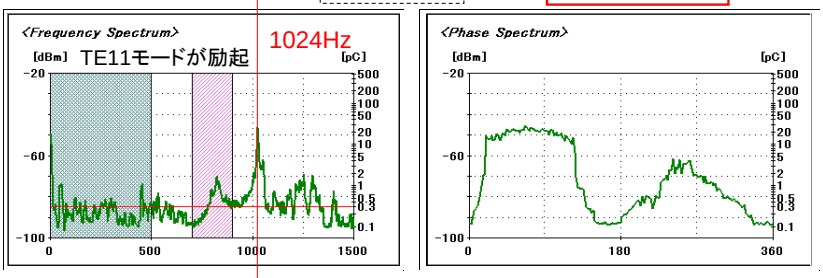

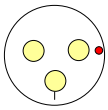

R0 32kV 3atm UHF A　Protrusion → Mobile Phone

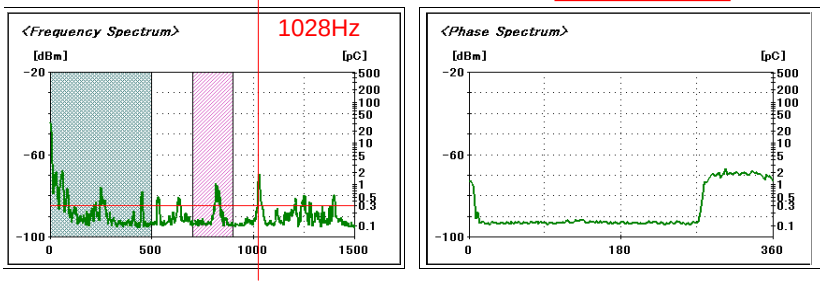

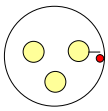

207

S270とR0の比較(UHF B)

S270 36kV 3atm UHF B　Protrusion → Particle on Spacer

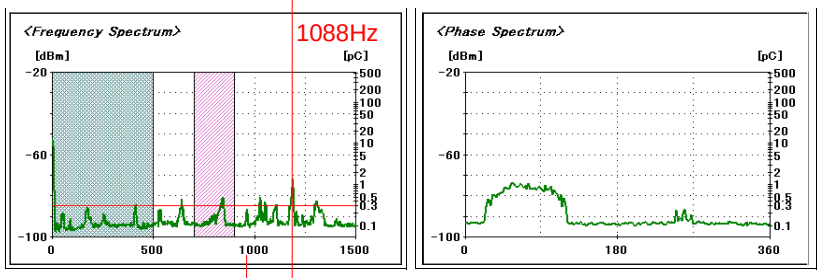

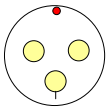

R0 32kV 3atm UHF B　Protrusion → Mobile Phone

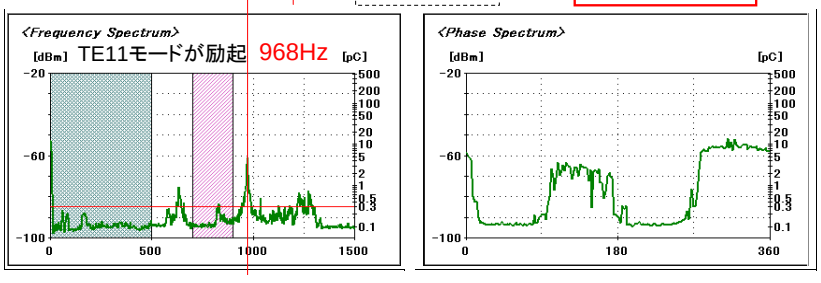

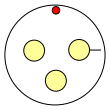

208

R0 3atm 32kV UHF A

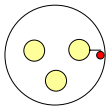

2007/12/06 20:51:32	Internal	1028 Hz	1.1 pC	-73 dBm	Normal	Mobile Phone	0
2007/12/06 20:47:56	Internal	1028 Hz	0.8 pC	-77 dBm	Normal	Mobile Phone	0
2007/12/06 20:44:21	Internal	1028 Hz	1.6 pC	-71 dBm	Normal	Mobile Phone	0
2007/12/06 20:40:47	Internal	1030 Hz	0.9 pC	-75 dBm	Normal	Mobile Phone	0
2007/12/06 20:37:18	Internal	1028 Hz	0.9 pC	-76 dBm	Normal	Mobile Phone	0
2007/12/06 20:33:49	Internal	1028 Hz	1.8 pC	-69 dBm	Normal	Mobile Phone	0
2007/12/06 20:30:21	Internal	1030 Hz	1.5 pC	-71 dBm	Normal	Mobile Phone	0
2007/12/06 20:26:53	Internal	1028 Hz	0.7 pC	-77 dBm	Normal	Mobile Phone	0
2007/12/06 20:23:25	Internal	1030 Hz	0.9 pC	-75 dBm	Normal	Mobile Phone	0

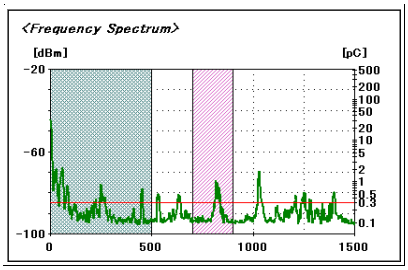

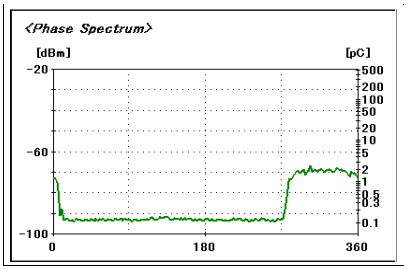

209

R0 3atm 32kV UHF B

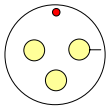

2007/12/06 20:52:44	Internal	970 Hz	3.8 pC	-63 dBm	Normal	Mobile Phone	0
2007/12/06 20:49:08	Internal	970 Hz	7.5 pC	-57 dBm	Normal	Mobile Phone	0
2007/12/06 20:45:33	Internal	970 Hz	4.8 pC	-61 dBm	Abnormal	Protrusion	5
2007/12/06 20:41:59	Internal	968 Hz	6.6 pC	-58 dBm	Normal	Mobile Phone	0
2007/12/06 20:38:26	Internal	970 Hz	4 pC	-63 dBm	Normal	Mobile Phone	0
2007/12/06 20:34:59	Internal	970 Hz	2.6 pC	-66 dBm	Normal	Mobile Phone	0
2007/12/06 20:31:30	Internal	970 Hz	7.2 pC	-57 dBm	Normal	Mobile Phone	0
2007/12/06 20:28:02	Internal	970 Hz	6.6 pC	-58 dBm	Normal	Mobile Phone	0
2007/12/06 20:24:34	Internal	968 Hz	3.8 pC	-63 dBm	Normal	Mobile Phone	0

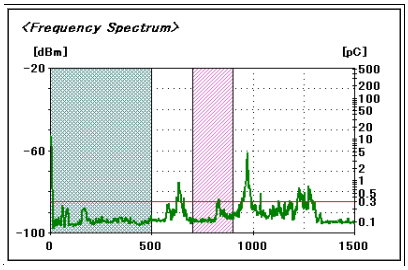

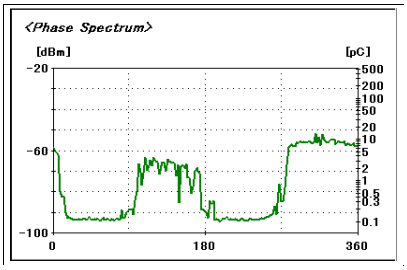

210

R0 3atm 32kV UHF C

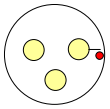

2007/12/06 20:53:56	Internal	1282 Hz	1.2 pC	-73 dBm	Normal	Mobile Phone	0
2007/12/06 20:50:20	Internal	1286 Hz	1.1 pC	-74 dBm	Normal	Mobile Phone	0
2007/12/06 20:46:44	Internal	1282 Hz	0.8 pC	-77 dBm	Normal	Mobile Phone	0
2007/12/06 20:43:10	Internal	1282 Hz	1.2 pC	-73 dBm	Normal	Mobile Phone	0
2007/12/06 20:39:36	Internal	1280 Hz	0.8 pC	-76 dBm	Normal	Mobile Phone	0
2007/12/06 20:36:09	Internal	1284 Hz	1.4 pC	-72 dBm	Normal	Mobile Phone	0
2007/12/06 20:32:40	Internal	1284 Hz	0.9 pC	-76 dBm	Normal	Mobile Phone	0
2007/12/06 20:29:11	Internal	1282 Hz	1 pC	-74 dBm	Normal	Mobile Phone	0
2007/12/06 20:25:44	Internal	1282 Hz	1 pC	-74 dBm	Normal	Mobile Phone	0

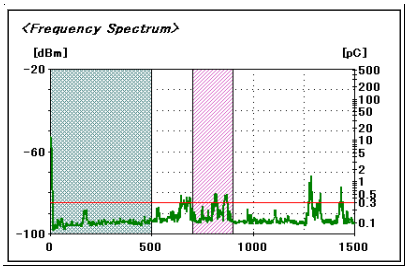

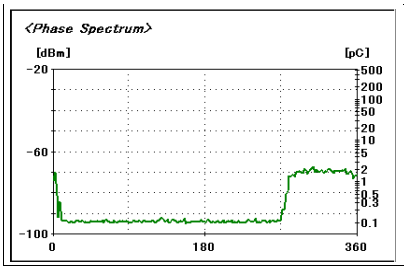

211

R225 8kV 3atm UHF A

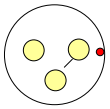

2007/12/05 17:53:10	Internal	1026 Hz	0.9 pC	-75 dBm	Abnormal	Protrusion	1
2007/12/05 17:49:36	Internal	1026 Hz	0.9 pC	-75 dBm	Abnormal	Protrusion	1
2007/12/05 17:46:03	Internal	1028 Hz	1.1 pC	-74 dBm	Abnormal	Protrusion	4
2007/12/05 17:42:30	Internal	1024 Hz	0.7 pC	-78 dBm	Abnormal	Protrusion	1
2007/12/05 17:38:58	Internal	1028 Hz	0.9 pC	-76 dBm	Abnormal	Protrusion	1
2007/12/05 17:35:26	Internal	1026 Hz	0.7 pC	-78 dBm	Abnormal	Protrusion	1
2007/12/05 17:31:56	Internal	1028 Hz	0.5 pC	-81 dBm	Abnormal	Protrusion	1
2007/12/05 17:28:26	Internal	1026 Hz	0.8 pC	-77 dBm	Abnormal	Protrusion	1

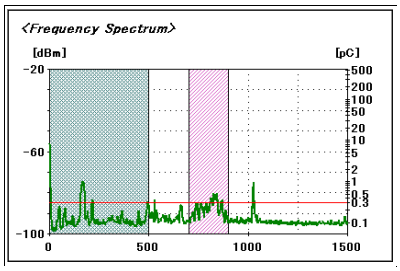

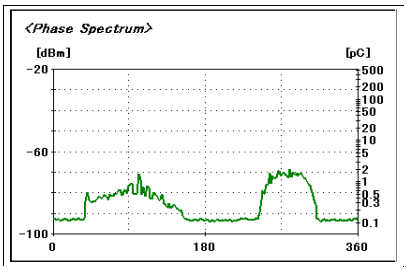

212

R225 8kV 3atm UHF B

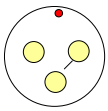

2007/12/05 17:54:21	Internal	604 Hz	0.2 pC	-89 dBm	Normal	Normal	0
2007/12/05 17:50:47	Internal	602 Hz	0.2 pC	-90 dBm	Normal	Normal	0
2007/12/05 17:47:13	Internal	530 Hz	0.2 pC	-90 dBm	Normal	Normal	0
2007/12/05 17:43:41	Internal	970 Hz	0.2 pC	-89 dBm	Normal	Protrusion	0
2007/12/05 17:40:08	Internal	968 Hz	0.2 pC	-89 dBm	Normal	Protrusion	0
2007/12/05 17:36:37	Internal	530 Hz	0.2 pC	-90 dBm	Normal	Normal	0
2007/12/05 17:33:06	Internal	602 Hz	0.2 pC	-90 dBm	Normal	Normal	0
2007/12/05 17:29:36	Internal	602 Hz	0.2 pC	-90 dBm	Normal	Normal	0
2007/12/05 17:26:06	Internal	970 Hz	0.2 pC	-87 dBm	Normal	Protrusion	0

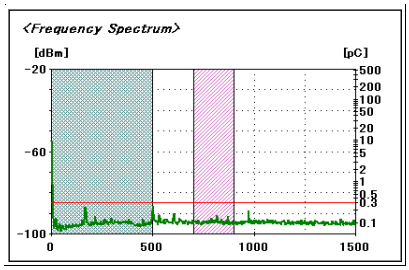

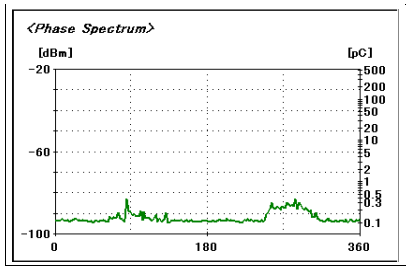

213

R225 8kV 3atm UHF C

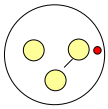

2007/12/05 17:55:33	Internal	530 Hz	0.5 pC	-81 dBm	Normal	External Noise	0
2007/12/05 17:51:58	Internal	530 Hz	0.5 pC	-81 dBm	Normal	External Noise	0
2007/12/05 17:48:25	Internal	530 Hz	0.5 pC	-81 dBm	Normal	External Noise	0
2007/12/05 17:44:51	Internal	530 Hz	0.5 pC	-81 dBm	Normal	External Noise	0
2007/12/05 17:41:19	Internal	916 Hz	0.8 pC	-77 dBm	Normal	Normal	0
2007/12/05 17:37:47	Internal	530 Hz	0.5 pC	-81 dBm	Normal	External Noise	0
2007/12/05 17:34:16	Internal	530 Hz	0.5 pC	-81 dBm	Normal	External Noise	0
2007/12/05 17:30:46	Internal	530 Hz	0.5 pC	-81 dBm	Normal	External Noise	0
2007/12/05 17:27:16	Internal	530 Hz	0.5 pC	-81 dBm	Normal	External Noise	0

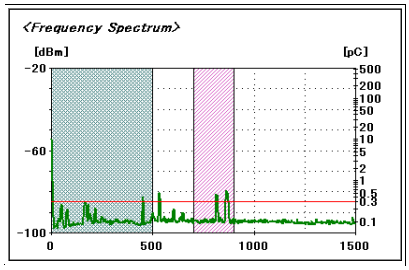

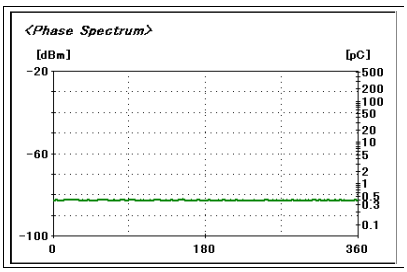

R225 12kV 3atm UHF A

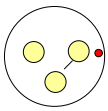

2007/12/05 18:26:25	Internal	1028 Hz	6.3 pC	-59 dBm	Abnormal	Protrusion	5
2007/12/05 18:22:45	Internal	1024 Hz	7.2 pC	-57 dBm	Abnormal	Protrusion	5
2007/12/05 18:19:05	Internal	1026 Hz	6.3 pC	-59 dBm	Abnormal	Protrusion	5
2007/12/05 18:15:27	Internal	1028 Hz	4.8 pC	-61 dBm	Abnormal	Protrusion	5
2007/12/05 18:09:33	Internal	1024 Hz	6.9 pC	-58 dBm	Abnormal	Protrusion	5
2007/12/05 18:06:02	Internal	1028 Hz	6.6 pC	-58 dBm	Abnormal	Protrusion	5
2007/12/05 18:02:32	Internal	1026 Hz	4.3 pC	-62 dBm	Abnormal	Protrusion	5
2007/12/05 17:59:02	Internal	1026 Hz	4.5 pC	-61 dBm	Abnormal	Protrusion	5

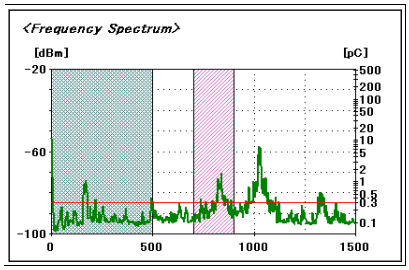

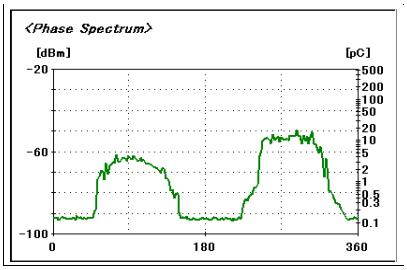

215

R225 12kV 3atm UHF B

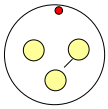

2007/12/05 18:27:38	Internal	970 Hz	1.4 pC	-71 dBm	Abnormal	Protrusion	4
2007/12/05 18:23:58	Internal	970 Hz	1.2 pC	-73 dBm	Abnormal	Protrusion	4
2007/12/05 18:20:18	Internal	1192 Hz	0.9 pC	-75 dBm	Abnormal	Protrusion	1
2007/12/05 18:16:40	Internal	972 Hz	0.9 pC	-75 dBm	Abnormal	Protrusion	1
2007/12/05 18:10:44	Internal	972 Hz	0.8 pC	-77 dBm	Abnormal	Protrusion	1
2007/12/05 18:07:12	Internal	972 Hz	0.8 pC	-76 dBm	Abnormal	Protrusion	1
2007/12/05 18:03:42	Internal	970 Hz	1.6 pC	-70 dBm	Abnormal	Protrusion	4
2007/12/05 18:00:12	Internal	968 Hz	1.1 pC	-74 dBm	Abnormal	Protrusion	4

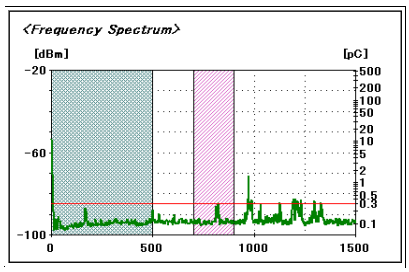

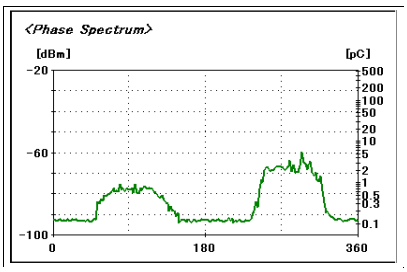

216

R225 12kV 3atm UHF C

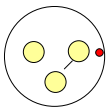

2007/12/05 18:28:52	Internal	1330 Hz	0.5 pC	-80 dBm	Abnormal	Protrusion	1
2007/12/05 18:25:11	Internal	1332 Hz	0.7 pC	-78 dBm	Abnormal	Protrusion	1
2007/12/05 18:21:31	Internal	530 Hz	0.5 pC	-81 dBm	Normal	External Noise	0
2007/12/05 18:17:52	Internal	1288 Hz	0.7 pC	-77 dBm	Abnormal	Protrusion	1
2007/12/05 18:14:16	Internal	530 Hz	0.5 pC	-81 dBm	Normal	External Noise	0
2007/12/05 18:13:06	Internal	530 Hz	0.5 pC	-81 dBm	Normal	External Noise	0
2007/12/05 18:11:55	Internal	530 Hz	0.5 pC	-81 dBm	Normal	External Noise	0
2007/12/05 18:08:23	Internal	530 Hz	0.5 pC	-81 dBm	Normal	External Noise	0

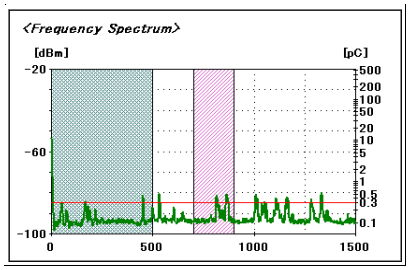

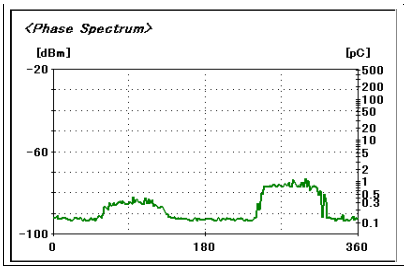

217

R225 16kV 3atm UHF A

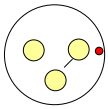

2007/12/05 19:02:03	Internal	1024 Hz	10.4 pC	-54 dBm	Abnormal	Protrusion	5
2007/12/05 18:58:23	Internal	1026 Hz	8.7 pC	-56 dBm	Abnormal	Protrusion	5
2007/12/05 18:54:44	Internal	1028 Hz	6.9 pC	-58 dBm	Abnormal	Protrusion	5
2007/12/05 18:51:06	Internal	1030 Hz	11.9 pC	-53 dBm	Abnormal	Protrusion	5
2007/12/05 18:47:29	Internal	1024 Hz	13.1 pC	-52 dBm	Abnormal	Protrusion	5
2007/12/05 18:43:53	Internal	1028 Hz	11.4 pC	-53 dBm	Abnormal	Protrusion	5
2007/12/05 18:40:18	Internal	1028 Hz	15.7 pC	-51 dBm	Abnormal	Protrusion	5
2007/12/05 18:36:44	Internal	1024 Hz	13.7 pC	-52 dBm	Abnormal	Protrusion	5
2007/12/05 18:33:10	Internal	1026 Hz	14.4 pC	-51 dBm	Abnormal	Free Particle	2

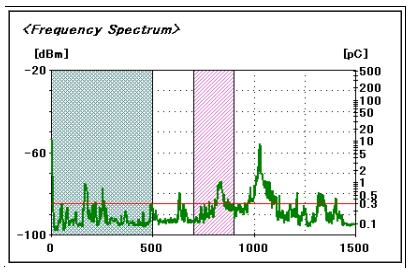

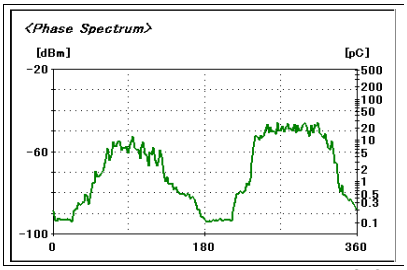

218

R225 16kV 3atm UHF B

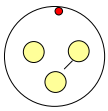

2007/12/05 19:03:16	Internal	972 Hz	1.7 pC	-70 dBm	Abnormal	Protrusion	4
2007/12/05 18:59:36	Internal	972 Hz	2.4 pC	-67 dBm	Abnormal	Protrusion	4
2007/12/05 18:55:57	Internal	970 Hz	2.1 pC	-68 dBm	Abnormal	Protrusion	4
2007/12/05 18:52:19	Internal	972 Hz	1.2 pC	-73 dBm	Abnormal	Protrusion	4
2007/12/05 18:48:42	Internal	966 Hz	0.9 pC	-75 dBm	Abnormal	Protrusion	1
2007/12/05 18:45:05	Internal	972 Hz	2.2 pC	-68 dBm	Abnormal	Protrusion	4
2007/12/05 18:41:30	Internal	970 Hz	1.9 pC	-69 dBm	Abnormal	Protrusion	4
2007/12/05 18:37:55	Internal	972 Hz	1.4 pC	-72 dBm	Abnormal	Protrusion	4
2007/12/05 18:34:21	Internal	968 Hz	3.3 pC	-64 dBm	Abnormal	Protrusion	5

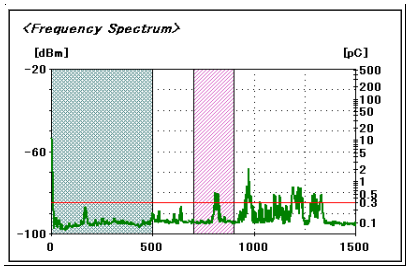

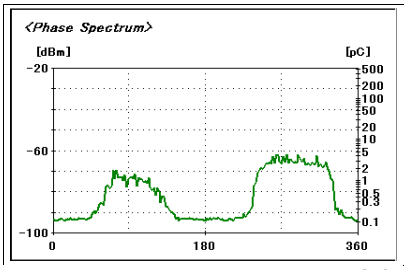

219

R225 16kV 3atm UHF C

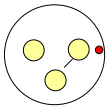

2007/12/05 19:04:30	Internal	1006 Hz	0.7 pC	-78 dBm	Abnormal	Protrusion	1
2007/12/05 19:00:49	Internal	1052 Hz	0.9 pC	-75 dBm	Abnormal	Protrusion	1
2007/12/05 18:57:10	Internal	1162 Hz	1.1 pC	-74 dBm	Abnormal	Protrusion	4
2007/12/05 18:53:32	Internal	1108 Hz	0.6 pC	-79 dBm	Abnormal	Protrusion	1
2007/12/05 18:49:54	Internal	1106 Hz	0.6 pC	-79 dBm	Abnormal	Protrusion	1
2007/12/05 18:46:17	Internal	1288 Hz	0.6 pC	-79 dBm	Abnormal	Protrusion	1
2007/12/05 18:42:42	Internal	1332 Hz	0.6 pC	-79 dBm	Abnormal	Protrusion	1
2007/12/05 18:39:07	Internal	1332 Hz	0.8 pC	-77 dBm	Abnormal	Protrusion	1
2007/12/05 18:35:32	Internal	1286 Hz	0.6 pC	-79 dBm	Abnormal	Protrusion	1

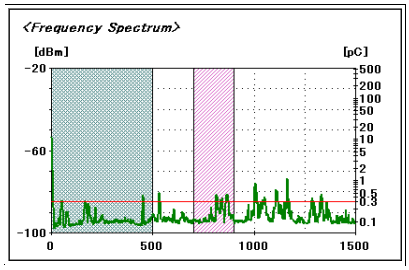

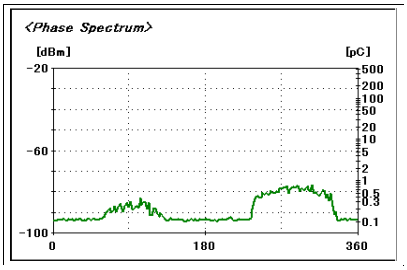

220

S135 3atm 12kV UHF A

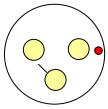

2007/12/07 14:06:01	Internal	516 Hz	1.2 pC	-73 dBm	Normal	External Noise	0
2007/12/07 14:02:25	Internal	502 Hz	3.4 pC	-64 dBm	Normal	External Noise	0
2007/12/07 13:58:52	Internal	916 Hz	2.5 pC	-67 dBm	Normal	External Noise	0
2007/12/07 13:55:20	Internal	502 Hz	1.9 pC	-69 dBm	Normal	External Noise	0
2007/12/07 13:51:47	Internal	512 Hz	1.5 pC	-71 dBm	Normal	External Noise	0
2007/12/07 13:48:17	Internal	516 Hz	1.1 pC	-74 dBm	Normal	External Noise	0
2007/12/07 13:44:49	Internal	502 Hz	1.8 pC	-69 dBm	Normal	External Noise	0
2007/12/07 13:41:20	Internal	504 Hz	1.6 pC	-70 dBm	Normal	External Noise	0
2007/12/07 13:37:53	Internal	502 Hz	3.3 pC	-64 dBm	Normal	External Noise	0

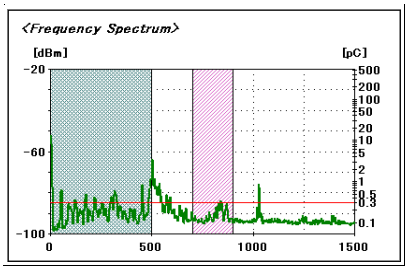

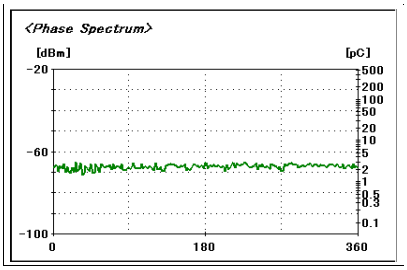

221

S135 3atm 12kV UHF B

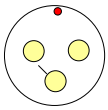

2007/12/07 14:07:13	Internal	1222 Hz	0.3 pC	-85 dBm	Normal	Particle on Spacer	0
2007/12/07 14:03:37	Internal	532 Hz	0.2 pC	-89 dBm	Normal	Normal	0
2007/12/07 14:00:03	Internal	922 Hz	0.3 pC	-85 dBm	Normal	Normal	0
2007/12/07 13:56:30	Internal	534 Hz	0.2 pC	-89 dBm	Normal	Normal	0
2007/12/07 13:52:58	Internal	1222 Hz	0.2 pC	-89 dBm	Normal	Particle on Spacer	0
2007/12/07 13:49:27	Internal	1230 Hz	0.2 pC	-88 dBm	Normal	Particle on Spacer	0
2007/12/07 13:45:58	Internal	972 Hz	0.2 pC	-87 dBm	Normal	Particle on Spacer	0
2007/12/07 13:42:30	Internal	972 Hz	0.2 pC	-87 dBm	Normal	Particle on Spacer	0
2007/12/07 13:39:02	Internal	968 Hz	0.3 pC	-85 dBm	Normal	Particle on Spacer	0

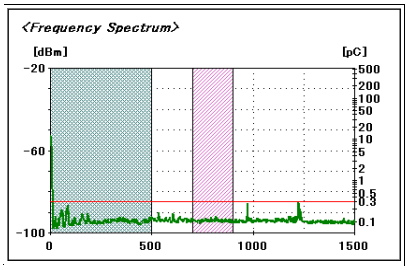

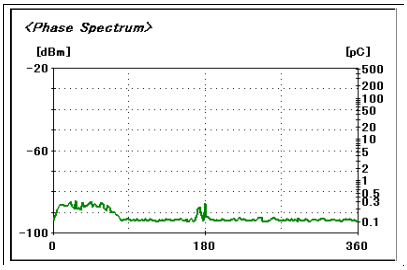

222

S135 3atm 12kV UHF C

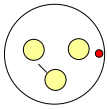

2007/12/07 14:08:25	Internal	648 Hz	0.3 pC	-86 dBm	Normal	Normal	0
2007/12/07 14:04:49	Internal	650 Hz	0.2 pC	-87 dBm	Normal	Normal	0
2007/12/07 14:01:14	Internal	648 Hz	0.2 pC	-87 dBm	Normal	Normal	0
2007/12/07 13:57:41	Internal	648 Hz	0.2 pC	-87 dBm	Normal	Normal	0
2007/12/07 13:54:09	Internal	926 Hz	0.7 pC	-77 dBm	Normal	Normal	0
2007/12/07 13:50:37	Internal	650 Hz	0.2 pC	-87 dBm	Normal	Normal	0
2007/12/07 13:47:08	Internal	648 Hz	0.2 pC	-87 dBm	Normal	Normal	0
2007/12/07 13:43:39	Internal	1322 Hz	0.5 pC	-81 dBm	Abnormal	Particle on Spacer	5
2007/12/07 13:40:11	Internal	650 Hz	0.2 pC	-88 dBm	Normal	Mobile Phone	0

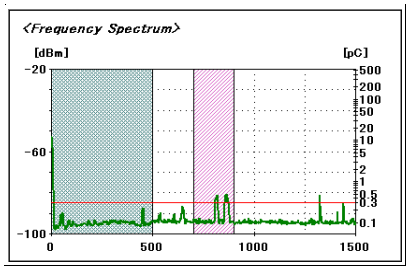

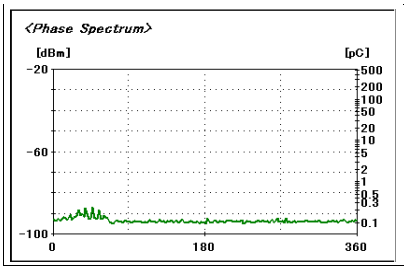

223

S135 3atm 16kV UHF A

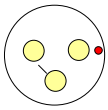

2007/12/07 14:39:32	Internal	536 Hz	0.9 pC	-75 dBm	Normal	External Noise	0
2007/12/07 14:35:56	Internal	502 Hz	3.6 pC	-63 dBm	Normal	External Noise	0
2007/12/07 14:32:21	Internal	502 Hz	3.6 pC	-63 dBm	Normal	External Noise	0
2007/12/07 14:28:46	Internal	502 Hz	1.5 pC	-71 dBm	Normal	External Noise	0
2007/12/07 14:25:13	Internal	502 Hz	1.4 pC	-72 dBm	Normal	External Noise	0
2007/12/07 14:21:40	Internal	502 Hz	1.5 pC	-71 dBm	Normal	External Noise	0
2007/12/07 14:18:08	Internal	502 Hz	2.2 pC	-68 dBm	Normal	External Noise	0
2007/12/07 14:14:37	Internal	502 Hz	2 pC	-69 dBm	Normal	External Noise	0
2007/12/07 14:11:07	Internal	502 Hz	2.6 pC	-66 dBm	Normal	External Noise	0

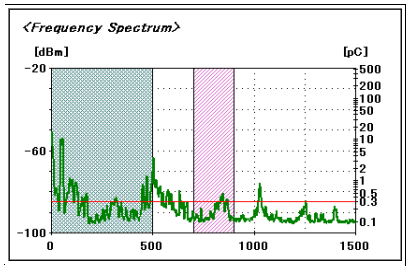

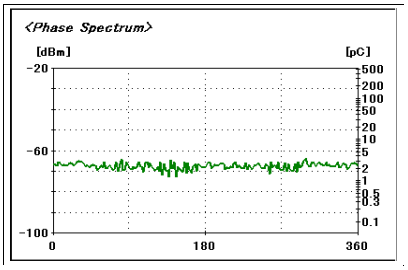

224

S135 3atm 16kV UHF B

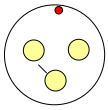

2007/12/07 14:40:44	Internal	924 Hz	0.6 pC	-79 dBm	Normal	Normal	0
2007/12/07 14:37:08	Internal	970 Hz	0.3 pC	-84 dBm	Abnormal	Particle on Spacer	5
2007/12/07 14:33:32	Internal	970 Hz	0.3 pC	-84 dBm	Abnormal	Particle on Spacer	5
2007/12/07 14:29:58	Internal	970 Hz	0.4 pC	-82 dBm	Abnormal	Particle on Spacer	5
2007/12/07 14:26:24	Internal	968 Hz	0.3 pC	-85 dBm	Abnormal	Particle on Spacer	5
2007/12/07 14:22:51	Internal	1228 Hz	0.3 pC	-84 dBm	Abnormal	Floating Electrode	1
2007/12/07 14:19:19	Internal	970 Hz	0.7 pC	-78 dBm	Abnormal	Particle on Spacer	5
2007/12/07 14:15:47	Internal	972 Hz	0.8 pC	-77 dBm	Abnormal	Particle on Spacer	5
2007/12/07 14:12:17	Internal	972 Hz	0.4 pC	-82 dBm	Abnormal	Particle on Spacer	5

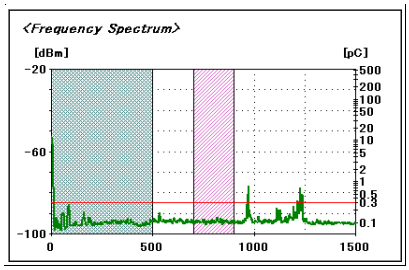

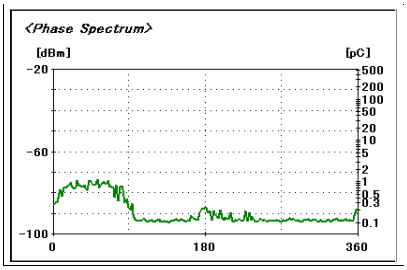

225

S135 3atm 16kV UHF C

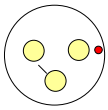

2007/12/07 14:41:58	Internal	918 Hz	3.6 pC	-63 dBm	Normal	Normal	0
2007/12/07 14:38:20	Internal	648 Hz	0.2 pC	-87 dBm	Normal	Normal	0
2007/12/07 14:34:44	Internal	916 Hz	1.7 pC	-70 dBm	Normal	Normal	0
2007/12/07 14:31:09	Internal	652 Hz	0.2 pC	-89 dBm	Normal	Particle on Spacer	0
2007/12/07 14:27:35	Internal	530 Hz	0.2 pC	-88 dBm	Normal	Normal	0
2007/12/07 14:24:02	Internal	648 Hz	0.3 pC	-86 dBm	Normal	Normal	0
2007/12/07 14:20:29	Internal	648 Hz	0.3 pC	-86 dBm	Normal	Normal	0
2007/12/07 14:16:58	Internal	648 Hz	0.2 pC	-88 dBm	Normal	Normal	0
2007/12/07 14:13:27	Internal	1334 Hz	0.2 pC	-87 dBm	Normal	Particle on Spacer	0

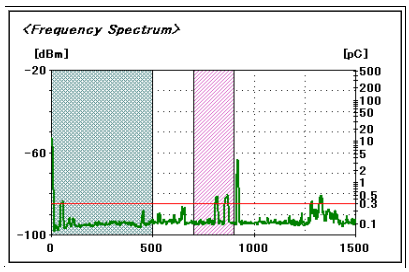

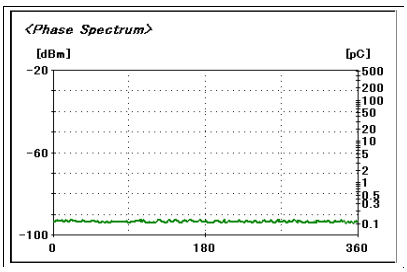

226

S135 3atm 24kV UHF A

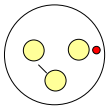

2007/12/07 15:34:26	Internal	1028 Hz	5.5 pC	-60 dBm	Abnormal	Particle on Spacer	5
2007/12/07 15:31:00	Internal	1028 Hz	6.9 pC	-58 dBm	Abnormal	Particle on Spacer	5
2007/12/07 15:27:32	Internal	1028 Hz	3.6 pC	-63 dBm	Abnormal	Particle on Spacer	5

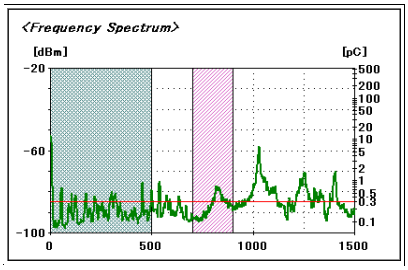

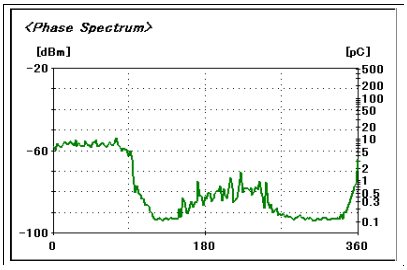

227

S135 3atm 24kV UHF B

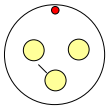

2007/12/07 15:35:34	Internal	1230 Hz	0.9 pC	-75 dBm	Abnormal	Particle on Spacer	5
2007/12/07 15:32:09	Internal	970 Hz	1.4 pC	-71 dBm	Abnormal	Particle on Spacer	5
2007/12/07 15:28:42	Internal	970 Hz	2.3 pC	-67 dBm	Abnormal	Particle on Spacer	5

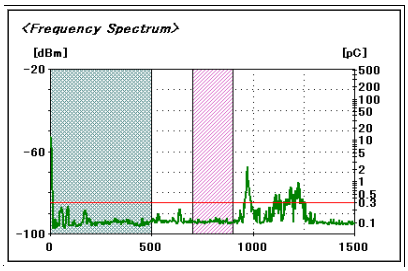

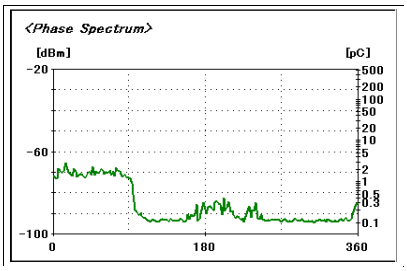

228

S135 3atm 24kV UHF A

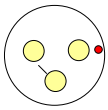

2007/12/07 15:36:44	Internal	926 Hz	1.5 pC	-71 dBm	Normal	Normal	0
2007/12/07 15:33:17	Internal	1330 Hz	0.6 pC	-79 dBm	Abnormal	Particle on Spacer	5
2007/12/07 15:29:51	Internal	644 Hz	0.6 pC	-79 dBm	Abnormal	Particle on Spacer	5

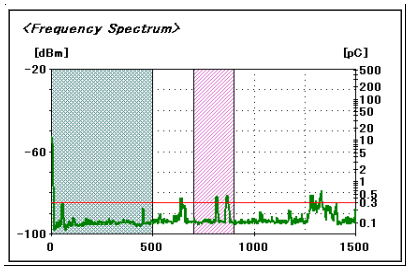

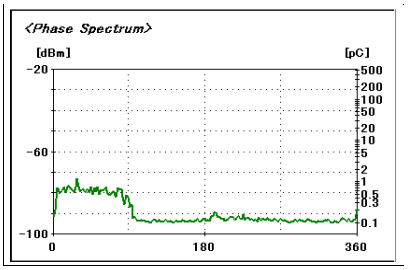

229

S270 3atm 24kV UHF A

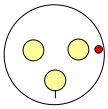

2007/12/07 22:56:37	Internal	1026 Hz	18.1 pC	-49 dBm	Abnormal	Particle on Spacer	5
2007/12/07 22:53:07	Internal	1024 Hz	15 pC	-51 dBm	Abnormal	Particle on Spacer	5
2007/12/07 22:49:37	Internal	1022 Hz	13.7 pC	-52 dBm	Abnormal	Particle on Spacer	5
2007/12/07 22:46:07	Internal	1026 Hz	21.7 pC	-48 dBm	Abnormal	Particle on Spacer	5
2007/12/07 22:42:38	Internal	1024 Hz	15 pC	-51 dBm	Abnormal	Particle on Spacer	5
2007/12/07 22:39:09	Internal	1024 Hz	7.2 pC	-57 dBm	Abnormal	Particle on Spacer	5
2007/12/07 22:35:41	Internal	1026 Hz	3.1 pC	-65 dBm	Abnormal	Particle on Spacer	5
2007/12/07 22:32:12	Internal	1024 Hz	9.9 pC	-55 dBm	Abnormal	Particle on Spacer	5
2007/12/07 22:28:45	Internal	1028 Hz	9.1 pC	-55 dBm	Abnormal	Particle on Spacer	5

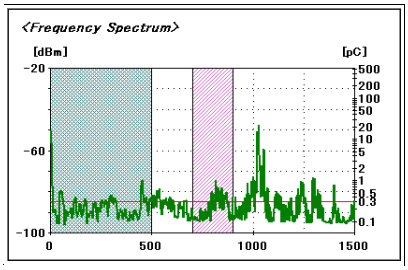

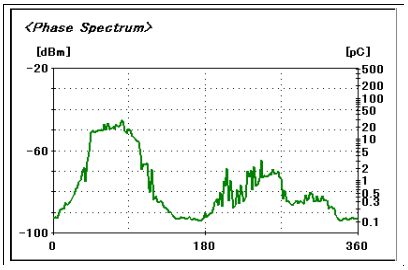

230

S270 3atm 24kV UHF B

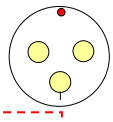

2007/12/07 22:57:47	Internal	1026 Hz	0.5 pC	-81 dBm	Abnormal	Particle on Spacer	5
2007/12/07 22:54:17	Internal	1184 Hz	0.9 pC	-75 dBm	Abnormal	Floating Particle	3
2007/12/07 22:50:47	Internal	1176 Hz	0.4 pC	-83 dBm	Abnormal	Floating Particle	3
2007/12/07 22:47:17	Internal	1188 Hz	0.9 pC	-76 dBm	Abnormal	Particle on Spacer	5
2007/12/07 22:43:48	Internal	1188 Hz	0.5 pC	-80 dBm	Abnormal	Floating Particle	3
2007/12/07 22:40:19	Internal	640 Hz	0.3 pC	-85 dBm	Abnormal	Floating Particle	3
2007/12/07 22:36:50	Internal	1188 Hz	0.4 pC	-83 dBm	Abnormal	Particle on Spacer	5
2007/12/07 22:33:22	Internal	1190 Hz	0.8 pC	-77 dBm	Abnormal	Floating Particle	3
2007/12/07 22:29:54	Internal	1188 Hz	0.3 pC	-84 dBm	Abnormal	Floating Particle	3

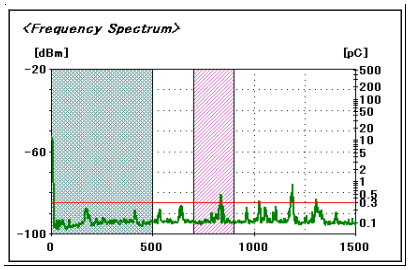

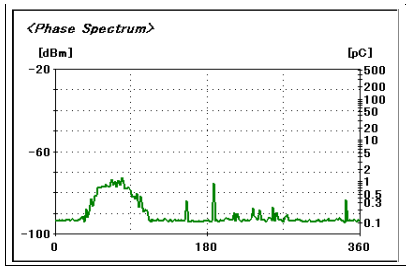

231

S270 3atm 24kV UHF D

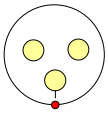

2007/12/07 22:58:57	Internal	1048 Hz	0.2 pC	-89 dBm	Abnormal	Protrusion	1
2007/12/07 22:55:27	Internal	1048 Hz	0.3 pC	-85 dBm	Abnormal	Floating Particle	3
2007/12/07 22:51:57	Internal	1052 Hz	0.5 pC	-81 dBm	Abnormal	Floating Particle	3
2007/12/07 22:48:27	Internal	638 Hz	0.2 pC	-89 dBm	Normal	Particle on Spacer	0
2007/12/07 22:44:58	Internal	1052 Hz	0.2 pC	-87 dBm	Normal	Floating Particle	0
2007/12/07 22:41:29	Internal	1056 Hz	0.3 pC	-86 dBm	Normal	Floating Particle	0
2007/12/07 22:38:00	Internal	638 Hz	0.2 pC	-91 dBm	Normal	Normal	0
2007/12/07 22:34:31	Internal	640 Hz	0.2 pC	-91 dBm	Normal	Normal	0
2007/12/07 22:31:03	Internal	1244 Hz	0.2 pC	-90 dBm	Normal	Normal	0

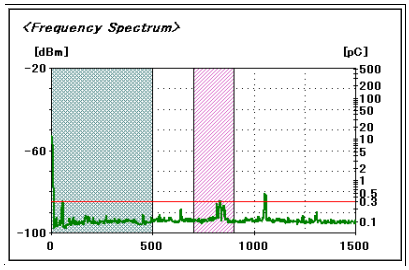

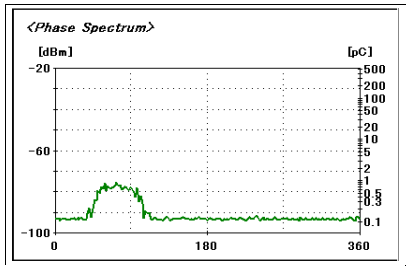

232

S270 3atm 36kV UHF A

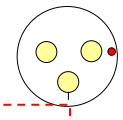

2007/12/07 22:21:48	Internal	1024 Hz	18.9 pC	-49 dBm	Abnormal	Particle on Spacer	5
2007/12/07 22:18:19	Internal	1024 Hz	26.1 pC	-46 dBm	Abnormal	Spacer Crack	5
2007/12/07 22:14:54	Internal	1024 Hz	15.7 pC	-51 dBm	Abnormal	Spacer Crack	5
2007/12/07 22:11:27	Internal	1024 Hz	13.7 pC	-52 dBm	Abnormal	Spacer Crack	5
2007/12/07 22:07:58	Internal	1026 Hz	18.9 pC	-49 dBm	Abnormal	Spacer Crack	5
2007/12/07 22:04:26	Internal	1022 Hz	15 pC	-51 dBm	Abnormal	Spacer Crack	5
2007/12/07 22:00:55	Internal	1026 Hz	13.1 pC	-52 dBm	Abnormal	Spacer Crack	5
2007/12/07 21:57:25	Internal	1022 Hz	9.9 pC	-55 dBm	Abnormal	Particle on Spacer	5
2007/12/07 21:53:56	Internal	1024 Hz	14.4 pC	-51 dBm	Abnormal	Particle on Spacer	5

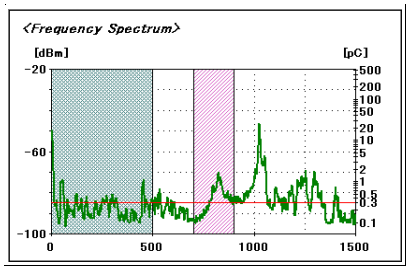

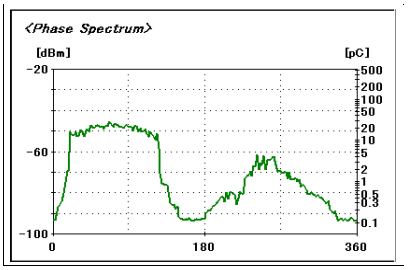

233

S270 3atm 36kV UHF B

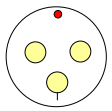

2007/12/07 22:22:56	Internal	1188 Hz	0.9 pC	-75 dBm	Abnormal	Protrusion	1
2007/12/07 22:19:27	Internal	1182 Hz	0.7 pC	-78 dBm	Abnormal	Particle on Spacer	5
2007/12/07 22:16:02	Internal	1186 Hz	0.7 pC	-78 dBm	Abnormal	Particle on Spacer	5
2007/12/07 22:12:39	Internal	1190 Hz	0.7 pC	-78 dBm	Abnormal	Particle on Spacer	5
2007/12/07 22:09:08	Internal	1188 Hz	1 pC	-74 dBm	Abnormal	Particle on Spacer	5
2007/12/07 22:05:37	Internal	1190 Hz	0.6 pC	-79 dBm	Abnormal	Particle on Spacer	5
2007/12/07 22:02:06	Internal	1188 Hz	1.4 pC	-72 dBm	Abnormal	Particle on Spacer	5
2007/12/07 21:58:35	Internal	1186 Hz	0.5 pC	-80 dBm	Abnormal	Particle on Spacer	5
2007/12/07 21:55:06	Internal	1180 Hz	0.3 pC	-84 dBm	Abnormal	Particle on Spacer	5

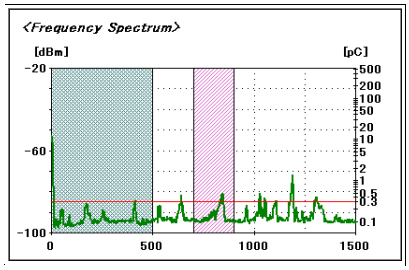

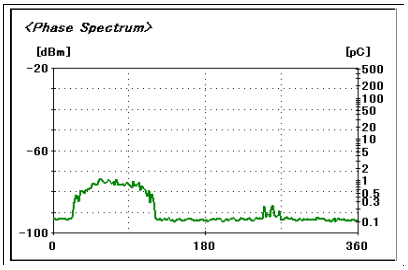

234

S270 3atm 36kV UHF D

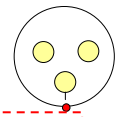

2007/12/07 22:24:04	Internal	1054 Hz	0.3 pC	-86 dBm	Abnormal	Particle on Spacer	5
2007/12/07 22:20:40	Internal	1052 Hz	0.4 pC	-82 dBm	Abnormal	Floating Particle	3
2007/12/07 22:17:11	Internal	1052 Hz	0.4 pC	-82 dBm	Abnormal	Particle on Spacer	5
2007/12/07 22:13:46	Internal	1054 Hz	0.4 pC	-83 dBm	Abnormal	Particle on Spacer	5
2007/12/07 22:10:19	Internal	1052 Hz	0.4 pC	-83 dBm	Abnormal	Particle on Spacer	5
2007/12/07 22:06:47	Internal	1050 Hz	0.4 pC	-83 dBm	Abnormal	Floating Particle	3
2007/12/07 22:03:16	Internal	1050 Hz	0.5 pC	-81 dBm	Abnormal	Particle on Spacer	5
2007/12/07 21:59:45	Internal	1050 Hz	0.4 pC	-83 dBm	Abnormal	Particle on Spacer	5
2007/12/07 21:56:15	Internal	1054 Hz	0.3 pC	-86 dBm	Normal	Particle on Spacer	0

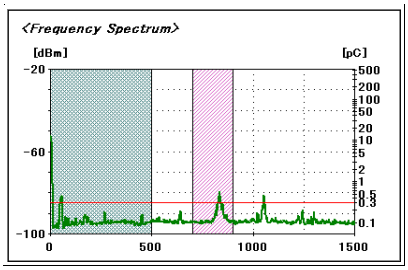

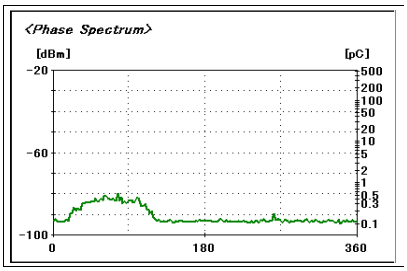

235

S45 3atm 12kV UHF A

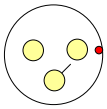

2007/12/10 14:17:27	Internal	1026 Hz	1.5 pC	-71 dBm	Abnormal	Protrusion	4
2007/12/10 14:13:58	Internal	1026 Hz	1.1 pC	-73 dBm	Abnormal	Protrusion	4
2007/12/10 14:10:28	Internal	1026 Hz	1.1 pC	-74 dBm	Abnormal	Protrusion	4
2007/12/10 14:06:59	Internal	1028 Hz	1.4 pC	-71 dBm	Abnormal	Floating Particle	3
2007/12/10 14:03:30	Internal	1028 Hz	1.1 pC	-73 dBm	Abnormal	Protrusion	4
2007/12/10 14:00:06	Internal	1028 Hz	1.5 pC	-71 dBm	Abnormal	Protrusion	4
2007/12/10 13:56:38	Internal	1028 Hz	1 pC	-75 dBm	Abnormal	Protrusion	1
2007/12/10 13:53:10	Internal	1028 Hz	1.6 pC	-71 dBm	Abnormal	Protrusion	4
2007/12/10 13:49:43	Internal	1024 Hz	0.9 pC	-75 dBm	Abnormal	Protrusion	1

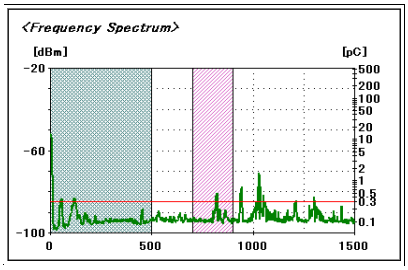

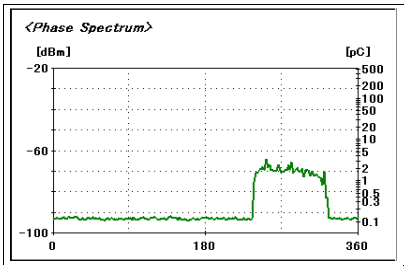

236

S45 3atm 12kV UHF B

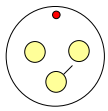

2007/12/10 14:18:38	Internal	964 Hz	0.6 pC	-79 dBm	Abnormal	Protrusion	1
2007/12/10 14:15:08	Internal	962 Hz	0.9 pC	-75 dBm	Abnormal	Protrusion	1
2007/12/10 14:11:38	Internal	960 Hz	0.7 pC	-78 dBm	Abnormal	Protrusion	1
2007/12/10 14:08:09	Internal	962 Hz	0.6 pC	-79 dBm	Abnormal	Protrusion	1
2007/12/10 14:04:40	Internal	964 Hz	0.7 pC	-77 dBm	Abnormal	Protrusion	1
2007/12/10 14:01:14	Internal	962 Hz	0.7 pC	-78 dBm	Abnormal	Protrusion	1
2007/12/10 13:57:47	Internal	962 Hz	0.8 pC	-76 dBm	Abnormal	Protrusion	1
2007/12/10 13:54:19	Internal	960 Hz	0.6 pC	-79 dBm	Abnormal	Protrusion	1
2007/12/10 13:50:52	Internal	962 Hz	0.8 pC	-77 dBm	Abnormal	Protrusion	1

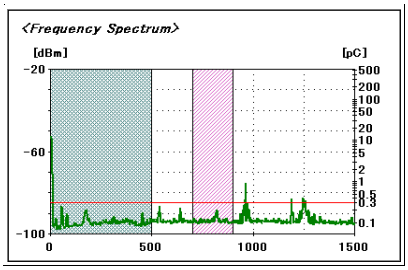

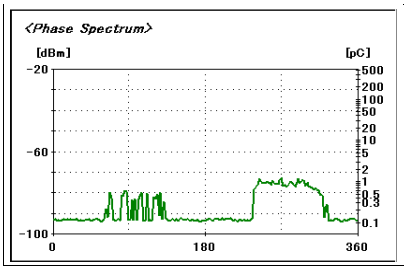

237

S45 3atm 12kV UHF D

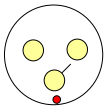

2007/12/10 14:19:48	Internal	638 Hz	0.2 pC	-88 dBm	Abnormal	Protrusion	1
2007/12/10 14:16:17	Internal	638 Hz	0.3 pC	-85 dBm	Abnormal	Protrusion	1
2007/12/10 14:12:48	Internal	534 Hz	0.2 pC	-89 dBm	Normal	Normal	0
2007/12/10 14:09:18	Internal	640 Hz	0.2 pC	-87 dBm	Abnormal	Protrusion	1
2007/12/10 14:05:49	Internal	638 Hz	0.3 pC	-84 dBm	Abnormal	Protrusion	1
2007/12/10 14:02:22	Internal	638 Hz	0.2 pC	-88 dBm	Normal	Protrusion	0
2007/12/10 13:58:55	Internal	534 Hz	0.2 pC	-87 dBm	Normal	Normal	0
2007/12/10 13:55:29	Internal	532 Hz	0.2 pC	-87 dBm	Normal	Normal	0
2007/12/10 13:52:01	Internal	532 Hz	0.2 pC	-88 dBm	Normal	Normal	0

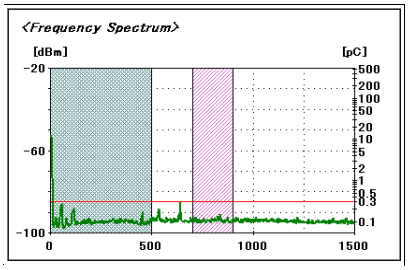

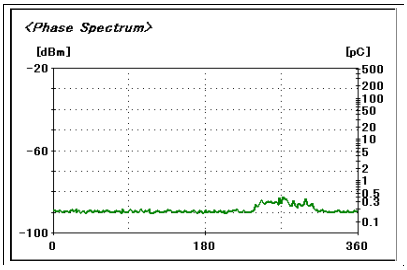

238

S45 3atm 16kV UHF A

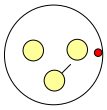

2007/12/10 14:52:30	Internal	1026 Hz	6 pC	-59 dBm	Abnormal	Protrusion	5
2007/12/10 14:49:00	Internal	1028 Hz	2.4 pC	-67 dBm	Abnormal	Protrusion	4
2007/12/10 14:45:30	Internal	1026 Hz	4.8 pC	-61 dBm	Abnormal	Protrusion	5
2007/12/10 14:41:59	Internal	1028 Hz	2.1 pC	-68 dBm	Abnormal	Protrusion	4
2007/12/10 14:38:35	Internal	1028 Hz	3.6 pC	-63 dBm	Abnormal	Protrusion	5
2007/12/10 14:35:04	Internal	1026 Hz	3 pC	-65 dBm	Abnormal	Protrusion	4
2007/12/10 14:31:31	Internal	1026 Hz	2.7 pC	-66 dBm	Abnormal	Protrusion	4
2007/12/10 14:28:00	Internal	1028 Hz	2.1 pC	-68 dBm	Abnormal	Protrusion	4
2007/12/10 14:24:32	Internal	1028 Hz	2.4 pC	-67 dBm	Abnormal	Protrusion	4

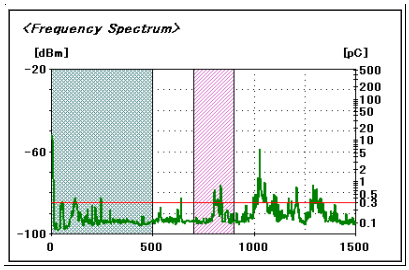

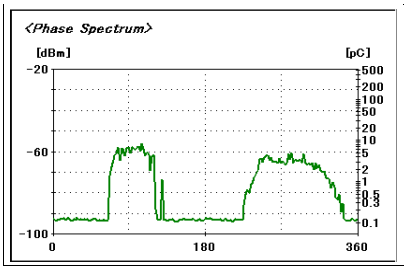

239

S45 3atm 16kV UHF B

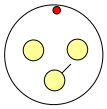

2007/12/10 14:53:41	Internal	964 Hz	1.5 pC	-71 dBm	Abnormal	Protrusion	4
2007/12/10 14:50:10	Internal	962 Hz	1.1 pC	-73 dBm	Abnormal	Protrusion	4
2007/12/10 14:46:40	Internal	960 Hz	1.1 pC	-73 dBm	Abnormal	Protrusion	4
2007/12/10 14:43:09	Internal	964 Hz	1.6 pC	-71 dBm	Abnormal	Protrusion	4
2007/12/10 14:39:43	Internal	1188 Hz	1.4 pC	-72 dBm	Abnormal	Protrusion	4
2007/12/10 14:36:15	Internal	958 Hz	1.5 pC	-71 dBm	Abnormal	Protrusion	4
2007/12/10 14:32:42	Internal	962 Hz	2.1 pC	-68 dBm	Abnormal	Protrusion	4
2007/12/10 14:29:10	Internal	960 Hz	2 pC	-69 dBm	Abnormal	Protrusion	4
2007/12/10 14:25:41	Internal	964 Hz	1.5 pC	-71 dBm	Abnormal	Protrusion	4

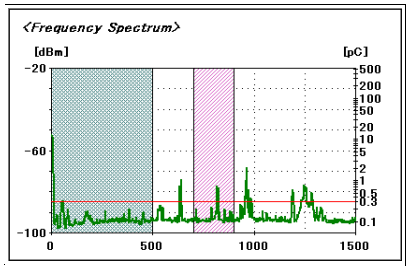

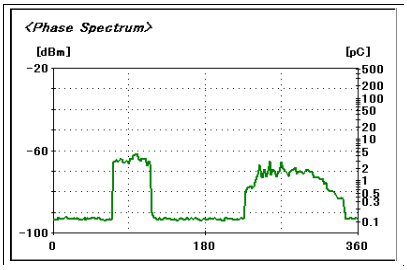

240

S45 3atm 16kV UHF D

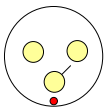

2007/12/10 14:54:51	Internal	642 Hz	0.5 pC	-81 dBm	Abnormal	Protrusion	1
2007/12/10 14:51:20	Internal	644 Hz	0.4 pC	-83 dBm	Abnormal	Protrusion	1
2007/12/10 14:47:50	Internal	638 Hz	0.3 pC	-84 dBm	Abnormal	Protrusion	1
2007/12/10 14:44:20	Internal	642 Hz	0.5 pC	-81 dBm	Abnormal	Protrusion	1
2007/12/10 14:40:51	Internal	640 Hz	0.9 pC	-75 dBm	Abnormal	Protrusion	1
2007/12/10 14:37:27	Internal	640 Hz	0.3 pC	-86 dBm	Abnormal	Protrusion	1
2007/12/10 14:33:53	Internal	640 Hz	0.9 pC	-75 dBm	Abnormal	Protrusion	1
2007/12/10 14:30:20	Internal	642 Hz	0.7 pC	-78 dBm	Abnormal	Protrusion	1
2007/12/10 14:26:50	Internal	642 Hz	0.4 pC	-83 dBm	Abnormal	Protrusion	1

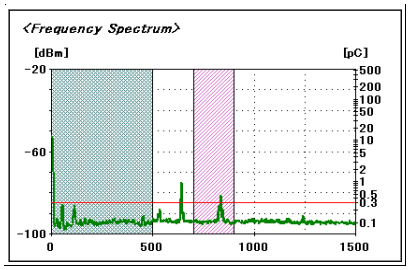

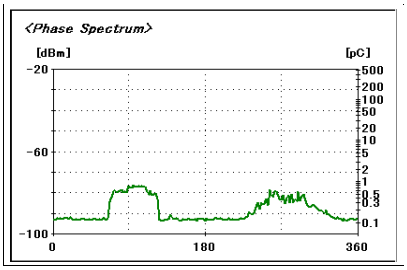

241

EFFECT OF PARTICLE POSITIONS AND PHASE SHIFT SETTING ON SUCCES RATE

EXPERIMENT RESULTS: UHF A, 3 atm (β=0), 2 atm (β=Δ)

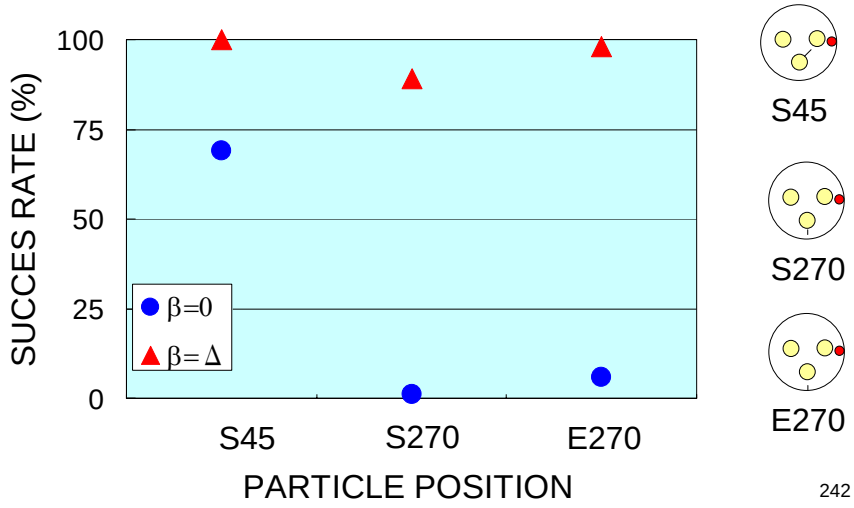

242

EFFECT OF SENSOR POSITIONS AND PHASE SHIFT SETTING ON SUCCES RATE

EXPERIMENT RESULTS: S270, 3 atm, 36 kV, β=150⁰

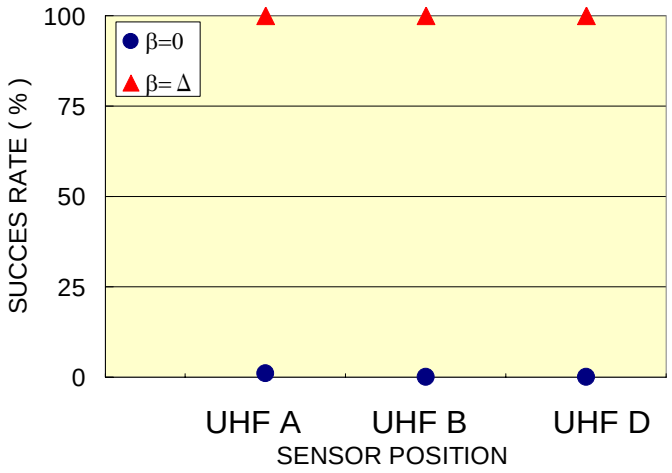

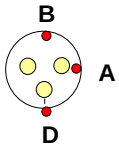

243

S270 36kV 3atm UHF A shift 150

2007/12/09 18:24:02	Internal	1024 Hz	27.4 pC	-46 dBm	Abnormal	Protrusion	5
2007/12/09 18:20:30	Internal	1020 Hz	31.4 pC	-45 dBm	Abnormal	Protrusion	5
2007/12/09 18:16:59	Internal	1026 Hz	17.3 pC	-50 dBm	Abnormal	Protrusion	5
2007/12/09 18:13:29	Internal	1026 Hz	20.8 pC	-48 dBm	Abnormal	Protrusion	5
2007/12/09 18:09:58	Internal	1026 Hz	28.6 pC	-45 dBm	Abnormal	Protrusion	5
2007/12/09 18:06:29	Internal	1026 Hz	12.5 pC	-53 dBm	Abnormal	Protrusion	5
2007/12/09 18:03:00	Internal	1026 Hz	15.7 pC	-51 dBm	Abnormal	Protrusion	5
2007/12/09 17:59:31	Internal	1026 Hz	17.3 pC	-50 dBm	Abnormal	Protrusion	5
2007/12/09 17:56:01	Internal	1024 Hz	1.5 pC	-71 dBm	Abnormal	Protrusion	4

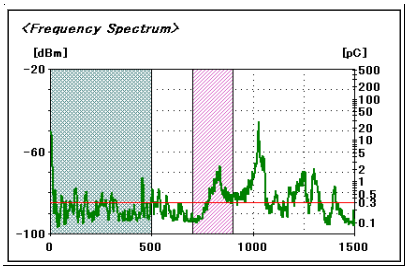

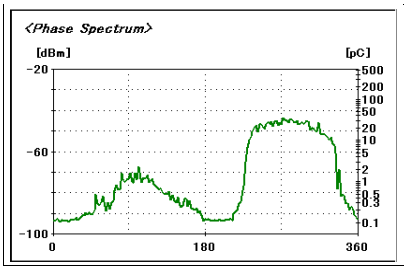

244

S270 36kV 3atm UHF B shift 150

2007/12/09 18:25:13	Internal	1180 Hz	0.7 pC	-78 dBm	Abnormal	Protrusion	1
2007/12/09 18:21:41	Internal	1184 Hz	0.8 pC	-76 dBm	Abnormal	Protrusion	1
2007/12/09 18:18:10	Internal	1188 Hz	0.7 pC	-78 dBm	Abnormal	Protrusion	1
2007/12/09 18:14:39	Internal	1190 Hz	0.7 pC	-77 dBm	Abnormal	Protrusion	1
2007/12/09 18:11:09	Internal	1190 Hz	0.6 pC	-79 dBm	Abnormal	Protrusion	1
2007/12/09 18:07:39	Internal	1190 Hz	0.5 pC	-80 dBm	Abnormal	Protrusion	1
2007/12/09 18:04:09	Internal	1188 Hz	0.5 pC	-80 dBm	Abnormal	Protrusion	1
2007/12/09 18:00:40	Internal	1190 Hz	1.1 pC	-74 dBm	Abnormal	Protrusion	4
2007/12/09 17:57:12	Internal	1178 Hz	0.4 pC	-82 dBm	Abnormal	Protrusion	1

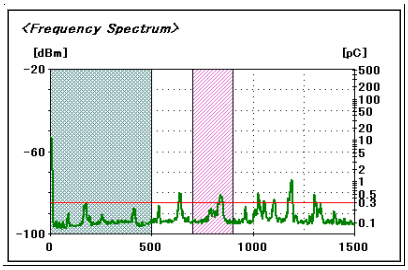

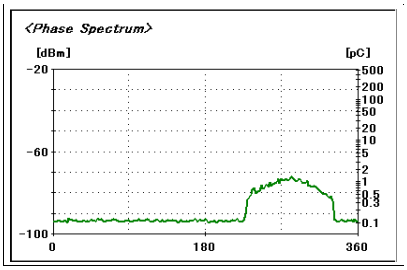

245

S270 36kV 3atm UHF D shift 150

2007/12/09 18:26:23	Internal	1054 Hz	0.4 pC	-82 dBm	Abnormal	Protrusion	1
2007/12/09 18:22:52	Internal	1054 Hz	0.5 pC	-81 dBm	Abnormal	Protrusion	1
2007/12/09 18:19:20	Internal	1050 Hz	0.5 pC	-81 dBm	Abnormal	Protrusion	1
2007/12/09 18:15:49	Internal	1052 Hz	0.5 pC	-81 dBm	Abnormal	Protrusion	1
2007/12/09 18:12:19	Internal	1054 Hz	0.4 pC	-83 dBm	Abnormal	Protrusion	1
2007/12/09 18:08:49	Internal	1052 Hz	0.4 pC	-83 dBm	Abnormal	Protrusion	1
2007/12/09 18:05:19	Internal	1052 Hz	0.3 pC	-84 dBm	Abnormal	Protrusion	1
2007/12/09 18:01:50	Internal	1052 Hz	0.5 pC	-80 dBm	Abnormal	Protrusion	1
2007/12/09 17:58:21	Internal	1050 Hz	0.3 pC	-84 dBm	Abnormal	Protrusion	1

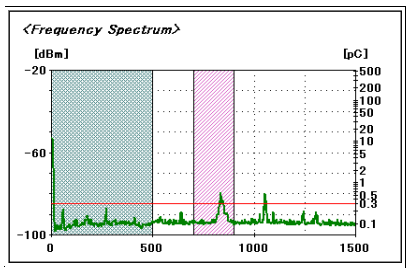

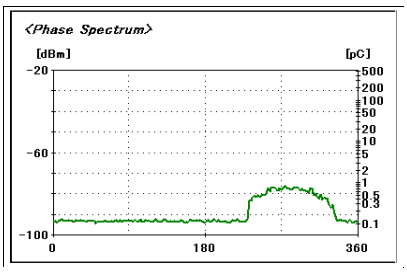

246

S270 3atm 36kV shift 0 UHF D

2007/12/07 22:24:04	1054 Hz	0.3 pC	-86 dBm	Abnormal	Particle on Spacer	5
2007/12/07 22:20:40	1052 Hz	0.4 pC	-82 dBm	Abnormal	Floating Particle	3
2007/12/07 22:17:11	1052 Hz	0.4 pC	-82 dBm	Abnormal	Particle on Spacer	5
2007/12/07 22:13:46	1054 Hz	0.4 pC	-83 dBm	Abnormal	Particle on Spacer	5
2007/12/07 22:10:19	1052 Hz	0.4 pC	-83 dBm	Abnormal	Particle on Spacer	5
2007/12/07 22:06:47	1050 Hz	0.4 pC	-83 dBm	Abnormal	Floating Particle	3
2007/12/07 22:03:16	1050 Hz	0.5 pC	-81 dBm	Abnormal	Particle on Spacer	5
2007/12/07 21:59:45	1050 Hz	0.4 pC	-83 dBm	Abnormal	Particle on Spacer	5
2007/12/07 21:56:15	1054 Hz	0.3 pC	-86 dBm	Normal	Particle on Spacer	0

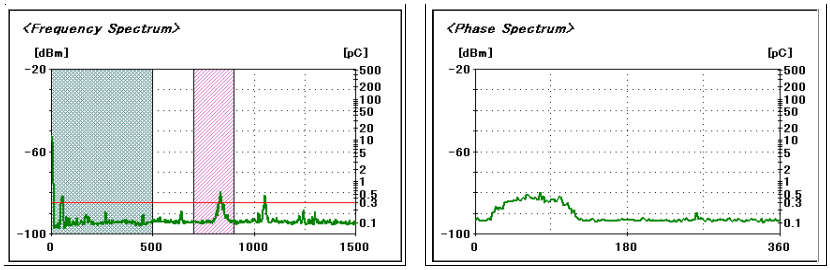

247

EFFECT OF SENSOR POSITIONS AND PHASE SHIFT SETTING ON SUCCES RATE

EXPERIMENT RESULTS: S270, 2 atm, 16 kV, β=150⁰

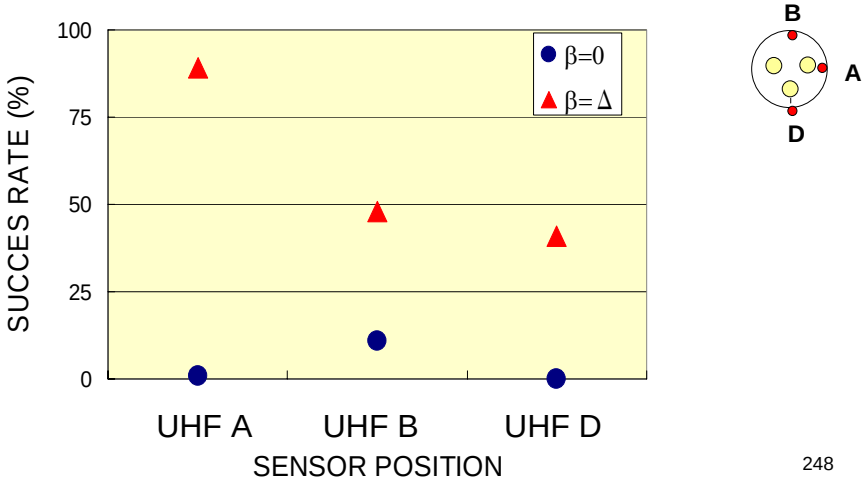

248

S270 2atm 16kV UHF A

Measurement time	nter freque	detection	detection	GIS Condition	Confidence	Risk
2008/02/21 18:27:12	1026 Hz	2.7 pC	-66 dBm	Abnormal	Protrusion	4
2008/02/21 18:23:43	1024 Hz	2.9 pC	-65 dBm	Abnormal	Floating Particle	3
2008/02/21 18:20:14	1026 Hz	2.2 pC	-68 dBm	Abnormal	Protrusion	4
2008/02/21 18:16:46	1024 Hz	4.1 pC	-62 dBm	Abnormal	Protrusion	5
2008/02/21 18:13:18	1026 Hz	4.1 pC	-62 dBm	Abnormal	Protrusion	5
2008/02/21 18:09:50	1028 Hz	2.7 pC	-66 dBm	Abnormal	Protrusion	4
2008/02/21 18:06:22	1018 Hz	1.4 pC	-72 dBm	Abnormal	Floating Particle	3
2008/02/21 18:02:55	1026 Hz	1.3 pC	-72 dBm	Abnormal	Floating Particle	3
2008/02/21 16:51:58	1026 Hz	2.3 pC	-67 dBm	Abnormal	Protrusion	4
2008/02/21 16:48:30	1026 Hz	2.3 pC	-67 dBm	Abnormal	Protrusion	4
2008/02/21 16:45:00	1028 Hz	6.9 pC	-58 dBm	Abnormal	Protrusion	5
2008/02/21 16:41:31	1026 Hz	2.5 pC	-67 dBm	Abnormal	Protrusion	4
2008/02/21 16:38:02	1028 Hz	6.6 pC	-58 dBm	Abnormal	Protrusion	5
2008/02/21 16:34:34	1020 Hz	2.5 pC	-67 dBm	Abnormal	Protrusion	4
2008/02/21 16:31:06	1024 Hz	2.7 pC	-66 dBm	Abnormal	Protrusion	4
2008/02/21 16:27:39	1026 Hz	3.8 pC	-63 dBm	Abnormal	Protrusion	5
2008/02/21 16:24:12	1026 Hz	2.6 pC	-66 dBm	Abnormal	Protrusion	4

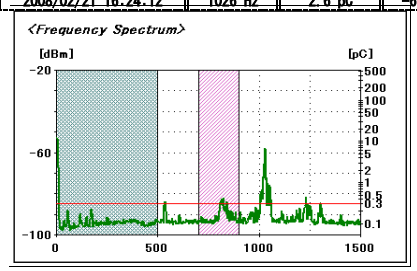

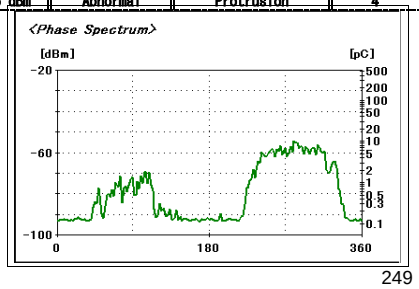

249

S270 2atm 16kV UHF B

Measurement time	nter frequen	detection	k detection [dB	GIS Condition	Confidence	Risk
2008/02/21 18:56:32	698 Hz	0.2 pC	-88 dBm	Normal	Normal	0
2008/02/21 18:53:00	696 Hz	0.2 pC	-88 dBm	Normal	Mobile Phone	0
2008/02/21 18:49:28	1302 Hz	0.2 pC	-87 dBm	Abnormal	Protrusion	1
2008/02/21 18:45:57	698 Hz	0.2 pC	-88 dBm	Normal	Normal	0
2008/02/21 18:42:25	696 Hz	0.2 pC	-88 dBm	Normal	Normal	0
2008/02/21 18:38:54	698 Hz	0.2 pC	-88 dBm	Abnormal	Particle on Spacer	5
2008/02/21 18:35:23	696 Hz	0.2 pC	-88 dBm	Abnormal	Protrusion	1
2008/02/21 18:31:52	698 Hz	0.2 pC	-88 dBm	Normal	Normal	0
2008/02/21 18:28:22	1024 Hz	0.3 pC	-85 dBm	Abnormal	Protrusion	1
2008/02/21 18:24:53	1030 Hz	0.3 pC	-84 dBm	Abnormal	Protrusion	1
2008/02/21 18:21:24	696 Hz	0.5 pC	-81 dBm	Abnormal	Protrusion	1
2008/02/21 18:17:55	696 Hz	0.2 pC	-87 dBm	Normal	Normal	0
2008/02/21 18:14:27	698 Hz	0.3 pC	-86 dBm	Normal	Protrusion	0
2008/02/21 18:10:59	696 Hz	0.2 pC	-88 dBm	Normal	Normal	0
2008/02/21 18:07:32	974 Hz	0.3 pC	-85 dBm	Normal	Normal	0
2008/02/21 18:04:04	698 Hz	0.2 pC	-88 dBm	Normal	Protrusion	0
2008/02/21 16:53:05	532 Hz	0.2 pC	-90 dBm	Normal	Normal	0
2008/02/21 16:49:40	1306 Hz	0.2 pC	-88 dBm	Abnormal	Protrusion	1
2008/02/21 16:46:10	1306 Hz	0.3 pC	-84 dBm	Abnormal	Protrusion	1
2008/02/21 16:42:41	532 Hz	0.2 pC	-89 dBm	Normal	Normal	0
2008/02/21 16:39:12	1302 Hz	0.2 pC	-87 dBm	Normal	Protrusion	0

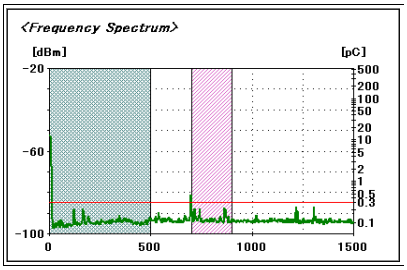

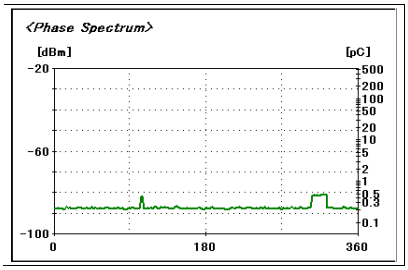

250

S270 2atm 16kV UHF D

2008/02/21 18:36:33	638 Hz	0.5 pC	-80 dBm	Normal	External Noise	0
2008/02/21 18:33:02	638 Hz	0.5 pC	-81 dBm	Normal	External Noise	0
2008/02/21 18:29:32	636 Hz	0.4 pC	-82 dBm	Normal	External Noise	0
2008/02/21 18:26:02	640 Hz	0.5 pC	-80 dBm	Abnormal	Protrusion	1
2008/02/21 18:22:33	638 Hz	0.5 pC	-81 dBm	Normal	External Noise	0
2008/02/21 18:19:05	640 Hz	0.6 pC	-79 dBm	Abnormal	Protrusion	1
2008/02/21 18:15:36	640 Hz	0.5 pC	-80 dBm	Abnormal	Protrusion	1
2008/02/21 18:12:09	638 Hz	0.5 pC	-81 dBm	Normal	External Noise	0
2008/02/21 18:08:41	1028 Hz	0.6 pC	-79 dBm	Abnormal	Protrusion	1
2008/02/21 18:05:13	640 Hz	0.5 pC	-81 dBm	Abnormal	Protrusion	1
2008/02/21 16:54:13	640 Hz	0.5 pC	-81 dBm	Abnormal	Protrusion	1
2008/02/21 16:50:50	640 Hz	0.5 pC	-80 dBm	Abnormal	Protrusion	1
2008/02/21 16:47:20	640 Hz	0.5 pC	-80 dBm	Abnormal	Floating Particle	3
2008/02/21 16:43:50	638 Hz	0.5 pC	-80 dBm	Normal	External Noise	0
2008/02/21 16:40:21	640 Hz	0.6 pC	-79 dBm	Abnormal	Protrusion	1
2008/02/21 16:36:53	640 Hz	0.5 pC	-80 dBm	Abnormal	Protrusion	1
2008/02/21 16:33:25	638 Hz	0.5 pC	-81 dBm	Normal	External Noise	0
2008/02/21 16:29:57	640 Hz	0.5 pC	-80 dBm	Abnormal	Protrusion	1
2008/02/21 16:26:30	640 Hz	0.5 pC	-81 dBm	Abnormal	Particle on Spacer	5

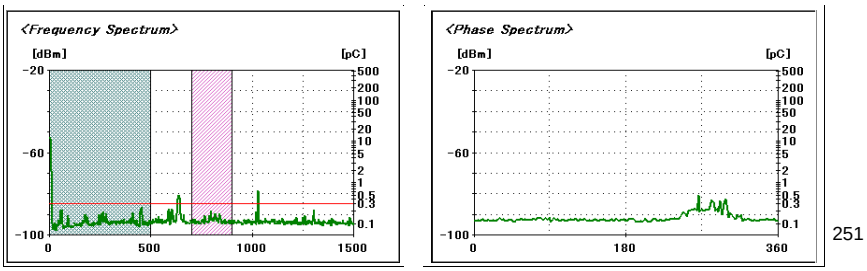

251

EFFECT OF SENSOR POSITIONS AND PHASE SHIFT SETTING ON SUCCES RATE

EXPERIMENT RESULTS: S45, 2 atm, 16 kV

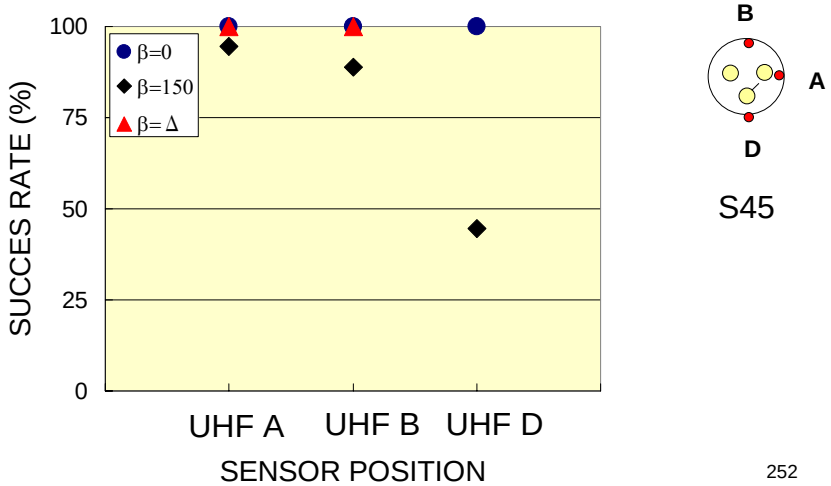

252

S45 2atm 16kV shift 0 UHF D

2008/02/15 17:52:02	1296 Hz	1.5 pC	-71 dBm	Abnormal	Protrusion	4
2008/02/15 17:48:29	970 Hz	0.8 pC	-77 dBm	Abnormal	Protrusion	1
2008/02/15 17:44:56	968 Hz	2 pC	-69 dBm	Abnormal	Protrusion	4
2008/02/15 17:41:24	972 Hz	1.5 pC	-71 dBm	Abnormal	Protrusion	4
2008/02/15 17:37:51	1312 Hz	1 pC	-75 dBm	Abnormal	Protrusion	1
2008/02/15 17:34:20	972 Hz	1.8 pC	-69 dBm	Abnormal	Protrusion	4
2008/02/15 17:30:48	1298 Hz	0.8 pC	-77 dBm	Abnormal	Protrusion	1
2008/02/15 17:27:16	972 Hz	1.6 pC	-70 dBm	Abnormal	Protrusion	4
2008/02/15 17:23:44	972 Hz	1.1 pC	-73 dBm	Abnormal	Protrusion	4
2008/02/15 17:20:13	970 Hz	1.4 pC	-72 dBm	Abnormal	Protrusion	4
2008/02/15 17:16:42	972 Hz	2.1 pC	-68 dBm	Abnormal	Protrusion	4
2008/02/15 17:13:11	972 Hz	1.4 pC	-72 dBm	Abnormal	Protrusion	4
2008/02/15 17:09:41	974 Hz	1 pC	-75 dBm	Abnormal	Protrusion	1
2008/02/15 17:06:11	972 Hz	1.2 pC	-73 dBm	Abnormal	Protrusion	4
2008/02/15 17:02:42	972 Hz	1 pC	-74 dBm	Abnormal	Protrusion	1
2008/02/15 16:59:13	1266 Hz	0.8 pC	-76 dBm	Abnormal	Protrusion	1
2008/02/15 16:55:45	972 Hz	1.6 pC	-71 dBm	Abnormal	Protrusion	4

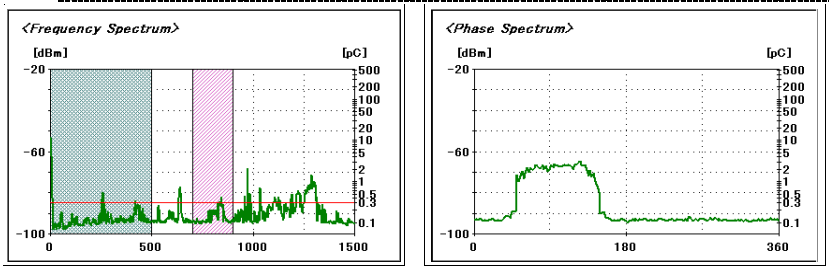

253

S45 16kV 2atm UHF A
shift 150

ニューロ診断結果詳細			
Normal	0.00%	Particle on Spacer	0.00%
External Noise	20.70%	Spacer Crack	0.00%
Mobile Phone	22.20%	Void in Spacer	0.00%
Protrusion	50.10%	Floating Electrode	0.00%
Free Particle	6.80%		
Floating Particle	0.10%		

2008/01/17 20:36:08	Internal	1026 Hz	8.3 pC	-56 dBm	Abnormal	Protrusion	5
2008/01/17 20:32:38	Internal	1026 Hz	5.7 pC	-59 dBm	Abnormal	Free Particle	2
2008/01/17 20:29:08	Internal	1028 Hz	7.2 pC	-57 dBm	Normal	Mobile Phone	0
2008/01/17 20:25:39	Internal	1028 Hz	4.1 pC	-62 dBm	Abnormal	Free Particle	1
2008/01/17 20:22:10	Internal	1030 Hz	6.6 pC	-58 dBm	Normal	Mobile Phone	0
2008/01/17 20:18:42	Internal	1024 Hz	3.8 pC	-63 dBm	Normal	Mobile Phone	0
2008/01/17 20:15:14	Internal	1026 Hz	3.3 pC	-64 dBm	Abnormal	Protrusion	5
2008/01/17 20:11:47	Internal	1026 Hz	3.1 pC	-65 dBm	Abnormal	Protrusion	5
2008/01/17 20:08:21	Internal	1026 Hz	4.1 pC	-62 dBm	Abnormal	Protrusion	5

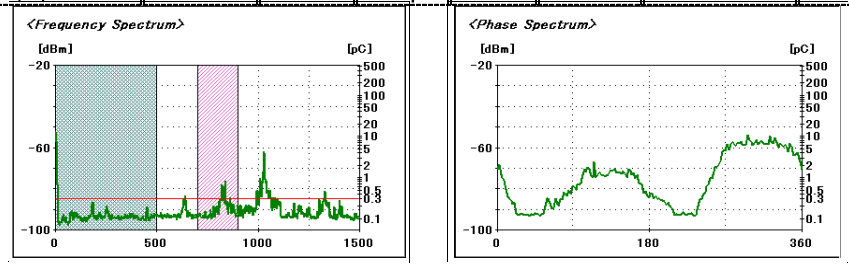

254

S45 16kV 2atm UHF B
shift 150

ニューロ診断結果詳細			
Normal	0.10%	Particle on Spacer	0.00%
External Noise	15.10%	Spacer Crack	0.00%
Mobile Phone	37.20%	Void in Spacer	0.00%
Protrusion	43.60%	Floating Electrode	0.00%
Free Particle	0.00%		
Floating Particle	4.00%		

2008/01/17 20:37:18	Internal	970 Hz	0.8 pC	-77 dBm	Abnormal	Protrusion	1
2008/01/17 20:33:48	Internal	970 Hz	0.6 pC	-79 dBm	Normal	Mobile Phone	0
2008/01/17 20:30:18	Internal	970 Hz	1.9 pC	-69 dBm	Normal	Mobile Phone	0
2008/01/17 20:26:49	Internal	970 Hz	0.7 pC	-78 dBm	Abnormal	Protrusion	1
2008/01/17 20:23:20	Internal	974 Hz	1.2 pC	-73 dBm	Normal	Mobile Phone	0
2008/01/17 20:19:51	Internal	968 Hz	1.2 pC	-73 dBm	Normal	Mobile Phone	0
2008/01/17 20:16:24	Internal	972 Hz	0.7 pC	-78 dBm	Abnormal	Protrusion	1
2008/01/17 20:12:56	Internal	972 Hz	0.7 pC	-77 dBm	Abnormal	Protrusion	1
2008/01/17 20:09:30	Internal	1216 Hz	0.4 pC	-82 dBm	Normal	Mobile Phone	0

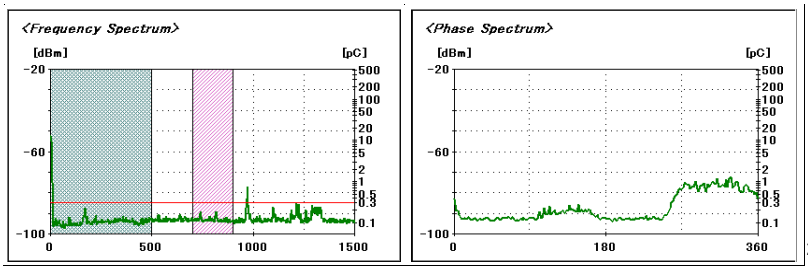

255

S45 16kV 2atm UHF A
shift 167

ニューロ診断結果詳細			
Normal	0.30%	Particle on Spacer	0.00%
External Noise	0.00%	Spacer Crack	0.00%
Mobile Phone	0.00%	Void in Spacer	0.00%
Protrusion	98.90%	Floating Electrode	0.00%
Free Particle	0.90%		
Floating Particle	0.00%		

2008/01/17 21:12:14	Internal	1028 Hz	6.3 pC	-59 dBm	Abnormal	Protrusion	5
2008/01/17 21:08:46	Internal	1024 Hz	1.9 pC	-69 dBm	Abnormal	Protrusion	4
2008/01/17 21:05:18	Internal	1028 Hz	7.2 pC	-57 dBm	Abnormal	Protrusion	5
2008/01/17 21:01:51	Internal	1026 Hz	8.3 pC	-56 dBm	Abnormal	Protrusion	5
2008/01/17 20:56:40	Internal	1026 Hz	4.8 pC	-61 dBm	Abnormal	Protrusion	5
2008/01/17 20:53:17	Internal	1032 Hz	4.5 pC	-61 dBm	Abnormal	Protrusion	5
2008/01/17 20:49:54	Internal	1028 Hz	10.9 pC	-54 dBm	Abnormal	Protrusion	5
2008/01/17 20:46:27	Internal	1030 Hz	4 pC	-63 dBm	Abnormal	Protrusion	5
2008/01/17 20:43:00	Internal	1028 Hz	5 pC	-61 dBm	Abnormal	Protrusion	5

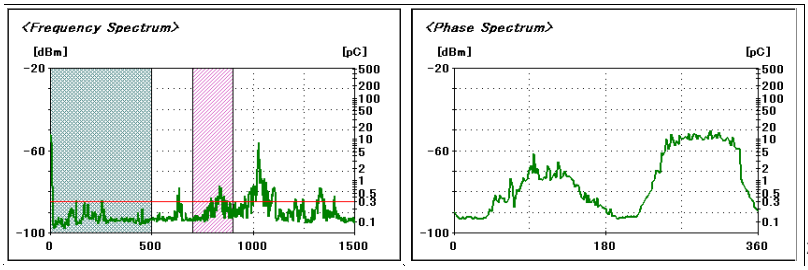

256

S45 16kV 2atm UHF B
shift 167

ニューロ診断結果詳細			
Normal	0.50%	Particle on Spacer	0.00%
External Noise	0.00%	Spacer Crack	0.00%
Mobile Phone	0.00%	Void in Spacer	0.00%
Protrusion	99.30%	Floating Electrode	0.00%
Free Particle	0.00%		
Floating Particle	0.20%		

2008/01/17 21:13:24	Internal	968 Hz	0.8 pC	-77 dBm	Abnormal	Protrusion	1
2008/01/17 21:09:55	Internal	972 Hz	1.1 pC	-73 dBm	Abnormal	Protrusion	4
2008/01/17 21:06:27	Internal	970 Hz	1.3 pC	-73 dBm	Abnormal	Protrusion	4
2008/01/17 21:03:00	Internal	970 Hz	1 pC	-75 dBm	Abnormal	Protrusion	1
2008/01/17 20:57:48	Internal	974 Hz	0.6 pC	-79 dBm	Abnormal	Protrusion	1
2008/01/17 20:54:25	Internal	970 Hz	1.4 pC	-71 dBm	Abnormal	Protrusion	4
2008/01/17 20:51:02	Internal	970 Hz	0.8 pC	-77 dBm	Abnormal	Protrusion	1
2008/01/17 20:47:36	Internal	970 Hz	0.8 pC	-77 dBm	Abnormal	Protrusion	1
2008/01/17 20:44:09	Internal	972 Hz	0.9 pC	-76 dBm	Abnormal	Protrusion	1

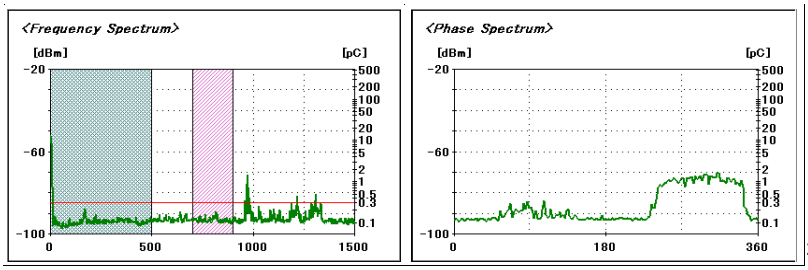

257

EFFECT OF APPLIED VOLTAGE AND PHASE SHIFT SETTING ON SUCCES RATE

EXPERIMENT RESULTS: S270, 3 atm, UHF A, Δ=150⁰

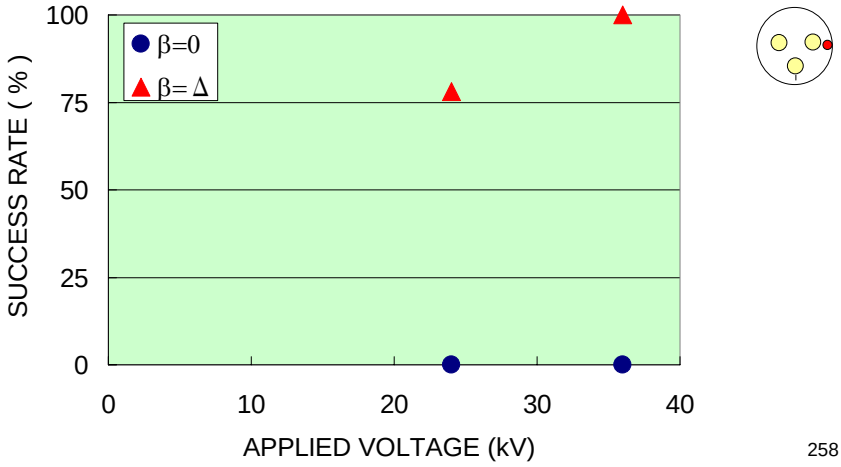

258

EFFECT OF APPLIED VOLTAGE AND PHASE SHIFT SETTING ON SUCCES RATE

EXPERIMENT RESULTS: S270, 2 atm, UHF A, Δ = 150⁰

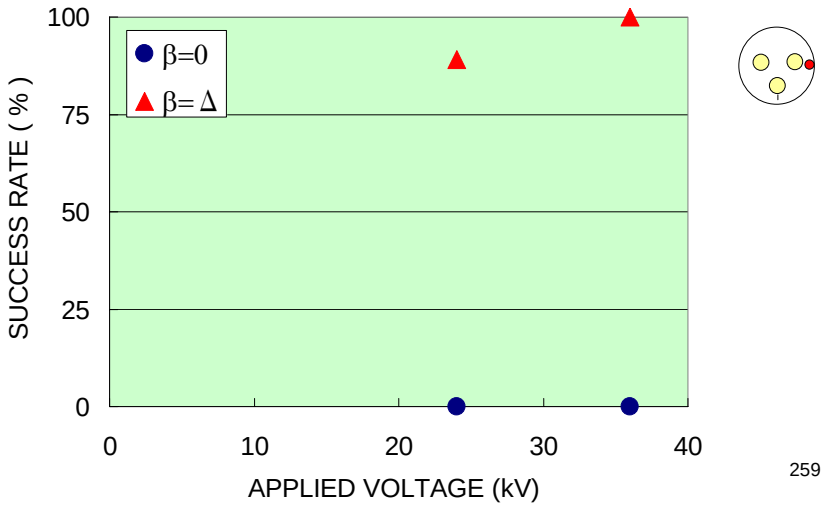

259

S90 1atm 24kV shift 0 UHF A

2007/12/20 20:55:26	1028 Hz	1.5 pC	-71 dBm	Spacer Crack	5
2007/12/20 20:51:55	1028 Hz	3.4 pC	-64 dBm	Spacer Crack	5
2007/12/20 20:48:26	1028 Hz	1.5 pC	-71 dBm	External Noise	0
2007/12/20 20:44:57	1028 Hz	2.4 pC	-67 dBm	Spacer Crack	5
2007/12/20 20:41:28	1030 Hz	1.7 pC	-70 dBm	Particle on Spacer	5
2007/12/20 20:38:00	1028 Hz	2 pC	-69 dBm	Spacer Crack	5
2007/12/20 20:34:32	1028 Hz	1.9 pC	-69 dBm	Spacer Crack	5
2007/12/20 20:31:05	1028 Hz	1.8 pC	-69 dBm	Spacer Crack	5
2007/12/20 20:27:41	1028 Hz	1.6 pC	-70 dBm	Spacer Crack	5

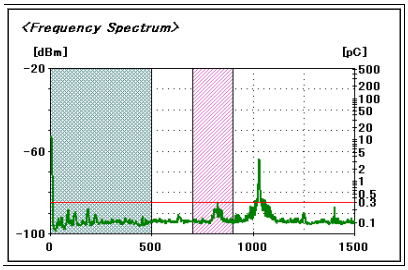

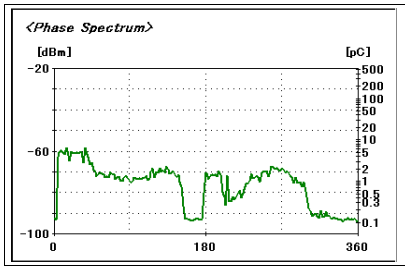

260

S90 1atm 24kV shift 150 UHF A

	2007/12/20 19:53:10	1028 Hz	2.3 pC	-67 dBm	Free Particle	1
	2007/12/20 19:49:40	1028 Hz	1.8 pC	-69 dBm	Free Particle	1
	2007/12/20 19:46:10	1030 Hz	1.9 pC	-69 dBm	Free Particle	1
●	2007/12/20 19:42:41	1028 Hz	3.1 pC	-65 dBm	Free Particle	1
	2007/12/20 19:39:13	1030 Hz	2.1 pC	-68 dBm	Free Particle	1
	2007/12/20 19:35:45	1028 Hz	3.1 pC	-65 dBm	Free Particle	1
	2007/12/20 19:32:18	1028 Hz	1.4 pC	-71 dBm	Free Particle	1
	2007/12/20 19:28:50	1030 Hz	1.4 pC	-71 dBm	Free Particle	1
	2007/12/20 19:25:24	1028 Hz	2.1 pC	-68 dBm	Free Particle	1
	2007/12/20 19:21:58	1030 Hz	1.6 pC	-71 dBm	Free Particle	1

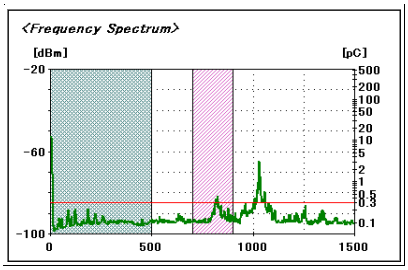

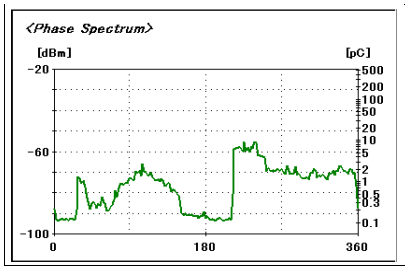

261

S90 1atm 24kV shift 30 UHF A

	2007/12/20 19:11:18	1026 Hz	1.4 pC	-71 dBm	Floating Electrode	1
	2007/12/20 19:07:48	1028 Hz	1.4 pC	-72 dBm	Floating Electrode	1
	2007/12/20 19:04:20	1028 Hz	1.7 pC	-70 dBm	Particle on Spacer	5
	2007/12/20 19:00:50	1028 Hz	1.8 pC	-69 dBm	External Noise	0
●	2007/12/20 18:57:21	1024 Hz	1.8 pC	-69 dBm	Particle on Spacer	5
	2007/12/20 18:53:51	1028 Hz	1.5 pC	-71 dBm	Particle on Spacer	5
	2007/12/20 18:50:23	1030 Hz	1.6 pC	-71 dBm	Particle on Spacer	5
	2007/12/20 18:46:55	1028 Hz	1.3 pC	-72 dBm	Particle on Spacer	5

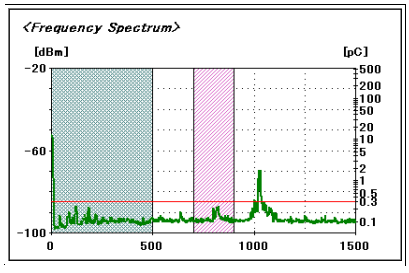

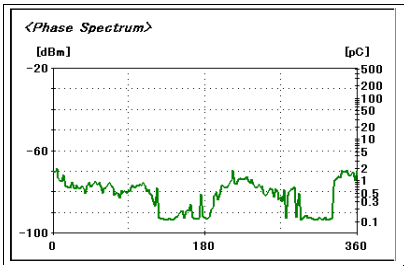

262

S90 1atm 16kV shift 0 UHF A

	2007/12/20 21:30:02	1028 Hz	1.1 pC	-74 dBm	Particle on Spacer	5
	2007/12/20 21:26:32	1028 Hz	1.2 pC	-73 dBm	Particle on Spacer	5
	2007/12/20 21:23:02	1028 Hz	1.1 pC	-73 dBm	Particle on Spacer	5
	2007/12/20 21:19:32	1028 Hz	1 pC	-74 dBm	Particle on Spacer	5
	2007/12/20 21:16:03	1028 Hz	1.6 pC	-70 dBm	Particle on Spacer	5
●	2007/12/20 21:12:35	1028 Hz	1.6 pC	-70 dBm	Particle on Spacer	5
	2007/12/20 21:09:07	1026 Hz	1.4 pC	-71 dBm	Particle on Spacer	5
	2007/12/20 21:05:40	1026 Hz	1 pC	-75 dBm	Particle on Spacer	5

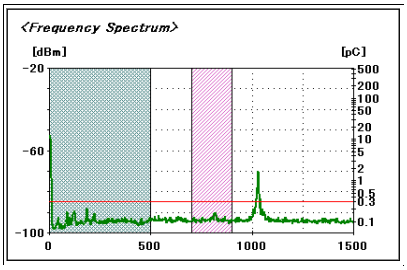

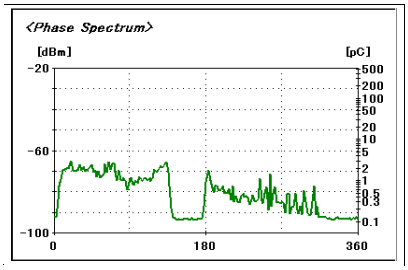

263

S90 1atm 16kV shift 150 UHF A

	2008/01/17 15:26:44	1026 Hz	1 pC	-74 dBm	Free Particle	1
	2008/01/17 15:23:13	1028 Hz	1 pC	-74 dBm	Free Particle	1
	2008/01/17 15:19:42	1028 Hz	1.1 pC	-73 dBm	Free Particle	1
	2008/01/17 15:16:12	1026 Hz	1.1 pC	-73 dBm	Free Particle	1
●	2008/01/17 15:12:43	1030 Hz	1.4 pC	-72 dBm	Protrusion	4
	2008/01/17 15:09:14	1030 Hz	1.1 pC	-74 dBm	Free Particle	1
	2008/01/17 15:05:50	1030 Hz	1.4 pC	-71 dBm	Free Particle	1
	2008/01/17 15:02:23	1028 Hz	1.7 pC	-70 dBm	Free Particle	1
	2008/01/17 14:58:54	1028 Hz	1.1 pC	-74 dBm	External Noise	0

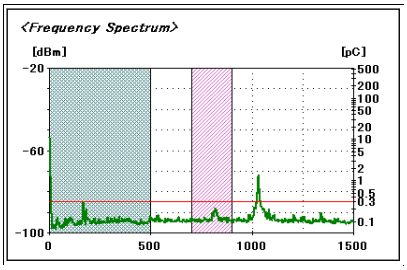

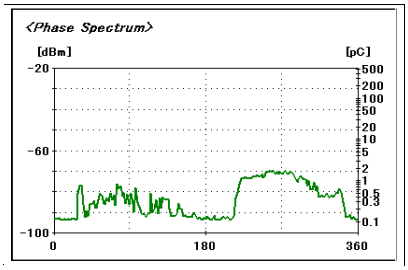

264

S90 1atm 16kV shift 270 UHF A

	2008/01/17 16:01:00	1026 Hz	1.1 pC	-74 dBm	External Noise	0
	2008/01/17 15:57:30	1028 Hz	1.5 pC	-71 dBm	External Noise	0
	2008/01/17 15:54:01	1026 Hz	1.2 pC	-73 dBm	External Noise	0
	2008/01/17 15:50:32	1030 Hz	1.5 pC	-71 dBm	External Noise	0
	2008/01/17 15:47:02	1028 Hz	0.9 pC	-75 dBm	External Noise	0
	2008/01/17 15:43:33	1028 Hz	1.4 pC	-72 dBm	External Noise	0
	2008/01/17 15:40:03	1030 Hz	1.3 pC	-72 dBm	External Noise	0
●	2008/01/17 15:36:35	1028 Hz	2 pC	-69 dBm	External Noise	0
	2008/01/17 15:33:07	1030 Hz	1.8 pC	-69 dBm	External Noise	0

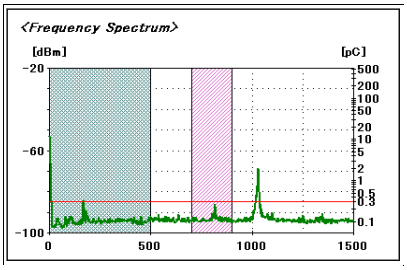

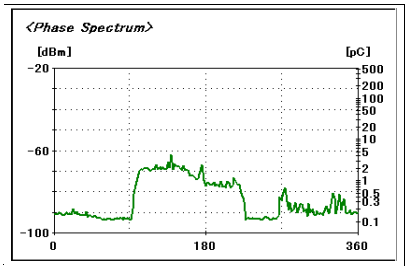

265